

Advanced Magnetic Materials

GUEST EDITORS: ARCADY ZHUKOV, MITSUTERU INOUE,
MANH-HUONG PHAN, AND VLADIMIR SHAVROV





Advanced Magnetic Materials

Physics Research International

Advanced Magnetic Materials

Guest Editors: Arcady Zhukov, Mitsuteru Inoue,
Manh-Huong Phan, and Vladimir Shavrov



Copyright © 2012 Hindawi Publishing Corporation. All rights reserved.

This is a special issue published in "Physics Research International." All articles are open access articles distributed under the Creative Commons Attribution License, which permits unrestricted use, distribution, and reproduction in any medium, provided the original work is properly cited.

Editorial Board

Faustino Aguilera-Granja, Mexico
Rajeev Ahuja, Sweden
N. P. Bigelow, USA
Peter Blunden, Canada
W. Niel Brandt, USA
Sean Cadogan, Canada
Maria G. Castellano, Italy
Arthur E. Champagne, USA
Ashok Chatterjee, India
W. Y. Ching, USA
Anil R. Chourasia, USA
Debashish Chowdhury, India
Thomas D. Cohen, USA
Mike Cottam, Canada
G. Das, India Avishai Dekel, Israel
Jerry P. Draayer, USA
Ehud Duchovni, Israel
Douglas J. Durian, USA
Dipankar Dutta, USA
Simon I. Eidelman, Russia
Faramarz Farahi, USA
Israel Felner, Israel
Yuan Ping Feng, Singapore
Lee Samuel Finn, USA
Moshe Gai, USA Lian Gao, China
Luis Gimeno, Spain
Nikos D. Giokaris, Greece
Leonardo Golubovic, USA
David Goodstein, USA
Christoph Grab, Switzerland
Robert D. Guenther, USA
Atul Gurtu, India

Robert B. Hallock, USA
Yilong Han, Hong Kong
Shlomo Havlin, Israel
Ernest M. Henley, USA
Juan Jose Hernandez-Rey, Spain
Alfred C. Huan, Singapore
Nathan Ida, USA
Martin Kröger, Switzerland
Pablo Laguna, USA
Shaun Lovejoy, Canada
David Lowe, USA
Yuli Lyanda-Geller, USA
Z. Mao, USA
Thomas G. Mason, USA
Grant J. Mathews, USA
P. V. E. McClintock, UK
Paul J. Meakin, USA
Baruch Meerson, Israel
E. Meyer, Switzerland
Sergey B Mirov, USA
Andre Mischke, The Netherlands
W. B. Mori, USA
Franco Nori, USA
K. Alexander Nugent, Australia
Jeremy O'Brien, UK
Hans Rudolf Ott, Switzerland
Ravindra R. Pandey, USA
Byungwoo Park, Korea
Jeevak M. Parpia, USA
Anand Pathak, India
Lorenzo Pavesi, Italy
A. John Peter, China

Jean-François Pinton, France
Viktor A. Podolskiy, USA
Han Pu, USA
Rajeev K. Puri, India
B. Raveau, France
Ali Hussain Reshak, Czech Republic
Slava V. Rotkin, USA
Angel Rubio, Spain
James A. Sauls, USA
Nir J. Shaviv, Israel
Steven Sherwood, Australia
Bellave Shivaram, USA
Theo Siegrist, USA
Ved Ram Singh, India
Roman Sobolewski, USA
H. E. Stanley, USA
Neil S. Sullivan, USA
Uwe Claus Tauber, USA
Ichiro Terasaki, Japan
Frank Tsui, USA
Jack Adam Tuszynski, Canada
Gautam Vemuri, USA
Donepudi Venkateswara Rao, India
Jacobus Verbaarschot, USA
Bennie F. L. Ward, USA
Yue Wu, USA
F. Yakuphanoglu, Turkey
Weitao Yang, USA
Harold J. W. Zandvliet, The Netherlands
Jianhui Zhong, USA

Contents

Advanced Magnetic Materials, Arcady Zhukov, Mitsuteru Inoue, Manh-Huong Phan, and Vladimir Shavrov
Volume 2012, Article ID 385396, 2 pages

Microscopic Theory of Multipole Ordering in f -Electron Systems, Takashi Hotta
Volume 2012, Article ID 762798, 9 pages

Magnetic and Magnetoelectric Properties of Rare Earth Molybdates, B. K. Ponomarev and A. Zhukov
Volume 2012, Article ID 276348, 22 pages

Influence of Magnesium Substitution on Thermal and Electrical Properties of NiCuZn Ferrites for Microinductor Core Applications, M. Venkata Ramana, N. Ramamanohar Reddy, and K. V. Siva kumar
Volume 2012, Article ID 861690, 8 pages

Improvement of Thermal Stability of Nd-Tb-Fe-Co-B Sintered Magnets by Additions of Pr, Ho, Al, and Cu, A. A. Lukin, E. I. Il'yashenko, A. T. Skjeltorp, and G. Helgesen
Volume 2012, Article ID 416717, 4 pages

Fundamental Problems of the Electrodynamics of Heterogeneous Media, N. N. Grinchik and Yu. N. Grinchik
Volume 2012, Article ID 185647, 28 pages

Magneto-Optical and Magnetic Studies of Co-Rich Glass-Covered Microwires, Alexander Chizhik and Valentina Zhukova
Volume 2012, Article ID 690793, 20 pages


Sintering of Soft Magnetic Material under Microwave Magnetic Field, Sadatsugu Takayama, Jun Fukushima, Junichi Nishijo, Midori Saito, Saburo Sano, and Motoyasu Sato
Volume 2012, Article ID 165849, 4 pages

Metamagnetic Phase Transitions in $(\text{Sm}_{0.5}\text{Gd}_{0.5})_{0.55}\text{Sr}_{0.45}\text{MnO}_3$ Ceramics, Fedor N. Bukhanko
Volume 2012, Article ID 632016, 7 pages

Novel Applications of Ferrites, Raúl Valenzuela
Volume 2012, Article ID 591839, 9 pages

Investigation of Multicritical Phenomena in ANNNI Model by Monte Carlo Methods, A. K. Murtazaev and J. G. Ibaev
Volume 2012, Article ID 730812, 4 pages

Softening the Crystal Scaffold for Lifes Emergence, Gargi Mitra-Delmotte and Asoke Nath Mitra
Volume 2012, Article ID 232864, 13 pages



Tailoring of Magnetocaloric Effect in $\text{Ni}_{45.5}\text{Mn}_{43.0}\text{In}_{11.5}$ Metamagnetic Shape Memory Alloy, W. O. Rosa, L. González, J. García, T. Sánchez, V. Vega, Ll. Escoda, J. J. Suñol, J. D. Santos, M. J. P. Alves, R. L. Sommer, V. M. Prida, and B. Hernando
Volume 2012, Article ID 794171, 5 pages

Correlation between the Magnetoresistance, IR Magnetorefectance, and Spin-Dependent Characteristics of Multilayer Magnetic Films, V. G. Kravets
Volume 2012, Article ID 323279, 8 pages

Editorial

Advanced Magnetic Materials

Arcady Zhukov,¹ Mitsuteru Inoue,² Manh-Huong Phan,³ and Vladimir Shavrov⁴

¹ *Departamento de Física de Materiales, Universidad del País Vasco, UPV/EHU, 20018 San Sebastián, Spain and IKERBASQUE, Basque Foundation for Science, 48011 Bilbao, Spain*

² *Department of Electrical and Electronic Information Engineering, Toyohashi University of Technology, -1 Hibarigaoka, Toyohashi 441-8580, Japan*

³ *Department of Physics, University of South Florida, Tampa, FL 33620, USA*

⁴ *Institute of Radioengineering and Electronics, Russian Academy of Sciences, 125009 Moscow, Russia*

Correspondence should be addressed to Arcady Zhukov, arkadi.joukov@ehu.es

Received 11 March 2012; Accepted 11 March 2012

Copyright © 2012 Arcady Zhukov et al. This is an open access article distributed under the Creative Commons Attribution License, which permits unrestricted use, distribution, and reproduction in any medium, provided the original work is properly cited.

This special issue is inspired by a rapidly growing interest in the research of magnetism and magnetic materials, discoveries of novel magnetic materials, and recent progress in the development of functional materials with improved magnetic and magnetotransport properties. The research is demanded by the last advances in technology and engineering and greatly associated with the development of advanced magnetic materials with improved magnetic and magnetotransport properties. Certain industrial sectors, such as magnetic sensors, microelectronics, security, and energy-efficient magnetic refrigerators, demand cost-effective materials with reduced dimensionality and desirable magnetic properties (i.e., enhanced magnetic softness, giant magnetic field sensitivity, large magnetocaloric effect, large shape memory effect, etc.). In particular, the miniaturization of modern magnetoelectronic devices tends to stimulate a rapid development of nanoscale magnetic materials. However, the development of soft magnetic materials in different forms of ribbons, wires, microwires, and multilayered thin films still continues to attract significant attention from the scientific community, as the discovery of the so-called giant magnetoimpedance effect in these materials makes them very attractive for a wide range of high-performance sensor applications ranging from engineering, industry, to biomedicine. In another research area, the development of advanced magnetocaloric materials for advanced magnetic refrigeration technology has also generated growing interest among scientists. The majority of magnetic refrigeration is to develop new materials that are cost effective and possess high cooling efficiencies (i.e., large magnetocaloric

effect over a wide temperature range). In all cases, a comprehensive understanding of the processing-structure-property relationship in the fabricated materials is of critical importance. Consequently, great efforts have been (and are being) focused on systematic theoretical and experimental studies with the overall aim of advancing our current knowledge of the origins of the material properties related to the existence of some special arrangements at the nanometric scale and/or to the prevision of novel unusual macroscopic properties.

This special issue aims to provide most up-to-date information about recent developments in magnetic materials for advanced technologies. It covers a wide range of experimental and theoretical works highlighting the following main topics:

- (i) soft magnetic materials and sensor applications,
- (ii) magnetocaloric materials and magnetic refrigeration,
- (iii) magnetic shape alloys and related applications,
- (iv) amorphous and nanocrystalline magnetic materials and applications,
- (v) metamagnetism,
- (vi) ferrites,
- (vii) electrodynamics of heterogeneous media.

We hope this issue will stimulate further interest in magnetic materials research.

Acknowledgment

Last but not least, we would like to acknowledge all the editorial members, contributed authors and dedicated referees for their invaluable time, great contributions and assistance to this volume. Without such efforts we would not be able to accomplish and bring this special issue to the interested readers.

Arcady Zhukov
Mitsuteru Inoue
Manh-Huong Phan
Vladimir Shavrov

Research Article

Microscopic Theory of Multipole Ordering in f -Electron Systems

Takashi Hotta^{1,2}

¹ Department of Physics, Tokyo Metropolitan University, Hachioji, Tokyo 192-0397, Japan

² Advanced Science Research Center, Japan Atomic Energy Agency, Tokai, Ibaraki 319-1195, Japan

Correspondence should be addressed to Takashi Hotta, hotta@tmu.ac.jp

Received 31 August 2011; Accepted 2 February 2012

Academic Editor: Vladimir Shavrov

Copyright © 2012 Takashi Hotta. This is an open access article distributed under the Creative Commons Attribution License, which permits unrestricted use, distribution, and reproduction in any medium, provided the original work is properly cited.

A microscopic framework to determine multipole ordering in f -electron systems is provided on the basis of the standard quantum field theory. For the construction of the framework, a seven-orbital Hubbard Hamiltonian with strong spin-orbit coupling is adopted as a prototype model. A type of multipole and ordering vector is determined from the divergence of multipole susceptibility, which is evaluated in a random phase approximation. As an example of the application of the present framework, a multipole phase diagram on a three-dimensional simple cubic lattice is discussed for the case of $n = 2$, where n denotes the average f -electron number per site. Finally, future problems concerning multipole ordering and fluctuations are briefly discussed.

1. Introduction

Recently, complex magnetism in rare-earth and actinide compounds has attracted much attention in the research field of condensed matter physics [1–3]. Since in general, spin-orbit coupling between electrons in $4f$ and $5f$ orbitals is strong, spin and orbital degrees of freedom are tightly coupled in f -electron materials. Thus, when we attempt to discuss magnetic ordering in f -electron systems, it is necessary to consider the ordering of spin-orbital complex degrees of freedom, that is, *multipole*. In fact, ordering of higher-rank multipole has been actively investigated both from experimental and theoretical sides in the research field of strongly correlated f -electron systems [2, 3]. Moreover, due to recent remarkable developments in experimental techniques and measurements, nowadays it has been possible to detect directly and/or indirectly the multipole ordering. Note, however, that only spin degree of freedom often remains, when orbital degeneracy is lifted, for instance, due to the effect of crystal structure with low symmetry. In order to promote the research of multipole phenomena, f -electron compounds crystallizing in the cubic structure with high symmetry are quite important. For instance, octupole ordering has been discussed in the phase IV of $\text{Ce}_{0.7}\text{La}_{0.3}\text{B}_6$ [4] and NpO_2 [3, 5–8] with cubic structure. As for NpO_2 , recently, a possibility of dotriacontapole ordering has been also pointed out [9, 10].

Here we emphasize that the study of multipole phenomena has been activated due to the focusing research of filled skutterudite compounds $\text{LnT}_4\text{X}_{12}$ with lanthanide Ln, transition metal atom T, and pnictogen X [11]. Since these compounds crystallize in the cubic structure of T_h point group, they have provided us an ideal stage for the research of multipole physics. Furthermore, many isostructural materials with different kinds of rare-earth and actinide ions have been successfully synthesized, leading to the development of systematic research on multipole ordering. In fact, recent experiments in close cooperation with phenomenological theory have revealed that multipole ordering frequently appears in filled skutterudites. For instance, a rich phase diagram of $\text{PrOs}_4\text{Sb}_{12}$ with field-induced quadrupole order has been unveiled experimentally and theoretically [12–14]. Furthermore, antiferro- Γ_1 -type higher multipole order [2] has been discussed for $\text{PrRu}_4\text{P}_{12}$ [15, 16] and $\text{PrFe}_4\text{P}_{12}$ [17–19].

Now we turn our attention to theoretical research on multipole order. Thus far, theory of multipole ordering has been developed mainly from a phenomenological viewpoint on the basis of an LS coupling scheme for multi- f -electron state. It is true that several experimental results have been explained by those theoretical studies, but we believe that it is also important to promote microscopic approach for understanding of multipole phenomena in parallel with

phenomenological research. Based on this belief, the present author has developed a microscopic theory for multipole-related phenomena with the use of a j - j coupling scheme [1, 20–22]. In particular, octupole ordering in NpO_2 has been clarified by the evaluation of multipole interaction with the use of the standard perturbation method in terms of electron hopping [6–8, 23]. We have also discussed possible multipole states of filled skutterudites by analyzing multipole susceptibility of a multiorbital Anderson model based on the j - j coupling scheme [24–29].

On the other hand, it is still difficult to understand intuitively the physical meaning of multipole degree of freedom due to the mathematically complicated form of multipole operator defined by using total angular momentum. As mentioned above, multipole is considered to be spin-orbital complex degree of freedom. In this sense, it seems to be natural to regard multipole as anisotropic spin-charge density. This point has been emphasized in the visualization of multipole order [6–8, 23]. Then, we have defined multipole as spin-charge density in the form of one-body operator from the viewpoint of multipole expansion of electromagnetic potential from charge distribution in electromagnetism [30, 31]. Due to the definition of multipole in the form of one-electron spin-charge density operator, it has been possible to discuss unambiguously multipole state by evaluating multipole susceptibility even for heavy rare-earth compounds with large total angular momentum [30].

As for the determination of the multipole state, we have proposed to use the optimization of multipole susceptibility on the basis of the standard linear response theory. We have analyzed an impurity Anderson model including seven f orbitals with the use of the numerical renormalization group technique and checked the effectiveness of the microscopic model on the basis of the j - j coupling scheme for the description of multipoles. We have also shown the result for multipole susceptibility of several kinds of filled skutterudite compounds. With the use of the seven-orbital Anderson model, we have discussed field-induced multipole phenomena in Sm-based filled skutterudites, [32] multipole Kondo effect, [33] and multipole state of Yb- and Tm-based filled skutterudites [34]. We have also discussed possible multipole state in transuranium systems such as AmO_2 [35] and magnetic behavior of CmO_2 [36].

From our previous investigations on the basis of the multiorbital Anderson model, it has been clarified that the multipole can be treated as spin-orbital complex degree of freedom in the one-electron operator form. However, in order to discuss the ordering of multipole, it is necessary to consider a periodic system including seven f orbitals per atomic site with strong spin-orbit coupling. The validity of the model on the basis of the j - j coupling scheme can be also checked by such consideration. Namely, for the steady promotion of multipole physics, it is highly expected to treat the multipole ordering in a seven-orbital periodic model by overcoming a heavy task to solve the model including 14 states per atomic site.

In this paper, we define a seven-orbital Hubbard model with strong spin-orbit coupling and explain a procedure to define the multipole ordering by the divergence of multipole

susceptibility from a microscopic viewpoint. For the evaluation of multipole susceptibility, we introduce a random phase approximation. In principle, we can treat all the cases for $n = 1 \sim 13$ on the same footing, but here we focus on the case of $n = 2$ corresponding to Pr and U compounds. As a typical example of the present procedure, we show a phase diagram including quadrupole ordering in a three-dimensional simple cubic lattice. Finally, we also discuss some future problems such as superconductivity induced by multipole fluctuations near the multipole phase.

The organization of this paper is as follows. In Section 2, we explain each part of the seven-orbital Hubbard model with strong spin-orbit coupling. For the reference of readers, we show the list of hopping integrals among f -orbitals along x , y , and z -axes through σ , π , δ , and ϕ bonds. In Section 3, we define the multipole operator as the complex spin-charge degree of freedom in the one-electron form. Then, we explain a scheme to determine the multipole ordering from the multipole susceptibility. Here we use a random phase approximation for the evaluation of the multipole susceptibility. In Section 4, we show the results for the case of $n = 2$ in a three-dimensional simple cubic lattice. We discuss the phase diagram of the multipole ordering. In Section 5, we discuss some future problems and summarize this paper. Throughout this paper, we use such units as $\hbar = k_B = 1$.

2. Model Hamiltonian

The model Hamiltonian H is split into two parts as

$$H = H_{\text{kin}} + H_{\text{loc}}, \quad (1)$$

where H_{kin} denotes a kinetic term and H_{loc} is a local part for potential and interaction. The latter term is further given by

$$H_{\text{loc}} = H_{\text{so}} + H_{\text{CEF}} + H_{\text{C}}, \quad (2)$$

where H_{so} is a spin-orbit coupling term, H_{CEF} indicates crystalline electric field (CEF) potential term, and H_{C} denotes Coulomb interaction term. We explain each term in the following.

2.1. Local f -Electron Term. Among the three terms of H_{loc} , the spin-orbit coupling part is given by

$$H_{\text{so}} = \lambda \sum_{\mathbf{i}, m, \sigma, m', \sigma'} \zeta_{m, \sigma; m', \sigma'} f_{\mathbf{i}m\sigma}^\dagger f_{\mathbf{i}m'\sigma'}, \quad (3)$$

where $f_{\mathbf{i}m\sigma}$ is an annihilation operator of f -electron at site \mathbf{i} , $\sigma = +1$ (-1) for up (down) spin, m is the z -component of angular momentum $\ell = 3$, λ is the spin-orbit interaction, and the matrix elements are expressed by

$$\zeta_{m, \sigma; m, \sigma} = \frac{m\sigma}{2}, \quad (4)$$

$$\zeta_{m+\sigma, -\sigma; m, \sigma} = \frac{\sqrt{\ell(\ell+1) - m(m+\sigma)}}{2},$$

and zero for other cases.

Next we consider the CEF term, which is expressed as

$$H_{\text{CEF}} = \sum_{\mathbf{i}, m, m', \sigma} B_{m, m'} f_{i m \sigma}^\dagger f_{i m' \sigma}, \quad (5)$$

where $B_{m, m'}$ is the CEF potential for f electrons from the ligand ions, which is determined from the table of Hutchings for angular momentum $\ell = 3$ [37]. For the cubic structure with O_h symmetry, $B_{m, m'}$ is expressed by using three CEF parameters, B_{40} and B_{60} , as

$$\begin{aligned} B_{3,3} &= B_{-3,-3} = 180B_{40} + 180B_{60}, \\ B_{2,2} &= B_{-2,-2} = -420B_{40} - 1080B_{60}, \\ B_{1,1} &= B_{-1,-1} = 60B_{40} + 2700B_{60}, \\ B_{0,0} &= 360B_{40} - 3600B_{60}, \\ B_{3,-1} &= B_{-3,1} = 60\sqrt{15}(B_{40} - 21B_{60}), \\ B_{2,-2} &= 300B_{40} + 7560B_{60}. \end{aligned} \quad (6)$$

Note the relation of $B_{m, m'} = B_{m', m}$. Following the traditional notation [38], we define

$$\begin{aligned} B_{40} &= \frac{Wx}{F(4)}, \\ B_{60} &= \frac{W(1 - |x|)}{F(6)}, \end{aligned} \quad (7)$$

where W determines an energy scale for the CEF potential, x specifies the CEF scheme for O_h point group, and $F(4) = 15$ and $F(6) = 180$ for $\ell = 3$.

Finally, the Coulomb interaction term H_C is given by

$$H_1 = \sum_{\mathbf{i}, m_1 \sim m_4} \sum_{\sigma, \sigma'} I_{m_1 m_2 m_3 m_4} f_{i m_1 \sigma}^\dagger f_{i m_2 \sigma'}^\dagger f_{i m_3 \sigma'} f_{i m_4 \sigma}, \quad (8)$$

where the Coulomb integral $I_{m_1 m_2 m_3 m_4}$ is expressed by

$$I_{m_1 m_2 m_3 m_4} = \sum_{k=0}^6 F^k c_k(m_1, m_4) c_k(m_2, m_3). \quad (9)$$

Here F^k is the Slater-Condon parameter and c_k is the Gaunt coefficient which is tabulated in the standard textbooks of quantum mechanics [39]. Note that the sum is limited by the Wigner-Eckart theorem to $k = 0, 2, 4$, and 6 . The Slater-Condon parameters should be determined for the material from the experimental results, but in this paper, for a purely theoretical purpose, we set the ratio among the Slater-Condon parameters as physically reasonable values, given by

$$F^0 : F^2 : F^4 : F^6 = 10 : 5 : 3 : 1. \quad (10)$$

Note that F^6 is considered to indicate the scale of Hund's rule interaction among f orbitals.

2.2. Kinetic Term. Next we consider the kinetic term of f electrons. When we discuss magnetic properties of f -electron materials as well as the formation of heavy quasiparticles, it is necessary to include simultaneously both conduction electrons with wide bandwidth and f electrons

with narrow bandwidth, since the hybridization is essentially important for the formation of heavy quasiparticles. In this sense, it is more realistic to construct orbital-degenerate periodic Anderson model for the theory of multipole ordering in heavy-electron systems.

However, if we set the starting point of the discussion in the periodic Anderson model, the calculations for multipole susceptibility will be very complicated. Thus, we determine our mind to split the problem into two steps: namely, first we treat the formation of heavy quasiparticles and then, we discuss the effective model for such heavy quasiparticles. If we correctly include the symmetry of f -electron orbital, we believe that it is possible to grasp qualitatively correct points concerning the multipole ordering by using an effective kinetic term for f electrons.

Based on the above belief, we consider the effective kinetic term in a tight-binding approximation for f electrons. Then, H_{kin} is expressed as

$$H_{\text{kin}} = \sum_{\mathbf{i}, \mathbf{a}, m, m', \sigma} t_{m, m'}^{\mathbf{a}} f_{i m \sigma}^\dagger f_{i + \mathbf{a} m' \sigma}, \quad (11)$$

where $t_{m, m'}^{\mathbf{a}}$ indicates the f -electron hopping between m - and m' -orbitals of adjacent atoms along the \mathbf{a} direction. The hopping amplitudes are obtained from the table of Slater-Koster integrals, [40–42] but, for convenience, here we show explicitly $t_{m, m'}^{\mathbf{a}}$ on the three-dimensional cubic lattice.

The hopping integrals along the z -axis are given in quite simple forms as

$$\begin{aligned} t_{0,0}^z &= (ff\sigma), \\ t_{-1,-1}^z &= t_{1,1}^z = (ff\pi), \\ t_{-2,-2}^z &= t_{2,2}^z = (ff\delta), \\ t_{-3,-3}^z &= t_{3,3}^z = (ff\phi), \end{aligned} \quad (12)$$

and zeros for other cases. Here $(ff\ell)$ denotes the Slater-Koster integral through ℓ bond between nearest neighbor sites. Note that the above equations are closely related to the definitions of $(ff\sigma)$, $(ff\pi)$, $(ff\delta)$, and $(ff\phi)$.

On the other hand, hopping integrals along the x - and y -axes are given by the linear combination of $(ff\sigma)$, $(ff\pi)$, $(ff\delta)$, and $(ff\phi)$. We express $t_{m, m'}^{\mathbf{a}}$ as

$$t_{m, m'}^{\mathbf{a}} = \sum_{\ell} (ff\ell) E_{m, m'}^{\mathbf{a}\ell}, \quad (13)$$

where the coefficient $E_{m, m'}^{\mathbf{a}\ell}$ indicates the two-center integral along \mathbf{a} direction between m and m' orbitals and ℓ runs among σ , π , δ , and ϕ . In Table 1, we show the values of $E_{m, m'}^{\mathbf{a}\ell}$. Other components are zeros unless they are obtained with the use of relation of $E_{m, m'}^{\mathbf{a}\ell} = E_{m', m}^{\mathbf{a}\ell} = E_{-m, -m'}^{\mathbf{a}\ell}$.

By using the experimental results concerning the Fermi-surface sheets for actual materials, it is possible to determine the Slater-Koster parameters, $(ff\sigma)$, $(ff\pi)$, $(ff\delta)$, and $(ff\phi)$, so as to reproduce the experimental results. Namely, the hopping integrals should be effective ones for quasiparticles, as mentioned above. Here it is important to include correctly the symmetry of local f orbitals in the evaluation of hopping amplitudes, although the whole energy scale will be adjusted by experimental results and band-structure calculations.

TABLE 1: Coefficients $E_{m,m'}^{a\ell}$ along the x - and y -axes between f orbitals of nearest neighbor sites. Note that in double signs, the upper and lower signs correspond to the value along the x - and y -axes, respectively.

m	m'	σ	π	δ	ϕ
-3	-3	5/16	15/32	3/16	1/32
-3	-1	$\mp\sqrt{15}/16$	$\mp\sqrt{15}/32$	$\pm\sqrt{15}/16$	$\pm\sqrt{15}/32$
-3	1	$\sqrt{15}/16$	$-\sqrt{15}/32$	$-\sqrt{15}/16$	$\sqrt{15}/32$
-3	3	$\mp 5/16$	$\pm 15/32$	$\mp 3/16$	$\pm 1/32$
-2	-2	0	5/16	1/2	3/16
-2	0	0	$\mp\sqrt{30}/16$	0	$\pm\sqrt{30}/16$
-2	2	0	5/16	-1/2	3/16
-1	-1	3/16	1/32	5/16	5/32
-1	1	$\mp 3/16$	$\pm 1/32$	$\mp 5/16$	$\pm 5/32$
0	0	0	3/8	0	5/8

3. Multipole Ordering

In order to discuss the multipole ordered phase from the itinerant side, we evaluate the multipole susceptibility χ by following the standard quantum field theory. The multipole susceptibility is defined by

$$\chi(\mathbf{q}, i\nu_n) = \int_0^{1/T} d\tau e^{i\nu_n \tau} \langle \hat{X}_{\mathbf{q}}(\tau) \hat{X}_{-\mathbf{q}}^\dagger(0) \rangle, \quad (14)$$

where $\hat{X}_{\mathbf{q}}$ denotes the multipole operator with momentum \mathbf{q} , $\nu = 2\pi Tn$ is the boson Matsubara frequency with an integer n , T is a temperature, $X_{\mathbf{q}}(\tau) = e^{H\tau} X_{\mathbf{q}} e^{-H\tau}$, and $\langle \dots \rangle$ indicates the thermal average by using H . In the following, we introduce the multipole operator and explain a method to evaluate the susceptibility.

3.1. Multipole Operator. In any case, first it is necessary to define multipole. As for the definition of multipole, readers should consult with [30, 31], but here we briefly explain the definition in order to make this paper self-contained. We define X in the one-electron density-operator form as

$$\hat{X}_{\mathbf{q}} = \sum_{k,\gamma} p_{k,\gamma}(\mathbf{q}) \hat{T}_{\gamma}^{(k)}(\mathbf{q}), \quad (15)$$

where k denotes the rank of multipole, γ indicates the irreducible representation for cubic point group, and $\hat{T}_{\gamma}^{(k)}(\mathbf{q})$ indicates the cubic tensor operator, expressed in the second-quantized form as

$$\hat{T}_{\gamma}^{(k)}(\mathbf{q}) = \sum_{\mathbf{k}, m, \sigma, m', \gamma'} T_{m\sigma, m'\sigma'}^{(k,\gamma)} f_{\mathbf{k}m\sigma}^\dagger f_{\mathbf{k}+\mathbf{q}m'\sigma'}. \quad (16)$$

Here the matrix elements of the coefficient $\hat{T}_{\gamma}^{(k,\gamma)}$ are calculated from the Wigner-Eckert theorem as [43]

$$T_{m\sigma, m'\sigma'}^{(k,\gamma)} = \sum_{j, \mu, \mu', q} G_{\gamma, q}^{(k)} \frac{\langle j || T^{(k)} || j \rangle}{\sqrt{2j+1}} \langle j\mu | j\mu' kq \rangle \times \left\langle j\mu \left| \ell m s \frac{\sigma}{2} \right. \right\rangle \left\langle j\mu' \left| \ell m' s \frac{\sigma'}{2} \right. \right\rangle, \quad (17)$$

where $\ell = 3$, $s = 1/2$, $j = \ell \pm s$, μ runs between $-j$ and j , q runs between $-k$ and k , $G_{\gamma, q}^{(k)}$ is the transformation matrix between spherical and cubic harmonics, $\langle JM || J' M' J'' M'' \rangle$ denotes the Clebsch-Gordan coefficient, and $\langle j || T^{(k)} || j \rangle$ is the reduced matrix element for spherical tensor operator, given by

$$\langle j || T^{(k)} || j \rangle = \frac{1}{2^k} \sqrt{\frac{(2j+k+1)!}{(2j-k)!}}. \quad (18)$$

Note that $k \leq 2j$ and the highest rank is $2j$. When we define multipoles as tensor operators in the space of total angular momentum J on the basis of the LS coupling scheme, there appear multipoles with $k \geq 8$ for the cases of $J \geq 4$, that is, for $2 \leq n \leq 4$ and $8 \leq n \leq 12$, where n is local f -electron number. If we need such higher-rank multipoles with $k \geq 8$, it is necessary to consider many-body operators beyond the present one-body definition.

Note that when we express the multipole moment as (16) and (17), we normalize each multipole operator so as to satisfy the orthonormal condition [44]

$$\text{Tr} \{ \hat{T}^{(k,\gamma)} \hat{T}^{(k',\gamma')} \} = \delta_{kk'} \delta_{\gamma\gamma'}, \quad (19)$$

where $\delta_{kk'}$ denotes the Kronecker's delta.

3.2. Multipole Susceptibility. Now we move to the evaluation of multipole susceptibility. In order to determine the coefficient $p_{k,\gamma}(\mathbf{q})$ in (15), it is necessary to calculate the multipole susceptibility in the linear response theory. The multipole susceptibility is expressed as

$$\chi(\mathbf{q}, i\nu_n) = \sum_{k\gamma, k'\gamma'} p_{k,\gamma} \chi_{k\gamma, k'\gamma'}(\mathbf{q}, i\nu_n) p_{k',\gamma'}^*, \quad (20)$$

where the susceptibility matrix is given by

$$\chi_{k\gamma, k'\gamma'}(\mathbf{q}, i\nu_n) = \sum_{m_1 \sim m_4} \sum_{\sigma_1 \sim \sigma_4} T_{m_1 \sigma_1, m_3 \sigma_3}^{(k,\gamma)} \times \chi_{m_1 \sigma_1, m_2 \sigma_2, m_3 \sigma_3, m_4 \sigma_4}(\mathbf{q}, i\nu_n) T_{m_2 \sigma_2, m_4 \sigma_4}^{(k,\gamma)*}. \quad (21)$$

Then, χ and $p_{k,\gamma}$ are determined by the maximum eigenvalue and the corresponding normalized eigenstate of the susceptibility matrix equation (21).

In order to calculate actually the multipole susceptibility, it is necessary to introduce an appropriate approximation. In this paper, we use a random phase approximation (RPA) for the evaluation of multipole susceptibility. For the purpose, we redivide the Hamiltonian H into two parts as

$$H = H_0 + H_1, \quad (22)$$

where H_0 indicates the one-electron part given by $H_0 = H_{\text{kin}} + H_{\text{so}} + H_{\text{CEF}}$ and H_1 is the interaction part, which is just equal to H_C in the present case. Then, we consider the perturbation expansion in terms of the Coulomb interaction.

The susceptibility diagrams are shown in Figure 1 and they are expressed in a compact matrix form as

$$\hat{\chi} = \hat{\chi}^{(0)} [\hat{1} - \hat{U} \hat{\chi}^{(0)}]^{-1} + \hat{\chi}^{(0)} [\hat{1} + \hat{J} \hat{\chi}^{(0)}]^{-1} - \hat{\chi}^{(0)}, \quad (23)$$

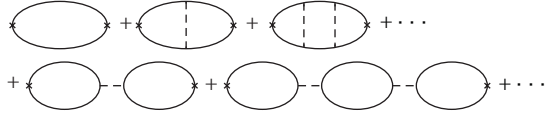


FIGURE 1: Feynman diagrams for multipole susceptibility in the RPA. The solid curve and broken line denote the noninteracting Green's function $G^{(0)}$ and Coulomb interaction, respectively.

where \hat{U} and \hat{J} are, respectively, given by

$$\begin{aligned} U_{m_1\sigma_1 m_2\sigma_2, m_3\sigma_3 m_4\sigma_4} &= I_{m_1 m_2, m_3 m_4} \delta_{\sigma_1 \sigma_4} \delta_{\sigma_2 \sigma_3}, \\ J_{m_1\sigma_1 m_2\sigma_2, m_3\sigma_3 m_4\sigma_4} &= I_{m_1 m_2, m_4 m_3} \delta_{\sigma_1 \sigma_3} \delta_{\sigma_2 \sigma_4}, \end{aligned} \quad (24)$$

and the dynamical susceptibility $\hat{\chi}^{(0)}$ is given by

$$\begin{aligned} \chi_{m_1\sigma_1 m_2\sigma_2, m_3\sigma_3 m_4\sigma_4}^{(0)}(\mathbf{q}, i\nu_n) \\ = -T \sum_{n'} \sum_{\mathbf{k}} G_{m_1\sigma_1, m_4\sigma_4}^{(0)}(\mathbf{k}, i\omega_{n'}) \\ \times G_{m_2\sigma_2, m_3\sigma_3}^{(0)}(\mathbf{k} + \mathbf{q}, i\omega_{n'} + i\nu_n). \end{aligned} \quad (25)$$

Here $G^{(0)}$ is the one-electron Green's function defined by the noninteracting part H_0 .

In order to determine the multipole ordering, it is necessary to detect the divergence of χ at $\nu_n = 0$. We cannot evaluate the susceptibility just at a diverging point, but we find such a critical point by the extrapolation of $1/\chi_{\max}$ as a function of U , where U indicates the energy scale of the Slater-Condon parameters and χ_{\max} denotes the maximum eigenvalue of susceptibility matrix equation (21) for $\nu_n = 0$. When we increase the magnitude of U , $1/\chi_{\max}$ is gradually decreased from the value in the weak-coupling limit. In actual calculations, we terminate the calculation when $1/\chi_{\max}$ arrives at a value in the order of unity. By using the calculated values of $1/\chi_{\max}$, we make an extrapolation of $1/\chi_{\max}$ as a function of U . Then, we find a critical value of U at which $1/\chi_{\max}$ becomes zero. As for the type of multipole and ordering vector in the ordered phase, we extract such information from the eigenvectors of the susceptibility matrix corresponding to the maximum eigenvalue. By performing the above calculations, it is possible to find the multipole ordered phase from a microscopic viewpoint in principle.

4. Results

In the previous sections, we have explained the model Hamiltonian and the procedure to determine the type of multipole ordering. We believe that the present procedure can be applied to actual materials, but there are so many kinds of materials and multipole phenomena. Here we show the calculated results for the case of $n = 2$ concerning Γ_3 non-Kramers quadrupole ordering, in order to see how the present procedure works. The results for actual materials will be discussed elsewhere.

4.1. CEF States. First we discuss the local CEF states in order to determine the CEF parameter. We consider the case of

$n = 2$ corresponding to Pr^{3+} and U^{4+} ions. Since we discuss the local electron state, the energy unit is taken as F^6 . As for the spin-orbit coupling, here we take $\lambda/F^6 = 0.1$. Concerning the value of W , it should be smaller than λ and we set W as $W/F^6 = 0.001$.

In Figure 2, we show the CEF energies as functions of x . As easily understood from the discussion in the *LS* coupling scheme, the ground state multiplet for $n = 2$ is characterized by $J = 4$, where J is total angular momentum given by $J = |L - S|$ with angular momentum L and spin momentum S . For $n = 2$, we find $L = 5$ and $S = 1$ from the Hund's rules and, thus, we obtain $J = 4$. Due to the effect of cubic CEF, the nonet of $J = 4$ is split into four groups as Γ_1 singlet, Γ_3 non-Kramers doublet, Γ_4 triplet, and Γ_5 triplet. In the present diagonalization of H_{loc} , we find such CEF states, as shown in Figure 2. When we compare this CEF energy diagram with that of the *LS* coupling scheme [38], we find that the shape of curves and the magnitude of excitation energy are different with each other. However, from the viewpoint of symmetry, the structure of the low-energy states is not changed between the *LS* and *j-j* coupling schemes [1]. Since we are interested in a possibility of Γ_3 quadrupole ordering, we choose the value of x as $x = 0.0$ in the following.

4.2. Energy Bands. Next we consider the band structure obtained by the diagonalization of $H_0 = H_{\text{kin}} + H_{\text{CEF}} + H_{\text{so}}$. As for the Slater-Koster integrals, it is one way to determine them so as to reproduce the Fermi-surface sheets of actual materials, but here we determine them from a theoretical viewpoint as

$$-(ff\sigma) = (ff\delta) = t, \quad (ff\pi) = (ff\phi) = -t/2, \quad (26)$$

where t indicates the magnitude of hopping amplitude. The size of t should be determined by the quasi-particle bandwidth, but here we simply treat it as an energy unit.

In Figure 3, we depict the eigen energies of H_0 along the lines connecting some symmetric points in the first Brillouin zone. As for the spin-orbit coupling and CEF parameters, we set $\lambda/t = 0.1$ and $W/t = 0.001$. First we note that there exist seven bands and each band has double degeneracy due to time-reversal symmetry, which is distinguished by pseudospin. Since the magnitude of λ is not so large, we do not observe a clear splitting between $j = 7/2$ octet and $j = 5/2$ sextet bands. Around at Γ point, we find that $j = 5/2$ sextet is split into two groups, Γ_7 doublet and Γ_8 quartet. Here we note that the energy of Γ_8 quartet is lower than that of Γ_7 . Since the Γ_8 has orbital degeneracy, it becomes an origin of the formation of Γ_3 non-Kramers doublet, when we accommodate a couple of electrons per site.

Note that the Fermi level is denoted by a horizontal line, which is determined by the condition of $n = 2$, where n is the average electron number per site. When we pay our attention to the band near the Fermi level, we find that the orbital degeneracy exists in the bands on the Fermi surface. For instance, we see the degenerate bands on the Fermi surface around the Γ point. Such orbital degeneracy in the momentum space is considered to be a possible source

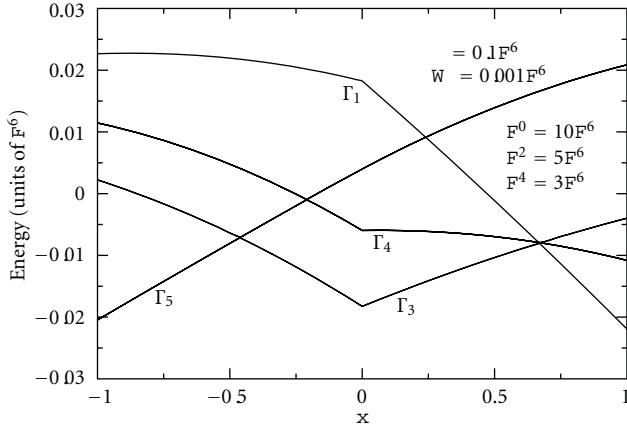


FIGURE 2: CEF energy levels obtained by the diagonalization of H_{loc} for $\lambda/F^6 = 0.1$ and $W/F^6 = 0.001$ with $F^0 = 10F^6$, $F^2 = 5F^6$, and $F^4 = 3F^6$.

of Γ_3 quadrupole ordering, which will be discussed in the next subsection. Finally, in the present case, we expect the appearance of the large-volume Fermi surface as well as the small-size pocket-like Fermi surface. Such mixture of the Fermi surface sheets with different topology may be an important issue for the appearance of higher-rank multipole ordering.

4.3. Phase Diagram. Now we show the phase diagram of the multipole state. First it is necessary to calculate the susceptibility equation (25) at $\nu_n = 0$. As for the momentum \mathbf{q} , we divide the first Brillouin zone into $16 \times 16 \times 16$ meshes. Concerning the momentum integration in (25), we exploit the Gauss-Legendre quadrature with due care. At low temperatures such as $T/t = 0.01$, it seems to be enough to divide the range between $-\pi$ and π into 60 segments along each direction axis. As found in (25), $\chi^{(0)}$ has 14^4 components in the spin-orbital space, but it is not necessary to calculate all the components due to the symmetry argument. We have checked that it is enough to evaluate 1586 components of $\chi^{(0)}$.

We set the parameters as $\lambda/t = 0.1$, $x = 0.0$, $W/t = 0.001$, $F^2 = 0.5F^0$, $F^4 = 0.3F^0$, $F^6 = 0.1F^0$, $-(ff\sigma) = (ff\delta) = t$, and $(ff\pi) = (ff\phi) = -t/2$. Note that the ratio among the Slater-Condon parameters is the same as that in Figure 2. We also note that the hopping amplitude t is relatively large compared with local potential and interactions, since we consider the multipole ordering from the itinerant side. Here we emphasize that our framework actually works for the microscopic discussion on the multipole ordering. A way to determine more realistic parameters in the model will be discussed elsewhere.

By changing the values of temperature T/t , we depict the phase diagram in the plane of t/F^0 and T/t . Note that t^2/F^0 corresponds to the typical magnitude of multipole-multipole interaction between nearest neighbor sites. As naively understood, when the temperature is increased, larger value of U is needed to obtain the ordered state. Then, the phase diagram is shown in Figure 4. We evaluate

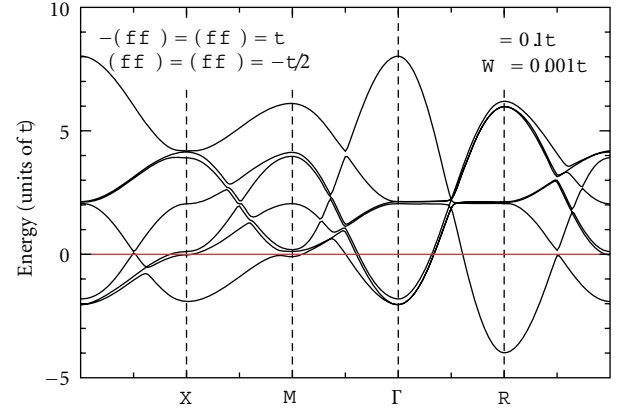


FIGURE 3: Energy band structure obtained by the diagonalization of H_0 for $(ff\sigma) = -t$, $(ff\pi) = -t/2$, $(ff\delta) = t$, $(ff\phi) = -t/2$, $\lambda/t = 0.1$, and $W/t = 0.001$. Note that we show the eigen energies along the lines of $\Gamma \rightarrow X \rightarrow M \rightarrow \Gamma \rightarrow R \rightarrow X$.

the maximum eigenvalue of the multipole susceptibility by increasing F^0/t . One may think that the magnitude of t/F^0 in Figure 4 is too small to obtain reasonable results in the RPA calculations. Here we note that the total bandwidth of the seven-orbital system is in the order of $10t$, as shown in Figure 3. Namely, the critical value of the interaction F_c^0 at low enough temperatures is considered to be in the order of the total bandwidth. In this sense, we consider that the value of t/F^0 in Figure 4 is *not* small for the RPA calculations. Note also that when the temperature is increased, the magnitude of noninteracting susceptibility is totally suppressed, leading to the enhancement of F_c^0 . Thus, t/F^0 is decreased when T is increased, as observed in Figure 4.

At low temperatures as $T/t < 0.3$, we obtain that the maximum eigen value of susceptibility matrix is characterized by the multipole with Γ_3 symmetry and the ordering vector $\mathbf{Q} = (\pi, \pi, \pi)$. The component of the multipole depends on the temperature, but the 90% of the optimized multipole is rank 2 (quadrupole). Others are rank 4 (hexadecapole) and rank 6 (tetrahexacontapole) components, which are about 10%. Note again that the multipoles with the same symmetry are mixed in general, even if the rank of the multipole is different. Namely, quadrupole is the main component, while hexadecapole and tetrahexacontapole are included with significant amounts. Note also that the phase diagram is shown only in the region of $T/t < 1$, but the boundary curve approaches the line of $t/F^0 = 0$. Since the case with very large F^0 is unrealistic, we do not pay our attention to the phase for $T > t$, although we can continue the calculation in such higher temperature region.

When we increase the temperature, the magnetic phase is observed for $T/t > 0.3$. The main component is Γ_4 dipole and the ordering vector is $\mathbf{Q} = (0, 0, 0)$. Note that the susceptibility for Γ_4 multipole moment does not mean magnetic susceptibility, which is evaluated by the response of magnetic moment $\mathbf{L} + 2\mathbf{S}$, that is, $\mathbf{J} + \mathbf{S}$. At $T/t = 0.4$, admixture of the multipole is as follows: rank 1 (dipole) 90.7%, rank 3 (octupole) 6.5%, rank 5 (dotriacontapole) 2.1%, and rank

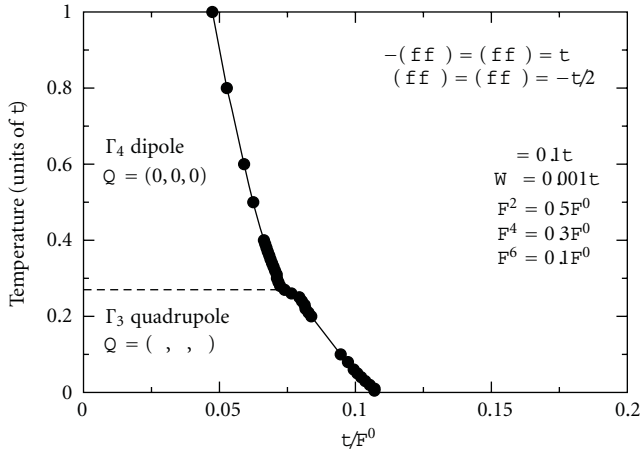


FIGURE 4: Phase diagram of the multipole ordering for $n = 2$ on the three-dimensional simple cubic lattice.

7 (octacosahedron) 0.7%. The amounts are changed by the temperature, but the main component is always dipole. We have found the low-temperature antiferroquadrupole state and the high-temperature ferromagnetic phase. Such a combination of nonmagnetic and magnetic phases can be observed in other parameter sets including quadrupole ordering.

5. Discussion and Summary

We have constructed the microscopic framework to discuss the multipole ordering due to the evaluation of multipole susceptibility in f -electron systems on the basis of the seven-orbital Hubbard model with strong spin-orbit coupling. For the evaluation of multipole susceptibility, we have used the RPA and found the critical point from $1/\chi_{\max}$. As an example of the present scheme, we have shown the results for the case of $n = 2$ concerning quadrupole ordering on the three-dimensional simple cubic lattice. If we specify the lattice structure and determine the hopping parameter from the comparison with the experimental results on the Fermi-surface sheets, in principle, it is possible to determine the type of multipole ordering with the use of appropriate local CEF parameters and Coulomb interactions.

Although the microscopic theory of multipole ordering has been proposed, it is necessary to elaborate the present scheme both from theoretical and experimental viewpoints. In order to enhance the effectiveness of the present procedure, we should increase the applicability of the theory. For instance, we have not considered at all the sublattice structure in this paper, but in actuality, the staggered-type multipole ordering has been observed. In order to reproduce the structure, it is necessary to maximize the multipole susceptibility by taking into account the sublattice structure. It is one of future problems from a theoretical viewpoint.

It is also highly expected that the present scheme should be applied to actual materials in order to explain the origin of multipole ordering. For instance, it is interesting to seek for the origin of peculiar incommensurate quadrupole ordering

observed in PrPb_3 [45]. At the first glance, it seems to be quite difficult to explain the origin of the Γ_3 quadrupole ordering with the ordering vector of $\mathbf{Q} = (\pi/2 \pm \delta, \pi/2 \pm \delta, 0)$ with $\delta = \pi/8$. However, if we use the present scheme, it may be possible to find a solution in a systematic way. Another issue is the revisit to octupole and higher-rank multipole ordering in NpO_2 . The significant amount of dotriacontapole component may be understood naturally in the present scheme.

Another interesting future problem is the emergence of superconductivity near the multipole ordered phase. It has been widely accepted that anisotropic d -wave superconductivity appears in the vicinity of the antiferromagnetic phase, as observed in several kinds of strongly correlated electron materials. In general, near the quantum phase transition, anisotropic superconducting pairs are formed due to the effect of quantum critical fluctuations. Thus, also in the vicinity of multipole ordering, superconductivity is generally expected to occur. Even from purely theoretical interest, it is worthwhile to investigate superconductivity near the antiferroquadrupole phase in Figure 4. When we turn our attention to actual material, in $\text{PrIr}_2\text{Zn}_{20}$, superconductivity has been observed and quadrupole fluctuations have been considered to play some roles [46]. Within the RPA, it is possible to discuss the appearance of superconductivity in the vicinity of quadrupole ordering in the present scheme. It is another future problem.

In summary, we have proposed the prescription to determine the type of multipole ordering from a microscopic viewpoint on the basis of the seven-orbital Hubbard model. The multipole susceptibility has been obtained in the RPA and the quadrupole ordering has been actually discussed in a way similar to that for the spin ordering in the single-orbital Hubbard model. The application to actual f -electron materials will be discussed elsewhere, but we believe that the present scheme is useful to consider the origin of multipole ordering. In addition, a possibility of superconductivity near the multipole ordering is an interesting future problem.

Acknowledgments

The author thanks K. Ueda for discussions on heavy-electron systems. This work has been supported by a Grant-in-Aid for Scientific Research on Innovative Areas “Heavy Electrons” (no. 20102008) of The Ministry of Education, Culture, Sports, Science, and Technology, Japan. The computation in this work has been partly done with the use of the facilities of the Supercomputer Center of Institute for Solid State Physics, University of Tokyo.

References

- [1] T. Hotta, “Orbital ordering phenomena in d - and f -electron systems,” *Reports on Progress in Physics*, vol. 69, no. 7, article R02, pp. 2061–2155, 2006.
- [2] Y. Kuramoto, H. Kusunose, and A. Kiss, “Multipole orders and fluctuations in strongly correlated electron systems,” *Journal of the Physical Society of Japan*, vol. 78, no. 7, Article ID 072001, 2009.

- [3] P. Santini, S. Carretta, G. Amoretti, R. Caciuffo, N. Magnani, and G. H. Lander, "Multipolar interactions in f -electron systems: the paradigm of actinide dioxides," *Reviews of Modern Physics*, vol. 81, no. 2, pp. 807–863, 2009.
- [4] K. Kuwahara, K. Iwasa, M. Kohgi, N. Aso, M. Sera, and F. Iga, "Detection of neutron scattering from phase IV of $\text{Ce}_{0.7}\text{La}_{0.3}\text{B}_6$: a confirmation of the octupole order," *Journal of the Physical Society of Japan*, vol. 76, no. 9, Article ID 093702, 2007.
- [5] Y. Tokunaga, Y. Homma, S. Kambe et al., "NMR evidence for triple- \vec{q} multipole structure in NpO_2 ," *Physical Review Letters*, vol. 94, no. 13, Article ID 137209, 2005.
- [6] K. Kubo and T. Hotta, "Microscopic theory of multipole ordering in NpO_2 ," *Physical Review B*, vol. 71, no. 14, Article ID 140404, 2005.
- [7] K. Kubo and T. Hotta, "Analysis of f -p model for octupole ordering in NpO_2 ," *Physical Review B*, vol. 72, no. 13, Article ID 132411, 2005.
- [8] K. Kubo and T. Hotta, "Multipole ordering in f -electron systems on the basis of a j - j coupling scheme," *Physical Review B*, vol. 72, no. 14, Article ID 144401, 2005.
- [9] P. Santini, S. Carretta, N. Magnani, G. Amoretti, and R. Caciuffo, "Hidden order and low-energy excitations in NpO_2 ," *Physical Review Letters*, vol. 97, no. 20, Article ID 207203, 2006.
- [10] M.-T. Suzuki, N. Magnani, and P. M. Oppeneer, "First-principles theory of multipolar order in neptunium dioxide," *Physical Review B*, vol. 82, no. 24, Article ID 241103, 2010.
- [11] H. Sato, H. Sugawara, Y. Aoki, and H. Harima, "Magnetic properties of filled skutterudites," in *Handbook of Magnetic Materials*, K. H. J. Buschow, Ed., vol. 18, pp. 1–110, Elsevier, Amsterdam, The Netherlands, 2009.
- [12] Y. Aoki, T. Namiki, S. Ohsaki, S. R. Saha, H. Sugawara, and H. Sato, "Thermodynamical study on the heavy-fermion superconductor $\text{PrOs}_4\text{Sb}_{12}$: evidence for field-induced phase transition," *Journal of the Physical Society of Japan*, vol. 71, no. 9, pp. 2098–2101, 2002.
- [13] T. Tayama, T. Sakakibara, H. Sugawara, Y. Aoki, and H. Sato, "Magnetic phase diagram of the heavy fermion superconductor $\text{PrOs}_4\text{Sb}_{12}$," *Journal of the Physical Society of Japan*, vol. 72, no. 6, pp. 1516–1522, 2003.
- [14] R. Shiina and Y. Aoki, "Theory of field-induced phase transition in $\text{PrOs}_4\text{Sb}_{12}$," *Journal of the Physical Society of Japan*, vol. 73, no. 3, pp. 541–544, 2004.
- [15] T. Takimoto, "Antiferro-hexadecapole scenario for metal-insulator transition in $\text{PrRu}_4\text{P}_{12}$," *Journal of the Physical Society of Japan*, vol. 75, no. 3, Article ID 034714, 2006.
- [16] K. Iwasa, L. Hao, K. Kuwahara et al., "Evolution of 4f electron states in the metal-insulator transition of $\text{PrRu}_4\text{P}_{12}$," *Physical Review B*, vol. 72, no. 2, Article ID 024414, 2005.
- [17] A. Kiss and Y. Kuramoto, "Scalar order: possible candidate for order parameters in skutterudites," *Journal of the Physical Society of Japan*, vol. 75, no. 10, Article ID 103704, 2006.
- [18] O. Sakai, J. Kikuchi, R. Shiina et al., "Experimental and theoretical studies of NMR in $\text{PrFe}_4\text{P}_{12}$," *Journal of the Physical Society of Japan*, vol. 76, no. 2, Article ID 024710, 2007.
- [19] J. Kikuchi, M. Takigawa, H. Sugawara, and H. Sato, "On the symmetry of low-field ordered phase of $\text{PrFe}_4\text{P}_{12}$: ^3P NMR," *Journal of the Physical Society of Japan*, vol. 76, no. 4, Article ID 043705, 2007.
- [20] T. Hotta and K. Ueda, "Construction of a microscopic model for f -electron systems on the basis of a j - j coupling scheme," *Physical Review B*, vol. 67, no. 10, Article ID 104518, 2003.
- [21] T. Hotta, "Spin and orbital structure of uranium compounds on the basis of a j - j coupling scheme," *Physical Review B*, vol. 70, no. 5, pp. 054405–10, 2004.
- [22] H. Onishi and T. Hotta, "An orbital-based scenario for the magnetic structure of neptunium compounds," *New Journal of Physics*, vol. 6, article 193, 2004.
- [23] K. Kubo and T. Hotta, "Multipole ordering in f -electron systems," *Physica B*, vol. 378–380, pp. 1081–1082, 2006.
- [24] T. Hotta, "Magnetic fluctuations of filled skutterudites emerging in the transition region between singlet and triplet states," *Physical Review Letters*, vol. 94, no. 6, Article ID 067003, 2005.
- [25] T. Hotta, "Microscopic approach to magnetism and superconductivity of f -electron systems with filled skutterudite structure," *Journal of the Physical Society of Japan*, vol. 74, no. 4, pp. 1275–1288, 2005.
- [26] T. Hotta, "Multipole fluctuations in filled skutterudites," *Journal of the Physical Society of Japan*, vol. 74, no. 9, pp. 2425–2429, 2005.
- [27] T. Hotta and H. Harima, "Effective crystalline electric field potential in a j - j coupling scheme," *Journal of the Physical Society of Japan*, vol. 75, no. 12, Article ID 124711, 2006.
- [28] T. Hotta, "Microscopic aspects of multipole properties of filled skutterudites," *Journal of Magnetism and Magnetic Materials*, vol. 310, no. 2, pp. 1691–1697, 2007.
- [29] T. Hotta, "Multipole susceptibility of multi-orbital Anderson model coupled with Jahn-Teller phonons," *Journal of the Physical Society of Japan*, vol. 76, no. 3, Article ID 034713, 2007.
- [30] T. Hotta, "Multipole state of heavy lanthanide filled skutterudites," *Journal of the Physical Society of Japan*, vol. 76, no. 8, Article ID 083705, 2007.
- [31] T. Hotta, "Multipole as f -electron spin-charge density in filled skutterudites," *Journal of the Physical Society of Japan*, vol. 77, supplement A, pp. 96–101, 2008.
- [32] T. Hotta, "Field-induced multipole states of Sm-based filled skutterudites," *Journal of the Physical Society of Japan*, vol. 77, no. 7, Article ID 074716, 2008.
- [33] T. Hotta, "Magnetically robust multipole Kondo effect," *Journal of Physics: Conference Series*, vol. 150, no. 4, Article ID 042061, 2009.
- [34] T. Hotta, "Construction of a microscopic model for Yb and Tm compounds on the basis of a j - j coupling scheme," *Journal of the Physical Society of Japan*, vol. 79, no. 9, Article ID 094705, 2010.
- [35] T. Hotta, "Microscopic analysis of multipole susceptibility of actinide dioxides: a scenario of multipole ordering in AmO_2 ," *Physical Review B*, vol. 80, no. 2, Article ID 024408, 2009.
- [36] F. Niikura and T. Hotta, "Magnetic behavior of curium dioxide with a nonmagnetic ground state," *Physical Review B*, vol. 83, no. 17, Article ID 172402, 2011.
- [37] M. T. Hutchings, "Point-charge calculations of energy levels of magnetic ions in crystalline electric fields," *Solid State Physics*, vol. 16, pp. 227–273, 1964.
- [38] K. R. Lea, M. J. M. Leask, and W. P. Wolf, "The raising of angular momentum degeneracy of f -electron terms by cubic crystal fields," *Journal of Physics and Chemistry of Solids*, vol. 23, no. 10, pp. 1381–1405, 1962.
- [39] J. C. Slater, *Quantum Theory of Atomic Structure*, McGraw-Hill, New York, NY, USA, 1960.
- [40] J. C. Slater and G. F. Koster, "Simplified LCAO method for the periodic potential problem," *Physical Review*, vol. 94, no. 6, pp. 1498–1524, 1954.

- [41] R. R. Sharma, "General expressions for reducing the Slater-Koster linear combination of atomic orbitals integrals to the two-center approximation," *Physical Review B*, vol. 19, no. 6, pp. 2813–2823, 1979.
- [42] K. Takegahara, Y. Aoki, and A. Yanase, "Slater-Koster tables for f -electrons," *Journal of Physics C*, vol. 13, no. 4, article 016, pp. 583–588, 1980.
- [43] T. Inui, Y. Tanabe, and Y. Onodera, *Group Theory and Its Applications in Physics*, Springer, Berlin, Germany, 1996.
- [44] K. Kubo and T. Hotta, "Magnetic susceptibility of multiorbital systems," *Journal of the Physical Society of Japan*, vol. 75, no. 1, Article ID 013702, 2006.
- [45] T. Onimaru, T. Sakakibara, N. Aso, H. Yoshizawa, H. S. Suzuki, and T. Takeuchi, "Observation of modulated quadrupolar structures in PrPb_3 ," *Physical Review Letters*, vol. 94, no. 19, Article ID 197201, 2005.
- [46] T. Onimaru, K. T. Matsumoto, Y. F. Inoue et al., "Antiferroquadrupolar ordering in a Pr-based superconductor $\text{PrIr}_2\text{Zn}_{20}$," *Physical Review Letters*, vol. 106, no. 17, Article ID 177001, 2011.

Review Article

Magnetic and Magnetoelectric Properties of Rare Earth Molybdates

B. K. Ponomarev¹ and A. Zhukov^{2,3}

¹*Institute of Solid State Physics, Russian Academy of Sciences, 142432 Chernogolovka, Russia*

²*IKERBASQUE, Basque Foundation for Science, 48011 Bilbao, Spain*

³*Departamento de Física de Materiales, Facultad de Químicas, UPV/EHU, 20009 San Sebastian, Spain*

Correspondence should be addressed to A. Zhukov, arkadi.joukov@ehu.es

Received 27 July 2011; Accepted 14 February 2012

Academic Editor: Mitsuteru Inoue

Copyright © 2012 B. K. Ponomarev and A. Zhukov. This is an open access article distributed under the Creative Commons Attribution License, which permits unrestricted use, distribution, and reproduction in any medium, provided the original work is properly cited.

We present results on ferroelectric, magnetic, magneto-optical properties and magnetoelectric effect of rare earth molybdates (gadolinium molybdate, GMO, and terbium molybdate, TMO, and samarium molybdate, SMO), belonging to a new type of ferroelectrics predicted by Levanyuk and Sannikov. While cooling the tetragonal β -phase becomes unstable with respect to two degenerate modes of lattice vibrations. The β - β' transition is induced by this instability. The spontaneous polarization appears as a by-product of the lattice transformation. The electric order in TMO is of antiferroelectric type. Ferroelectric and ferroelastic GMO and TMO at room temperature are paramagnets. At low temperatures GMO and TMO are antiferromagnetic with the Neel temperatures $T_N = 0.3$ K (GMO) and $T_N = 0.45$ K (TMO). TMO shows the spontaneous destruction at 40 kOe magnetic field. Temperature and field dependences of the magnetization in TMO are well described by the magnetism theory of singlets at 4.2 K $\leq T \leq 30$ K. The magnetoelectric effect in SMO, GMO and TMO, the anisotropy of magnetoelectric effect in TMO at $T = (1.8-4.2)$ K, the Zeeman effect in TMO, the inversion of the electric polarization induced by the laser beam are discussed. The correlation between the magnetic moment of rare earth ion and the magnetoelectric effect value is predicted. The giant fluctuations of the acoustic resonance peak intensity near the Curie point are observed.

1. Introduction

At the end of 1960s, there was a great interest in the rare earth molybdates family $R_2(\text{MoO}_4)_3$ (RMO) ($R = \text{Pr, Nd, Sm, Eu, Gd, Tb}$ and Dy) because these compounds exhibited the phenomena of ferroelectricity and ferroelasticity [1].

RMO from $\text{Pr}_2(\text{MoO}_4)_3$ (PMO) to TMO crystallizes to the tetragonal β -structure with a space group $P4_2m$ (point symmetry group is $42m$). Their melting points are 1045°C for PMO and 1172°C for TMO. $\text{Dy}_2(\text{MoO}_4)_3$ (DMO) crystallizes to cubic γ -phase at 1222°C and transforms to β -structure at 1030°C . While cooling the family undergoes a transformation from the tetragonal β -phase to the monoclinic α -Phase. The temperatures of the β - α transformation are 987°C for PMO and 805°C for DMO.

However, the transformation is sluggish and, therefore, the high-temperature phase can be quenched in. If the thermodynamically metastable β -phases of RMO are further cooled, they undergo the second transformation leading to the lower symmetry ferroelastic-ferroelectric orthorhombic $Pba2$ β' -structures (point symmetry group $mm2$). They are also thermodynamically metastable. The temperatures of β - β' phase transitions are 235°C for PMO and 145°C for DMO.

The single crystal samples of RMO are transparent in the visible light.

Both β and β' phases are piezoelectric. The β' phase is ferroelectric. The spontaneous electric polarization values are of $\approx 2 \times 10^{-7}$ Coul/cm². The dielectric permeability peak at the Curie temperature is of ≈ 10 for GMO.

The ferroelastic properties are well exhibited. In a single-domain sample of (001) cut, the switching of the ferroelectric

TABLE 1

The ion	The ground state	The spin, S	The angular Momentum, L	The total Momentum, J
Sm ³⁺	⁶ H _{5/2}	5/2	5	5/2
Gd ³⁺	⁸ S _{7/2}	7/2	0	7/2
Tb ³⁺	⁷ F ₆	3	3	6

domain can be observed visually in polarized light at compressing the sample along the [010] axis.

Orthorhombic β' -phases of rare earth molybdates are paramagnetic down to temperatures below 1 K.

In RMO with R = Sm, Gd, Tb and in mixed molybdates DyGd(MoO₄)₃ (DGMO), TbGd(MoO₄)₃ (TGMO) the non-linear magnetoelectric effect was observed experimentally. In TMO and in TGMO, the switching of ferroelectric domains by the magnetic field was observed experimentally. These are the first substances in which the possibility was found to switch the ferroelectric domains by the magnetic field.

The longitudinal Zeeman effect was investigated in TMO in the magnetic field $H \leq 20$ T along the [001] and [110] axes at $T = 4.2$ K and 1.7 K. The experimental field dependences of the wave numbers of the absorption peaks $\nu_i(H)$ were obtained. The analysis of the dependences shows that the excited multiplet ⁵D₄ of Tb³⁺ ion in the crystal field of TMO can be considered as consisting from five singlets and two quasidoublets. The field dependences of the energy levels $E_i(H)$ were obtained from the experimental data in the magnetic field along the [001] axis for the ⁵D₄ multiplet. The experimental dependences $E_i(H)$ were described well by the theory of the magnetism of singlets.

The dependences of the photoinduced voltage in TMO upon the time t of the illumination by a laser beam were measured at room temperature at $0.1 \text{ s} \leq t \leq 4500 \text{ s}$. The power of the laser radiation was 0.4 W. The distribution of the intensity along the sample was varied from highly inhomogeneous to homogeneous. It was found that the photoinduced voltages of two types with the opposite signs appear due to the inhomogeneous illumination. The model was proposed to explain the appearance of the photoinduced voltage due to the inhomogeneous illumination.

The qualitative explanation of the mechanisms of these two effects was given. To make quantitative estimates, it is necessary to measure the dependences of the effect upon the temperature of the sample and upon the intensity of the light.

The temperature dependence of the intensity of the main acoustic resonant peak in GMO was measured at temperatures from 22°C to 165°C. This temperature range includes the Curie point ($T_C = 159^\circ\text{C}$). The low-frequency fluctuations of the amplitude of the resonant current in GMO were observed near the Curie point. The corresponding variations of the measured voltage were 0.1 Volt. The typical times of the fluctuations were (10–100) sec. The relative values of the corresponding fluctuations of the piezoacoustic impedance in GMO are two orders of magnitude larger than the values of the fluctuations of the physical parameters in the solids that were known before.

Such fluctuations of the physical properties of the solids were observed visually never before.

In [2], the point symmetry group C_2 for the nearest surrounding of Gd³⁺ ions in GMO was established experimentally. The calculated value of the spontaneous polarization, assuming point charges Gd³⁺ and (MoO₄)²⁻, was $260 \cdot 10^{-9}$ Coul/cm². This result can be considered as being in a satisfactory agreement with the experimental value $200 \cdot 10^{-9}$ Coul/cm². All rare earth molybdates are isomorphic to GMO. So, the rare earth ions in RMO crystal lattice are assumed to be trivalent and the point symmetry group of the local crystal field at R³⁺ sites is assumed to be C_2 . The experimental data discussed below relates mostly to Sm₂(MoO₄)₃, Gd₂(MoO₄)₃, and Tb₂(MoO₄)₃. Table 1 contains the quantum numbers for corresponding free R³⁺ ions in the ground state.

It is worth mentioning that starting from 90-th magnetic shape-memory alloys (MSMAs) attract special interest owing to significant magnetic-field-induced strain (MFIS), also referred as the “magnetic shape-memory effect” originated from coupling between magnetic and structural ordering. Such strain arises through the magnetic-field-induced motion of twin boundaries [3]. Since the magnetic shape-memory effect is useful for actuation purposes, the inverse effect may be utilized for sensing and energy harvesting applications [4]. Consequently, the direct and inverse magnetic shape-memory effects cause magnetic field-induced superelasticity, which is the magnetically induced recovery of a large mechanically induced deformation [4]. It is worth mentioning that, in fact, magnetic-field-induced strain (MFIS) effect has been previously observed and described in the same terms at the beginning of 90-th in ferroelectrics (rare-earth molybdates) [5]. Particularly, terbium molybdate shows so strong field-induced strain, that the spontaneous destruction in a constant magnetic field of 40 kOe along the [100] axis at $T = 1.5$ K has been observed [5], but at that time, most attention has been paid to magnetic-field-induced electric polarization and magnetoelectric effects.

Latter family of magnetic shape memory alloys (MSMA) has been introduced, where the coupling between magnetic and structural ordering in conjunction with the magnetic and structural transformations giving rise to various functional properties: the magnetocaloric effect, the magnetic-field-induced martensitic transformation, as well as its reverse transformation, giant magnetoresistance, and electric polarization [4].

In this paper, we will present the review on ferroelectric, magnetic, electric, and structural properties of the rare earth molybdates family R₂(MoO₄)₃ (RMO) (R = Pr, Nd, Sm, Eu, Gd, Tb, and Dy).

2. Ferroelectric Properties

Here, only a short description of ferroelectric properties of RMO will be given. The detailed review of this question is available in [1].

RMO belongs to a new type of ferroelectrics (improper ferroelectrics) theoretically predicted by Levanyuk and San-nikov [6].

While cooling the tetragonal β -phase becomes unstable with respect to two degenerate modes (soft modes) of lattice vibrations, this instability induces the displacive phase transition of the first order to the ferroelastic-ferroelectric β' -GMO-type structure. The β - β' transition temperature is also the Curie temperature of the orthorhombic β' -RMO. The spontaneous polarization appears at the transition as a by-product of the lattice transformation and cannot be considered as the order parameter. This conclusion was obtained for GMO by Petzelt and Dvořák [7] using group analysis. They confirmed this result experimentally by far-infrared reflectivity and transmission measurements in GMO.

Analogous result was obtained for TMO from neutron-scattering experiments [8, 9]. In [6], from the examination of the soft mode, it was shown that the primary-order parameter, which necessarily shows large fluctuations, near T_C , have no macroscopic polarization but have instead antipolar. The freezing in of this antiferroelectric static displacement couples to the shear strain which in turn produces the electric polarization by piezoelectric coupling.

The displacive mechanism of β - β' transition is valid for all the members of RMO family because they are isomorphic to GMO and TMO.

The crystal structure of β' -GMO was solved in [2, 10, 11]. Above the Curie temperature, the structure is tetragonal with space group $P\bar{4}2_1m$ and point group $\bar{4}2_1m$. Below the Curie temperature, it is orthorhombic with space group $Pba2$ and point group $mm2$. The reduction in point group symmetry from $\bar{4}2_1m$ to $mm2$ allows the formation of twin domains. They can be distinguished in polarized light. After cooling through the Curie point, the RMO single crystals always are in a polydomain state. When cooled through the Curie temperature, the equivalent [110] and $[\bar{1}\bar{1}0]$ axes of the tetragonal phase become the [100] and [010] axes of the orthorhombic phase. These orthorhombic axes are unequal. The b parameter along the [010] axis is larger than the a parameter along the [100] axis: $(b-a)/a \approx 3 \times 10^{-3}$. So, the crystal changes its shape during the transition. The axes [100] and [010] of the tetragonal phase become the axes $[\bar{1}\bar{1}0]$ and [110] of the orthorhombic phase and the right angle between them changes by the value of $\approx 10^\circ$. This is the shear angle of the transition. It is determined by the relation $(b-a)/a$. The relative change of the [001] axis parameter $\Delta c/c$ during the transition is smaller than 10^{-4} , but the structure of the [001] axis is changed drastically. It is not polar in the tetragonal phase and it becomes polar in the orthorhombic phase. This is the origin of the ferroelectric order.

The applied electric field along the [001] axis can reverse the [001] axis. This is accompanied by the mutual interchange of the orthorhombic [100] and [010] axes.

Due to the difference between b and a parameters, the mechanical compression along the [010] axis switches the orientational state. This is the origin of the ferroelasticity. A material is said to be ferroelastic if it has two or more stable orientational states in the absence of the external mechanical stress and if it can be reproducibly transformed from one to another of these states by the application of mechanical stress. Ferroelasticity was established in RMO by Aizu [12].

Ferroelasticity can be used to transform a multidomain sample into a single domain state. In a polydomain state due to a very small value of the shear angle, the direction of the [010] axes in domains with positive [001] axes almost coincides with the [100] axes in domains with negative [001] axes. So, a compression along [010] axes of positive domains makes them unstable. Simultaneously, this compression makes the negative domains more stable. Then, the domains with the [100] axes along the compression should grow and the domains with the [010] axes along the compression should disappear. This is the way to obtain a single domain sample.

The temperature dependence of the spontaneous electric polarization P_S in GMO was measured in [13] over the temperature range from 4.2 K up to the Curie point $T_C = 432.3$ K. The electric polarization takes values of $P_S \approx 290 \times 10^{-9}$ Coul/cm² at $T = 4.2$ K and $P_S \approx 40 \times 10^{-9}$ Coul/cm² at $T = T_C = 432.3$ K. The abrupt jump in the $P_S(T)$ curve was observed at $T = T_C = 432.3$ K with a hysteresis loop of $\Delta T \approx 0.1$ K width. This is a direct indication on the phase transition of the first order. Room temperature values of P_S in SMO, EMO, GMO, and TMO are in the range of $P_S \approx 140 \times 10^{-9}$ Coul/cm² for EMO and $P_S \approx 240 \times 10^{-9}$ Coul/cm² for SMO [14].

The temperature dependences of electric and elastic properties of GMO were measured in [15]. The dielectric permittivity of the clamped crystal ϵ_{33}^E does not depend on the temperature and shows no anomaly at the Curie point, while the elastic constant c_{66}^E shows strong temperature dependence with a marked anomaly at the Curie point. The dielectric permittivity at constant and zero stress shows a weak anomaly at the Curie point due to the piezoelectric coupling. This result indicates that the ferroelectric ordering in GMO is a secondary effect. It appears as a consequence of the structural β - β' phase transition.

The pyroelectric properties of GMO were studied in [16, 17]. Near T_C , hard-to-control spurious domain nucleation was observed. It was explained by small thermal gradients caused by the thermal signal being detected.

Both β and β' phases of RMO are piezoelectric [17]. The electromechanical coupling coefficient is 4% at room temperature and 22% near T_C .

The presence of the domain walls significantly influences the resonant behavior of a crystal.

3. Magnetic Properties

Magnetic properties of a single-crystal and single-domain spherical sample of GMO were investigated in [18–22]. In [18–20], the magnetization along the [001], [010] and [100]

axes, respectively, was measured at temperatures from 0.3 K to 4.2 K in magnetic field up to 90 kOe. The saturation magnetization values at low temperatures and in high magnetic field along all crystal directions correspond to the magnetic moment $\mu_S = 7\mu_B$ which is typical for Gd^{3+} ion in the ground state $^8S_{7/2}$. At temperatures above ≈ 1 K, the field dependences of the magnetization show a typically paramagnetic behavior. At $T = 0.5$ K, the field dependence of the magnetization exhibits a weak anomaly at $H = (2-3)$ kOe that indicates on the field induced transformation in the antiferromagnetic structure from the antiparallel to parallel orientation of ionic magnetic moments [18]. At $T = 0.35$ K, this anomaly becomes more pronounced. On the basis of these data, the authors conclude that GMO becomes antiferromagnetic at temperatures lower than ≈ 0.3 K.

Figure 1 shows the field dependences of the magnetization of GMO at $T = 1$ K in the magnetic field along the [001] axis (open circles), the [100] axis (triangles), and the [010] axis (crosses). These dependences were calculated from the tables published in [18–20]. The solid line is the Brillouin function $B_{7/2}(\mu_S H/kT)$ that corresponds to a free Gd^{3+} ion in the ground state $^8S_{7/2}$ as it should be in a usual paramagnetic substance. The Brillouin function describes qualitatively the experimental magnetization curve along the [001] axis. One can see that the magnetization of the paramagnetic GMO at $T = 1$ K is saturated at the magnetic field $H \approx 60$ kOe. The saturation magnetization is $M_S = 39 \text{ kG} \cdot \text{cm}^3/\text{mole Gd}^{3+} = 6.98\mu_B/\text{Gd}^{3+}$ ion. This value agrees well with the magnetic moment $\mu_S = 7\mu_B$ of Gd^{3+} ion in the ground state $^8S_{7/2}$. The dependences of the magnetization in the magnetic field along the [100] and [010] axes are placed noticeably lower than for [001]. It is due to the natural magnetic crystalline anisotropy. The magnetization curves along the [100] and [010] axes are indistinguishable. It means that the [001] axis is the easy magnetization direction in GMO.

Figure 2 shows the experimental field dependence of the anisotropy energy for the magnetic field along the [100] axis. It was calculated from the data of Figure 1 using the relation:

$$E_a(H) = \int_0^H [M_{[001]}(H) - M_{[100]}(H)] dH. \quad (1)$$

In the state of the saturation ($H = H_S \approx 60$ kOe), the anisotropy energy is $E_a(H_S) = E_S \approx 10^5 \text{ erg/g} \approx 4.5 \times 10^{-5} \text{ eV/Gd}^{3+}$ ion. This value is higher than the anisotropy constant of ferromagnetic iron at room temperature ($K_1 \approx 0.6 \times 10^5 \text{ erg/g}$). This is the energy needed to align all magnetic moments of Gd^{3+} ions in the paramagnetic GMO along the hard direction [100] at $T = 1$ K.

Figure 3 shows the dependence of the anisotropy energy in GMO $E_a(m_r)$ upon the reduced magnetization $m_r = M_{[100]}/M_S$ along [100]. $E_a(m_r)$ is derived from

$$E_a(M_{[100]}) = \int_0^{M_{[100]}} [H_{[100]}(M) - H_{[001]}(M)] dM; \quad (2)$$

by introducing a new variable $m_r = M_{[100]}/M_S$.

It is seen that this dependence is described well by the relation:

$$E_a(m_r) = E_S m_r^4. \quad (3)$$

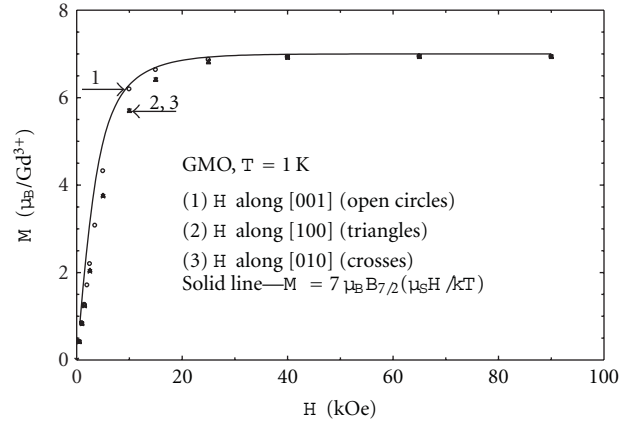


FIGURE 1: The field dependences of the magnetization of GMO at $T = 1$ K in the magnetic field directed along the [001] axis (open circles), the [100] axis (triangles) and the [010] axis (crosses).

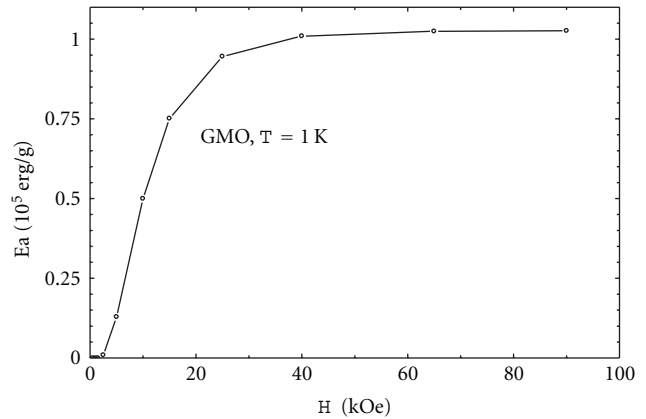


FIGURE 2: The field depends on the natural magnetic crystalline anisotropy energy upon the magnetic field along the [100] axis.

Here, E_S is the anisotropy energy of a paramagnetic substance in a saturated state.

In [21], the magnetization curves of GMO were measured in the magnetic field along the [001] axis in the temperature range (0.1–0.5) K using the method of adiabatic demagnetizing. The sharp jump was observed on the isentropic magnetization curve in the magnetic field $H = 1.615$ kOe. The temperature of the jump was 0.11 K. The magnetic field $H = 1.615$ kOe is the critical field of the destruction of the antiferromagnetic order in GMO at $T = 0.11$ K. The magnetization was $350 \text{ G} \cdot \text{cm}^3/\text{mole Gd}^{3+}$ at the beginning of the jump and $\approx 30 \text{ kG} \cdot \text{cm}^3/\text{mole Gd}^{3+}$ at the end of the jump. The magnetization curve between these two points was a vertical straight line. So, the phase transition from the antiferromagnetic to the paramagnetic state in GMO goes without the stage of the spin-flop.

The heat capacity of GMO was measured in the magnetic field up to 90 kOe at the temperatures (0.1–4.2) K in papers [18–22]. The thermodynamic functions were calculated using the measured values of the magnetization and the heat capacity.

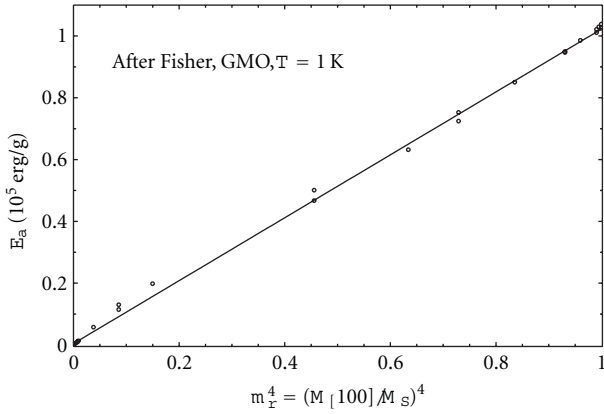


FIGURE 3: The energy of the natural magnetic crystalline anisotropy of GMO versus the reduced magnetization. The magnetic field is directed along the [100] axis.

In [23], the magnetization and heat capacity of a single-crystal and single-domain spherical sample of TMO were measured over the range (0.4–4.2) K with fields up to 90 kOe directed along the [001] axis. The magnetization was measured also along the [100] axis, but these measurements could not be performed in the field above 25 kOe because of the mechanical destruction of the sample.

According to [23], the temperature dependences of the heat capacity at zero field and at $H = 0.5$ kOe show λ -type anomalies with pronounced maxima at $T = 0.44$ K and 0.45 K, respectively. As the magnetic field is raised, the λ maxima shift toward the lower temperatures. The temperature dependences of the magnetization and magnetic susceptibility show the broad maxima around $T = 1.6$ K. All of the above facts indicate on the antiferromagnetic ordering of the Tb^{3+} magnetic moments along the easy [001] axis with the Neel temperature $T_N \approx (0.44\text{--}1.6)$ K.

Above these temperatures, the magnetization curves along the [001] axis look like for a paramagnetic substance at very low temperatures and in extremely high magnetic fields; but the experimental value of the magnetic saturation $M_S = 7.7\mu_B/\text{Tb}^{3+}$ differs noticeably from $M_S = 9\mu_B/\text{Tb}^{3+}$ for a usual paramagnetic substance with Tb^{3+} ion in the ground state 7F_6 . On the basis of this difference, the authors in [23] conclude that the total mechanical moment of the ground state doublet is $J_z = \pm 5$. In the following, we will show on the basis of our magnetic measurements and the observations of Zeeman effect that it is not correct. The unusual value of the magnetic moment in TMO can be explained strictly by the quantum mechanical theory of magnetism of singlets with nondiagonal matrix elements in the angular momentum operator of Tb^{3+} ion.

The magnetization curves along the [100] axis were measured only up to 25 kOe. The crystal was broken when the magnetic field was increased above 40 kOe. The authors explain the destruction of the sample by the magnetic torque. It is not a complete explanation of the self-destruction of TMO single crystal. Our later measurements showed that a sample of TMO at certain conditions can survive at $T = 4.2$ K even in the field of 200 kOe along the [100] axis.

The absence of the magnetization data for TMO along the [100] axis at high magnetic fields makes it impossible to plot the anisotropy energy dependencies upon the magnetic field and the magnetization analogous to those for GMO on Figures 2 and 3. The estimate of the anisotropy energy of TMO at $H = 25$ kOe and $T = 1$ K gives $E_a \approx 10^6$ erg/g. From Figure 2, the corresponding value for GMO is $\approx 10^5$ erg/g, that is, ten times lower than for TMO.

It was established from the measurements of the heat capacity in [23] that the relaxation time of the nuclear spin system of $^{159}\text{Tb}^{3+}$ becomes very long at high fields and low temperatures. For example, in the magnetic field $H = 90$ kOe at the temperature $T \approx 1$ K, the order of magnitude of the relaxation time is several hundred seconds. The heat capacity values taken below those temperatures are not in equilibrium. The higher the magnetic field the higher is, the temperature below which one cannot reach the equilibrium between the nuclear system and the lattice formed by electronic shells of ions. This phenomenon complicates the magnetic measurements in TMO at low temperatures and in high magnetic fields.

In [5], the magnetization of single-crystal single-domain samples of TMO was measured in pulsed magnetic fields up to 300 kOe with pulse duration of 0.01 s. The magnetization curves were measured at $T = 4.2$ K and 78 K along [001] axis and in the (001) plane. The magnetization process was adiabatic. The magnetization was highly anisotropic. The magnetization curves along the [001] axis were close to the paramagnetic saturation at both temperatures. At $T = 78$ K, $H = 300$ kOe, the magnetization reached $7.2\mu_B/\text{Tb}^{3+}$ and at $T = 4.2$ K, $H = 240$ kOe, it was $7.8\mu_B/\text{Tb}^{3+}$. Along the [010] axis, the magnetization was $3.4\mu_B/\text{Tb}^{3+}$ at $T = 78$ K, $H = 300$ kOe, and $4.2\mu_B/\text{Tb}^{3+}$ at $T = 4.2$ K, $H = 240$ kOe. The energy of the natural magnetic crystalline anisotropy of paramagnetic TMO was estimated qualitatively using the magnetization curves along the [001] axis and in the (001) plane. It proved to be of the order of $E_a \approx 2 \cdot 10^7$ erg/g at both temperatures. The magnetic anisotropy of the kind is unusual for a paramagnetic substance. It is the order of magnitude larger than the magnetic anisotropy constant of ferromagnetic cobalt $K_1 \approx 10^6$ erg/g at 78 K.

Figure 4 shows the magnetization curves of TMO in the plane (001) at $T = 4.2$ K. At the beginning of the pulse of the magnetic field, the [100] axis of the sample was oriented along the field. At $H = 190$ kOe, there was an anomaly on the magnetization curve. In the decreasing field, the magnetization curve was placed above that in the increasing field. Inspection of the sample in the polarized light after these measurements showed that the [100] and [010] axes were interchanged as compared to the state of the sample before switching on the pulse of the field. So, one could get the difference between the magnetization values for the field along the [100] and [010] axes. At $H = 180$ kOe, it was $\approx 0.6\mu_B/\text{Tb}^{3+}$. This interchange was observed also in [24, 25] from the measurements of the magnetostriction and the magnetoelectric effect. The interchange took place when the applied magnetic field was directed along the [100] axis and reached some critical value. In [26], the magnetization of

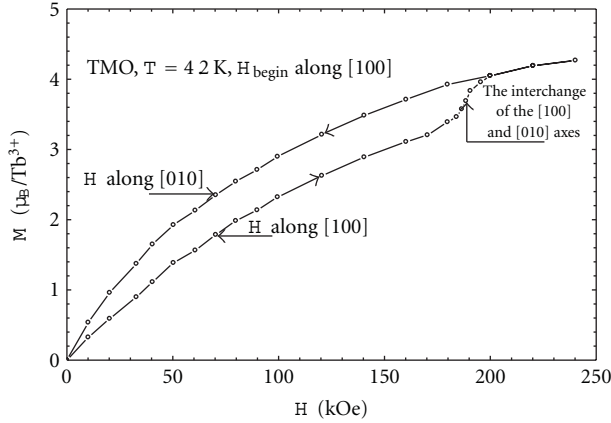


FIGURE 4: The magnetization isentropes in TMO at the initial temperature of the sample, $T = 4.2$ K. On the lower branch, the magnetic field is directed along the $[100]$ axis. The anomaly at $H \approx 190$ kOe shown by the arrow is due to the interchange of the $[100]$ and $[010]$ axes. On the upper branch, the field is parallel to the $[010]$ axis.

a single-crystal single-domain sample of TMO was measured in the direct current magnetic field up to 190 kOe in the temperature range $T = (4.2\text{--}300)$ K. The magnetization curves at $T = 4.2$ K along the directions $[001]$, $[010]$ and $[100]$ are shown on Figure 5. The magnetization curves along $[010]$ and $[100]$ on Figure 5 differ noticeably from the corresponding curves on Figure 4. The magnetization on Figure 4 is smaller than that on Figure 5. It is because the curves on Figure 5 are isotherms and those on Figure 4 are isentropes. The adiabatic process of magnetizing the sample on Figure 4 is accompanied by an increase of the temperature due to the magnetocaloric effect. According to our estimations, the temperature of the sample at $H = 240$ kOe on Figure 4 is $\approx (10\text{--}20)$ K higher than at zero field. Respectively, the magnetization of Figure 4 is smaller than that of Figure 5.

There is no evidence of the interchange of the $[100] \leftrightarrow [010]$ axes of Figure 5. On the contrary, Figure 4 shows the obvious transition of the sample from the state with the $[100]$ axis parallel to the field into the state with the $[010]$ axis parallel to the field at $H = 190$ kOe. This can be explained by the temperature dependence of the critical field of the $[100] \leftrightarrow [010]$ interchange $H_{cr}(T)$ and the magnetocaloric effect in pulsed fields. Our measurements of the magnetoelectric effect showed that the critical field $H_{cr}(T)$ decreases from approximately 130 kOe at $T = 10$ K down to 30 kOe at $T = 30$ K. The $[100] \leftrightarrow [010]$ interchange of Figure 4 was observed because of increasing the temperature due to the magnetocaloric effect and the corresponding decreasing of $H_{cr}(T)$.

It is seen that, along the easy direction $[001]$, the saturation magnetization per one terbium ion $M_S \approx 8\mu_B/\text{Tb}^{3+}$ is not equal to the magnetic moment of a free Tb^{3+} ion $M_{\text{Tb}^{3+}} = 9\mu_B/\text{Tb}^{3+}$. This is the result of the interaction of the angular momentum of Tb^{3+} ion with the crystal field. So, to describe the experiment, one should use the singlet magnetism theory.

Before describing this theory, it is very useful to remind the main starting points of the standard theory of paramagnetism of noninteracting ions.

The Zeeman energy is given by the following equation:

$$\hat{V}_Z = -\hat{\mu}_L \vec{H} - \hat{\mu}_S \vec{H} = -\mu_B (\hat{L} + 2\hat{S}) \vec{H} = -\mu_B g_J \hat{J} \vec{H}. \quad (4)$$

The Hamiltonian of the problem is

$$\hat{H} = \hat{H}_{CR} + \hat{V}_Z = H_{CR} - g_J \mu_B (H_x \hat{J}_x + H_y \hat{J}_y + H_z \hat{J}_z); \quad (5)$$

\hat{H}_{CR} is the Hamiltonian of the crystal field; \hat{J}_x , \hat{J}_y , and \hat{J}_z are operators of projections of the total mechanical momentum on the x , y , and z axes. This consideration gives only one of three contributions to the magnetic moment of the ion—the paramagnetism of orientation. We do not consider here the paramagnetism of polarization according to Van Vleck and the diamagnetism of precession.

Consider a free Tb^{3+} ion in the magnetic field along z -axis. This is the case of the full degeneracy of the orbital multiplet:

$$\hat{H}_{CR} = 0; \quad (6)$$

$$H_x = H_y = 0.$$

From (5) and (6), the Hamiltonian of a free ion is obtained:

$$\hat{H} = -g_J \mu_B H_z \hat{J}_z; \quad (7)$$

$$\hat{J}_z = -i \frac{\partial}{\partial \varphi}. \quad (8)$$

Here, φ is the angle in the x, y plane. The φ -dependent parts of normalized wave functions of \hat{J}_z for degenerate levels of the multiplet of a free ion are [27]

$$|J, m\rangle = \Phi_m(\varphi) = \frac{\exp(im\varphi)}{\sqrt{2\pi}}. \quad (9)$$

The fact is that a wave function is given by only one exponent plays a decisive role.

Due to this fact, only diagonal elements of the Hamiltonian (7) can have non zero values. So, the secular equation is

$$\prod_{m=-J}^{-J} (g\mu_B m H_z - E_m) = 0. \quad (10)$$

Solutions of (10) give the eigenvalues of the energy of a free ion:

$$E_m = g\mu_B m H_z; \quad (11)$$

$$m = -J, (-J+1), \dots, 0, \dots, (J-1), J. \quad (12)$$

The components of the degenerate multiplet (11) possess the field independent magnetic moments:

$$M_{zm} = -\frac{\partial E_m}{\partial H_z} = -g\mu_B m; \quad (13)$$

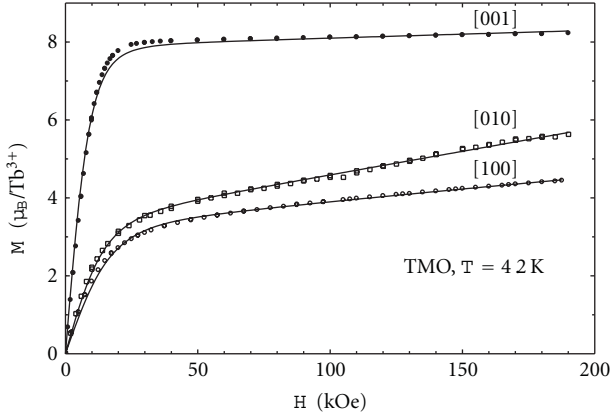


FIGURE 5: The magnetization curves of TMO at $T = 4.2$ K along main crystallographic directions. Solid lines are calculated using the theory of magnetism of singlets.

Using (11) and (12) and the statistics of Maxwell-Boltzman, one obtains the Brillouin function to describe the field and temperature dependence of the magnetization in a system of free ions:

$$M_z(H, T) = gJ\mu_B B_J \left(\frac{gJ\mu_B H_z}{kT} \right) = gJ\mu_B \left[\frac{2J+1}{2J} \text{cth} \left(\frac{2J+1}{2J} \times \frac{gJ\mu_B H_z}{kT} \right) - \frac{1}{2J} \text{cth} \left(\frac{1}{2J} \times \frac{gJ\mu_B H_z}{kT} \right) \right]. \quad (14)$$

The total mechanical momentum of Tb^{3+} ion in ${}^7\text{F}_6$ ground state is

$$J = L + S = 3 + 3 = 6; \quad (15)$$

L and S are the angular and spin moments, respectively. The g -factor is [28]

$$g = 1 + \frac{J(J+1) + S(S+1) - L(L+1)}{2J(J+1)} = \frac{3}{2}. \quad (16)$$

The corresponding saturation magnetic moment is $\mu_s = gJ\mu_B = 9\mu_B$.

The singlet magnetism theory describes the magnetic properties of ions in the crystal field. It is based on the Jahn-Teller theorem [29]. According to this theorem, the surrounding of the ion cannot be stable if the ground state of the ion in the crystal field is degenerate (excluding the case of Kramers degeneracy for ions with an odd number of outer electrons [30]). The spontaneous rearrangement of the crystal lattice goes on because the development of the instability reduces the symmetry of the crystal field and removes the degeneracy of the ground state. It means that rare earth ions with the even number of 4f electrons unavoidably have the singlet ground state [31]. If two lowest singlets are separated by a narrow gap of the order of $2\Delta_0 \approx (1-5) \text{ cm}^{-1}$ and are much more away from other singlets, then the former two singlets can be considered as

a quasidoublet. The magnetic moment of the ion with the quasidoublet as a ground state should be calculated by the singlet magnetism theory [31].

The main distinction of this theory from the standard theory of the paramagnetism of free ions (6)–(16) is that the wave functions of the orbital singlets cannot be described by only one exponent like (9). The crystal field splits the degenerate multiplet of a free ion that is given by (11)–(12) and mixes the wave functions (9) of these levels. The wave functions of the singlets are linear combinations of the functions given by (9) with the values of m given by (12). The forms of the combinations are determined by the symmetry of the crystal field and of the operators: \hat{f}_x , \hat{f}_y , and \hat{f}_z .

The point symmetry group of the surrounding of Tb^{3+} ion in TMO is C_2 [2]. For this symmetry, the Hamiltonian matrix for the magnetic field along z axis is

$$\begin{vmatrix} -\Delta_0 & gJ_{\text{eff}}\mu_B H_z \\ gJ_{\text{eff}}\mu_B H_z & +\Delta_0 \end{vmatrix}. \quad (17)$$

Here, $2\Delta_0$ is the splitting of energy levels of the quasi-doublet under consideration.

J_{eff} is a nondiagonal matrix element of the total mechanical momentum operator. It is given by the relation:

$$J_{\text{eff}} = \langle \psi_z | \hat{f}_x | \psi_s \rangle = 6a_6^s a_6^z + 4a_4^s a_4^z + 2a_2^s a_2^z; \quad (18)$$

ψ_s and ψ_z are the wave functions of the lower and upper levels of the quasidoublet, respectively. The difference between M_s and $M_{\text{Tb}^{3+}}$ is not too large. This result indicates that the main harmonics that form the quasidoublet are $(|6, 6\rangle - |6, -6\rangle)/\sqrt{2}$ and $(|6, 6\rangle + |6, -6\rangle)/\sqrt{2}$. From here, it follows

$$\begin{aligned} \psi_s &= \frac{1}{\sqrt{2}} [a_6^s(|6, 6\rangle + |6, -6\rangle) \\ &\quad + a_4^s(|6, 4\rangle + |6, -4\rangle) + a_2^s(|6, 2\rangle + |6, -2\rangle) + a_0^s]; \\ \psi_z &= \frac{1}{\sqrt{2}} [a_6^z(|6, 6\rangle - |6, -6\rangle) \\ &\quad + a_4^z(|6, 4\rangle - |6, -4\rangle) + a_2^z(|6, 2\rangle - |6, -2\rangle)]. \end{aligned} \quad (19)$$

One can see from (17) that for an ion with the ground state in the form of a quasidoublet the diagonal matrix elements do not depend upon the magnetic field and the nondiagonal elements are not zero and depend upon the magnetic field. This is a main distinction of the magnetic properties of the spectrum of singlets compared to the degenerate spectrum (11). The secular equation of the Hamiltonian (17) is

$$\begin{vmatrix} -\Delta_0 - E & gJ_{\text{eff}}\mu_B H_z \\ gJ_{\text{eff}}\mu_B H_z & +\Delta_0 - E \end{vmatrix} = 0. \quad (20)$$

From (20), one obtains the eigenvalues of the energy of the quasi-doublet $E_{1,2}$ in the magnetic field H_z :

$$E_{1,2} = \mp \sqrt{\Delta_0^2 + (gJ_{\text{eff}}\mu_B H_z)^2}. \quad (21)$$

Here, E_1 —the energy of the lower level of the quasidoublet; E_2 —the energy of the upper level of the quasidoublet. Magnetic moments of the components of the quasidoublet are given by the following relation:

$$M_{z1,2} = -\frac{\partial E_{1,2}}{\partial H_z} = \pm \frac{2g^2 J_{\text{eff}}^2 \mu_B^2 H_z}{2\sqrt{\Delta_0^2 + (gJ_{\text{eff}}\mu_B H_z)^2}}. \quad (22)$$

There is a principal distinction between ions with the nondegenerate spectrum (21) and ions with the degenerate spectrum (11). The energy levels of ions with the degenerate spectrum (11) have the field independent magnetic moments (13). These moments are not zero in the absence of the magnetic field if $m \neq 0$.

As it is seen from (22), the magnetic moments of the levels of the quasidoublet essentially depend upon the magnetic field. They are zero at zero magnetic field. In other words, the ion with the nondegenerate spectrum of singlets can be magnetically polarized in the magnetic field. This is the paramagnetism of the polarization. So we came to the recognition of a very important fact that the idea of some definite and field independent magnetic moment of the ion is applicable only to a narrow class of problems in which the potential of the ion has the spherical symmetry and the spectrum of the ion is degenerate. The sample of the kind is GMO where Gd^{3+} ion in the ground state $^8S_{7/2}$ has zero angular momentum and hence the spherical symmetry of the ionic potential. The overwhelming majority of problems, and TMO among them, insist on taking account of the field dependence of the ionic magnetic moment. This is done in the singlet magnetism theory by the relation (22).

Using the Maxwell-Boltzman statistics, one can obtain the field and temperature dependence of the magnetization per ion for a singlet magnetic substance in the field directed along the [001] axis:

$$M_z(H, T) = \frac{g^2 J_{\text{eff}}^2 \mu_B^2 H_z}{\sqrt{\Delta_0^2 + (gJ_{\text{eff}}\mu_B H_z)^2}} \cdot \text{th} \frac{\sqrt{\Delta_0^2 + (gJ_{\text{eff}}\mu_B H_z)^2}}{kT}. \quad (23)$$

This is a two-level version of the singlet magnetism theory. It does not describe the anisotropy of the experimental results shown in Figure 5. It gives a zero value for the magnetization along the [100] and [010] axes. To describe the anisotropy, one should take account of not less than three lowest singlets of the spectrum.

The nearest surrounding of Tb^{3+} ion in TMO is an octahedron formed by seven oxygen ions [2]. The point symmetry group of the octahedron can be described as C_2 . The axis of the second order is a polar axis of the octahedron. Due to this symmetry, the [100] and [010] components of the magnetic moment M_x and M_y are zero in the two singlet model. Nonzero values for M_x and M_y appear when taking account of the nearest excited singlet. This is a three-level model of singlet magnetism theory.

The sites of Tb^{3+} ions in TMO are of two types. The directions of the polar axes of the octahedrons at nonequivalent sites are approximately opposite to each other

and parallel or antiparallel (approximately) to the [001] axis. The octahedrons at the nonequivalent sites are rotated with respect to each other by the angle of approximately 90° around the [001] axis. It means that the axes of the easy magnetization in the (001) plane should be different for ions disposed at the nonequivalent sites: the angle between them should be of 90° .

Taking account of the nonequivalent sites for Tb^{3+} ions, one obtains in the three-level modification of the theory the following expression for the field and the temperature dependence of the magnetization:

$$M_p(H_p, T) = \sum_{i=1,2} \frac{\mu_{ip}^2 H_p \text{th}(B_{ip}/kT)/B_{ip}}{2(1 + \exp(d_{ip}/kT)/2\text{ch}(B_{ip}/kT))} + \chi_p H_p. \quad (24)$$

Here, p indicates the direction in the crystal and takes values [001], [010] and [100].

i indicates the type of the site. $B_{ip} = \sqrt{b_{ip}^2 + (\mu_{ip} H_p)^2}$. H_p is a projection of the field on the direction p . M_p is a projection of the magnetic moment per one Tb^{3+} ion on the direction of the magnetic field. μ_{ip} are the saturation magnetic moments of Tb^{3+} ions at sites of two types for main directions in the crystal. χ_p —Van Vleck susceptibility along the direction p . k —Boltzmann constant. b_{ip} and d_{ip} are coefficients of the theory that can be found from energy gaps Δ_n and δ_m between the singlets. Δ_n is the energy gap between the n -th excited singlet and the ground singlet for the sites of the first type, δ_m is the same for the sites of the second type. Δ_n and δ_m can be taken from the photoluminescence spectrum of Tb^{3+} ion in TMO [5]: $\Delta_1 \approx \delta_1 = (2.7 \pm 0.35) \text{ cm}^{-1}$; $\Delta_2 \approx \delta_2 = (5.4 \pm 0.35) \text{ cm}^{-1}$. Using these values of Δ_n and δ_m , the coefficients b_{ip} and d_{ip} were found. Then, the magnetization curves $M_p(H_p)$ were calculated at the temperature $T = 4.2 \text{ K}$ for the directions [001], [010] and [100] by fitting expression (24) to the corresponding experimental curves. In these calculations, the coefficients μ_{ip} and χ_p were used as the fitting parameters. It was found that the values $\mu_{1[001]} = \mu_{2[001]} = 7.9\mu_B/\text{Tb}^{3+}$ along the [001] axis are identical for the nonequivalent sites. Along the [100] axis, the saturation magnetic moments for nonequivalent sites are different: $\mu_{1[100]} = 6.4\mu_B/\text{Tb}^{3+} \gg \mu_{2[100]} = 1\mu_B/\text{Tb}^{3+}$. For the [010] direction, the opposite nonequality occurs: $\mu_{1[010]} = 0.05\mu_B/\text{Tb}^{3+} \ll \mu_{2[010]} = 6.9\mu_B/\text{Tb}^{3+}$. This result reflects the difference in the symmetry of the nonequivalent sites of Tb^{3+} ions. A good agreement with the experiment takes place at $T = 4.2 \text{ K}$ for main directions. One can see that the difference between the experimental saturation magnetic moment of TMO and the magnetic moment of free Tb^{3+} ion in the ground state 7F_6 is explained completely by the singlet magnetism theory. So, the additional assumption about the ground state of Tb^{3+} ion in TMO with $J = \pm 5$ [23] is not necessary.

The comparison of the magnetization curves of GMO and TMO indicates definitely the role of the angular momentum L of the trivalent rare earth ion in the formation of the magnetic properties in rare earth molybdates.

The L value determines the main contribution to the energy E_a of the natural magnetic crystalline anisotropy. In GMO, Gd^{3+} ion in the ground state $^8S_{7/2}$ has $L = 0$, and the energy of anisotropy in the magnetically saturated state is $E_a \approx 10^5$ erg/g. The magnetization reaches the saturation along hard directions [100] and [010] at $H \approx 60$ kOe (see Figures 1 and 2). In TMO, Tb^{3+} ion in the ground state 7F_6 has $L = 3$, and the magnetization along hard directions [100] and [010] is far from saturation even in the magnetic field $H = 190$ kOe (see Figure 5). The energies of anisotropy at $H = 190$ kOe found using relation (1) are $E_{a[100]} \approx 1.13 \cdot 10^7$ erg/g and $E_{a[010]} \approx 0.96 \cdot 10^7$ erg/g that is two orders of magnitude larger than in GMO. There is a strong correlation between the angular momentum value and the anisotropy energy. The ion with the nonzero angular momentum has a nonspherical charge cloud of the outer 4f-electrons. Magnetizing the crystal containing nonspherical ions like Tb^{3+} rotates these ions and hence changes the coupling between the ions and the crystal field much more than in the crystal with spherically isotropic ions like Gd^{3+} . So, TMO is magnetically more anisotropic than GMO. The anisotropy energy values for TMO found in [26] agree by the order of magnitude with the value $E_a \approx 2 \cdot 10^7$ erg/g found from the measurements in pulsed fields in [5]. The difference is mainly due to the adiabatic character of magnetizing in [5] in contradiction to the isothermal one in [26].

The samples investigated in [5, 26] were not destroyed in contradiction to the result of [23] despite that magnetic fields in [5, 27] were three times higher than in [23]. It means that the magnetic torque acting on the sample in [5, 26] was also larger than in [23]. So, the reason of the destroying the sample in [23] was not the magnetic torque in spite of conclusion made in [23].

The rotation of the nonspherical rare earth ions while magnetizing RMO crystals distorts the crystal lattice of RMO. The distortions of a ferroelectric crystal lattice unavoidably change its electric polarization due to the piezoelectric effect. This is the origin of the magnetoelectric effect to be discussed in the following section.

4. Magnetoelectric Effect

The presence of rare earth ions with nonzero angular momentum and nonzero total momentum in the crystal lattice of a ferroelectric substance leads to the large magnetoelectric effect (MEE). Rare earth ions with nonzero angular momentum possess the spatially anisotropic charge cloud of outer 4f-electrons. The spatial anisotropy of the magnetic ions determines large values of the natural magnetic crystalline anisotropy and the magnetostriction. These properties in the ferroelectric crystal ensure the strong dependence of the electric polarization upon the magnetic field, that is, MEE.

MEE was predicted in [32], but the consideration of the problem was restricted by the linear magnetoelectric effect. It was established that this effect is possible only in the antiferromagnetic crystals. In [33], the prediction of linear MEE was given for a specific substance Cr_2O_3 . The first

experimental observations of linear MEE in Cr_2O_3 were done in [34, 35].

The most important point of MEE in rare earth molybdates is the absence of the restrictions related to the magnetic structure. The general consideration of the problem shows that nonlinear MEE in rare earth molybdates can exist in the paramagnetic state.

The first observation of nonlinear MEE in the paramagnetic tetragonal $\text{NiSO}_4 \cdot 6\text{H}_2\text{O}$ was published in [36].

In [37], nonlinear MEE was observed in paramagnetic TMO at $T = 77$ K. That was the first observation of MEE in the rare earth molybdate family. In [38], MEE was measured in TMO and GMO in pulsed magnetic fields up to 110 kOe at $T = (77-290)$ K.

Figure 6 shows the field dependence of the magnetically induced electric polarization (MEP) in TMO at $T = 77$ K [38]. The field was applied along the orthorhombic axis [110]. MEP was measured along the [110] axis. As the spontaneous polarization \bar{P}_S is directed along the [001] axis, this result can be considered as the rotation of the \bar{P}_S in the magnetic field.

The dependence of MEP upon the magnetic field is quadratic with a good accuracy. MEP is $P = 4.12 \cdot 10^{-9}$ Coul/cm² at $H = 10$ T. It is small compared to the spontaneous electric polarization $P_S = 180 \cdot 10^{-9}$ Coul/cm² [14].

MEP in GMO was equal to zero in the limit of the experimental error.

The standard symmetry consideration [39] shows that, at a given geometry of the experiment, the components of the magnetically induced electrical polarization in the orthorhombic paramagnetic crystal are proportional to the products of the magnetization components:

$$\begin{aligned} P_x &\sim M_x \cdot M_z; \\ P_y &\sim M_y \cdot M_z. \end{aligned} \quad (25)$$

For a usual paramagnetic crystal,

$$M_z = \chi_{zz} H_z. \quad (26)$$

Here x, y, z correspond to the [100], [010], [001] axes, respectively; χ_{zz} is a component of the diagonal tensor of the magnetic susceptibility. It follows from (25) and (26) that the effect on Figure 6 should be zero.

The contradiction between the result of calculations [39] and the experimental observation of the nonzero effect in [37, 38] can be eliminated by taking account of the local symmetry of Tb^{3+} ions surrounding. As it was noted in Section 3, the nearest surrounding of Tb^{3+} ion in TMO is an octahedron formed by seven oxygen ions [2]. The octahedron has the C_2 point symmetry group. The axis of the second order is a polar axis of the octahedron. The symmetry axes of the octahedron do not coincide with the symmetry axes of the crystal. The polar axis of the octahedron makes an angle with the [001] axis, and the magnetic field applied in the (001) plane has a nonzero projection on the polar axis of the octahedron. According to the theory of magnetism of singlets, the magnetic field

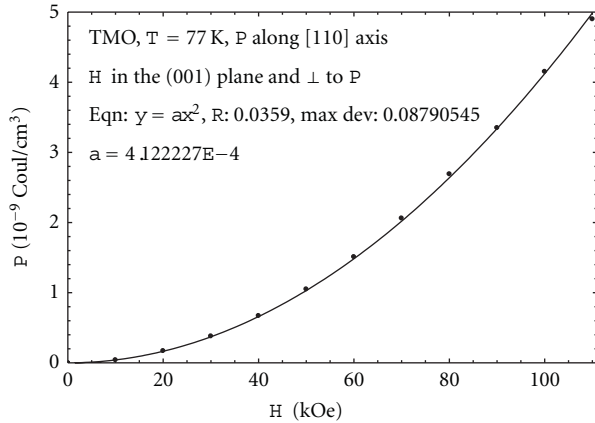


FIGURE 6: The field dependence of the magnetically induced electric polarization in TMO along the [110] axis at $T = 77$ K. The pulsed magnetic field is directed along the $[1\bar{1}0]$ axis. The solid line is the least-square fitting by $P = p_0 H^2$. $p_0 = 4.12 \cdot 10^{-19}$ Coul \cdot cm $^{-2} \cdot$ Oe $^{-2}$.

applied along the polar axis of the octahedron magnetically polarizes Tb^{3+} ion with the magnetic moment along the polar axis. So, the magnetic field applied in the (001) plane of the crystal induces a magnetic moment on Tb^{3+} ion along the polar axis of the octahedron. This moment, in turn, has a nonzero projection on the [001] axis of the crystal and, consequently, induces the electric polarization components along [100] and [010] axes according to (25). Hence, the bulk magnetic susceptibility tensor of TMO single crystal should have nonzero nondiagonal components and (26) should be replaced by

$$M_z = (\chi_{xz} + \chi_{yz} + \chi_{zz})H_z. \quad (27)$$

Then, there would be no contradiction between the measurements [37, 38] and the calculations [39]. The relation (27) should be verified experimentally.

The magnetic susceptibility tensor of an individual Tb^{3+} ion with the main directions along the symmetry axes of the oxygen octahedron has only diagonal components.

At the beginning of this section, it was pointed out on the role of the angular momentum of a rare earth ion. A rare earth ion with a nonzero angular momentum has a nonspherical charge cloud of magnetoactive 4f-electrons. This charge cloud is coupled strongly with an ionic magnetic moment due to a strong spin-orbit interaction. It means that the rotation of the ionic magnetic moment by means of the magnetic field should result in the rotation of the charge cloud. The rotation of a nonspherical charge cloud induces strains in a crystal lattice—the magnetostriction. This should change the electric polarization of a crystal due to the piezo-effect giving rise to MEE. The effect is large in those molybdates, in which rare earth ions have large magnetic moments $\mu_S = gJ\mu_B$ and nonzero angular moments L .

In line with this mechanism, it was suggested that the MEP was due to the change of the spontaneous electric polarization of TMO induced by the single ion magnetostriction of Tb^{3+} ions [38]. This suggestion is the base of the

magnetostriction model of MEE in rare earth molybdates. According to this model, the dependence of MEP upon the inverse temperature squared should be linear at high temperatures and at not very strong field. This can be shown as follows. MEP is caused by the piezo-effect. So it depends linearly on the strains. The strains are due to the magnetostriction. The magnetostriction at high temperatures and at not very strong magnetic field is proportional to the magnetization squared. The magnetization at these conditions is inversely proportional to the temperature. This leads to the linear dependence of MEP upon the inverse temperature squared $P(T^{-2})$. This prediction was confirmed experimentally in [38].

Figure 7 shows the experimental dependence $P(T^{-2})$ in TMO. MEP was measured along the [110] axis in pulsed magnetic field of 104.5 kOe directed along the $[1\bar{1}0]$ axis. Solid line presents the least-square fitting. One can see that the prediction is fulfilled well.

The movement of the ferroelectric domain walls initiated in $\text{TbGd}(\text{MoO}_4)_3$ (TGMO) by the pulsed magnetic field of 100 kOe at $T = 78$ K was observed in [40, 41]. It was the first observation of the reversal of the spontaneous electric polarization due to the magnetic field.

Figure 8 shows the field dependence of the electric polarization in a single-domain sample of TMO at $T = 20$ K [42]. The polarization was measured along the [001] axis that is along the spontaneous electric polarization. In the initial state, the magnetic field was directed along the axis [100]. The negative sign was ascribed to the initial value of the spontaneous electric polarization on Figure 8. It is seen from Figure 8 that the magnetic field directed along the [100] axis decreases the absolute value of the spontaneous polarization. This decreasing is due to the negative paraprocess in the ferroelectric subsystem that is the decreasing of the parameter of the ferroelectric order. The negative paraprocess continues up to a critical field $H = H_C$ at which the magnetoelastic strains become large enough to nucleate a new domain. The new domain differs from the old one by the opposite direction of \vec{P}_S and by the mutual interchange of [100] and [010] axes. In orthorhombic rare earth molybdates, the ferroelectric domains are identical to the structural twin domains.

The samples investigated in [42] were put into the single domain state by the mechanical compression along the [010] axis. In the samples of this kind, the nucleation of the reversed domain usually goes on by arising of a flat domain wall in the (110) or $(1\bar{1}0)$ plane. This is the beginning of the reversal of electric polarization. The reversal results in a jump of the electric polarization near a critical value of $H = H_C \approx 50$ kOe.

The process of the displacement of the domain wall starts when the new domain reaches the critical size and begins to grow. In Figure 8, the start of the displacement takes place at $H \approx 45$ kOe. The new domain grows at the expense of the old one. During the growth, the domain wall move in the direction normal to its plane that is along the [110] or $[1\bar{1}0]$ axes. At first, when the new domain is smaller than the old one, the absolute value of polarization of the sample being the sum of opposite polarizations of the two domains

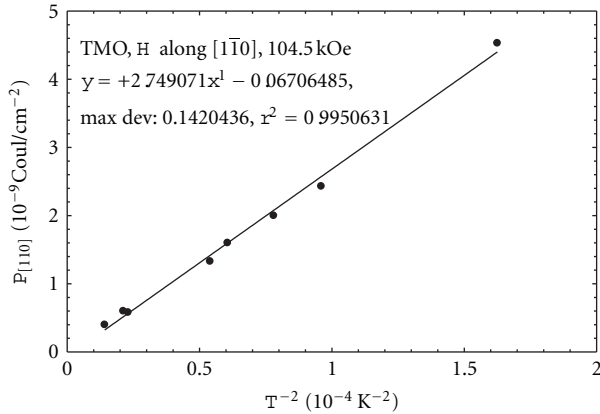


FIGURE 7: The dependence of the electrical polarization in TMO along the [110] axis in pulsed magnetic field of 104.5 kOe directed along [110] axis.

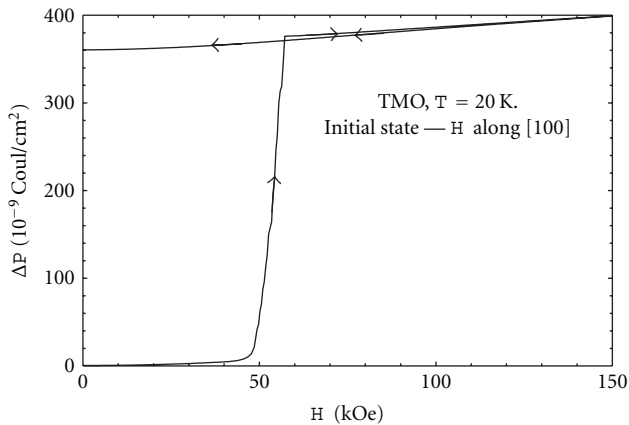


FIGURE 8: The field dependence of the electric polarization in TMO measured along the [001] axis. $T = 20$ K. At $H < 50$ kOe, the field was directed along the [100] axis. At $H > 50$ kOe, the field was directed along the [010] axis.

is decreasing. At $H \approx 53$ kOe, the opposite domains are equal in size ($P = 0$). Further, the absolute value of the polarization began to grow. If the critical field is applied for a long time, the new domain occupies all the volume of the sample. At $H \approx 57$ kOe, the reversal of the electric polarization is completed and the displacement process ceases.

After this, the increase of the polarization goes on by the mechanism of the positive paraprocess.

The examination of the sample in polarized light after the measurements of Figure 8 showed that after the jump the axes [100] and [010] were mutually interchanged. It is known that this interchange is accompanied by the reversal of the electric polarization. This supports the above interpretation of Figure 8.

These experiments were the first to realize the reversal of the electric polarization in a ferroelectric crystal without using the electric field. The temperature dependence $H_C(T)$ was measured in [42]. While decreasing the temperature from 100 K down to 30 K, the critical field decreases from

60 kOe to 30 kOe. Further decrease of the temperature results in an increase of the critical field up to 130 kOe at $T = 15$ K. At lower temperatures down to 4.2 K, the reversal of the electric polarization was not observed up to 200 kOe.

During the growth of the new domain in TMO, small rotations of the tetrahedrons MoO_4 take place [2]. These rotations create defects in the crystal lattice. The more defects are in the lattice the larger is the critical field. That is why every reversal of the spontaneous electric polarization increases the critical field. When the number of the reversal cycles was large enough the sample was mechanically destroyed into small particles at the next in turn reversal.

Figure 9 shows the field dependence of MEP with a sharp break down of MEP at $H = 71.5$ kOe. It is due to the mechanical destruction of the sample. Before the destruction, the spontaneous polarization of the sample was reversed 5 times at temperatures from 98 K to 20 K. One can compare this number of complete reversals with the only attempt to magnetize the sample of TMO along the [100] axis in Fishers experiment [23]. That attempt failed at $H = 40$ kOe because of the destruction of the sample. To the authors' opinion, the reasons of the destruction were the spherical shape and the pin holes of Fishers sample. The pin holes were the origins of a large number of the domain walls of different orientations. The domain walls intersected each other and very large stresses were concentrated at those intersections. These stresses destroyed the sample. The spherical shape stopped the movement of the domain walls because when a flat domain wall moves through the sphere, the area of the wall has to change its size and this also generates the stresses with the evident destruction. The samples used in [42] were rectangular parallelepipeds. They had dimensions $7 \times 7 \times 1$ mm³. The large face of the sample was the (001) plane and the small faces were the (110) and $(1\bar{1}0)$ faces. At this orientation, the domain walls were always parallel to the small faces and normal to the large face of the sample. This orientation ensured the easiest conditions for the domain walls to move. So, the samples sustained several reversals of the spontaneous electric polarization and several tens of magnetizing up to $H = 200$ kOe along the [100] axis without the reversal.

The anisotropy of MEE in TMO was investigated experimentally in [43] in the magnetic field up to 60 kOe at temperatures 4.2 K; 1.8 K and at $T = 0.39$ K up to $H = 100$ kOe. MEP was measured along the [001] axis. The magnetic field was applied in the (001) plane. The angle φ between the [010] axis and the magnetic field was varied from 0 to 90°. The experimental angular dependences of MEP did not obey the relations of the standard theory of the anisotropy of MEE in a paramagnetic crystal derived in [36]. According to [36], the dependence of MEP in a tetragonal paramagnetic crystal upon the strength of the magnetic field and upon its direction can be described by the relation:

$$\Delta P = \xi H^2 \cdot \sin 2\varphi. \quad (28)$$

Here, φ is the angle between the magnetic field and the tetragonal axis; ξ is the constant of the theory.

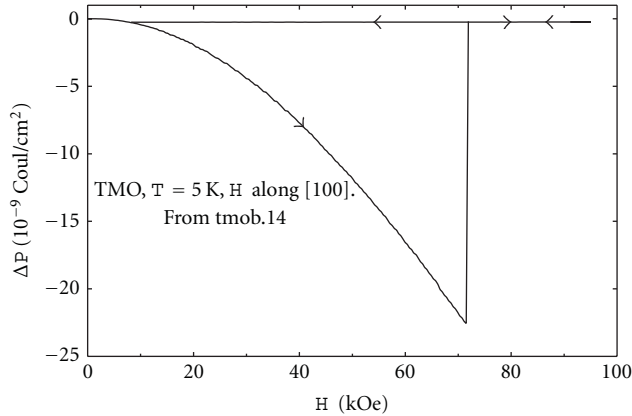


FIGURE 9: The field dependence of MEP in TMO at $T = 5$ K. The field is directed along the $[100]$ axis. The positive direction of the spontaneous polarization coincides with that one of the ΔP axis. A sharp breakdown of MEP at $H = 71.5$ kOe is due to the mechanical destruction of the sample.

Figure 10 displays some of the experimental isotherms of MEP measured along the $[001]$ axis in TMO at 4.2 K (curves 1–5) and at 0.39 K (curves 6–10) for various directions of the field in the (001) plane. The sign of $\Delta P(H)$ in Figure 10 was determined by comparing it with the sign of the jump of the electric polarization when the spontaneous polarization switches in the critical magnetic field (see Figure 8). The field dependences of MEP are nonlinear. MEP is positive in the magnetic field directed along the $[010]$ axis (a positive paraelectric process in the ferroelectric subsystem at $\varphi = 0$, curves 1 and 6). MEP is negative in the magnetic field directed along the $[100]$ axis (a negative paraprocess at $\varphi = 90^\circ$, curves 5 and 10).

The field dependences $\Delta P(H)$ do not agree with (28) and what is more unusual is that the $\Delta P(H)$ itself depends upon the direction of the field.

The angular dependences of MEP in TMO do not agree with (28) neither.

Figure 11 displays some of the experimental angular dependences of MEP in TMO at temperatures $T = 4.2$ K (curves 1–3) and $T = 0.39$ K (curve 4). Curves 1, 2, 3 were measured at $H = 20$ kOe, 40 kOe, and 60 kOe, respectively. Curve 4 was measured at $H = 100$ kOe. The line 4 is drawn for the eyes guide. The lines 1–3 are calculated following the theory of mean quadrupole moments [43, 44]. The points refer to the experimental values of $\Delta P(H, \varphi)$. Their arrangement is not symmetric relative to $\varphi = 45^\circ$ contrary to (28). The absolute values of $\Delta P(\varphi = 0)$ and $\Delta P(\varphi = 90^\circ)$ are different. The values of $\Delta P(\varphi = 45^\circ) \neq 0$. So, (28) of the theory [36] does not describe MEE in TMO. Obviously, a new approach is needed to describe MEE in TMO. This approach was developed in [44] and applied to the problem in [43] using the experimental field dependences of the magnetization [26].

The magnetic-field-induced electric polarization in crystals (MEP) is, like the magnetostriction and magnetic linear birefringence, an even-parity magnetic effect. The classical

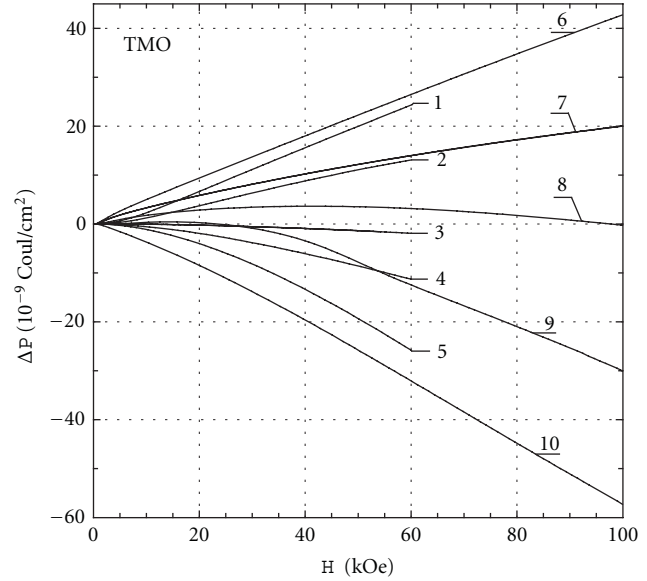


FIGURE 10: MEP in TMO induced along the $[001]$ axis by the magnetic field applied in the (001) plane for various values of the angle φ between the field and the $[010]$ axis at $T = 4.2$ K (curves 1–5) and $T = 0.39$ K (curves 6–10); (1) $\varphi = 0^\circ$; (2) 35.5° ; (3) 57.7° ; (4) 66.6° ; (5) 90° ; (6) 0° ; (7) 35.5° ; (8) 57.7° ; (9) 68.8° ; (10) 90° .

theory of even effects was developed in [45, 46]. This theory describes well the properties of weakly anisotropic compounds, in particular, of those containing d-ions. The situation with f-ions is more complicated. According to [44], even magnetic effects in rare earth compounds are governed by magnetic susceptibilities of the mean multipole moments of the rare earth ions 4f-shell. Their calculation requires knowledge of the energy levels and wave functions of these ions. It was established in [26] that the ground state of Tb^{3+} ions in TMO is apparently a combination of three close-lying singlets, which belongs to different irreducible representations of the symmetry group of the ion environment and are separated by 2.7 cm^{-1} in energy.

In this case, at the magnetic field in the (001) plane, the following relation takes place [43]:

$$\begin{aligned} \Delta P_z(T, H, \varphi) = & AH_x M_x(T) + BH_y M_y(T) + CH_x M_y(T) \\ & + DH_y M_x(T) + EH_x^2 + FH_x H_y + GH_y^2. \end{aligned} \quad (29)$$

Here, T is the temperature. It should not be very high, but the condition $T \gg T_N$ should be fulfilled. T_N is the temperature of the antiferromagnetic ordering. In TMO, $T_N = 0.45$ K [23].

A, B, C, D, E, F , and G are constants of the theory which do not depend on the temperature; $H_x = H_{[010]}$ is the magnetic field component along the $[010]$ axis:

$$M_x = M_{[010]} - \chi_{VV[010]} H_{[010]}; \quad (30)$$

$M_{[010]}$ is the magnetization component along the $[010]$ axis.

$H_y = H_{[100]}$ is the magnetic field component along the [100] axis:

$$M_y = M_{[100]} - \chi_{VV[100]} H_{[100]}; \quad (31)$$

$M_{[100]}$ is the magnetization component along the [100] axis.

$\chi_{VV[010]}$ and $\chi_{VV[100]}$ are the Van Vleck susceptibilities along the [010] and [100] axes, respectively. M_x and M_y are the magnetization components of the Tb^{3+} ion quasitriplet in the (001) plane. The values of the constants A, B, C, D, E, F , and G were determined in [43] using corresponding experimental dependences $\Delta P(H)$ from [43] and $M_{x,y}(H_{x,y})$ from [26]. The solid lines 1, 2, and 3 on Figure 11 were calculated using (29), the values of A, B, C, D, E, F, G , and the dependences (30) and (31) that were calculated in turn for various values of φ from the experimental data of [26]. It is seen that the theory agrees well with the experiment. A satisfactory agreement was obtained in analogous calculations for $T = 1.8 \text{ K}$. At $T = 0.39 \text{ K}$, there is no agreement between the theory and the experiment because the theory does not take account of the antiferromagnetic order that arises at $T_N = 0.45 \text{ K}$.

Four mechanisms of changing the electric polarization were established in TMO: the positive and negative paraelectric processes, the rotation of the electric polarization, and the displacement of the domain wall.

As it was noted above, MEE in $\text{Gd}_2(\text{MoO}_4)_3$ (GMO) at $T = 77 \text{ K}$ was not observed. This fact is in a qualitative agreement with the magnetostrictive model [38]. However, MEE in GMO is not forbidden utterly by this model. In spite of a zero angular momentum of Gd^{3+} ion, the natural magnetic crystalline anisotropy in GMO is not zero. The calculations based on data of Figure 1 derived from results of [18–20] give for the anisotropy energy of GMO in the magnetically saturated state at $T = 1 \text{ K}$ the value of $\approx 10^5 \text{ erg/g}$. It is higher than the anisotropy constant in iron at room temperature. It is well known that the existence of the magnetic crystalline anisotropy involves the existence of the magnetostriction. From these reasoning, it follows that MEE can exist in GMO at low temperatures. MEP in GMO was measured in [47] along the [001] axis at $T = (5\text{--}300) \text{ K}$ for two directions of the magnetic field along the [100] and [010] axes and for $H \leq 190 \text{ kOe}$.

At $T = 5 \text{ K}$ and $H = 190 \text{ kOe}$, MEP was $\Delta P \approx 0.3 \cdot 10^{-9} \text{ Coul/cm}^2$. This fact confirmed the magnetostrictive model of MEE. In [48], the anisotropy of MEE in GMO was investigated in the magnetic field up to 200 kOe at temperatures $T = 4.2 \text{ K}$ and 0.4 K . The experimental angular dependences of MEP at $T = 0.4 \text{ K}$ and various field values are shown on Figure 12. The solid lines are calculated by (28) shifted along the φ axis by $\varphi_0 = \pi/2$. One can see that the experimental dependences $\Delta P(\varphi)$ agree with the relation (28) through the whole field range investigated. The experimental dependences $\Delta P(\varphi)$ at $T = 4.2 \text{ K}$ agree with (28) as well. It is evident that at higher temperatures, the theory [36] developed for a paramagnetic substance should work also. So, (28) of the standard theory [36] describes the angular dependences of MEE in GMO satisfactorily in

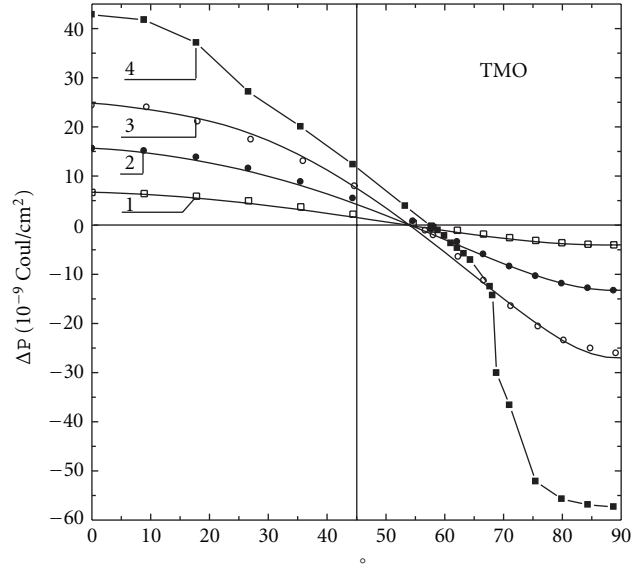


FIGURE 11: The angular dependences of MEP in TMO. MEP was measured along the [001] axis. The field was applied in the (001) plane. φ is the angle between the [010] axis and the field. Curves 1, 2, and 3 were measured at $T = 4.2 \text{ K}$ in various fields: curve 1 at $H = 20 \text{ kOe}$; 2— 40 kOe ; 3— 60 kOe . Curve 4 was measured at $T = 0.39 \text{ K}$ and $H = 100 \text{ kOe}$.

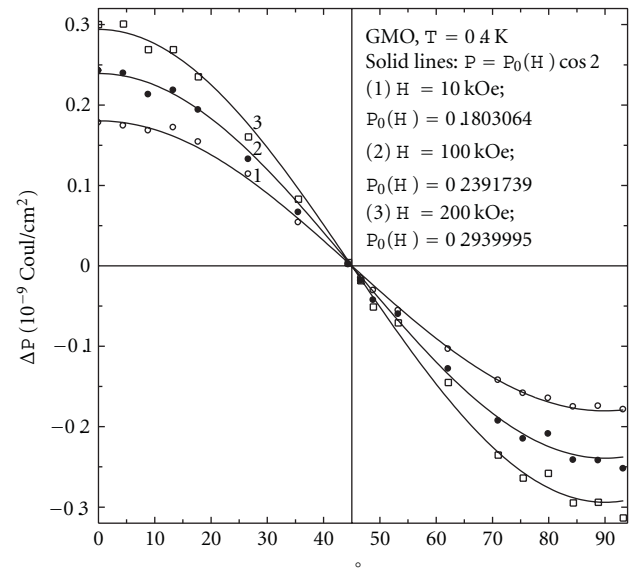


FIGURE 12: Angular dependences of MEP in GMO at various values of the magnetic fields. φ° is the angle between the [010] axis and the magnetic field. $T = 0.4 \text{ K}$. Curve (1) $H = 10 \text{ kOe}$; (2) 100 kOe ; (3) 200 kOe .

the ranges of variables $H = (0\text{--}200) \text{ kOe}$ and $T > 0.4 \text{ K}$ satisfactorily.

The experimental field dependences $\Delta P(H^2)$ in GMO at $T = 4.2 \text{ K}$ and $0 < H < 20 \text{ kOe}$ are shown in Figure 13 for two orientations of the field along the [010] axis (filled circles) and along the [100] axis (open circles).

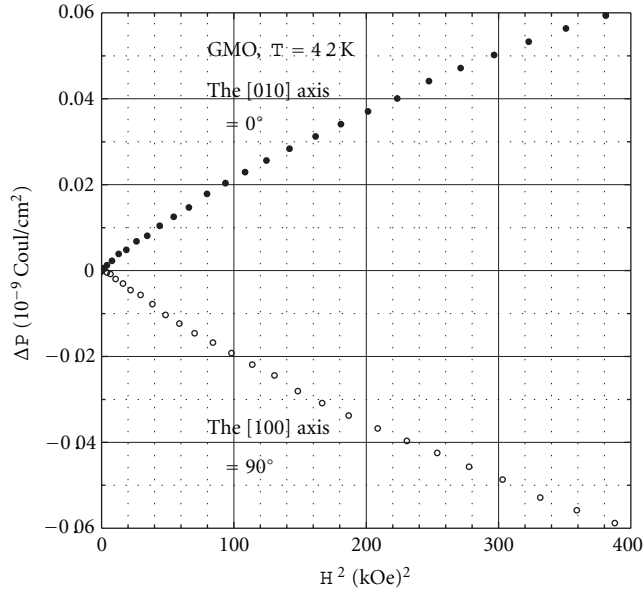


FIGURE 13: The dependences of MEP in GMO upon the magnetic field squared at $T = 4.2$ K. Filled circles were obtained in the magnetic field along the [010] axis; open ones—the field along the [100] axis.

It is seen that, for both directions of the field, the experimental isotherms agree with the relation (28) only at $H^2 < 40$ (kOe) 2 , that is, $H < 6.3$ kOe. At higher fields, the disagreement increases. At $T = 0.4$ K, the theory [36] fails utterly. So, the theory [36] is practically inapplicable to the description of MEE in GMO at low temperatures. The main origin of the magnetoelectric effect in rare earth molybdates is the single ion magnetostriction of rare earth ions [37, 38]. So, we supposed that the experimental dependence $P(m)$ in GMO can be described by the relation analogous to that obtained in [49] for the single ion magnetostriction:

$$\Delta P(m(H, T)) = \Delta P_0 \cdot \hat{I}_{l+1/2}[L^{-1}(m(H, T))]. \quad (32)$$

Here, $\hat{I}_{l+1/2}(x)$ is a normalized hyperbolic Bessel function of l -th order:

$$\begin{aligned} \hat{I}_{l+1/2}(x) &= [I_{l+1/2}(x)]/[I_{l/2}(x)]; \\ I_{l+1/2}(x) &= \int_{-1}^1 P_l(y) \exp(xy) dy; \end{aligned} \quad (33)$$

$P_l(y)$ is the Legendre polynomial. $L^{-1}(m)$ is the inverse Langevin function of the reduced magnetization $m = M/M_S$. For the case considered, $l = 2$ has been defined by the second-order symmetry of the angular dependence $P(\varphi)$ obtained from Figure 12. For $l = 2$, the reduced hyperbolic Bessel function is given by the relation:

$$\hat{I}_{5/2}(x) = 1 + \frac{3}{x^2} - \frac{3}{x} \text{cth } x. \quad (34)$$

Relation (32) was used to describe the field dependence of MEE in GMO. Results are shown on Figure 14. Points on this

figure present experimental dependences of MEP in GMO upon the reduced magnetization m . The circles present MEP values measured in the field directed along the [010] axis. The squares correspond to the field along the [100] axis. Filled symbols refer to the temperature $T = 0.4$ K, open symbols refer to $T = 4.2$ K. The experimental values of MEP do not exceed $\Delta P \approx 0.3 \cdot 10^{-9}$ Coul/cm 2 .

Calculated dependences $\Delta P(m)$ are shown by solid lines in Figure 14 for $T = 4.2$ K (curves 1 and 2). Coefficients ΔP_0 are $-0.18 \cdot 10^{-9}$ C/cm 2 and $0.17 \cdot 10^{-9}$ C/cm 2 for the [100] and [010] axes, respectively. For $0 < m < 0.8$, the divergence between the experiment and the theory is $\delta(\Delta P)/(\Delta P) < 0.02$. So, the relation (32) obtained from the theory of the single ion magnetostriction agrees to the experiment well at $0 < m < 0.8$. For $m = 0.95$, $\delta(\Delta P)/(\Delta P) = 0.09$. The value $m = 0.95$ in the case of GMO corresponds to the field $H \approx 56, 7$ kOe. It is seen that the range of validity of relation (32) is wider than relation (28) [36]. Nevertheless, the most part of the field range is not described.

The anomaly near $m = 1$ indicates some additional effects that should be considered. The dependences $P(m)$ at $T = 0.4$ K cannot be explained by the theory of the single ion magnetostriction in its present form because this theory does not take account of the antiferromagnetic structure. The magnetic phase transition paramagnetism-antiferromagnetism that takes place in GMO at $T = 0.3$ K may affect the results of the measurements at $T = 0.4$ K. The solid lines 3 and 4 are drawn only for the eyes guide.

MEE in $\text{Sm}_2(\text{MoO}_4)_3$ (SMO) was investigated in direct current magnetic field up to 200 kOe at temperatures from 4.4 K to 0.43 K [50]. MEP was measured along the [001] axis in the magnetic field along the [010] axis and [100] axis.

Figure 15 represents a cycle of the MEP variation (abcde) observed in a single domain sample of SMO at $T = 1.4$ K in the magnetic field directed along the [010] axis. At the ascending branch of the cycle (ab), the magnetic field was increased at a rate $dH/dt = 0.755$ kOe/s. The branch ab was passed for 265 s. It represents the experimental dependence of MEP in the increasing field $\Delta P_{e1}(H)$. At the b point ($H = 200$ kOe), the MEP was $\Delta P_{e1} = -5.46 \cdot 10^{-9}$ Coul/cm 2 . At this point, the magnetic field was fixed and remained unvaried for 232 s. During this time, the MEP relaxed to $\Delta P_{e1} = -3.01 \cdot 10^{-9}$ Coul/cm 2 (point c). At point c, the magnetic field started to decrease at a rate $dH/dt = -0.755$ kOe/s. The descending branch cd represents the experimental dependence of MEP in the decreasing field $\Delta P_{e1}(H)$. At point d, the magnetic field reached zero and was fixed. The MEP was found to be $\Delta P_{e1} = 3.12 \cdot 10^{-9}$ Coul/cm 2 at this point. After fixing the magnetic field at zero, the MEP was measured for 338 s. During this time, it relaxed to $\Delta P = 1.4 \cdot 10^{-9}$ Coul/cm 2 .

This variation of the MEP is plotted as de on Figure 15. Thus, the MEP in SMO relaxes in a fixed magnetic field. The relaxation is not due to the charge leakage through the electrometer input circuit because the times of measurements at a fixed field 232 s and 338 s are two orders of magnitude shorter than the time constant of the electrometer $\tau_{em} > 10^4$ s. Analogous measurements of the MEP cycles were performed for other magnetic field

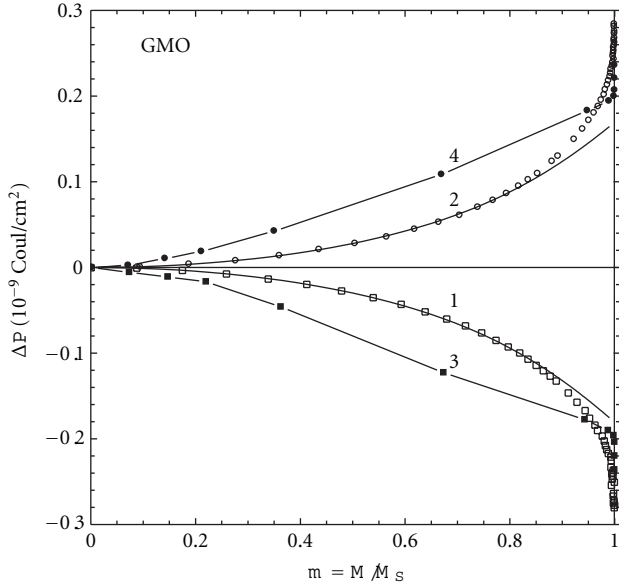


FIGURE 14: Dependences of MEP along the [001] axis in GMO upon the reduced magnetization $m = M/M_S$ at various temperatures and magnetic field directions. $T = 4.2$ K: curve (1) the magnetic field along the [100] axis; curve (2) the field along the [010] axis. $T = 0.4$ K: curve (3) the field along the [100] axis; curve (4) the field along the [010] axis.

orientations and temperatures. The time dependences of MEP on the segments bc and de were fitted well by the exponents:

$$\Delta P_e(H = \text{const}, t) = \Delta P_0 \exp\left(-\frac{t}{\tau}\right) + P_R. \quad (35)$$

The relaxation time τ increased with decreasing temperature. It depended upon the magnetic field only weakly.

Table 2 presents the values of τ obtained at various temperatures in the field 200 kOe.

The relaxation of the MEP noticeably affected the MEP field dependences because the measurement time 265 s was comparable with the relaxation time τ . Our measurements showed that the relation between ΔP_0 and P_R can be approximately described by the expression $P_R \approx \beta(\Delta P_0)$ where $\beta \ll 1$ is a constant. In this case, a time-dependent contribution could be eliminated from the experimental field dependences $\Delta P_{e\uparrow\downarrow}(H)$ using the relations:

$$\Delta P_{\uparrow}(H) = \Delta P_{e\uparrow}(H) + \int_0^H \frac{\Delta P_{e\uparrow}(H)}{\alpha\tau(1+\beta)} dH; \quad (36)$$

$$\Delta P_{\downarrow}(H) = \Delta P_{e\downarrow}(H) - \int_{H_m}^H \frac{\Delta P_{e\downarrow}(H)}{\alpha\tau(1+\beta)} dH + P_{\uparrow}(H_m) - P_{e\downarrow}(H_m). \quad (37)$$

Here, $P_{\uparrow\downarrow}(H)$ does not depend on the time. The \uparrow and \downarrow arrows denote the values obtained under increasing and decreasing field respectively; H_m is the maximum field reached in the measurements; $\alpha = dH/dt$ is the rate of the

TABLE 2: Relaxation time τ of MEP in SMO at various temperatures in the field 200 kOe.

T (K)	The field along [010], τ (s)	The field along [100], τ (s)
4.4	127	128
2.6	279	192
1.4	337	403
0.9	490	490
0.43	534	828

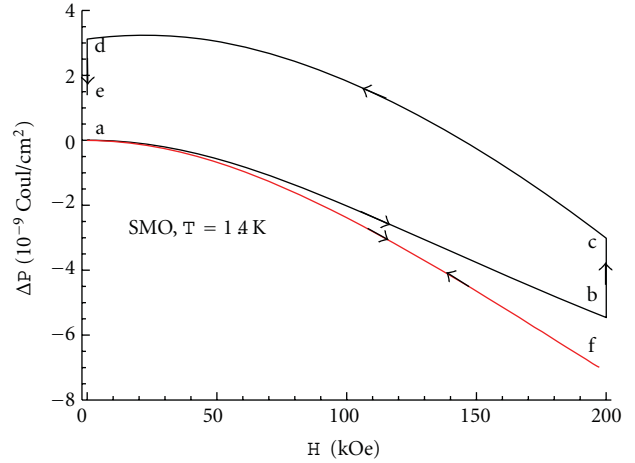


FIGURE 15: Field dependences of MEP in $\text{Sm}_2(\text{MoO}_4)_3$ at $T = 1.4$ K. The field is directed along the [010] axis. Curves ab and cd present experimental dependences $\Delta P_{e\uparrow\downarrow}(H)$ in increasing and decreasing field, respectively. Straight lines bc and de present the relaxation of ΔP with the time at $H = 200$ kOe and $H = 0$, respectively. Curves af and fa are calculated from the curves ab and cd using (36) and (37), respectively.

magnetic field variation with the time; $P_{\uparrow}(H_m)$ is the true MEP at the maximum field calculated from the experimental curve $P_{e\uparrow}(H)$ using (36); $P_{e\uparrow}(H_m)$ is the experimental value of MEP at the start of the decrease in the field (point c in the cycle in Figure 15). Curves ab and cd were used to obtain the af and fa curves (Figure 15) by means of (36) and (37), respectively. One can see that elimination of the time-dependent contribution from the experimental $\Delta P_{e\uparrow\downarrow}(H)$ dependences yields a hysteresis-free $P(H)$ relation. Analogous results were obtained at the temperatures 0.9; 1.4; 2.6; 4.4 K in the field along the [010] and [100] axes.

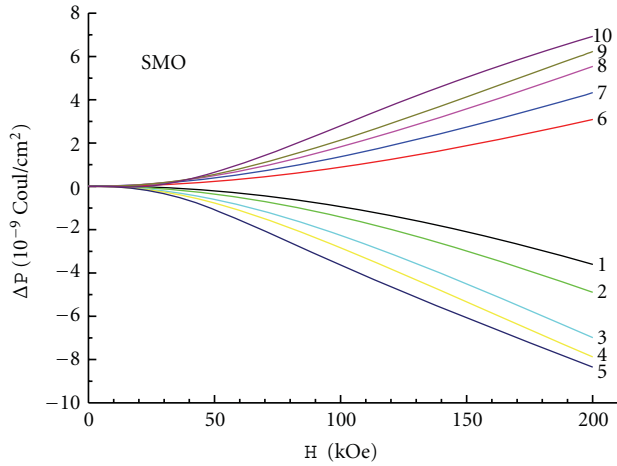
Corresponding curves are shown in Figure 16. The dependences 1 and 6 obtained at 4.4 K are fitted well by the relation (28) at $\varphi = 0; \pi/2$ and $H < 50$ kOe. At higher fields and lower temperatures, this relation fails.

The data described in Section 4 qualitatively confirm the magnetostriction mechanism of MEE in rare earth molybdates. This mechanism is based on the assumption that the magnetostriction affects the electric polarization of these ferroelectric compounds.

Table 3 shows the values of MEP in the three rare earth molybdates investigated here at fixed temperature and field values. The values of g and J were taken from [51]. There is a clear qualitative correlation between the values of the angular

TABLE 3: A comparison of MEP absolute values in TMO, GMO, and SMO at $T = 4.2$ K and $H = 100$ kOe.

Compound	Figure	T (K)	ΔP (10^{-9} Coul/cm 2)	L of R^{3+} ion	gJ of R^{3+} ion
TMO	Figure 11	0.39	$\approx (42-57)$	3	9
GMO	Figure 12	0.4	≈ 0.25	0	7
SMO	Figure 16	0.43	≈ 3	5	0.7

FIGURE 16: Field dependences of MEP in SMO after the elimination of the time-dependent contribution. Curves 1–5 are measured in the field along the [010] axis; curves 6–10 are measured in the field along the [100] axis. The temperatures: curves (1, 6) $T = 4.4$ K; (2, 7) 2.6 K; (3, 8) 1.4 K; (4, 9) 0.9 K; (5, 10) 0.43 K.

momentum L and the values of ΔP . GMO with zero angular momentum of R^{3+} ion possesses the least ΔP value. The angular momentum L characterizes the spatial anisotropy of an ion. It is obvious that the rotation of an anisotropic ion with $L \neq 0$ produces more strains in a crystal lattice than the rotation of a spherically symmetrical ion with $L = 0$. So, the change of the electric polarization (MEP = ΔP) is larger for $L \neq 0$ than for $L = 0$. There is some incongruity in this conclusion: the angular momentum of Sm^{3+} ion is larger than that of Tb^{3+} ion, but the ΔP value in SMO is the order of magnitude smaller than that in TMO. This fact can be explained qualitatively by relations between the ionic magnetic moments $gJ\mu_B$ of R^{3+} ions under consideration. Here, g is g -factor; $J = L \pm S$ is the total mechanical moment of R^{3+} ion; S is the spin mechanical moment of R^{3+} ion. The sign “–” corresponds to light rare earth ions from Ce to Eu, and the sign “+” corresponds to heavy rare earth ions from Tb to Yb. μ_B is the Bohr magneton. One can see that the magnetic moment of Tb^{3+} ion is larger than that one of Sm^{3+} ion. So, one should conclude that the total effect of the space anisotropy and the magnetic moment of Tb^{3+} ion is larger than that one of Sm^{3+} ion. It can be because of that the ion with the larger magnetic moments rotates by the larger angle than the ion with a smaller magnetic moment in the same magnetic field. The final result is determined by the quantitative contributions of the spatial anisotropy of ions and the angles of their rotations due to the interaction of their magnetic moments with the applied magnetic field.

5. Magneto-Optical Properties

In [26], the experimental dependences of the magnetization in terbium molybdate β' - $\text{Tb}_2(\text{MoO}_4)_3$ (TMO) upon the magnetic field and the temperature $M(H, T)$ were described satisfactorily using the theory of the magnetism of singlets [31] at low temperatures $T < 30$ K. At higher temperatures, the agreement was not good. It was due to increasing population of highest levels of 7F_6 multiplet of Tb^{3+} ions. For the calculation of the magnetization at high temperatures, the highest levels of 7F_6 multiplet should be known. To calculate the spectrum of 7F_6 multiplet, one should know the crystal field acting on Tb^{3+} -ion. Now, there is no theory that enables one to calculate the crystal field parameters from the first principles. So, the investigations that allow obtain directly the data about the spectra of multiplets are very useful. For example, the knowledge of the spectrum of the excited multiplet 5D_4 can simplify the calculations of the crystal field parameters in the case under investigation. The spectrum of 5D_4 multiplet can be found from the experimental data for the optical absorption in TMO at low temperatures. The optical absorption in TMO was studied at zero magnetic field in [52]. 14 well-resolved absorption peaks were observed. It was established that those peaks correspond to the transitions $^7F_6 \Rightarrow ^5D_4$ in Tb^{3+} ions.

In [53], the absorption spectra were measured in TMO in the nonpolarized light in the magnetic field $H \leq 200$ kOe along the [001] and [110] axes at $T = 4.2$ K and $T = 1.7$ K. A wave vector of the light was parallel to the magnetic field. At zero field, 14 well-resolved peaks with wave numbers $\nu = 20519 \text{ cm}^{-1} - 20655 \text{ cm}^{-1}$ ($\lambda = 4873.5 \text{ \AA} - 4841.4 \text{ \AA}$) were observed. The magnetic field shifted the spectrum toward large ν values. The spectra were measured at 29 different field values. The experimental field dependences of the wave numbers of the absorption peaks $\nu_i(H)$ were obtained for both directions of the field.

The spectra did not depend upon the temperature. There was a pronounced dependence of the peak numbers and of the rate of their shift with the field $d\nu_i/dH$ upon the direction of the field. The analysis of these dependences showed that the excited multiplet 5D_4 of Tb^{3+} ion in the crystal field of TMO could be considered as consisting of five singlets and two quasidoublets. On the base of the measurements and analysis of the absorption spectra in terbium molybdate, the field dependence of the energy spectrum $E_i(H)$ of the excited multiplet 5D_4 of Tb^{3+} ion in the crystal field with the point group symmetry C_2 was found for the magnetic field up to 200 kOe along the [001] axis. The experimental dependences $E_i(H)$ could be described well by the theory of the magnetism of singlets.

The number of the absorption peaks was explained by the existing of two types of nonequivalent sites for Tb^{3+} ions in the crystal lattice of TMO.

6. Anomalously High Photo Voltages

In [54], an anomalously high photoinduced voltage (APV effect) in TMO was observed. The illumination of a single crystal of TMO by the beam of the argon laser with a wave length of $\lambda = 4880 \text{ \AA}$ and a power of 0.5 W induced in the ferroelectric single domain sample an additional electric polarization. The wave length corresponded to a proper absorption band of TMO. The laser beam was directed along the $[110]$ axis. The surface of polarization of the laser beam was normal to the (001) plane. The direction of the photoinduced polarization was the same as that of the spontaneous polarization. The laser beam was focused to a spot with an area 10^{-2} cm^2 . It means that the distribution of the intensity of the light was highly inhomogeneous. The average value of the intensity in the illuminated spot was $\approx 50 \text{ W/cm}^2$. The photoinduced electric polarization of the crystal depended upon the time of the illumination. After the illumination during 4.5 h , the photoinduced polarization was approximately three times larger than the spontaneous electric polarization and showed the tendency to the saturation.

The laser beam with the wave length 4880 \AA induced in TMO the luminescence in the green part of the visible spectrum with the wave length $\approx 5430 \text{ \AA}$. The quantum output constituted 20% .

In [55], the dependences of the photoinduced voltage in TMO upon the time t of the illumination by a laser beam were measured at room temperature at $0.1 \text{ s} \leq t \leq 4500 \text{ s}$. The power of the laser radiation was 0.4 W . The distribution of the intensity along the sample was varied from highly inhomogeneous to homogeneous. It was found that the photoinduced voltages of two types with opposite signs appear due to the inhomogeneous illumination.

In [55], the APV effect in TMO was measured at heightened sensibility, respectively, to the photoinduced electric polarization of the crystal.

Due to this, it was possible to observe relatively small contribution to the photoinduced polarization ΔP_{ph} that was directed opposite to the spontaneous electric polarization P_S . This effect was observed at a small duration of illumination $t < 80 \text{ s}$. It was called APV-1. The effect that was observed in [54] was called APV-2. The sign of APV-1 was opposite to the sign of APV-2. The voltage and the relaxation time of APV-1 were essentially smaller than those of APV-2. That is why the APV-1 effect was not observed on the background of the APV-2 effect in [54].

The first observation of APV-effect was reported for a single crystal sample of ferroelectric $\text{SbSI}_{0.35}\text{Br}_{0.65}$ [56]. A phenomenological theory of the APV effect was described in [57]. In works published up to now, the diffusion contribution to the photoinduced current was ignored [57, 58]. According to [57], the time dependences of the

photoinduced current and the photoinduced voltage are given by the following expressions:

$$i(t) = i_0 \exp\left(-\frac{t}{\tau}\right); \quad (38)$$

$$V(t) = V_0 \left[1 - \exp\left(-\frac{t}{\tau}\right)\right]. \quad (39)$$

The effect APV-1 is well described by the expressions (38) and (39). The effect APV-2 does not follow these expressions.

Figure 17 shows experimental time dependences of the photoinduced current $i(t)$ (curve 1) and the photoinduced voltage $V(t)$ (curve 2).

These curves were obtained on the sample number 1 with size $6 \times 7 \times 1 \text{ mm}^3$. The large face of the sample was parallel to the plane (001) .

The $[100]$ and $[010]$ crystal axes were directed along the bisectors of the right angles of the (001) sides. The laser beam was focused on the $7 \times 1 \text{ mm}^2$ face of the sample by a cylinder lens to the spot with dimensions $2 \times 0.5 \text{ mm}^2$. The large size of the spot was along the $[001]$ axis of the crystal. The intensity of the light in the spot was $\approx 40 \text{ W/cm}^2$.

Arrows show the time when the light was switched on and off. These dependences are in a good agreement with expressions (38) and (39) respectively. The constants are $i_0 \approx 0.2 \cdot 10^{-9} \text{ A}$; $V_0 \approx -10 \text{ V}$; $\tau \approx 5 \text{ s}$. The stepped form of the curve 1 is due to the resolution of the equipment. When the light is switched on, the negative voltage $V(t)$ appears. This voltage is due to the photoinduced electric polarization $\Delta \vec{P}_{\text{ph}}$ that is directed opposite to the spontaneous electric polarization \vec{P}_S . The value $V_0 \approx -10 \text{ V}$ corresponds to the decreasing of \vec{P}_S by the value $\Delta P_{\text{ph}} = 4.8 \cdot 10^{-9} \text{ C/cm}^2$. When the light is switched off, the photoinduced voltage decreases exponentially with the time constant $\tau \approx 5 \text{ s}$. The photoinduced voltage and the photoinduced current on Figure 17 are due to the effect APV-1.

Figure 18 shows the dependences $\Delta P_{\text{ph}}(t)$ for various distributions of the light intensity along the sample. The switching on and off the light are shown by the arrows. Curve 1 was measured on the sample number 1 at the same conditions as in Figure 17. One can see that the type of the dependence shown in Figure 17 occurs only during short time of $\approx 200 \text{ s}$ after the light is switched on. At $t \approx (250 - 300) \text{ s}$, the $\Delta P_{\text{ph}}(t)$ value reaches a minimum of $\Delta P_{\text{ph}} \approx -4.8 \cdot 10^{-9} \text{ C/cm}^2$ and begins to increase with increasing t .

At $t \approx 1700 \text{ s}$, the sign of $\Delta P_{\text{ph}}(t)$ is changed. The positive sign of $\Delta P_{\text{ph}}(t)$ at $t > 1700 \text{ s}$ corresponds to the coincidence of the directions of \vec{P}_S and $\Delta \vec{P}_{\text{ph}}$. The tendency to the saturation of $\Delta P_{\text{ph}}(t)$ is seen at large values of t . At switching off the light, the positive jump of the photoinduced polarization occurs. It is of the same absolute value as the negative jump at switching on the light. After this jump, the photoinduced polarization continues to increase slowly: an after-effect takes place. In other words, the long negative pulse of the polarization due to the effect APV-1 exists on the background of slow positive drift of the polarization. This drift is due to the effect APV-2.

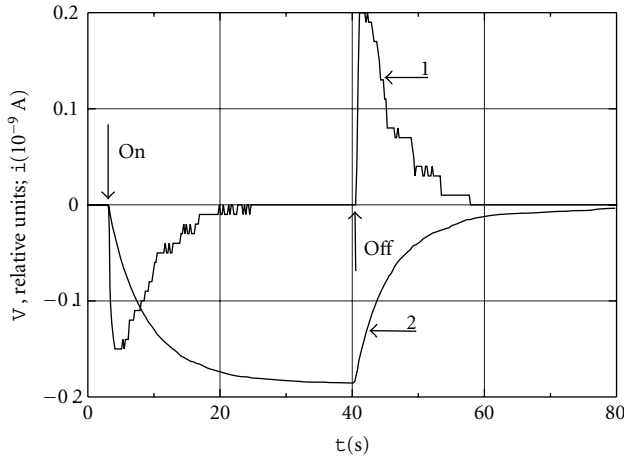


FIGURE 17: The dependence upon the time of the photoinduced current (curve 1) and the photoinduced voltage (curve 2) in TMO. Sample number 1. The cross-section of the beam has size $0.5 \text{ mm} \times 2 \text{ mm}$.

Curve 2 in Figure 18 was measured on the sample number 1 with a homogeneous distribution of the intensity across the $7 \times 1 \text{ mm}^2$ face of the sample. The cross-section of the laser beam had a circular form with diameter $\phi = 7 \text{ mm}$. So, the intensity of the illumination was lower than for curve 1, and the photoinduced polarization was smaller. One can see that curve 2 shows a smaller relative contribution of the slow positive drift to the resulting polarization than curve 1. It should be pointed out that in spite of the homogeneous illumination of the $7 \times 1 \text{ mm}^2$ side the distribution of the intensity of the light was not homogeneous inside the sample along the direction of the propagation of the light due to the absorption. To obtain the $\Delta P_{\text{ph}}(t)$ dependence at still more homogeneous illumination, the measurements were performed on the sample number 2. The sample number 2 was a cube of the size of $2 \times 2 \times 2 \text{ mm}^3$. The relative directions of the crystal axes and of the laser beam were the same as for sample number 1. The cross-section of the beam was as for curve 2.

As the illuminated face of the sample number 2 was smaller than that for sample number 1, the $\Delta P_{\text{ph}}(t)$ value also was smaller. As the size of the sample number 2 along the direction of the propagation of the light was three times smaller than for the sample number 1, the relative nonhomogeneity of the illumination was also smaller. Curve 3 in Figure 18 was measured on the sample number 2. One can see that in this case the change of the sign of the voltage was not observed during all the time of the illumination. At these conditions, the positive drift due to APV-2 is so small that one can neglect it.

Figure 19 shows curve 1 from Figure 18 contracted along the t -axis and its prolongation for large t values that describes the relaxation of the photopolarization. The relaxation curve gives qualitative information that is important for explanation of the APV effect in TMO. The curve shows a very durable aftereffect. The increase of the photoinduced voltage continues during $\approx 3500 \text{ s}$ after the light is switched

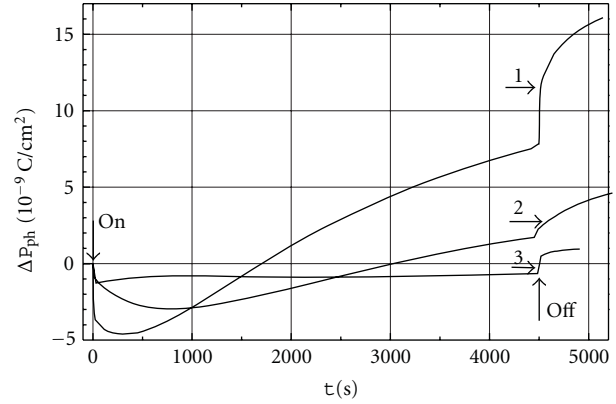


FIGURE 18: The dependence of the photoinduced electric polarization in TMO upon the time. Curve 1. Sample number 1. A nonhomogeneous illumination. Curve 2. Sample number 1. A homogeneous illumination of the face of the sample. A nonhomogeneous distribution of the intensity in the sample due to the absorption. Curve 3. Sample number 2. An approximately homogeneous distribution of the intensity in the sample.

off. The voltage reaches the maximum $V_{\text{max}} \approx 35 \text{ V}$ at $t \approx 8000 \text{ s}$ and then decreases.

The value of $V_{\text{max}} \approx 35 \text{ V}$ corresponds to the photopolarization $\Delta P_{\text{ph2}} \approx 17 \cdot 10^{-9} \text{ C} \cdot \text{cm}^{-2}$. The relaxation time is $\tau_{\text{relax}} \approx 20 \text{ h} = 7.2 \cdot 10^4 \text{ s}$. It is more than the time constant of the input circuit of the electrometer τ_{input} . Due to this, the dependence $V(t)$ of the relaxation process is not reproduced correctly. So, only the initial part of the relaxation curve is shown in Figure 19. The complete relaxation of the APV-2 effect for the present experiment was achieved at $t_R \approx 150 \text{ h} = 5.4 \cdot 10^5 \text{ s}$. Due to the relation between τ_{input} and τ_{relax} , this value of t_R should be considered as a bottom estimate.

The two effects described above show quite different dependences upon the conditions of the experiment.

The APV-1 effect exists both at homogeneous and nonhomogeneous illuminations (Figure 18). It reaches the saturation at $t \approx 40 \text{ s}$ (Figure 17). The APV-2 effect exists only at nonhomogeneous illumination.

It was not observed at a homogeneous illumination (Figure 18, curve 3). It depends on the time and the geometry of the beam cross-section (Figure 18).

The time constant of the APV-1 effect is $\tau = 5 \text{ s}$. From Figures 17 and 18, one can see that APV-1 effect reaches the saturation in a relatively short time and after this the voltage due to APV-1 effect is constant. Contrary to APV-1 effect, the voltage due to APV-2 effect grows for a very long time of the order of several thousand seconds showing only very weak tendency to the saturation.

The APV-2 effect possesses the after-effect: the P_{ph2} value increases during several thousand seconds after the light is switched off (Figure 19). No after-effect was observed while measuring the APV-1 effect.

The APV-1 effect has a feature that is common to photo-induced currents measured in [59–62]. It is a strong correlation between the switching the light off and the change of the direction of the photoinduced current. The

photoinduced voltage due to this effect begins to decrease immediately after the light is switched off. At the same time, the direction of the corresponding current is changed. The APV-2 effect is essentially different from those observed in [59–62]. The photoinduced voltage due to this effect is growing during a long time (almost an hour) after the light is switched off. The photoinduced current due to this effect changes its sign with a very long delay after the light is switched off. So, it is ascertained that there are two different effects: APV-1 and APV-2. They have quite different mechanisms.

In [55], it was concluded that the APV-1 effect originates due to the transitions of Tb^{3+} ions from the ground state $^7\text{F}_6$ to the excited state $^5\text{D}_4$ induced by the laser irradiation. The saturation of the APV-1 effect is reached when the dynamic equilibrium between the numbers of straightforward and backward transitions is established. The lattice accommodation explains the large value of the time constant $\tau \approx 5\text{ s}$ of the APV-1 effect. The process of the accommodation takes some time. That is why the time constant τ is essentially larger than the life time of a free Tb^{3+} ion in the excited state $^5\text{D}_4$.

The APV-2 effect originates from the autoionization of the excited Tb^{3+} ions and the subsequent diffusion of the knocked out electrons in the electric field of the spontaneous polarization through the crystal. The autoionization can be caused by the internal electrical field related to the ferroelectric order. The autoionization results in appearance of a Tb^{4+} hole and a nonequilibrium electron. If the light is nonhomogeneous, the diffusion of these carriers from illuminated part of the sample to the nonilluminated one gives rise to the photoinduced current. The sign of the effect is determined by the fact that a pair $\text{Tb}^{4+}-(\text{MoO}_4)^{2-}$ appears instead of a pair $\text{Tb}^{3+}-(\text{MoO}_4)^{2-}$. So, autoionization increases the resulting electrical dipole moment, and the polarization of the sample increases as well.

7. Fluctuations Near the β - β' Phase Transition

In [63], giant fluctuations of the amplitude of the acoustic resonant peak were observed experimentally in orthorhombic $\text{Gd}_2(\text{MoO}_4)_3$ (GMO) near the Curie temperature. The temperature dependence of the intensity of the acoustic main resonant peak was measured in the temperature range (22–165)°C including the Curie temperature, $T_C = 159^\circ\text{C}$. The low-frequency fluctuations of the amplitude of the resonant current through the sample were observed in the vicinity of the Curie temperature. The sample was cut in the (001) plane. Its dimensions were $7 \times 7 \times 1\text{ mm}^3$. The diagonals of the (001) face were parallel to the orthorhombic [100] and [010] axis.

The piezo-acoustic resonance was investigated. The scheme recommended in the list of standards on measurements of piezo-electric crystals [64] was used. Acoustic oscillations in the sample were generated using self-exciting method. An oscilloscope was used as a detector of oscillations in the sample. Frequency dependences of the amplitude of the sinusoidal input voltage of the oscilloscope V_1 were

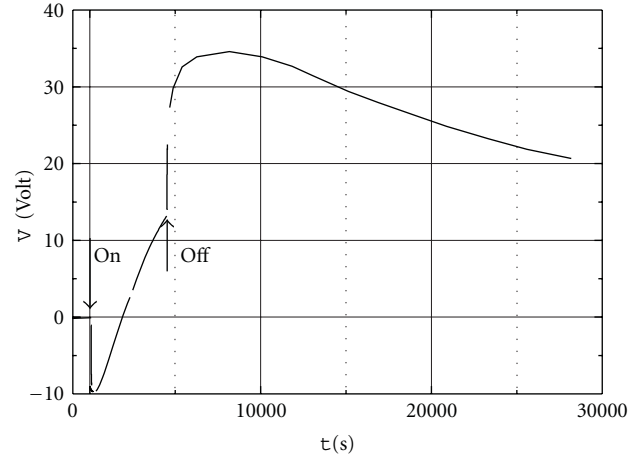


FIGURE 19: The relaxation of the photoinduced voltage in terbium molybdate after measuring curve 1 on Figure 18.

measured at fixed amplitude of the output voltage of the generator V_0 in the frequency range (20–300) kHz at $T = (22\text{--}165)^\circ\text{C}$. Under the influence of an alternative voltage, the alternative strains arise in a piezoelectric crystal as a consequence of the inverse piezoeffect. Under the influence of these strains, the alternative electric polarization arises in the crystal as a consequence of the direct piezoeffect. This alternative polarization is equivalent to appearing of an additional alternative electric current. The dependence of this additional current upon the frequency and the value of the voltage of the generator is described in terms of an equivalent electrical oscillating contour. This contour consists of an active resistance R , an inductivity L , and a capacity C that are connected in series [65, 66]. The capacity C depends upon the elastic and piezoelectric properties of the crystal, its dielectric permittivity, the dimensions of the sample, and the oscillation mode. The inductivity L depends upon the crystal density, its piezoelectric constants and the dimensions of the sample. The resistance R is determined by the dissipation of the oscillation energy due to the internal friction and depends on the viscosity, the piezoelectric constants, and the dimensions of the sample.

The equivalent contour, the static resistance of the sample R_1 (the resistance in the absence of the oscillations), and the static capacity of the sample C_1 (the capacity in the absence of the oscillations) are connected in parallel. When the generator frequency is equal to the resonant frequency of the equivalent contour, the impedance of the contour decreases and becomes equal to its active resistance R . The decreasing of the sample impedance results in an increase of the current through the sample. This results in an increase of the input voltage of the oscilloscope V_1 , and the resonant maximum appears on the frequency dependence $V_1(f)$ at

$$f = f_R = \frac{1}{2\pi\sqrt{LC}}. \quad (40)$$

The value of the maximum is given by the following equation:

$$V_1[f_R(T)] = V_R(T) = \frac{V_0[1 + \xi(T)C_1^2]}{\sqrt{\xi(T)C_2^2 + [1 + \xi(T)C_1(C_1 + C_2)]^2}}. \quad (41)$$

Here, T is the temperature; C_1 the static capacity of the sample; C_2 the input capacity of the oscilloscope;

$$\xi(T) = \frac{[R(T)]^2}{L(T)C(T)} = 4\pi^2[f_R(T)]^2[R(T)]^2; \quad (42)$$

R , L , C are the resistance, the inductivity, and the capacity of the equivalent contour, respectively. Equation (41) is derived for the case $R_1 \gg 1/(\omega C_1)$; $R_2 \gg 1/(\omega C_2)$. R_2 is the active input resistance of the oscilloscope. It was assumed that the values R , C_1 , and C_2 do not shift noticeably the resonance term $\omega^2 LC = 1$.

Figure 20 shows the experimental temperature dependence of the resonant peak intensity $V_R(T)$.

At temperatures higher than $\approx 130^\circ\text{C}$, the intensity $V_R(T)$ displays large and slow fluctuations at constant values of the temperature and the frequency. These fluctuations can be fixed visually.

The time of fluctuations reaches tens of seconds. Figure 20 shows maximum (open circles) and minimum (filled circles) values of V_R . The maximum and the minimum values of V_R were found from the observation during two minutes at fixed values of the temperature and the frequency. The variations of V_R due to the fluctuations reached 0.1 Volt. The fluctuations could be observed only in the limit of the resonant peak width $\Delta f_R \approx 1$ kHz. Out of the resonance, they were zero with the accuracy of $0.008V_R \approx 0.0003$ Volt. Curves are drawn only for the eyes guide.

Figure 21 shows the time dependence of the resonant peak intensity $V_R(t)$ at $T = 154.25^\circ\text{C}$ and $f_R = 154.9$ kHz. The oscillating line is a spline. The horizontal line is a mean value of V_R over the time of observations. The mean square fluctuation of V_R is ≈ 33 mV.

It constitutes $\approx 15\%$ of the mean value $\bar{V}_R \approx 0.22$ Volt. The real frequency spectrum of the fluctuations is wider than that of the curve on Figure 21. Rapid fluctuations occur with periods much less than one second. So fast variations of $V_R(t)$ can be seen but it is impossible to fix them visually. Observed fluctuations of $V_R(t)$ occurs due to the fluctuations of the resonant current through the sample. When the temperature of the sample is near the temperature of the phase transition, various parameters of the crystal fluctuate and lead to the fluctuations of the impedance of the equivalent contour. This results in the fluctuations of the current through the sample. The value V_R at the resonance is related to the parameters of the equivalent contour by (41). It is seen from (41) that the value of V_R and consequently the values of its fluctuations can be presented as a function of the only variable $\xi = R^2/LC$. It can be shown that ξ depends on four material constants. They are the elastic constant, the dielectric permeability, the coefficient of the internal friction, and the piezoelectric constant. ξ depends

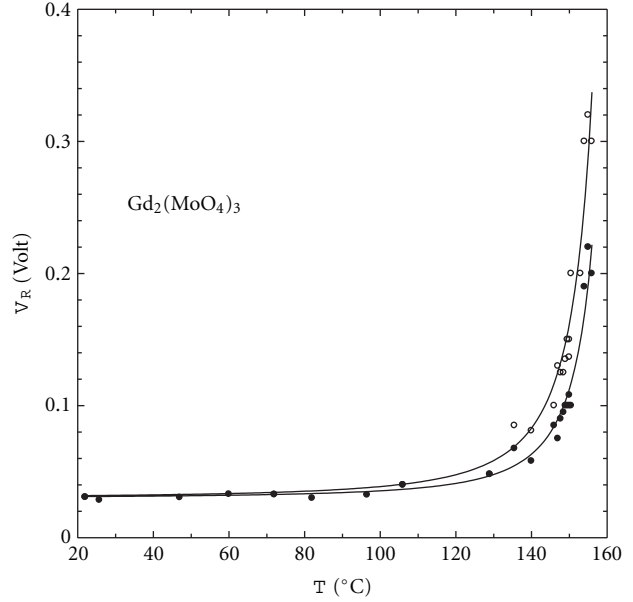


FIGURE 20: The temperature dependences of the maximum (open circles) and minimum (filled circles) intensities of the fluctuating resonant peak V_R . Lines are drawn for the eyes guide.

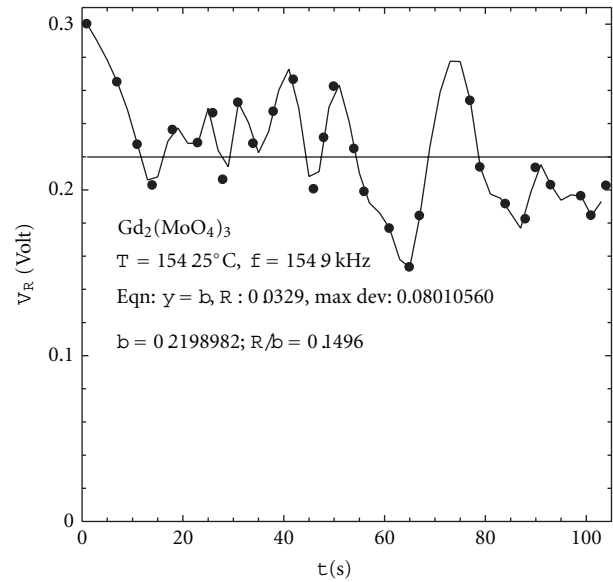


FIGURE 21: Fluctuations at $T = 154.25^\circ\text{C}$ and $f_R = 154.9$ kHz. The oscillating line is a spline. The horizontal line is a mean value of V_R over the time of observations.

also upon the density ρ , but fluctuations of the density cannot reach so large values as shown on Figure 21. The observed fluctuations of the piezoacoustic impedance in GMO exceeds fluctuations of parameters of a crystal reported up to now [67] by the two orders of magnitude.

Acknowledgments

A. Zhukov wishes to underline that most scientific contribution in the field of RMO belongs to Prof. B. K. Ponomarev,

who recently passed away. Consequently, the role of A. Zhukov, apart of magnetic measurements performed in 1990s, was mostly the preparation of this publication. This work was supported by EU ERA-NET Program under Project "SoMaMicSens" (MANUNET-2010-Basque-3), by Spanish Ministry of Science and Innovation, MICINN under Project MAT2010-18914 and by the Basque Government under Saiotek 11 MIMAGURA Project (S-PE11UN087). A. Zhukov wishes to acknowledge the support of the Basque Government under Program of Mobility of the Investigating Personnel of the Department of Education, Universities and Investigation, Grant nos. MV-2009-2-21 and MV-2010-2-31.

References

- [1] L. H. Brixner, J. R. Barkley, and W. Jeitschko, "Rare-earth molybdates (VI)," in *Handbook on the Physics and Chemistry of Rare Earths*, K. A. Gschneidner Jr. and L. Eyring, Eds., vol. chapter 30, pp. 610–655, North-Holland Publishing Company, 1979.
- [2] E. T. Keve, S. C. Abrahams, and J. L. Bernstein, "Ferroelectric ferroelastic paramagnetic β - $\text{Gd}_2(\text{MoO}_4)_3$ crystal structure of the transition-metal molybdates and tungstates. VI," *The Journal of Chemical Physics*, vol. 54, no. 7, pp. 3195–3206, 1971.
- [3] K. Ullakko, J. K. Huang, C. Kantner, R. C. O'Handley, and V. V. Kokorin, "Large magnetic-field-induced strains in Ni_2MnGa single crystals," *Applied Physics Letters*, vol. 69, no. 13, pp. 1966–1968, 1996.
- [4] D. C. Dunand and P. Müllner, "Size effects on magnetic actuation in Ni-Mn-Ga shape-memory alloys," *Advanced Materials*, vol. 23, no. 2, pp. 216–232, 2011.
- [5] Boris K. Ponomarev, Sergey A. Ivanov, Valery D. Negrii et al., "Giant magnetic anisotropy in paramagnetic $\text{Tb}_2(\text{MoO}_4)_3$," *Ferroelectrics*, vol. 151, no. 1–4, pp. 103–108, 1994.
- [6] A. P. Levanyuk and D. G. Sannikov, "On closed by the temperature phase transitions of the second type," *JETP Letters*, vol. 55, pp. 256–265, 1968.
- [7] J. Petzelt and V. Dvořák, "New type of ferroelectric soft mode in gadolinium molybdate," *Physica Status Solidi (b)*, vol. 46, pp. 413–423, 1971.
- [8] J. D. Axe, B. Dorner, and G. Shirane, "Mechanism of the ferroelectric phase transformation in rare-earth molybdates," *Physical Review Letters*, vol. 26, no. 9, pp. 519–523, 1971.
- [9] B. Dorner, J. D. Axe, and G. Shirane, "Neutron-scattering study of the ferroelectric phase transformation in $\text{Tb}_2(\text{MoO}_4)_3$," *Physical Review B*, vol. 6, no. 5, pp. 1950–1963, 1972.
- [10] W. Jeitschko, "The crystal structure of ferroelectric gadolinium molybdate, $\text{Gd}_2(\text{MoO}_4)_3$," *Die Naturwissenschaften*, vol. 57, no. 11, p. 544, 1970.
- [11] W. Jeitschko, "A comprehensive X-ray study of the ferroelectric-ferroelastic and paraelectric-paraelastic phases of $\text{Gd}_2(\text{MoO}_4)_3$," *Acta Crystallographica B*, vol. 28, pp. 60–76, 1972.
- [12] K. Aizu, "Possible species of "Ferroelastic" crystals and of simultaneously ferroelectric and ferroelastic Crystals," *Journal of the Physical Society of Japan*, vol. 27, no. 2, pp. 387–396, 1969.
- [13] E. Sawaguchi and L. E. Cross, "Spontaneous polarization of $\text{Gd}_2(\text{MoO}_4)_3$," *Journal of Applied Physics*, vol. 44, no. 6, pp. 2541–2544, 1973.
- [14] H. J. Borhardt and P. E. Bierstedt, "Ferroelectric rare-earth molybdates," *Journal of Applied Physics*, vol. 38, no. 5, pp. 2057–2061, 1967.
- [15] L. E. Cross, A. Fouskova, and S. E. Cummins, "Gadolinium molybdate, a new type of ferroelectric crystal," *Physical Review Letters*, vol. 21, no. 12, pp. 812–814, 1968.
- [16] F. G. Ullman, B. N. Ganguly, and J. R. Zeidler, "Pyroelectric detection properties of gadolinium molybdate (gmo)," *Journal of Electronic Materials*, vol. 1, no. 3, pp. 425–434, 1972.
- [17] F. G. Ullman, K. M. Cheung, G. A. Rakes, and B. N. Ganguly, "Re-examination of the pyroelectric current anomaly in gadolinium molybdate," *Ferroelectrics*, vol. 9, pp. 63–64, 1975.
- [18] R. A. Fisher, E. W. Hornung, G. E. Brodale, and W. F. Giauque, "Magnetothermodynamics of antiferromagnetic, ferroelectric β - $\text{Gd}_2(\text{MoO}_4)_3$. I. Heat capacity, entropy, magnetic moment of the electrically polarized form from 0.4 to 4.2°K with Fields to 90 kG along the c crystal axis," *The Journal of Chemical Physics*, vol. 56, no. 1, pp. 193–212, 1972.
- [19] E. W. Hornung, G. E. Brodale, R. A. Fisher, and W. F. Giauque, "Magnetothermodynamics of antiferromagnetic, ferroelectric β - $\text{Gd}_2(\text{MoO}_4)_3$. II. Heat capacity, entropy, magnetic moment of the electrically polarized form from 0.4 to 4.2°K with fields to 90 kG along the a crystal axis," *The Journal of Chemical Physics*, vol. 56, no. 10, pp. 5007–5018, 1972.
- [20] G. E. Brodale, R. A. Fisher, E. W. Hornung, and W. F. Giauque, "Magnetothermodynamics of antiferromagnetic, ferroelectric β - $\text{Gd}_2(\text{MoO}_4)_3$. III. Heat capacity, entropy, magnetic moment of the electrically polarized form from 0.4 to 4.2°K with fields to 90 kG along the b crystal axis," *The Journal of Chemical Physics*, vol. 56, no. 12, pp. 6118–6125, 1972.
- [21] R. A. Fisher, E. W. Hornung, G. E. Brodale, and W. F. Giauque, "Magnetothermodynamics of antiferromagnetic, ferroelectric, ferroelastic β - $\text{Gd}_2(\text{MoO}_4)_3$, IV Thermodynamic temperature and other properties without heat introduction below 0.5°K. Fields to 10 kG along the c⁺ crystal axis," *The Journal of Chemical Physics*, vol. 59, no. 11, pp. 5796–5809, 1973.
- [22] R. A. Fisher, E. W. Hornung, G. E. Brodale, and W. F. Giauque, "Magnetothermodynamics of antiferromagnetic, polarized ferroelectric, ferroelastic β - $\text{Gd}_2(\text{MoO}_4)_3$. V. Thermodynamic temperature and other properties with heat introduction below 0.5°K. Fields to 5 kG along the b crystal axis," *The Journal of Chemical Physics*, vol. 69, no. 6, pp. 2892–2900, 1978.
- [23] R. A. Fisher, E. W. Hornung, G. E. Brodale, and W. F. Giauque, "Magnetothermodynamics of ferroelectric, ferroelastic, antiferromagnetic β -terbium molybdate. I. Heat capacity, entropy, magnetic moment of the electrically polarized form from 0.4 to 4.2 °K with fields to 90 kG along the c crystal axis," *The Journal of Chemical Physics*, vol. 63, no. 3, pp. 1295–1308, 1975.
- [24] B. K. Ponomarev, Yu. F. Popov, and D. S. Red'kin, "Magnetostriiction of paramagnetic terbium molybdate in fields up to 150 kOe," *JETP Letters*, vol. 57, pp. 483–486, 1993.
- [25] B. K. Ponomarev, S. A. Ivanov, B. S. Red'Kin, and V. N. Kurlov, "Irreversible alterations of ferroelectric domain structure in paramagnetic rare earth molybdates induced by a magnetic field," *Journal of Applied Physics*, vol. 75, no. 12, pp. 8004–8007, 1994.

- [26] B. K. Ponomarev, A. I. Popov, J. Van Tol et al., "Magnetism of singlets in terbium molybdate," *Journal of Magnetism and Magnetic Materials*, vol. 258-259, pp. 510–512, 2003.
- [27] L. D. Landau and E. M. Lifshits, *Kvantovaya Mekhanika*, Nauka, Moscow, Russia, 1974.
- [28] J. Samuel Smart, *Effective Field Theories of Magnetism*, IBM Watson Research Center, New York, NY, USA, 1966.
- [29] H. A. Jahn and E. Teller, "Stability of polyatomic molecules in degenerate electronic states. I. Orbital degeneracy," *Proceedings of the Royal Society A*, vol. 161, pp. 220–235, 1937.
- [30] H. A. Kramers, "Theorie generale de la rotation paramagnetique dans les cristaux," *Proceedings Academy of Science, Amsterdam*, vol. 33, pp. 959–972, 1930.
- [31] A. K. Zvezdin, V. M. Matveev, A. A. Mukhin, and A. I. Popov, *Redkozemel'nye Iony v Magnito-Uporyadochennykh Kristallakh*, Nauka, Moscow, Russia, 1985.
- [32] L. D. Landau and E. M. Lifshits, *Electrodynamics of Continuum*, Gostekhizdat, Moscow, Russia, 1957.
- [33] I. E. Dzyaloshinskii, "Topological model of a heisenberg spin glass," *JETP Letters*, vol. 37, pp. 881–882, 1959.
- [34] D. N. Astrov, "The magnetoelectric effect in antiferromagnetics," *JETP Letters*, vol. 38, pp. 984–985, 1960.
- [35] D. N. Astrov, "Magnetoelectric effect in chromium oxide," *JETP Letters*, vol. 40, pp. 1035–1041, 1961.
- [36] S. L. Hou and N. Bloembergen, "Paramagnetoelectric effects in $\text{NiSO}_4 \cdot 6\text{H}_2\text{O}$," *Physical Review*, vol. 138, no. 4A, pp. A1218–A1226, 1965.
- [37] S. A. Ivanov, V. N. Kurlov, B. K. Ponomarev, and B. S. Red'kin, "Magnetoelectric effect in terbium molybdate," *JETP Letters*, vol. 52, no. 7, pp. 1003–1005, 1990.
- [38] B. K. Ponomarev, S. A. Ivanov, B. S. Red'kin, and V. N. Kurlov, "Magnetoelectrical effect in paramagnetic rare-earth molybdates," *Physica B*, vol. 177, no. 1–4, pp. 327–329, 1992.
- [39] I. E. Chupis, "Effect of magnetic field on ferroelectric properties of rare-earth molybdates," *Fizika Nizkikh Temperatur*, vol. 21, no. 9, pp. 941–949, 1995.
- [40] B. K. Ponomarev, S. A. Ivanov, B. S. Red'kin, and V. N. Kurlov, "Effect of a magnetic field on the ferroelectric domain structure of $\text{TbGd}(\text{MoO}_4)_3$," *JETP Letters*, vol. 55, pp. 353–361, 1992.
- [41] B. K. Ponomarev, V. D. Negrii, B. S. Red'kin, and Yu F. Popov, "Magneto-electro-elastic effects in some rare earth molybdates and related properties," *Journal of Physics D: Applied Physics*, vol. 27, no. 10, pp. 1995–2001, 1994.
- [42] H. Wiegmann, B. K. Ponomarev, J. van Tol, A. G. M. Jansen, P. Wyder, and B. S. Red'kin, "Magnetoelectric properties of ferroelectric rare earth molybdates," *Ferroelectrics*, vol. 183, pp. 195–204, 1996.
- [43] B. K. Ponomarev, A. I. Popov, E. Steep et al., *Fizika Tverdogo Tela*, vol. 47, no. 7, p. 1326, 2005.
- [44] N. F. Vedernikov, A. K. Zvezdin, R. Z. Levitin, and A. I. Popov, "Magnetic linear birefringence of rare-earth garnets," *JETP Letters*, vol. 93, p. 2161, 1987, *Soviet Physics—JETP*, vol. 66, no. 6, p. 1233, 1987.
- [45] N. S. Akulov, *Ferromagnetics*, Gostekhizdat, Moscow, Russia, 1939.
- [46] E. Callen and H. B. Callen, "Magnetostriiction, forced magnetostriiction, and anomalous thermal expansion in ferromagnets," *Physical Review*, vol. 139, no. 2A, pp. A455–A471, 1965.
- [47] B. K. Ponomarev, B. S. Red'kin, H. Wiegmann, A. G. M. Jansen, P. Wyder, and J. van Tol, "Magnetoelectric effect in orthorhombic $\text{Gd}_2(\text{MoO}_4)_3$," *Ferroelectric letters*, vol. 18, no. 3-4, pp. 133–140, 1994.
- [48] B. K. Ponomarev, E. Steep, H. Wiegmann, A. G. M. Jansen, P. Wyder, and B. S. Red'kin, "Anisotropy of the magnetoelectric effect in β' - $\text{Gd}_2(\text{MoO}_4)_3$," *Physics of the Solid State*, vol. 42, no. 4, pp. 716–738, 2000.
- [49] H. B. Callen and E. Callen, "The present status of the temperature dependence of magnetocrystalline anisotropy, and the $l(l+1)$ 2 power law," *Journal of Physics and Chemistry of Solids*, vol. 27, no. 8, pp. 1271–1285, 1966.
- [50] B. K. Ponomarev, B. S. Red'kin, E. Steep, H. Wiegmann, A. G. M. Jansen, and P. Wyder, "Magnetoelectric effect in samarium molybdate," *Physics of the Solid State*, vol. 44, no. 1, pp. 145–148, 2002.
- [51] K. P. Belov, M. A. Belyanchokova, R. Z. Levitin, and S. A. Nikitin, *Rare-Earth Ferromagnets and Antiferromagnets*, Nauka, Moscow, Russia, 1965.
- [52] B. K. Ponomarev, J. Zeman, G. Martinez et al., "The anisotropy of the intensity of the optical absorption in β' - $\text{Tb}_2(\text{MoO}_4)_3$," *Ferroelectrics*, vol. 204, pp. 279–288, 1997.
- [53] B. K. Ponomarev, A. I. Popov, B. S. Red'kin et al., "The longitudinal zeeman effect in terbium molybdate," *Journal of Magnetism and Magnetic Materials*, vol. 300, no. 1, pp. e422–e425, 2006.
- [54] B. K. Ponomarev, I. A. Kornev, V. D. Negrii, G. M. Vizdrik, and B. S. Red'kin, "Anomalously high photovoltages in terbium molybdate," *Physics of the Solid State*, vol. 40, pp. 661–663, 1998.
- [55] B. K. Ponomarev, V. D. Negrii, and B. S. Red'kin, "Two types of photo-induced voltages in terbium molybdate," *Ferroelectrics*, vol. 280, pp. 119–130, 2002.
- [56] A. A. Grekov, M. A. Malitskaia, V. D. Spitsina, and B. M. Fridkin, "Photoelectric effects in A5B6C7-type ferroelectrics-semiconductors with low-temperature phase transitions," *Kristallografiya*, vol. 15, pp. 500–509, 1970.
- [57] A. M. Glass, D. von der Linde, and T. J. Negran, "High-voltage bulk photovoltaic effect and the photorefractive process in LiNbO_3 ," *Applied Physics Letters*, vol. 25, no. 4, pp. 233–235, 1974.
- [58] V. M. Fridkin, *Fotosegnetoelektriki*, Nauka, Moscow, Russia, 1979.
- [59] A. G. Chynoweth, "Surface space-charge layers in barium titanate," *Physical Review*, vol. 102, no. 3, pp. 705–714, 1956.
- [60] P. V. Ionov, "Photosensitivity of ferroelectric niobates," *Fizika Tverdogo Tela*, vol. 15, no. 9, pp. 2827–2878, 1973.
- [61] P. V. Ionov, V. V. Voronov, and V. T. Gabrielyan, "Detection of photoinduced change of refraction in ferroelectric lead germanate," *Fizika Tverdogo Tela*, vol. 17, no. 4, pp. 1144–1146, 1975.
- [62] V. M. Fridkin, B. N. Popov, and K. A. Verkhovskaya, "Photovoltaic and photorefractive effects in ferroelectrics of kdp-group," *Fizika Tverdogo Tela*, vol. 20, no. 4, pp. 1263–1265, 1978.
- [63] B. K. Ponomarev and B. S. Red'kin, "Fluctuations of the piezoacoustic impedance in gadolinium molybdate near the curie temperature," *Fiz. Tverd. Tela*, vol. 49, pp. 1260–1264, 2007.
- [64] "IRE standards on piezoelectric crystals," *Proceedings of the IRE*, vol. 49, no. 7, pp. 1161–1169, 1961.
- [65] K. S. van Dyke, "The piezo-electric resonator and its equivalent network," *Proceedings of the IRE*, no. 16, pp. 742–764, 1928.
- [66] L. Bergmann, *Der Ultraschall und seine Anwendung in Wissenschaft und Technik*, Zürich, Switzerland, 1954.
- [67] I. A. Yakovlev and T. S. Velichkina, "Two new phenomena at phase transitions of second type," *Uspekhi Fizicheskikh Nauk*, vol. 63, no. 10, pp. 411–433, 1957.

Research Article

Influence of Magnesium Substitution on Thermal and Electrical Properties of NiCuZn Ferrites for Microinductor Core Applications

M. Venkata Ramana,^{1,2} N. Ramamanohar Reddy,¹ and K. V. Siva kumar¹

¹ Nanotechnology Laboratory, Department of Metallurgical and Materials Engineering, Indian Institute of Technology, Tamil Nadu, Chennai 600 036, India

² Ceramic Composite Materials Laboratory, Department of Physics, Sri Krishnadevaraya University, Ananthapur 505 003, India

Correspondence should be addressed to M. Venkata Ramana, venkat6slr@gmail.com

Received 22 July 2011; Revised 7 January 2012; Accepted 12 January 2012

Academic Editor: Arcady Zhukov

Copyright © 2012 M. Venkata Ramana et al. This is an open access article distributed under the Creative Commons Attribution License, which permits unrestricted use, distribution, and reproduction in any medium, provided the original work is properly cited.

Two series of NiMgCuZn ferrites, that is, (1) $\text{Ni}_x\text{Mg}_{0.6-x}\text{Cu}_{0.1}\text{Zn}_{0.3}\text{Fe}_2\text{O}_4$ and sample G: $\text{Ni}_{0.3}\text{Mg}_{0.3-y}\text{Cu}_{0.1}\text{Zn}_{0.5-y}\text{Fe}_2\text{O}_4$ with $x = 0.0, 0.1, 0.2, 0.3$ and (2) $\text{Ni}_x\text{Mg}_{0.6-x}\text{Cu}_{0.1}\text{Zn}_{0.3}\text{Fe}_2\text{O}_4$ with $y = 0.0, 0.1, 0.2$ were synthesized and prepared by conventional ceramic double-sintering process and to use them as core materials for microinductor applications. The formation of single phase was confirmed by X-ray diffraction. The temperature and compositional variation of DC, AC electrical conductivities (σ) and thermoelectric power (α) were studied on these two series of polycrystalline ferros spinels. The studies were carried out in wide range of temperature from 30 to 350°C. On the basis of thermoelectric study, the ferrites under present work were found to be shown as n-type and p-type transition. The electrical conduction in these ferros spinels is explained in the light of polaron hopping mechanism. These ferrite compositions have been developed for their use as core materials for microinductor applications.

1. Introduction

The polycrystalline NiMgCuZn soft ferrites are suitable for core materials in microinductor applications. In view of the extensive applications of NiCuZn ferrite [1–4], it is economical to replace nickel with magnesium and achieve desirable properties in NiMgCuZn ferrites. MgCuZn ferrite is a pertinent magnetic material suitable for high-frequency applications owing to its properties like high resistivity, fairly high Curie transition temperature, environmental stability, and low cost [5–8]. In the present investigation two series of NiMgCuZn ferros spinels were prepared, their temperature and compositional dependence of electrical properties like DC, AC electrical conductivities and Seebeck coefficient were studied, and the results were reported along with the conduction mechanism.

2. Experimental Procedure

2.1. Materials and Methods. Two series of soft ferrite compositions having the chemical formulas: (i) $\text{Ni}_x\text{Mg}_{0.6-x}\text{Cu}_{0.1}\text{Zn}_{0.3}\text{Fe}_2\text{O}_4$, where $x = 0.0, 0.1, 0.2, 0.3$ and (ii) $\text{Ni}_{0.3}\text{Mg}_{0.3-y}\text{Cu}_{0.1}\text{Zn}_{0.5-y}\text{Fe}_2\text{O}_4$, where $y = 0.0, 0.1, 0.2$ were prepared employing analytical grade NiO, MgO, CuO, ZnO, and Fe_2O_3 . These constituents were ball milled (Retsch PM-200, Germany) in acetone medium for 10 h and dried in an oven. These dried powders were calcined in the form of cakes in closed alumina crucibles at 800°C for 4 h. After presintering, these cakes were crushed and ball milled once again to obtain fine particles, and finally these powders were sieved to get uniform particle size. The presintered green powders were mixed with 2% PVA as a binder and were compacted in the form of pellets of 1.2 cm diameter and 2 mm thickness at 150 MPa. These compacted bodies were

finally sintered at 1250°C for 2 h using a programmable furnace and were cooled to room temperature at the rate of 80°C/hr. Sufficient care was taken to avoid zinc loss during the sintering process. All the samples were structurally characterized using Philips high-resolution X-ray diffraction system PM1710 with Cu K α radiation.

2.2. Experimental Details. DC electrical conductivity measurements were carried out by a cell having guard ring facility in addition to the two probes [9]. Silver paste (Du Pont) was applied to both the surfaces of the pellet to obtain good ohmic contacts. The measurements of conductivity were made by applying a constant voltage of 2 V from a regulated power supply, in the temperature range 30 to 350°C. The electrical conductivity (σ_{DC}) of NiMgCuZn ferrites under investigation has been computed using the relation

$$\sigma = \left(\frac{It}{VA} \right), \quad (1)$$

where I is the current passing through the specimen, V is the voltage applied to the specimen, t is the thickness of the sample, and A denotes the area of cross-section of the sample. The Curie transition temperature T_c of the samples was determined by magnetic permeability measurements [10]. Thermoelectric power (Seebeck coefficient) measurements were carried out in the temperature region 30 to 350°C by differential method similar to that of Reddy et al. [11] with a few modifications. A temperature difference of $\Delta T = 10$ K was maintained across the sample with the help of a microfurnace fitted to the sample holder assembly. Temperatures of both the surfaces of the pellet were measured with precalibrated chromel-alumel thermocouples. The Thermoelectric power “ α ” was measured from the relation

$$\alpha = \frac{\Delta V}{\Delta T}. \quad (2)$$

Following convention adopted by Lal et al. [12] the positive sign indicates negative charge carriers and vice versa.

The AC conductivity, σ_{AC} of these ferrites were evaluated from the dielectric measurements (ϵ' and loss tangent, $\tan \delta$), carried out at 1 kHz employing a computer-controlled low-frequency impedance analyzer (Hioki 3532-50 LCR Hi Tester, Japan) using the standard formulae in the temperature range 30 to 350°C. In order to understand the electrical conduction mechanism, the dielectric measurements were carried out in the frequency region 100 Hz to 1 MHz and σ_{AC} that was evaluated.

3. Results and Discussion

Table 1 gives the details of various oxides present in the two series of NiMgCuZn ferrites in mole percent. Typical XRD patterns of one sample each from the two series of NiMgCuZn ferrites (samples—B and G) are presented in Figure 1. X-ray analysis of these ferrite samples reveals the single-phase spinel structure. The lattice parameters of these ferrites were calculated from d-spacings. The variation of lattice parameter with the composition in these two series of

TABLE 1: Composition of various components of NiMgCuZn ferrites in mole percent.

S. No.	Sample	NiO	MgO	CuO	ZnO	Fe ₂ O ₃
<i>Series 1</i>						
(1)	A	0	30	5	15	50
(2)	B	5	25	5	15	50
(3)	C	10	20	5	15	50
(4)	D	15	15	5	15	50
<i>Series 2</i>						
(5)	E	15	5	5	25	50
(6)	F	15	10	5	20	50
(7)	G	15	15	5	15	50

Series 1: A: Mg_{0.6}Cu_{0.1}Zn_{0.3}Fe₂O₄, B: Ni_{0.1}Mg_{0.5}Cu_{0.1}Zn_{0.3}Fe₂O₄,

C: Ni_{0.2}Mg_{0.4}Cu_{0.1}Zn_{0.3}Fe₂O₄, D: Ni_{0.3}Mg_{0.3}Cu_{0.1}Zn_{0.3}Fe₂O₄.

Series 2: E: Ni_{0.3}Mg_{0.1}Cu_{0.1}Zn_{0.5}Fe₂O₄, F: Ni_{0.3}Mg_{0.2}Cu_{0.1}Zn_{0.4}Fe₂O₄, and

G: Ni_{0.3}Mg_{0.3}Cu_{0.1}Zn_{0.3}Fe₂O₄.

samples is given in Table 2. It can be observed from Table 2 that, in a given series, the lattice parameter is found to increase. The ionic radii of ions are Ni²⁺ = 0.72 Å, Mg²⁺ = 0.65 Å, Cu²⁺ = 0.72 Å, Zn²⁺ = 0.74 Å, and Fe²⁺ = 0.64 Å, respectively. The increasing trend of lattice constant in the two series of ferrites is attributed to the presence of Mg ion having a low ionic radius. The densities of the samples are presented in Table 2. In series 1 and 2 it can be noticed that when the nickel or magnesium concentrations are increased in the ferrites, the magnitude of density also increases.

The room temperature values of DC, AC conductivities and Seebeck coefficients for the two series of the ferrosinels studied in the present work are also presented in Table 2 for comparison.

The variation of DC conductivity (log σ_{DC}) with temperature is shown in Figures 2(a) and 2(b), and the variation of σ_{DC} with composition at room temperature is shown in Figure 2(c), for the series 1 and 2, respectively. The variation of DC conductivity with increase of temperature is almost linear in all the ferrites and shows a change of slope near 100 to 130°C. However, in all the ferrites studied in the present work, no slope change is noticed at Curie transition temperature. The activation energies are calculated from the following formula:

$$\sigma = \sigma_0 \exp\left(-\frac{E_{DC}}{kT}\right), \quad (3)$$

where E_{DC} is the activation energy, k is the Boltzmann constant, and T is the absolute temperature.

The activation energies in two regions calculated from the least square analysis of the data are given in Table 3.

An examination of data presented in Table 3 shows that, in sample A (sample without nickel) of series 1, the magnitudes of DC conductivity are high, and activation energy is found to be low compared to other ferrite samples. However, the addition of nickel decreases the conductivity and increases the activation energy in sample B. Further raise in nickel concentration in series 1 saturated the magnitudes of conductivity and decreased activation energies. In series 2

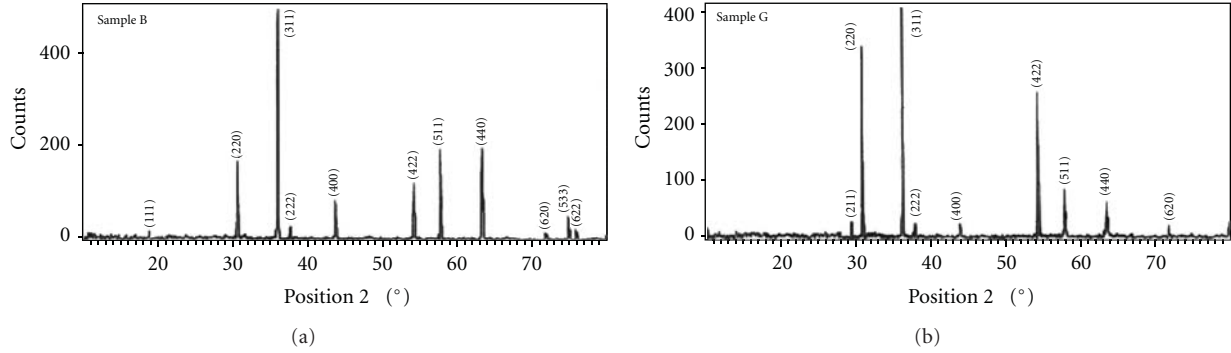


FIGURE 1: X-ray diffractograms of sample B: $\text{Ni}_x\text{Mg}_{0.6-x}\text{Cu}_{0.1}\text{Zn}_{0.3}\text{Fe}_2\text{O}_4$ and sample G: $\text{Ni}_{0.3}\text{Mg}_{0.3-y}\text{Cu}_{0.1}\text{Zn}_{0.3-y}\text{Fe}_2\text{O}_4$.

TABLE 2: Values of AC, DC conductivities and Seebeck coefficient at room temperature.

S. No.	Sample	Lattice parameter \AA	Density $\text{kg}\cdot\text{m}^{-3}$	σ_{DC} at RT $\Omega^{-1}\text{Cm}^{-1}$	σ_{AC} at RT $\Omega^{-1}\text{Cm}^{-1}$	Seebeck coefficient $\alpha\text{ }\mu\text{V/K}$
(1)	A	8.374	4.267	7.467×10^{-5}	1.799×10^{-4}	-79.55
(2)	B	8.274	4.442	5.676×10^{-7}	2.247×10^{-6}	2168
(3)	C	8.255	4.665	4.425×10^{-6}	8.475×10^{-6}	1966
(4)	D	8.234	5.321	2.755×10^{-6}	2.292×10^{-6}	1586
(5)	E	8.260	4.498	3.790×10^{-6}	3.958×10^{-6}	4830
(6)	F	8.252	4.534	2.729×10^{-6}	2.446×10^{-6}	1741
(7)	G	8.234	5.321	2.755×10^{-6}	2.292×10^{-6}	1586

TABLE 3: It shows the activation energies of DC conductivity at room temperature.

S. No.	Sample	T_c ($^{\circ}\text{C}$)	Activation energies of σ_{DC} (eV)		
			IR	ER	ΔE
(1)	A	230	0.599	0.141	0.458
(2)	B	270	1.025	0.726	0.298
(3)	C	290	1.026	0.467	0.559
(4)	D	300	1.113	0.386	0.727
(5)	E	210	0.855	0.536	0.319
(6)	F	280	1.008	0.428	0.580
(7)	G	300	1.113	0.386	0.727

IR: Intrinsic region, ER: Extrinsic Region, and T_c : Curie temperature.

with increase of magnesium and decrease of zinc contents, the activation energies increased in the intrinsic region while there is a decreasing trend of activation energy in extrinsic region. In series 1 as the nickel concentration is increased, the resistivity first increases and there after it decreases. This may be attributed to the fact that at low concentrations nickel exists in Ni^{2+} state, and it prefers A-site occupation. If the concentration of nickel is increased, Ni^{2+} converts into Ni^{3+} and goes to B sites due to their ionic sizes. However, since the copper concentration is maintained low, its contribution may be negligible. In series 2 the zinc concentration is more compared to series 1. Moreover, zinc ion has strong A-site preference. Due to the preferential occupation of zinc ions in A site it forces the nickel ions to occupy B sites. In view of this the conductivity increases in series 2. It can also be noticed from Table 3 that, in general, the activation energies

of intrinsic region are larger than the activation energies of the extrinsic region. Generally the electric conductivity is controlled by the migration of charge species under the influence of electric field and by the defect ion complexes, the polarization field, the relaxations, and so forth. At lower temperatures the defect ion complexes, grain boundaries also contribute to the conduction mechanism. The activation energy is less in this region (i.e., extrinsic region). At high-temperatures the charge species may not be subjected to any internal field. The defect ion complexes tend to dissociate. The activation energy in the high-temperature region may be the migration energy for the charges.

AC conductivity σ_{AC} was evaluated from the data of dielectric constant (ϵ') and loss, $\tan \delta$ using the relation

$$\sigma_{\text{AC}} = \epsilon' \epsilon_0 \omega \tan \delta, \quad (4)$$

where ϵ_0 is the vacuum permittivity and ω the angular frequency.

The plots of AC conductivity ($\log \sigma_{\text{AC}}$) with reciprocal temperature are shown in Figures 3(a) and 3(b), and the variation of σ_{AC} with composition at room temperature is shown in Figure 3(c). It can be noticed from the figures that there are peak-like regions which indicate the Curie transition temperatures of the corresponding ferrite samples. Electrical conductivity studies on transition metal oxides [13], rare earth oxides [14–16], indicated polaron conduction mechanism through hopping.

In the first series of ferrites, namely, (samples A, B, C, and D) the nickel concentration is increased while the magnesium concentration is decreased keeping copper and zinc fixed. The variation of AC conductivity ($\log \sigma_{\text{AC}}$)

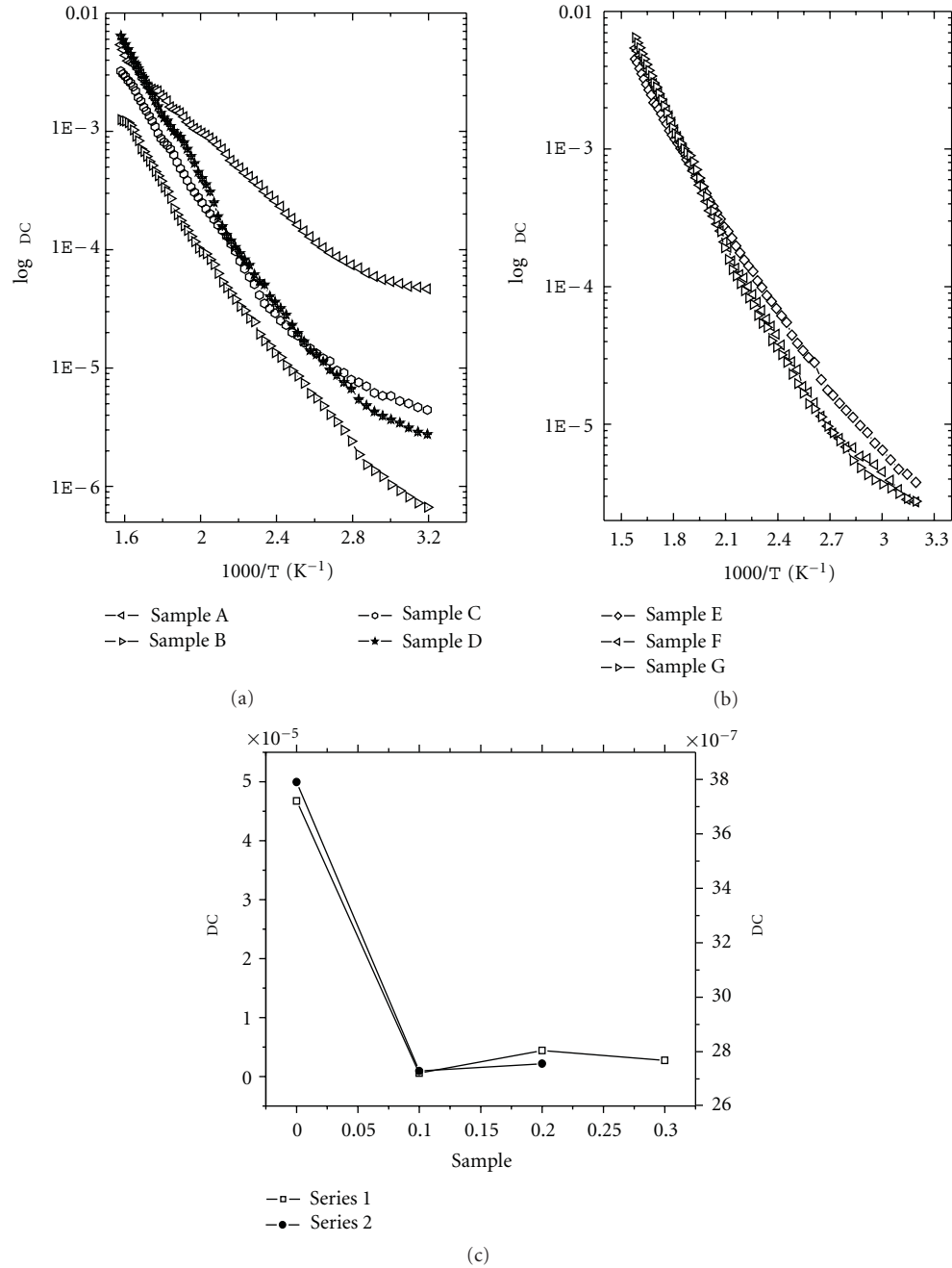


FIGURE 2: (a) Variation of $\log \sigma_{DC}$ with the T^{-1} for series 1. (b) Variation of $\log \sigma_{DC}$ with the T^{-1} for series 2. (c) Variation of $\log \sigma_{DC}$ with composition at room temperature.

with inverse temperature in these ferrites at the room temperature can be noticed from the figures that as the nickel concentration in the ferrite increases, the conductivity is low and found to be more with the addition of nickel in sample B further decreasing with increase of nickel content in series 1. However, the conductivity of series 2 is decreasing when magnesium and zinc concentration in the ferrite is varied keeping nickel and copper constant. The activation energy in the series 1 is found to be increasing in both paramagnetic and ferromagnetic region. While in series 2 it is decreasing in

both the regions, it may also be noted that activation energies vary from 0.1 to 1.1, and a high activation energy goes hand in hand with a low conductivity of the ferrites as shown by Samokhrlov and Rustmov [17].

Conduction by polarons is discussed by several workers [18–20]. Polarons are of two types: large and small polarons. In the large polaron model, the conductivity is by band mechanism at all temperatures, and the AC conductivity decreases with frequency. The small polarons conduct in band-like manner up to a certain temperature, and the

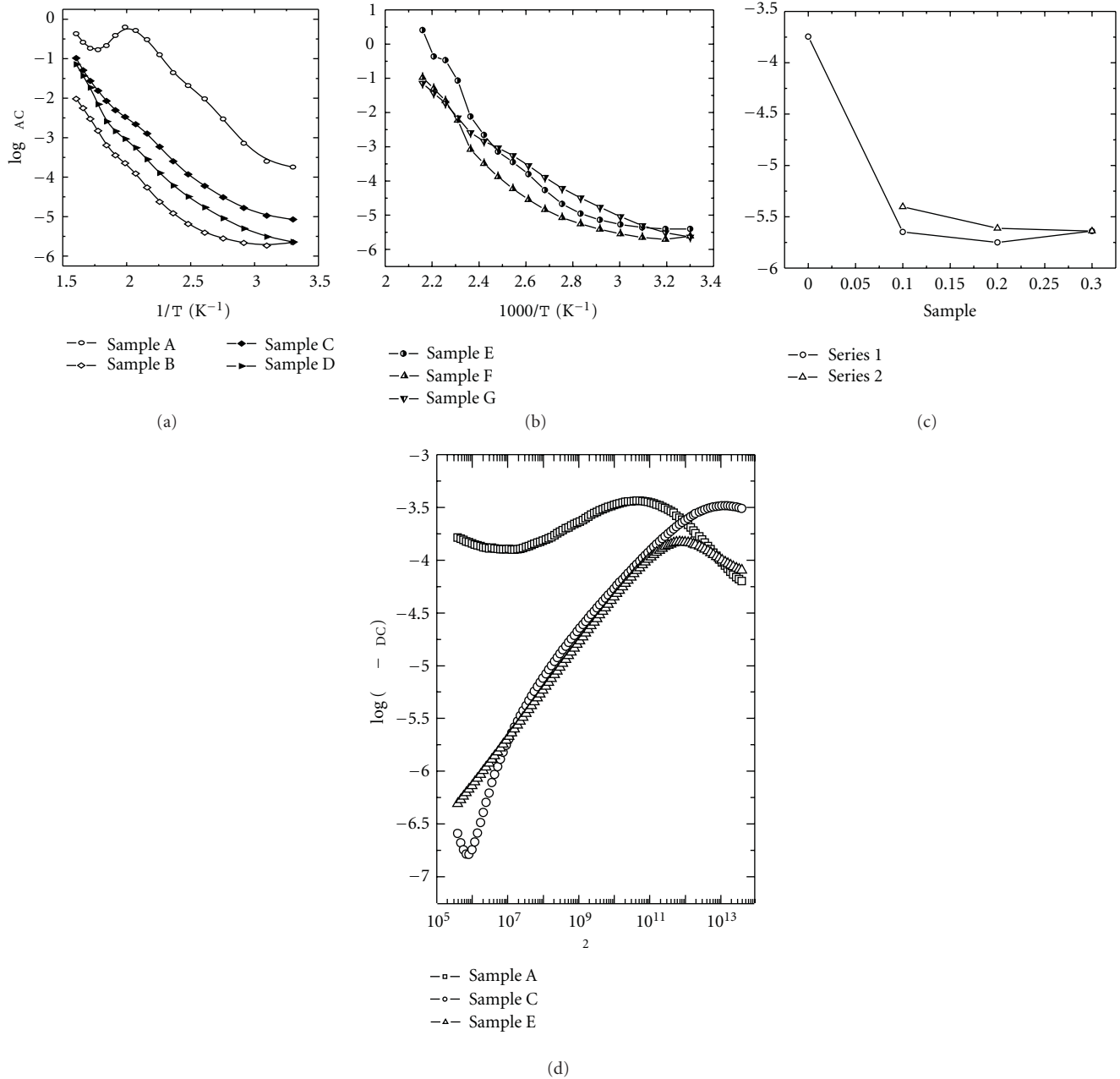


FIGURE 3: (a) Variation of $\log \sigma_{(AC)}$ with T^{-1} for series 1. (b) Variation of $\log \sigma_{(AC)}$ with T^{-1} for series 2. (c) Variation of $\log \sigma_{(AC)}$ with composition at room temperature. (d) Plots of $\log \sigma_{(AC-DC)}$ with $\log \omega^2$ one sample from each series.

conductivity shows an increase with frequency. At higher temperatures, the conduction is by thermally activated hopping mechanism. For small polaron model the conduction increases with the frequency, and follows the relation

$$\sigma_{\omega} - \sigma_{DC} = \frac{\omega^2 \tau^2}{(1 + \omega^2 \tau^2)}, \quad (5)$$

where ω is the angular frequency, and τ is the staying time ($\sim 10^{-10}$) for the frequencies $\omega^2 \tau^2 < 1$. $\log(\sigma_{\omega} - \sigma_{DC})$ versus $\log \omega^2$ that should be a straight line. Plot of $\log(\sigma_{\omega} - \sigma_{DC})$ as a function of $\log \omega^2$ at room temperature for three typical

sample is shown in Figure 3(d). It can be seen that in the plot there are regions of decreasing, increasing of $\log(\sigma_{\omega} - \sigma_{DC})$ with increasing frequency. It is not conformation to equation (5). It can be stated that in the present series of ferrospinel samples the results tend to indicate that the conduction mechanism is due to mixed polaron hopping.

The variation of thermoelectric power with the temperature in the low- and high-temperature regions for two series of ferrites are shown in Figures 4(a) and 4(b), and variation at room temperature value can be observed in Figure 4(c). The thermoelectric voltage ΔV developed across the pellet

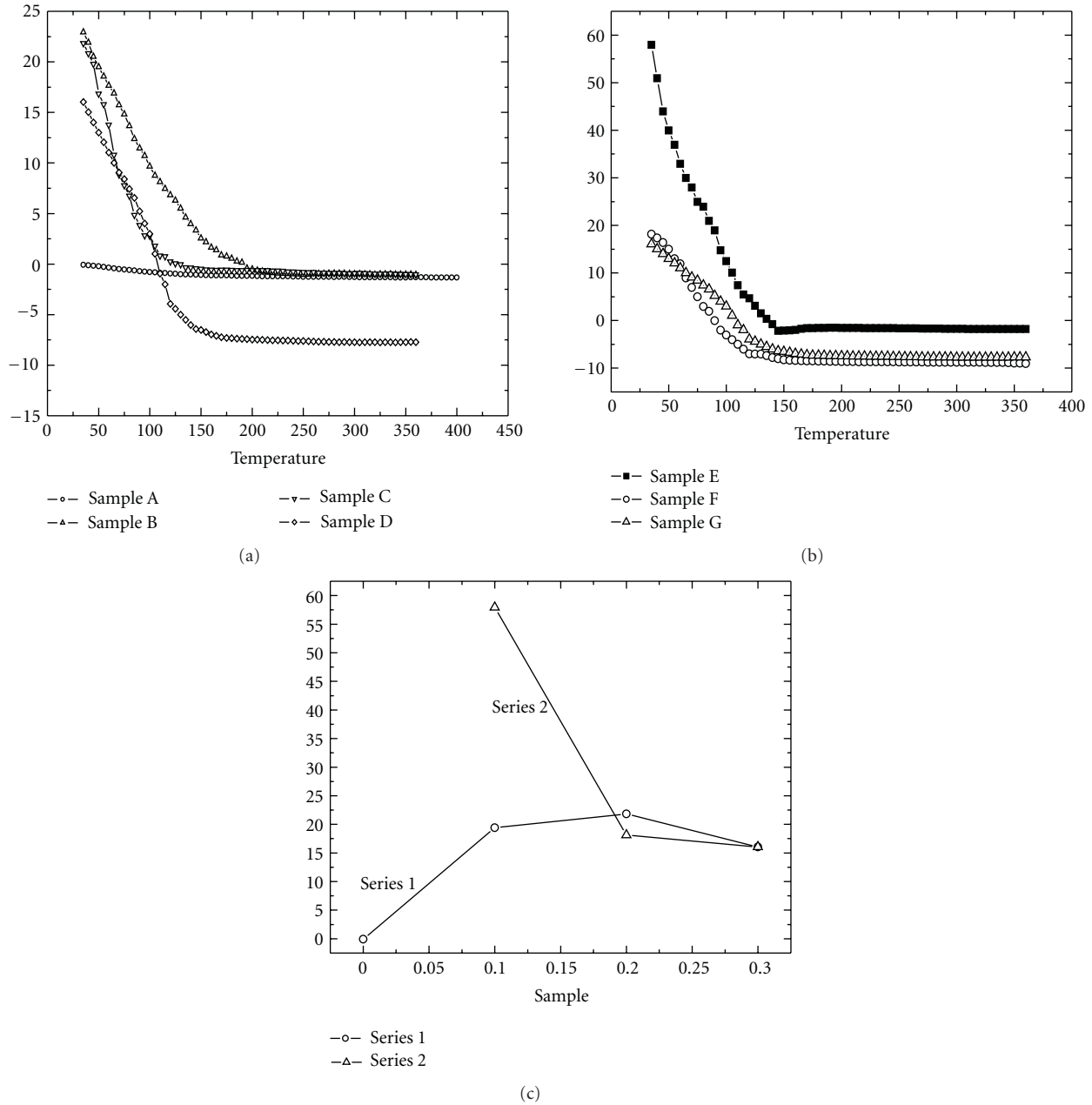


FIGURE 4: (a) Variation of the Seebeck coefficient with temperature for series 1. (b) Variation of the Seebeck coefficient with temperature for series 2. (c) Variation of Seebeck coefficient at room temperature for the two series of ferrites.

has a temperature gradient, and ΔT is shown as $\alpha = \Delta V / \Delta T$. The positive sign of α indicates negative charge carriers and vice versa.

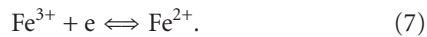
It can be seen from Table 2, at room temperature the Seebeck coefficient of pure magnesium copper zinc ferrite (i.e., Sample A) shows negative sign, and with the addition of nickel the Seebeck coefficient α has increased showing that positive sign further increase of nickel composition leads to the reduction of α value. While in the series 2, the sign of the Seebeck coefficient at room temperature is negative only for the samples and decreases with increase of magnesium. However, it can be seen that the copper concentration is kept

in concentration in both series. With the addition of nickel concentration, the thermoelectric power shows positive sign showing that from majority carriers n-type semiconductors it can be observed that as the temperature increases the Seebeck coefficient sign that shows positive sign, as such it behaves n-type and p-type semiconductors both the series 1 and 2 the same is observed. The temperature dependence of Seebeck coefficient (α) for the ferrites is satisfactorily described by the formula [21]

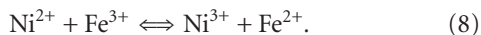
$$\alpha = A + \left(\frac{B}{T} \right), \quad (6)$$

where A and B are constants, and T is the temperature in K.

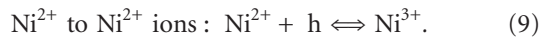
It can be seen from Table 2 that the sign of the Seebeck coefficient is transition from n-type and p-type semiconductors for all the ferrites on the basis of sign that the Ni substituted MgCuZn ferrites have been classified as n-type and p-type semiconductors. Thus, the conduction mechanism in these ferrites is predominantly due to hopping of electrons [22] from Fe^{2+} to Fe^{3+} ions



Ravinder [23] carried out the work and reported that the Seebeck coefficient is decreasing when nickel is increased, and this in turn leads to decrease in Zinc composition. All the mixed Ni-Zn ferrites are positive, and it shows that the majority of the charge carriers are holes. The presence of nickel on the octahedral sites favours the conduction mechanism [24]



The conduction mechanism in p-type samples is predominantly due to hole transfer from



It can be observed that Seebeck coefficient α is found to be decreasing in all the ferrites. Except in sample A it is increasing up to sample B and then starts decreasing due to the addition of nickel. All our results show good agreement with data from the literature.

4. Conclusions

The polycrystalline NiMgCuZn ferrite samples were prepared by the conventional method. X-ray diffraction patterns reveal the single phase spinel structure. The DC, AC and thermoelectric (Seebeck) coefficient was measured for these ferromagnetic spinels. The temperature variation of DC conductivity of series 1 indicates that the σ_{DC} is high and activation energy is low. In series 2, the activation energy is decreasing in extrinsic regions and increasing at the intrinsic region with increasing and decreasing of magnesium and zinc content in the present studied ferrites. The AC conductivity of these ferrites was calculated from the dielectric measurements. It indicates that the conduction mechanism is due to mixed polaron hopping. The temperature dependence of Seebeck coefficient of this ferrites is showing p-type and n-type semiconductor behavior.

Acknowledgments

This research was financially supported by Defence Research and Development Organization, (DRDO) under Grants ERIP/ER/0103301/M/1 dated 09.01.2002, New Delhi, India. The authors are thankful to Prof. A. Varadarajulu, Department of Polymer Science and Technology, Sri Krishnadevaraya University, Anantapur, A.P, India for valuable discussions in the preparation of the manuscript.

References

- [1] C. G. Koops, "On the dispersion of resistivity and dielectric constant of some semiconductors at audiofrequencies," *Physical Review*, vol. 83, no. 1, pp. 121–124, 1951.
- [2] G. Moltgen, "Dielectric analysis of ferrites," *Zeitschrift für Angewandte Physik*, vol. 4, pp. 216–224, 1952.
- [3] K. Iwauchi, "Dielectric properties of fine particles of Fe_3O_4 and some ferrites," *Japanese Journal of Applied Physics*, vol. 10, pp. 1520–1528, 1971.
- [4] L. G. Van Uiteret, "Dielectric properties of and conductivity in ferrites," *Proceedings of the IRE*, vol. 44, no. 10, pp. 1294–1303, 1956.
- [5] N. Rezlescu, E. Rezlescu, P. D. Popa, M. L. Craus, and L. Rezlescu, "Copper ions influence on the physical properties of a magnesium-zinc ferrite," *Journal of Magnetism and Magnetic Materials*, vol. 182, no. 1-2, pp. 199–206, 1998.
- [6] N. Rezlescu, L. Sachelarie, L. Rezlescu, and P. D. Popa, "Influence of PbO and Ta_2O_5 on some physical properties of MgCuZn ferrites," *Crystal Research and Technology*, vol. 36, no. 2, pp. 157–167, 2001.
- [7] L. Sachelarie, E. Rezlescu, and N. Rezlescu, "Influence of PbO on some properties of MgCuZn ferrites," *Physica Status Solidi*, vol. 179, no. 1, pp. R1–R3, 2000.
- [8] D. N. Bhosale, N. D. Choudhari, S. R. Sawant, and P. P. Bakare, "Initial permeability studies on high density Cu-Mg-Zn ferrites," *Journal of Magnetism and Magnetic Materials*, vol. 173, no. 1-2, pp. 51–58, 1997.
- [9] V. R. K. Murthy and J. Sobhanadri, "Electrical conductivity of some nickel-zinc ferrites," *Physica Status Solidi*, vol. 38, no. 2, pp. 647–651, 1976.
- [10] N. Varalaxmi, M. VenkataRamana, N. Ramamanohar Reddy, G. Rajitha, K. V. Sivakumar, and V. R. K. Murthy, in *Elastic behavior and internal friction of ferromagnetic spinels*, 2006.
- [11] V. D. Reddy, M. A. Malik, and P. V. Reddy, "Electrical transport properties of manganese-magnesium mixed ferrites," *Materials Science and Engineering B*, vol. 8, no. 4, pp. 295–301, 1991.
- [12] H. B. Lal, B. K. Verma, and V. Ram Yadav, "Electrical transport in heavy rare-earth iron garnets," *Journal of Materials Science*, vol. 17, no. 11, pp. 3317–3326, 1982.
- [13] D. Adler and J. Feinleib, "Electrical and optical properties of narrow-band materials," *Physical Review B*, vol. 2, no. 8, pp. 3112–3134, 1970.
- [14] G. V. S. Rao, S. Ramdas, P. N. Mehrotra, and C. N. R. Rao, "Electrical transport in rare-earth oxides," *Journal of Solid State Chemistry*, vol. 2, no. 3, pp. 377–384, 1970.
- [15] H. B. Lal, B. K. Verma, and N. Dar, "On the Electrical Transport and Dielectric Properties of Heavy Rare-Earth Sesquioxides," *Indian Journal of Cryogenics*, vol. 1, pp. 119–126, 1976.
- [16] H. B. Lal and N. Dar, "Magnetic susceptibility, electrical conductivity and dielectric constant of Er_2O_3 ," *Indian Journal of Pure and Applied Physics*, vol. 14, pp. 788–795, 1976.
- [17] A. A. Samokhralov and A. G. Rustmov, *Soviet Physics, Solid State*, vol. 7, p. 961, 1965.
- [18] J. Appel, in *Solid State Physics*, F. Seitz, D. Turnbull, and H. Ehrenreich, Eds., vol. 21, pp. 193–391, Academic press, New York, USA, 1968.
- [19] I. G. Austin and N. F. Mott, "Polarons in crystalline and non-crystalline materials," *Advances in Physics*, vol. 18, no. 71, pp. 41–102, 1969.
- [20] N. F. Mott and E. A. Davis, *Phonons and Polarons in Electronics Processing in Non Crystalline Materials*, Clarendon Press, Oxford, UK, 1971.

- [21] S. S. Flaschen and L. G. Van Uitert, "New low contact resistance electrode," *Journal of Applied Physics*, vol. 27, no. 2, p. 190, 1956.
- [22] L. G. Van Uitert, "Dc resistivity in the nickel and nickel zinc ferrite system," *The Journal of Chemical Physics*, vol. 23, no. 10, pp. 1883–1887, 1955.
- [23] D. Ravinder, "Electrical properties of zinc substituted nickel ferrites," *Indian Journal of Physics*, vol. 74, no. 3, pp. 331–333, 2000.
- [24] J. Smit and H. P. J. Wijn, *Ferrites*, Cleaver, London, UK, 1959.

Research Article

Improvement of Thermal Stability of Nd-Tb-Fe-Co-B Sintered Magnets by Additions of Pr, Ho, Al, and Cu

A. A. Lukin,¹ E. I. Il'yashenko,² A. T. Skjeltorp,³ and G. Helgesen³

¹ Research and production Company "Magnets and Magnetic Systems" Ltd., 127238 Moscow, Russia

² Department of Physics, Moscow State University, 117234 Moscow, Russia

³ Institute for Energy Technology, Kjeller and University of Oslo, 2027 Kjeller, Norway

Correspondence should be addressed to E. I. Il'yashenko, ileugene@yahoo.com

Received 29 July 2011; Revised 26 January 2012; Accepted 29 January 2012

Academic Editor: Arcady Zhukov

Copyright © 2012 A. A. Lukin et al. This is an open access article distributed under the Creative Commons Attribution License, which permits unrestricted use, distribution, and reproduction in any medium, provided the original work is properly cited.

The present work investigates the influence of Pr, Al, Cu, B and Ho which were introduced into the Co-containing sintered magnets of Nd-Dy-Tb-Fe-Co-B type on the magnetic parameters (α , iH_c , B_r , BH_{\max}). The effect of heat treatment parameters on magnetic properties was also studied. It was revealed that the essential alloying of NdFeB magnets by such elements as Dy, Tb, Ho, Co as well as by boron-forming elements, for example, by titanium, may lead to reducing of F-phase quantity, and, as a consequence, to decreasing of magnetic parameters. It was also shown that additional doping of such alloys by Pr, B, Al and Cu leads to a significant increase of the quantity of F-phase in magnets as well as solubility of the Dy, Tb, Ho and Co in it. This promotes the increase of magnetic parameters. It was possible to attain the following properties for the magnets $(Nd_{0.15}Pr_{0.35}Tb_{0.25}Ho_{0.25})_{15}(Fe_{0.71}Co_{0.29})_{bal} \cdot Al_{0.9}Cu_{0.1}B_{8.5}$ (at. %) after optimal thermal treatment {1175 K (3,6–7,2 ks) with slow (12–16 ks) cooling to 675 K and subsequently remaining at $T = 775$ K for 3,6 ks—hardening}: $B_r = 0,88$ T, $iH_c = 1760$ kA/m, $BH_{\max} = 144$ kJ/m³, $\alpha < |0,01|$ %/K in the temperature interval 223–323 K.

1. Introduction

High-energy (the maximum energy product, $BH_{\max} > 400$ kJ/m³) and high-coercive (intrinsic coercivity, $iH_c > 2400$ kA/m) sintered permanent magnets can be produced now on the base of Nd₂Fe₁₄B compound [1]. However, these magnets are significantly inferior to such materials as alnico, Sm₂(Co,Fe,Cu,Zr)₁₇, and SmCo₅ in reversible magnetic losses, which are characterized by remanence temperature reversible coefficient $\{\alpha = (\Delta B_r/B_r \cdot \Delta T) \cdot 100\%/K$, where is B_r —remanence $\}$.

Some improvement of this parameter is possible to achieve when replacing some Fe atoms by Co and some Nd ones by Dy (Tb). For example, $\alpha = -0.06\%/K$ in the temperature interval 295–375 K was attained on the sintered magnets of $\{Nd_{0.8}(Dy,Tb)_{0.2}\}_{15-16}(Fe_{0.8}Co_{0.2})_{bal} \cdot B_{6-8}$ type after heat treatment {remaining at $T = 1175$ K for 7.2 kilosecond (ks) followed by the cooling with the rate of 0.01–0.02 K/s down to 575–705 K and duration at this temperature for 3.6 ks} [2–5].

Experimental saturation magnetization temperature dependences for single-phase compound of $(Nd_{1-x}R_x^*)_2(Fe_{1-y}Co_y)_{14}B$, where R^* —Dy, Tb, Gd, and Ho are available [6–8]. It follows from these dependencies that for attaining near-zero α coefficient values in the operation temperature interval (295–375 K, in some case 225–425 K), it is necessary that x and y values should be 0.4–0.5 and 0.2–0.3 correspondingly.

However, if the content of R^* and Co is more than 7,5 at.% ($x > 0,2$) and 15 at.% ($y > 0,2$) in the alloy of $(Nd_{1-x}R_x^*)_{15-16}(Fe_{1-y}Co_y)_{bal} \cdot B_{6-8}$ type, regularities observed for the single-phase compound no further hold true: while α coefficient shows no further changes, B_r and iH_c decrease with the speed higher than that observed for the single-phase compound. This makes impossible to achieve near-zero α coefficient value and optimal B_r and iH_c parameters [2]. It was explained [2] by phase equilibrium shifting resulting in new additional phases of $(Nd,R^*)(Fe,Co,B)_2$, $(Nd,R^*)(Fe,Co)_4B$ and other types [9–11] formation and

decreasing of $(\text{Nd,R}^*)_2(\text{Fe,Co})_{14}\text{B}$ phase quantity when the alloy is doped by R^* and Co.

On the other hand, similar regularity of $\text{Nd}_2\text{Fe}_{14}\text{B}$ phase quantity decreasing and no further iH_c rising at the increasing of dysprosium (terbium) in the alloy were observed in $\{\text{Nd}_{0,8}(\text{Dy,Tb})_{0,2}\}_{15-16}(\text{Fe,Ti,Nb})_{\text{bal}} \cdot \text{B}_{6-7}$ type alloys. It was shown that doping of these alloys by Pr, Al, Cu as well as increasing of the boron content up to 8-9 at.% makes it possible to overcome this negative effect [2].

That is why the purpose of the present work was to investigate the influence of Pr, Al, Cu, B, and Ho introducing into the Co-containing sintered magnets of Nd-Dy-Tb-Fe-Co-B type on the magnetic parameters (α , iH_c , B_r , BH_{max}). The effect of heat treatment parameters on magnetic properties was also studied.

2. Experimental Procedure

Alloys of the $(\text{Nd,Pr,Tb,Dy,Ho})_{12,5-17,0}(\text{Fe,Co,Al,Nb,Ti,Cu})_{\text{bal}} \cdot \text{B}_{5,5-8,5}$ (at.%) type were prepared by vacuum-induction melting. Magnets were prepared using a conventional pattern [2]. Heat treatments in the 500–1275 K temperature interval were implemented for the selecting of the optimum schedule for the certain chemical composition alloy.

Investigations of remagnetization processes and magnetic properties evaluations were implemented with the help of hysteresisgraph and vibrating magnetometer. Chemical and phase composition of the alloys were controlled by a plasma emission spectrum method, local X-ray spectrum analysis, X-ray diffraction analysis, and Mössbauer's effect analysis according to procedures described in [2].

3. Experimental Results and Discussion

Figure 1 demonstrates demagnetizing parts of hysteresis loops of sintered magnets with the following chemical compositions: $(\text{Nd}_{0,3}\text{Pr}_{0,5}\text{Dy}_{0,2})_{15}(\text{Fe}_{0,8}\text{Co}_{0,2})_{\text{bal}} \cdot \text{Al}_{0,2}\text{B}_z$, where z is 5,3 (1, $iH_c = 980$ kA/m), 6,3 (2, $iH_c = 1070$ kA/m), 7,3 (3, $iH_c = 1190$ kA/m), 8,3 (4, $iH_c = 1250$ kA/m) at room temperature. The optimal heat treatment schedules for these magnets were the following: 1175–1275 K, 3,6 ks with subsequent quenching in inert gas ($z = 5,3-7,3$) and 1175 K, 3,6 ks + slow cooling (10–12 ks) + 900 K, 3,6 ks with subsequent quenching in inert gas ($z = 8,3$). Significant iH_c increasing is observed with the z raising from 5,3 up to 8,3. At the same time quadratality H_k (demagnetization field that reduces the intrinsic magnetization by 10%) of the curve was also improving.

Figure 2 demonstrates the dependences of iH_c on the heat treatment temperature for the $(\text{Nd}_{0,25}\text{Pr}_{0,4}\text{Dy}_{0,35})_{15}(\text{Fe}_{0,72}\text{Co}_{0,28})_{\text{bal}} \cdot \text{Al}_{0,2}\text{B}_{7,5}$ chemical composition. The upper curve reflects the results of the experiments when the samples were exposed to heat treatment only at some given temperature in the 675–1275 K interval with a 50 K step. Lower curve demonstrates the case when each sample was exposed to multistep heat treatment starting from 1275 K for 3,6 ks with the sequential

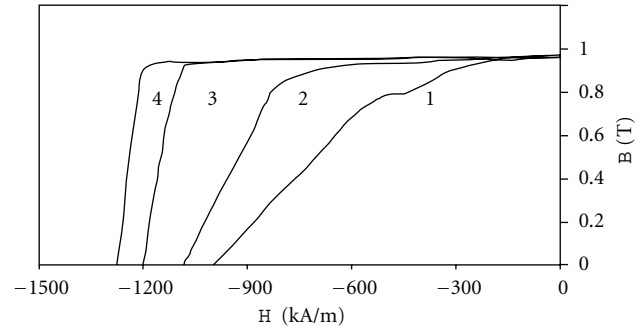


FIGURE 1: Demagnetizing parts of hysteresis loops of the magnets: $(\text{Nd}_{0,3}\text{Pr}_{0,5}\text{Dy}_{0,2})_{15}(\text{Fe}_{0,8}\text{Co}_{0,2})_{\text{bal}} \cdot \text{Al}_{0,2}\text{B}_z$, where z is 5,3 (1, $iH_c = 980$ kA/m), 6,3 (2, $iH_c = 1070$ kA/m), 7,3 (3, $iH_c = 1190$ kA/m), 8,3 (4, $iH_c = 1250$ kA/m).

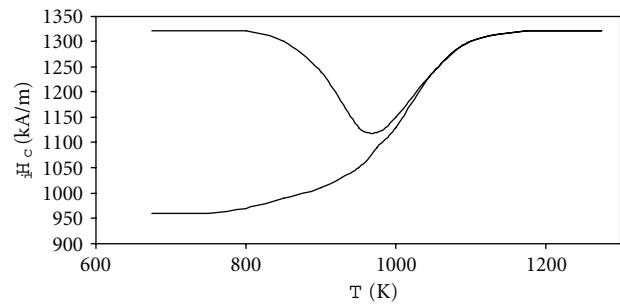


FIGURE 2: Dependences of iH_c of $(\text{Nd}_{0,25}\text{Pr}_{0,4}\text{Dy}_{0,35})_{15}(\text{Fe}_{0,72}\text{Co}_{0,28})_{\text{bal}} \cdot \text{Al}_{0,2}\text{B}_{7,5}$ magnets on the heat treatment temperature for the single (upper curve) and multistep heat treatment in the temperature 1275 K–675 K interval.

reducing of the temperature down to 675 K (interval between stages was 50 K; endurance on the each stage was 3,6 ks). The value of iH_c was measured after the each stage. As can be seen from Figure 2, minimum of iH_c on upper curve corresponds to 975 K, while for the lower curve monotonous decreasing of iH_c from 1320 kA/m (1275 K) down to 960 kA/m (675 K) is observed. Analogous regularities are observed for chemical compositions $\{(\text{Nd}_{0,35}\text{Pr}_{0,65})_{1-x}\text{Dy}_x\}_{15}(\text{Fe}_{1-y}\text{Co}_y)_{\text{bal}} \cdot \text{Al}_{0,2}\text{B}_{7,5}$ (at.%), $x = 0,3-0,4$, $y = 0,22-0,30$.

Higher level of magnetic properties ($B_r = 0,88$ T, $iH_c = 1760$ kA/m, magnetic field energy $BH_{\text{max}} = 144$ kJ/m³, $\alpha < |0,01|$ %/K in temperature interval 223–323 K) was obtained on sintered magnets with chemical composition $(\text{Nd}_{0,15}\text{Pr}_{0,35}\text{Tb}_{0,25}\text{Ho}_{0,25})_{15}(\text{Fe}_{0,71}\text{Co}_{0,29})_{\text{bal}} \cdot \text{Al}_{0,9}\text{Cu}_{0,1}\text{B}_{8,5}$ after the optimal heat treatment: 1175 K (3,6–7,2 ks) with slow (12–16 ks) cooling to 675 K and subsequently remaining at $T = 775$ K for 3,6 ks—hardening. Demagnetizing curves at various temperatures (from 293 K to 423 K) and the temperature iH_c dependence for the multistep heat treatment starting from 1175 K to 675 K with 3,6 ks endurance on the each stage are presented on Figures 3 and 4, respectively. The other part of the samples was continuously cooled from 1175 K to 675 K. Time of cooling was equal to the total endurance time during multistep heat treatment.

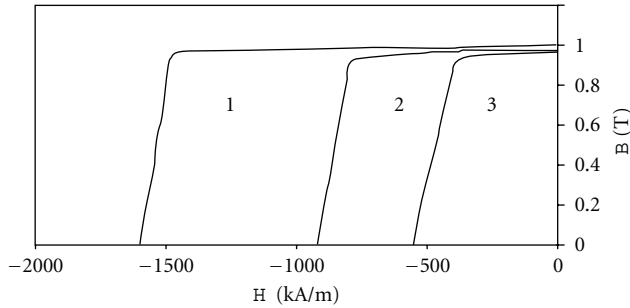


FIGURE 3: Demagnetizing parts of hysteresis loops of the magnets $(\text{Nd}_{0,15}\text{Pr}_{0,35}\text{Tb}_{0,25}\text{Ho}_{0,25})_{15}(\text{Fe}_{0,71}\text{Co}_{0,29})_{\text{bal}}\cdot\text{Al}_{0,9}\text{Cu}_{0,1}\text{B}_{8,5}$ at the temperatures 293 K (1, $iH_c = 1600$ kA/m), 373 K (2, $iH_c = 920$ kA/m), 423 K (3, $iH_c = 550$ kA/m).

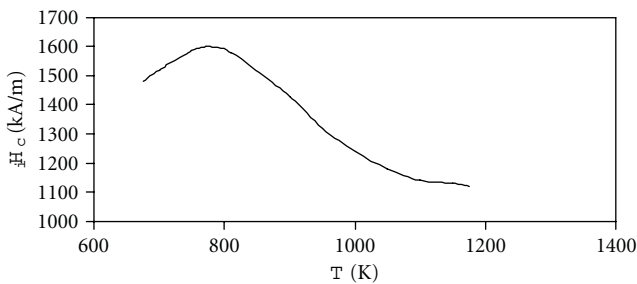


FIGURE 4: Temperature iH_c dependence of $(\text{Nd}_{0,15}\text{Pr}_{0,35}\text{Tb}_{0,25}\text{Ho}_{0,25})_{15}(\text{Fe}_{0,71}\text{Co}_{0,29})_{\text{bal}}\cdot\text{Al}_{0,9}\text{Cu}_{0,1}\text{B}_{8,5}$ magnets after multistep heat treatment (1175 K to 675 K).

It was noted that there is no significant difference in iH_c values between continuous and multistep changing of the temperature during heat treatment. Only total endurance time in the studied temperature interval is important. As a rule, it should be not less than 10 ks. Significant reduction of iH_c by 20–30% from the optimal value is observed at the rapid cooling (e.g., at the quenching in inert gas).

On the next stage we investigated the properties of the magnets additionally doped by titanium as it is known that this element increases iH_c in $\text{Nd}_{15}\text{Fe}_{\text{bal}}\cdot\text{B}_8$ magnets [2]. For the magnets $(\text{Nd}_{0,15}\text{Pr}_{0,35}\text{Tb}_{0,25}\text{Ho}_{0,25})_{15}(\text{Fe}_{0,71}\text{Co}_{0,29})_{\text{bal}}\cdot\text{Al}_{0,9}\text{Cu}_{0,1}\text{Ti}_{0,7-1,4}\text{B}_{8,5}$, the reduction of iH_c down to 1280–1360 kA/m occurs. The optimal heat treatment was revealed to be the high temperature at 1275 K with subsequent quenching down to the room temperature. Similar regularities were also observed for the alloy doped by Nb.

Significant iH_c increasing (up to 2100 kA/m) was observed in the sintered magnets, produced by the blending of the powders of the two alloys which had the extreme content of such elements as Tb, Ho, and Co (96 and 4 mass.% resp.): $(\text{Nd}_{0,15}\text{Pr}_{0,35}\text{Tb}_{0,25}\text{Ho}_{0,25})_{15}(\text{Fe}_{0,71}\text{Co}_{0,29})_{\text{bal}}\cdot\text{Al}_{0,9}\text{Cu}_{0,1}\text{B}_{8,5}$ and $(\text{Nd}_{0,2}\text{Pr}_{0,4}\text{Tb}_{0,4})_{15}(\text{Fe}_{0,8}\text{Co}_{0,2})_{\text{bal}}\cdot\text{Al}_{0,9}\text{Cu}_{0,1}\text{B}_{8,5}$. It might be explained by the chemical composition gradient in the near-boundary regions of the grains (higher Tb content and lower Co content).

It is known [2, 7, 8] that in order to increase thermal stability of $\text{Nd}_2\text{Fe}_{14}\text{B}$ compounds, such elements as Tb,

Dy, Ho, and Co are introduced into the alloys. However if their content exceeds the critical level in the magnets, as is the case for instance for the magnet compositions $\text{Nd}_{0,8-x}(\text{Tb,Dy,Ho})_x(\text{Fe}_{0,8-y}\text{Co}_y)_{\text{bal}}\cdot\text{B}_8$, where $x > 0,2$, $y > 0,2$, plummeting of the main magnetic parameters (B_r , iH_c , BH_{max}) occurs. However, it was revealed that if the alloy beside these elements additionally doped by Pr, Al, and Cu, and the content of B is increased, simultaneous improving of all magnetic parameters (B_r , iH_c , BH_{max} , α) is observed while $x = 0,3-0,4$ and $y = 0,2-0,3$. The optimal chemical composition was found to be $(\text{Nd}_{0,15}\text{Pr}_{0,35}\text{Tb}_{0,25}\text{Ho}_{0,25})_{15}(\text{Fe}_{0,71}\text{Co}_{0,29})_{\text{bal}}\cdot\text{Al}_{0,9}\text{Cu}_{0,1}\text{B}_{8,5}$ which provides the best combination of all investigated magnetic parameters including thermal stability. As follows from X-ray spectrum and Mössbauer effect analysis, this might be explained by the fact that alloying by Pr, Al, Cu, and B results in the simultaneous increasing both of F-phase content in magnets and the content of Dy, Tb, Ho, and Co in F-phase.

Parameters of optimal heat treatment for this composition are the following: 1175 K (3,6–7,2 ks) with subsequent (continuous or step) slow (10–12 ks) cooling to optimal temperature (775 K) and endurance at this temperature for 3,6 ks. It might be assumed that the improving of the main magnetic parameters after this treatment schedule is caused by the better isolation of the F-phase grains due to the Nd (or Nd and Pr) diffusion from F-phase into the grains boundaries [2, 12]. The temperature and endurance of the optimal thermal treatment depend on the F-phase homogeneity (in Nd or rare-earth element) region, which is determined by the chemical composition of the alloy and its production technology. Homogeneity region of F-phase is widened by such elements as Pr, Ga, and hydrogen and narrowed by Gd, Dy, Tb, Ho, Co, and Ni.

We assume to use these new compositions for recording heads for high coercivity media [13] and for GMFG {giant magnetic field gradient} devices for separation of dia-, para-, and weak magnetic materials [14].

4. Conclusion

Significant doping of NdFeB magnets by such elements as Dy, Tb, Ho, Co, Ti, and Nb might lead to the reducing of F-phase quantity and, as a consequence, to decrease of the main magnetic parameters. It was shown that additional alloying by Pr, Al, Cu and increasing of B content results in significant increase of F-phase the content in magnets as well as quantity of Dy, Tb, Ho, and Co in it. This promotes the increase of magnetic parameters.

It was possible to attain the following properties for the magnets $(\text{Nd}_{0,15}\text{Pr}_{0,35}\text{Tb}_{0,25}\text{Ho}_{0,25})_{15}(\text{Fe}_{0,71}\text{Co}_{0,29})_{\text{bal}}\cdot\text{Al}_{0,9}\text{Cu}_{0,1}\text{B}_{8,5}$ (at.%) after the optimal thermal treatment {1175 K (3,6–7,2 ks) with slow (12–16 ks) cooling to 675 K and subsequent endurance at $T = 775$ K for 3,6 ks—hardening}: $B_r = 0,88$ T, $iH_c = 1760$ kA/m, $BH_{\text{max}} = 144$ kJ/m³, $\alpha < |0,01|$ %/K in the temperature interval 223–323 K.

Acknowledgment

The authors express their thanks to S. Margarjan for the help in conducting the investigations using the Mössbauer spectroscopy.

References

- [1] Sagawa M., "Development and prospect of the Nd-Fe-B sintered magnets," in *Proceedings of the 21st International Workshop on Rare-Earth Permanent Magnets and their Applications*, pp. 183–186, Bled, Slovenia, 2010.
- [2] V. A. Glebov and A. A. Lukin, *Nanocrystal Rare-Earth Hard Magnetic Materials*, VNIINM, Moscow, Russia, 2007.
- [3] M. Tokunaga, M. Tobise, N. Meguro, and H. Harada, "Microstructure of R-Fe-B sintered magnet," *IEEE Transactions on Magnetics*, vol. 22, no. 5, pp. 904–909, 1986.
- [4] M. Tokunaga, H. Kogure, M. Endoh, and H. Harada, "Improvement of thermal stability of Nd-Dy-Fe-Co-B sintered magnets by additions of Al, Nb and Ga," *IEEE Transactions on Magnetics*, vol. 23, no. 5, pp. 2287–2289, 1987.
- [5] R. Grossinger, R. Krewenka, H. Buchner, and H. Harada, "A new analysis of Nd-Fe-B based permanent magnets," *Journal de Physique*, vol. 49, supplement 12, pp. C659–C660, 1988.
- [6] S. Hirosawa, Y. Matsuura, H. Yamamoto, S. Fujimura, M. Sagawa, and H. Yamauchi, "Magnetization and magnetic anisotropy of $R_2Fe_{14}B$ measured on single crystals," *Journal of Applied Physics*, vol. 59, no. 3, pp. 873–879, 1986.
- [7] M. Sagawa, S. Hirosawa, H. Yamamoto, S. Fujimura, and Y. Matsuura, "Nd-Fe-B Permanent Magnet Materials," *Japanese Journal of Applied Physics*, vol. 26, no. 6, pp. 785–800, 1987.
- [8] A. T. Pedziwiatr and W. E. Wallace, "Structure and magnetism of the $R_2Fe_{14-x}Co_xB$ ferromagnetic systems ($R = Dy$ and Er)," *Journal of Magnetism and Magnetic Materials*, vol. 233, pp. L136–L141, 2001.
- [9] W. J. Ren, D. Li, Y. C. Sui et al., "Structural and magnetic properties of Laves compounds $Dy_{1-x}Pr_x(Fe_{0.35}Co_{0.55}B_{0.1})_2$ ($0 \leq x \leq 1$)," *Journal of Applied Physics*, vol. 99, no. 8, Article ID 08M701, pp. 08M701-1–08M701-3, 2006.
- [10] M. Shimotomai, "Microstructural aspects of tough and Corrosion - resistant Nd-(FeCoNiTi)-B magnets," in *Proceedings of the 13th International Workshop on Rare Earth Permanent Magnets and their Applications*, pp. 267–281, Birmingham, UK, 1994.
- [11] B. A. Cook, J. L. Harringa, F. C. Laabs, K. W. Dennis, A. M. Russell, and R. W. McCallum, "Diffusion of Fe, Co, Nd, and Dy in $R_2(Fe_{1-x}Co_x)_{14}B$ where $R = Nd$ or Dy ," *Journal of Magnetism and Magnetic Materials*, vol. 66, pp. 63–68, 1987.
- [12] F. Vial, F. Joly, E. Nevalainen, M. Sagawa, K. Hiraga, and K. T. Park, "Improvement of coercivity of sintered NdFeB permanent magnets by heat treatment," *Journal of Magnetism and Magnetic Materials*, vol. 242–245, pp. 1329–1334, 2002.
- [13] "Magnetic recording head and method for high coercivity media, employing concentrated stray magnetic fields," Patent US 7,492,550.
- [14] "Method for forming a high-gradient magnetic field and a substance separation device based thereon," Canada Patent 2 595 721.

Research Article

Fundamental Problems of the Electrodynamics of Heterogeneous Media

N. N. Grinchik and Yu. N. Grinchik

*A. V. Luikov Heat and Mass Transfer Institute of the National Academy of Sciences of Belarus, Minsk, Belarus 15,
 P. Brovka Str., 2200072, Belarus*

Correspondence should be addressed to N. N. Grinchik, nngrin@yandex.ru

Received 28 July 2011; Accepted 26 October 2011

Academic Editor: Vladimir Shavrov

Copyright © 2012 N. N. Grinchik and Yu. N. Grinchik. This is an open access article distributed under the Creative Commons Attribution License, which permits unrestricted use, distribution, and reproduction in any medium, provided the original work is properly cited.

The consistent physic-mathematical model of propagation of an electromagnetic wave in a heterogeneous medium is constructed using the generalized wave equation and the Dirichlet theorem. Twelve conditions at the interfaces of adjacent media are obtained and justified without using a surface charge and surface current in explicit form. The conditions are fulfilled automatically in each section of counting schemes for calculations. A consistent physicomathematical model of interaction of nonstationary electric and thermal fields in a layered medium with allowance for mass transfer is constructed. The model is based on the methods of thermodynamics and on the equations of an electromagnetic field and is formulated without explicit separation of the charge carriers and the charge of an electric double layer.

1. Introduction

Let us consider the interface S between two media having different electrophysical properties. On each of its sides the magnetic-field and magnetic-inductance vectors as well as the electric-field and electric-displacement vectors are finite and continuous; however, at the surface S they can experience a discontinuity of the first kind. Furthermore, at the interface there arise induced surface charges σ and surface currents i (whose vectors lie in the plane tangential to the surface S) under the action of an external electric field.

The existence of a surface charge at the interface S between the two media having different electrophysical properties is clearly demonstrated by the following example. We will consider the traverse of a direct current through a flat capacitor filled with two dielectric materials having relative permittivities ϵ_1 and ϵ_2 and electrical conductivities λ_1 and λ_2 . A direct-current voltage U is applied to the capacitor plates; the total resistance of the capacitor is R (Figure 1). It is

necessary to calculate the surface electric charge induced by the electric current.

From the electric-charge conservation law follows the constancy of flow in a circuit; therefore, the following equation is fulfilled:

$$\lambda_1 E_{n_1} = \lambda_2 E_{n_2} = \frac{U}{(RS)}, \quad (1)$$

where E_{n_1} and E_{n_2} are the normal components of the electric-field vector.

At the interface between the dielectrics, the normal components of the electric-inductance vector change spasmodically under the action of the electric field by a value equal to the value of the induced surface charge σ :

$$\epsilon_0 \epsilon_1 E_{n_1} - \epsilon_0 \epsilon_2 E_{n_2} = \sigma. \quad (2)$$

Solving the system of (1) and (2), we obtain the expression for σ :

$$\sigma = \left(\frac{U}{RS} \right) \epsilon_0 \left[\left(\frac{\epsilon_1}{\lambda_1} \right) - \left(\frac{\epsilon_2}{\lambda_2} \right) \right]. \quad (3)$$

It follows from (3) that the charge σ is determined by the current and the multiplier accounting for the properties of the medium. If

$$\left(\frac{\epsilon_1}{\lambda_1} \right) - \left(\frac{\epsilon_2}{\lambda_2} \right) = 0, \quad (4)$$

a surface charge σ is not formed. What is more, recent trends are toward increased use of micromachines and engines made from plastic materials, where the appearance of a surface charge is undesirable. For oiling of elements of such machines, it is best to use an oil with a permittivity ϵ_{oil} satisfying the relation

$$\epsilon_1 < \epsilon_{oil} < \epsilon_2. \quad (5)$$

This oil makes it possible to decrease the electrization of the moving machine parts made from dielectric materials. In addition to the charge σ , a contact potential difference arises always independently of the current.

An electric field interacting with a material is investigated with the use of the Maxwell equation (1857). For convenience and correctness of further presentation we denote the axial vector of magnetic field strength, induction as \vec{H} and \vec{B}

$$\vec{j}_{total} = \nabla \times \vec{H}, \quad \nabla \cdot \vec{D} = \rho, \quad (6)$$

$$-\frac{\partial \vec{B}}{\partial t} = \nabla \times \vec{E}, \quad \nabla \cdot \vec{B} = 0, \quad (7)$$

where $\vec{j}_{total} = \lambda \vec{E} + \partial \vec{D} / \partial t$, $\vec{B} = \mu \mu_0 \vec{H}$. In this case, at the interface S the above system of equations is supplemented with the boundary conditions [1, 2]:

$$D_{n_1} - D_{n_2} = \sigma, \quad (8)$$

$$E_{\tau_1} - E_{\tau_2} = 0, \quad (9)$$

$$B_{n_1} - B_{n_2} = 0, \quad (10)$$

$$\vec{H}_{\tau_1} - \vec{H}_{\tau_2} = [\vec{l}_\tau \cdot \vec{n}]. \quad (11)$$

The indices (subscripts) n and τ denote the normal and tangential components of the vectors to the surface S , and the indices 1 and 2 denote the adjacent media with different electrophysical properties. The index τ denotes any direction tangential to the discontinuity surface. At the same time, a closing relation is absent for the induced surface charge σ , which generates a need for the introduction of an impedance matrix [3–7] that is determined experimentally or, in some cases, theoretically from quantum representations [8–12]. We note that the Maxwell equation of electromagnetic field does not coincide completely with the modern form of them (6), (7) which was first given by Hertz (1884) and independently of him by Heaviside (1885). The equations

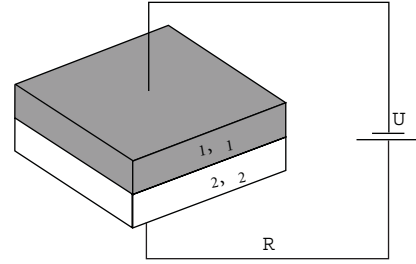


FIGURE 1: Dielectric media inside a flat capacitor.

of electromagnetic field with precise division of polar and axial vectors are of importance in considering the boundary conditions. One should bear in mind that electric field strength \vec{E} is a polar vector. Gradients of concentration and temperature are also polar vectors. On the contrary, magnetic field strength \vec{H} , as well as \vec{B} , are axial vectors, or pseudovectors. This is well seen from the formula for the Lorentz force $\vec{F} = q[\vec{V} \vec{H}]$. Indeed, the behavior of \vec{H} on reflection at the origin of coordinates and substitution $\vec{r} \rightarrow (-\vec{r})$ is determined by the behavior of the polar vectors \vec{F} and \vec{V} and the properties of their vector product. On substitution $\vec{r} \rightarrow (-\vec{r})$ the directions of the vectors \vec{F} and \vec{V} change to the opposite; the sign of the vector product also reverses. Consequently, on substitution $\vec{r} \rightarrow (-\vec{r})$ the vector \vec{H} must remain constant. This property is assumed to be an attribute of the axial vector.

The induced surface charge σ not only characterizes the properties of a surface, but also represents a function of the process, that is, $\sigma(\vec{E}(\partial \vec{E} / \partial t, \vec{H}(\partial \vec{H} / \partial t)))$; therefore, the surface impedances [3–7] are true for the conditions under which they are determined. These impedances cannot be used in experiments conducted under other experimental conditions.

The problem of determination of surface charge and surface current on metal-electrolyte boundaries becomes even more complicated in investigating and modeling non-stationary electrochemical processes, for example, pulse electrolysis, when lumped parameters L , C , and R cannot be used in principle.

We will show that σ can be calculated using the Maxwell phenomenological macroscopic electromagnetic equations and the electric-charge conservation law accounting for the special features of the interface between the adjacent media.

Separate consideration will be given to ion conductors. In constructing a physicomathematical model, we take into account that \vec{E} and \vec{H} are not independent functions; therefore, the wave equation for \vec{E} or \vec{H} is more preferable than the system of (6) and (7). It will be shown that in consideration of propagation, interference of waves in the heterogeneous medium it is preferable to use the wave equation for a polar vector of electric field strength.

2. Electron Conductors: New Closing Relations on the Boundaries of Adjacent Media

2.1. Generalized Wave Equation for E and Conditions on the Boundaries in the Presence of Strong Discontinuities of the Electromagnetic Field

2.1.1. Physicomathematical Model. We will formulate a physicomathematical model of propagation of an electromagnetic field in a heterogeneous medium. Let us multiply the left and right sides of the equation for the total current (see (6)) by $\mu\mu_0$ and differentiate it with respect to time. Acting by the operator rot on the left and right sides of the first equation of (7) on condition that $\mu = \text{const}$ we obtain

$$\frac{\partial \mathbf{j}_{\text{total}}}{\partial t} = \frac{1}{\mu\mu_0} \nabla^2 \mathbf{E} - \frac{1}{\mu\mu_0} \text{grad}(\text{div } \mathbf{E}). \quad (12)$$

In Cartesian coordinates, (12) will take the form

$$\begin{aligned} \frac{\partial \mathbf{j}_{\text{total}x}}{\partial t} &= \frac{1}{\mu\mu_0} \left(\frac{\partial^2 E_x}{\partial x^2} + \frac{\partial^2 E_x}{\partial y^2} + \frac{\partial^2 E_x}{\partial z^2} \right) \\ &\quad - \frac{1}{\mu\mu_0} \frac{\partial}{\partial x} \left(\frac{\partial E_x}{\partial x} + \frac{\partial E_y}{\partial y} + \frac{\partial E_z}{\partial z} \right), \\ \frac{\partial \mathbf{j}_{\text{total}y}}{\partial t} &= \frac{1}{\mu\mu_0} \left(\frac{\partial^2 E_y}{\partial x^2} + \frac{\partial^2 E_y}{\partial y^2} + \frac{\partial^2 E_y}{\partial z^2} \right) \\ &\quad - \frac{1}{\mu\mu_0} \frac{\partial}{\partial y} \left(\frac{\partial E_x}{\partial x} + \frac{\partial E_y}{\partial y} + \frac{\partial E_z}{\partial z} \right), \\ \frac{\partial \mathbf{j}_{\text{total}z}}{\partial t} &= \frac{1}{\mu\mu_0} \left(\frac{\partial^2 E_z}{\partial x^2} + \frac{\partial^2 E_z}{\partial y^2} + \frac{\partial^2 E_z}{\partial z^2} \right) \\ &\quad - \frac{1}{\mu\mu_0} \frac{\partial}{\partial z} \left(\frac{\partial E_x}{\partial x} + \frac{\partial E_y}{\partial y} + \frac{\partial E_z}{\partial z} \right). \end{aligned} \quad (13)$$

At the interface, the following relation [2] is also true:

$$\text{div } \mathbf{i}_r + I_{qx_1} - I_{qx_2} = -\frac{\partial \sigma}{\partial t}. \quad (14)$$

Let us write conditions (see (8)–(11)) in the Cartesian coordinate system:

$$D_{x_1} - D_{x_2} = \sigma, \quad (15)$$

$$E_{y_1} - E_{y_2} = 0, \quad (16)$$

$$E_{z_1} - E_{z_2} = 0, \quad (17)$$

$$B_{x_1} - B_{x_2} = 0, \quad (18)$$

$$H_{y_1} - H_{y_2} = i_z, \quad (19)$$

$$H_{z_1} - H_{z_2} = i_y, \quad (20)$$

where $\mathbf{i}_r = i_y \mathbf{j} + i_z \mathbf{k}$ is the surface-current density, and the coordinate x is directed along the normal to the interface. The densities i_y and i_z of the surface currents represent the electric charge carried in unit time by a segment of unit length positioned on the surface drawing the current perpendicularly to its direction.

The order of the system of differential equations (13) is equal to (16). Therefore, at the interface S , it is necessary to set, by and large, nine boundary conditions. Moreover, the three additional conditions (15), (19), and (20) containing (prior to the solution) unknown quantities should be fulfilled at this interface. Consequently, the total number of conjugation conditions at the boundary S should be equal to (12) for a correct solution of the problem.

As an example we consider a one-dimensional case of heat propagation in the layered material. As is known, to solve the problem we must specify two conditions at the interface: the equality of heat fluxes and the equality of temperatures, since in the heat conduction equation we have the second derivative with respect to the coordinate.

Differentiating expression (15) with respect to time and using relation (14), we obtain the following condition for the normal components of the total current at the medium-medium interface:

$$\text{div } \mathbf{i}_r + \mathbf{j}_{\text{total}x_1} = \mathbf{j}_{\text{total}x_2}, \quad (21)$$

that allows one to disregard the surface charge σ . Let us introduce the arbitrary function $f : [f]|_{x=\xi} = f_1|_{x=\xi+0} - f_2|_{x=\xi-0}$. In this case, expression (21) will take the form

$$[\text{div } \mathbf{i}_r + \mathbf{j}_{\text{total}x_1}]|_{x=\xi} = 0. \quad (22)$$

It is assumed that, at the medium-medium interface, E_x is a continuous function of y and z . Then, differentiating Equation (21) with respect to y and z , we obtain

$$\left[\frac{\partial}{\partial y} \mathbf{j}_{\text{total}x_1} \right] \Big|_{x=\xi} = -\frac{\partial(\text{div } \mathbf{i}_r)}{\partial y}, \quad (23)$$

$$\left[\frac{\partial}{\partial z} \mathbf{j}_{\text{total}x_1} \right] \Big|_{x=\xi} = -\frac{\partial(\text{div } \mathbf{i}_r)}{\partial z}.$$

Let us differentiate conditions (18)–(20) for the magnetic induction and the magnetic-field strength with respect to time. On condition that $\vec{\mathbf{B}} = \mu\mu_0 \vec{\mathbf{H}}$:

$$\left[\frac{\partial B_x}{\partial t} \right] \Big|_{x=\xi} = 0,$$

$$\left[\frac{1}{\mu\mu_0} \frac{\partial B_y}{\partial t} \right] \Big|_{x=\xi} = \frac{\partial i_z}{\partial t}, \quad (24)$$

$$\left[\frac{1}{\mu\mu_0} \frac{\partial B_z}{\partial t} \right] \Big|_{x=\xi} = \frac{\partial i_y}{\partial t}.$$

Using (7) and expressing (24) in terms of projections of the electric-field rotor, we obtain

$$[\text{rot}_x \mathbf{E}]|_{x=\xi} = 0, \quad \left[\frac{\partial E_z}{\partial y} - \frac{\partial E_y}{\partial z} \right] \Big|_{x=\xi} = 0, \quad (25)$$

$$\left[\frac{1}{\mu\mu_0} \text{rot}_y \mathbf{E} \right] \Big|_{x=\xi} = \frac{\partial i_z}{\partial t},$$

$$\text{or } \left[\frac{1}{\mu\mu_0} \left(\frac{\partial E_x}{\partial z} - \frac{\partial E_z}{\partial x} \right) \right] \Big|_{x=\xi} = \frac{\partial i_z}{\partial t}, \quad (26)$$

$$\left[\frac{1}{\mu\mu_0} \text{rot}_z \mathbf{E} \right] \Big|_{x=\xi} = \frac{\partial i_y}{\partial t},$$

$$\text{or } \left[\frac{1}{\mu\mu_0} \left(\frac{\partial E_y}{\partial x} - \frac{\partial E_x}{\partial y} \right) \right] \Big|_{x=\xi} = \frac{\partial i_y}{\partial t}. \quad (27)$$

Here, (25) is the normal projection of the electric-field rotor, (26) is the tangential projection of the rotor on y , and (27) is the rotor projection on z .

Assuming that E_y and E_z are continuous differentiable functions of the coordinates y and z , from conditions (16) and (17) we find

$$\left[\frac{\partial E_y}{\partial y} \right] \Big|_{x=\xi} = 0, \quad \left[\frac{\partial E_y}{\partial z} \right] \Big|_{x=\xi} = 0,$$

$$\left[\frac{\partial E_z}{\partial y} \right] \Big|_{x=\xi} = 0, \quad \left[\frac{\partial E_z}{\partial z} \right] \Big|_{x=\xi} = 0. \quad (28)$$

In accordance with the condition that the tangential projections of the electric field on z and y are equal and in accordance with conditions (16) and (17), the expressions for the densities of the surface currents i_z and i_y take the form

$$i_z = \bar{\lambda} E_z \Big|_{x=\xi}, \quad i_y = \bar{\lambda} E_y \Big|_{x=\xi}, \quad (29)$$

where

$$\bar{\lambda} = \frac{1}{2} (\lambda_1 + \lambda_2) \Big|_{x=\xi} \quad (30)$$

is the average value of the electrical conductivity at the interface between the adjacent media in accordance with the Dirichlet theorem for a piecewise-smooth, piecewise-differentiable function.

Consequently, formulas (28)–(30) yield

$$[\text{div } \vec{i}_\tau] \Big|_{x=\xi} = 0. \quad (31)$$

Relations (31) and (32) and hence the equality of the normal components of the total current were obtained (in a different manner) by Grinberg and Fok [13]. In this work, it has been shown that condition (31) leads to the equality of the derivatives of the electric field strength along the normal to the surface

$$\left[\frac{\partial E_x}{\partial x} \right] \Big|_{x=\xi} = 0. \quad (32)$$

With allowance for the foregoing we have twelve conditions at the interface between the adjacent media that are necessary for solving the complete system of (13):

- (a) the functions E_y and E_z are determined from (16) and (17);
- (b) E_x is determined from condition (22);
- (c) the values of $\partial E_x/\partial y$, $\partial E_x/\partial z$, and $\partial E_x/\partial x$ are determined from relations (23) with the use of the condition of continuity of the total-current normal component at the interface (22) and the continuity of the derivative of the total current with respect to the coordinate x ;
- (d) the values of $\partial E_y/\partial y$, $\partial E_y/\partial z$, and $\partial E_z/\partial z$ are determined from conditions (28) and (29) in consequence of the continuity of the tangential components of the electric field along y and z ;
- (e) the derivatives $\partial E_y/\partial x$ and $\partial E_z/\partial x$ are determined from conditions (26) and (27) as a consequence of the equality of the tangential components of the electric-field rotor along y and z .

Note that condition (21) was used by us in [14] in the numerical simulation of the pulsed electrochemical processes in the one-dimensional case. Condition (25) for the normal component of the electric-field rotor represents a linear combination of conditions (28) and (29); therefore, $\text{rot}_x E = 0$ and there is no need to use it in the subsequent discussion. The specificity of the expression for the general law of electric-charge conservation at the interface is that the components $\partial E_y/\partial y$ and $\partial E_z/\partial z$ are determined from conditions (28) and (29) that follow from the equality and continuity of the tangential components E_y and E_z at the boundary S .

Thus, at the interface between the adjacent media the following conditions are fulfilled: the equality of the total-current normal components; the equality of the tangential projections of the electric-field rotor; the electric-charge conservation law; the equality of the electric-field tangential components and their derivatives in the tangential direction; the equality of the derivatives of the total-current normal components in the direction tangential to the interface between the adjacent media, determined with account for the surface currents and without explicit introduction of a surface charge. They are true at each cross section of the sample being investigated.

2.1.2. Features of Calculation of the Propagation of Electromagnetic Waves in Layered Media. The electromagnetic effects arising at the interface between different media under the action of plane electromagnetic waves have a profound impact on the equipment because all real devices are bounded by the surfaces and are inhomogeneous in space. At the same time, the study of the propagation of waves in layered conducting media and, according to [15], in thin films is reduced to the calculation of the reflection and transmission coefficients; the function $E(x)$ is not determined in the thickness of a film, that is, the geometrical-optics approximation is used.

The physicomathematical model proposed allows one to investigate the propagation of an electromagnetic wave in a

layered medium without recourse to the assumptions used in [3–5, 7].

Since conditions (21)–(29) are true at each cross section of a layered medium, we will use schemes of through counting without an explicit definition of the interface between the media. In this case, it is proposed to calculate E_x at the interface in the following way.

In accordance with (15), $E_{x1} \neq E_{x2}$, that is, $E_x(x)$ experiences a discontinuity of the first kind. Let us determine the strength of the electric field at the discontinuity point $x = \xi$ on condition that $E_x(x)$ is a piecewise-smooth, piecewise-differentiable function having finite one-sided derivatives $E'_{x+}(x)$ and $E'_{x-}(x)$. At the discontinuity points x_i ,

$$\begin{aligned} E'_{x+}(x_i) &= \lim_{\Delta x_i \rightarrow +0} \frac{E(x_i + \Delta x_i) - E(x_i + 0)}{\Delta x_i}, \\ E'_{x-}(x_i) &= \lim_{\Delta x_i \rightarrow -0} \frac{E(x_i + \Delta x_i) - E(x_i - 0)}{\Delta x_i}. \end{aligned} \quad (33)$$

In this case, in accordance with the Dirichlet theorem [16], the Fourier series of the function $E(x)$ at each point x , including the discontinuity point ξ , converges and its sum is equal to

$$E_{x=\xi} = \frac{1}{2} [E(\xi - 0) + E(\xi + 0)]. \quad (34)$$

The Dirichlet condition (34) also has a physical meaning. In the case of contact of two solid conductors, for example, dielectrics or electrolytes in different combinations (metal-electrolyte, dielectric-electrolyte, metal-vacuum, and so on), at the interface between the adjacent media there always arises an electric double-layer (EDL) with an unknown (as a rule) structure that, however, substantially influences the electrokinetic effects, the rate of the electrochemical processes, and so on. It is significant that, in reality, the electrophysical characteristics λ , ε , and $E(x)$ change uninterruptedly in the electric double-layer; therefore, (34) is true for the case where the thickness of the electric double-layer, that is, the thickness of the interphase boundary, is much smaller than the characteristic size of a homogeneous medium. In a composite, for example, in a metal with embedments of dielectric balls, where the concentration of both components is fairly large and their characteristic sizes are small, the interphase boundaries can overlap and condition (34) can break down.

If the thickness of the electric double-layer is much smaller than the characteristic size L of an object, (34) also follows from the condition that $E(x)$ changes linearly in the EDL region. In reality, the thickness of the electric double-layer depends on the kind of contacting materials and can comprise several tens of angstroms [17]. In accordance with the modern views, the outer coat of the electric double-layer consists of two parts, the first of which is formed by the ions immediately attracted to the surface of the metal (a “dense” or a “Helmholtz” layer of thickness h), and the second is formed by the ions separated by distances larger than the ion radius from the surface of the layer, and the number of these ions decreases as the distance between them and the interface (the “diffusion layer”) increases. The distribution of

the potential in the dense and diffusion parts of the electric double-layer is exponential in actual practice [17], that is, the condition that $E(x)$ changes linearly breaks down; in this case, the sum of the charges of the dense and diffusion parts of the outer coat of the electric double-layer is equal to the charge of its inner coat (the metal surface). However, if the thickness of the electric double-layer h is much smaller than the characteristic size of an object, the expansion of $E(x)$ into a power series is valid and one can restrict oneself to the consideration of a linear approximation. In accordance with the more general Dirichlet theorem (1829), a knowledge of this function in the EDL region is not necessary to substantiate (34). Nonetheless, the above-indicated physical features of the electric double-layer lend support to the validity of condition (34).

The condition at interfaces, analogous to (34), has been obtained earlier [18] for the potential field (where $\text{rot } \mathbf{E} = 0$) on the basis of introduction of the surface potential, the use of the Green formula, and the consideration of the discontinuity of the potential of the double-layer. In [18], it is also noted that the consideration of the thickness of the double-layer and the change in its potential at $h/L \ll 1$ makes no sense in general; therefore, it is advantageous to consider, instead of the volume potential, the surface potential of any density. Condition (34) can be obtained, as was shown in [16], from the more general Dirichlet theorem for a nonpotential vorticity field [18].

Thus, the foregoing and the validity of conditions (15)–(17) and (23)–(29) at each cross-section of a layered medium show that, for numerical solution of the problem being considered it is advantageous to use schemes of through counting and make the discretization of the medium in such a way that the boundaries of the layers have common points.

The medium was divided into finite elements so that the nodes of a finite-element grid, lying on the separation surface between the media with different electrophysical properties, were shared by these media at a time. In this case, the total currents or the current flows at the interface should be equal if the Dirichlet condition (34) is fulfilled.

2.1.3. Results of Numerical Simulation of the Propagation of Electromagnetic Waves in Layered Media. Let us analyze the propagation of an electromagnetic wave through a layered medium that consists of several layers with different electrophysical properties in the case where an electromagnetic-radiation source is positioned on the upper plane of the medium. It is assumed that the normal component of the electric-field vector $E_x = 0$ and its tangential component $E_y = a \sin(\omega t)$, where a is the electromagnetic-wave amplitude (Figure 2).

In this example, for the purpose of correct specification of the conditions at the lower boundary of the medium, an additional layer is introduced downstream of layer 6; this layer has a larger conductivity and, therefore, the electromagnetic wave is damped out rapidly in it. In this case, the condition $E_y = E_z = 0$ can be set at the lower boundary of the medium. The above manipulations were made to limit the size of the medium being considered because,

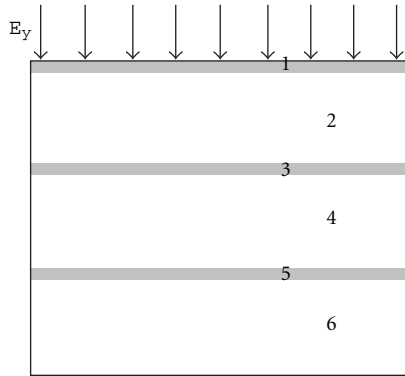


FIGURE 2: Scheme of a layered medium: layers 1, 3, and 5 are characterized by the electrophysical parameters ε_1 , λ_1 , and μ_1 , and layers 2, 4, and 6 by ε_2 , λ_2 , and μ_2 .

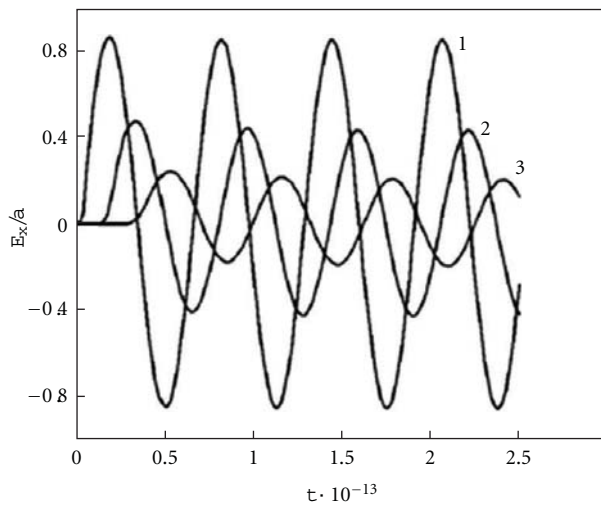


FIGURE 3: Time change in the tangential component of the electric-field strength at a distance of $1 \mu\text{m}$ (1), $5 \mu\text{m}$ (2), and $10 \mu\text{m}$ (3) from the surface of the medium at $\lambda_1 = 100$, $\lambda_2 = 1000$, $\varepsilon_1 = \varepsilon_2 = 1$, $\mu_1 = \mu_2 = 1$, and $\omega = 10^{14}$ Hz. t , sec.

in the general case, the electromagnetic wave is attenuated completely at an infinite distance from the electromagnetic-radiation source.

Numerical calculations of the propagation of an electromagnetic wave in the layered medium with electrophysical parameters $\varepsilon_1 = \varepsilon_2 = 1$, $\lambda_1 = 100$, $\lambda_2 = 1000$, and $\mu_1 = \mu_2 = 1$ were carried out. Two values of the cyclic frequency $\omega = 2\pi/T$ were used: in the first case, the electromagnetic-wave frequency was assumed to be equal to $\omega = 10^{14}$ Hz (infrared radiation), and, in the second case, the cyclic frequency was taken to be $\omega = 10^9$ Hz (radiofrequency radiation).

As a result of the numerical solution of the system of (13) with the use of conditions S (22)–(31) and (32) at the interfaces, we obtained the time dependences of the electric-field strength at different distances from the surface of the layered medium (Figure 3).

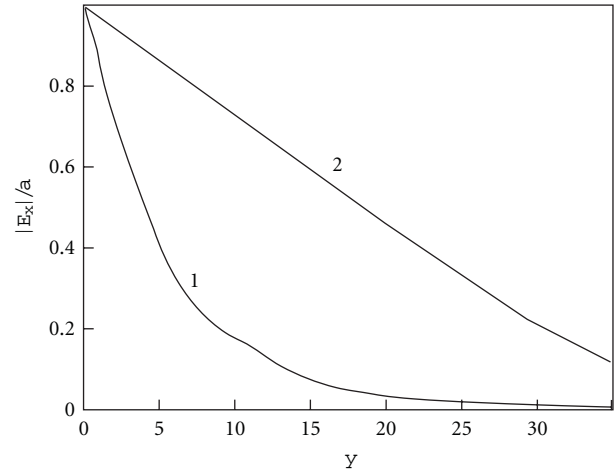


FIGURE 4: Distribution of the amplitude of the electric-field-strength at the cross section of the layered medium: $\omega = 10^{14}$ (1) and 10^9 Hz (2). y , μm .

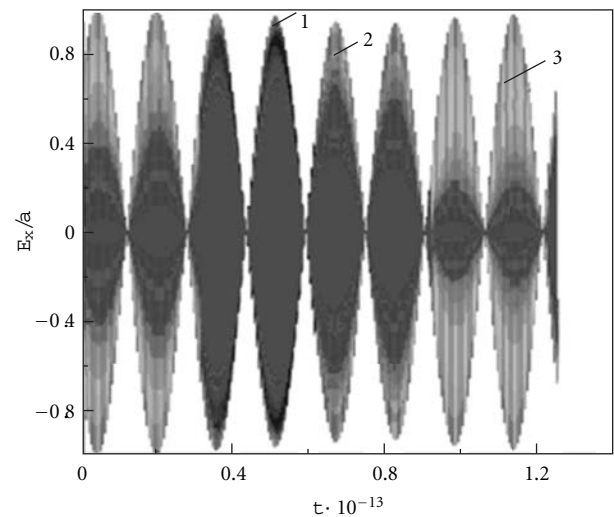


FIGURE 5: Time change in the electric-field strength at a distance of $1 \mu\text{m}$ (1), $5 \mu\text{m}$ (2), and $10 \mu\text{m}$ (3) from the surface of the medium. t , sec.

The results of our simulation (Figure 4) have shown that a high-frequency electromagnetic wave propagating in a layered medium is damped out rapidly, whereas a low-frequency electromagnetic wave penetrates into such a medium to a greater depth. The model developed was also used for calculating the propagation of a modulated signal of frequency 20 kHz in a layered medium. As a result of our simulation (Figure 5), we obtained changes in the electric-field strength at different depths of the layered medium, which points to the fact that the model proposed can be used to advantage for calculating the propagation of polyharmonic waves in layered media; such a calculation cannot be performed on the basis of the Helmholtz equation.

The physicomathematical model developed can also be used to advantage for simulation of the propagation of electromagnetic waves in media with complex geometric

parameters and large discontinuities of the electromagnetic field (Figure 6).

Figure 6(a) shows the cross-sectional view of a cellular structure representing a set of parallelepipeds with different cross-sections in the form of squares. The parameters of the materials in the large parallelepiped are denoted by Index 1, and the parameters of the materials in the small parallelepipeds (the squares in the figure) are denoted by Index 2.

An electromagnetic wave propagates in the parallelepipeds (channels) in the transverse direction. It is seen from Figure 6(b) that, in the cellular structure there are “silence regions,” where the amplitude of the electromagnetic-wave strength is close to zero, as well as inner regions where the signal has a marked value downstream of the “silence” zone formed as a result of the interference.

2.1.4. Results of Numerical Simulation of the Scattering of Electromagnetic Waves in Angular Structures. It is radiolocation and radio-communication problems that are among the main challenges in the set of problems solved using radio-engineering devices.

Knowledge of the space-time characteristics of diffraction fields of electromagnetic waves scattered by an object of location into the environment is necessary for solving successfully any radiolocation problem. Irradiated objects have a very intricate architecture and geometric shape of the surface consisting of smooth portions and numerous wedge-shaped for formations of different type-angular joints of smooth portions, surface fractures, sharp edges, and so forth, with rounded radii much smaller than the probing-signal wavelength. Therefore, solution of radiolocation problems requires the methods of calculation of the diffraction fields of electromagnetic waves excited and scattered by different surface portions of the objects, in particular, by wedge-shaped formations, be known, since the latter are among the main sources of scattered waves.

For another topical problem, that is, radio communication effected between objects, the most difficult are the issues of designing of antennas arranged on an object, since their operating efficiency is closely related to the geometric and radiophysical properties of its surface.

The issues of diffraction of an electromagnetic wave in wedge-shaped regions are the focus of numerous of the problems for a perfectly conducting and impedance wedge for monochromatic waves is representation of the diffraction field in an angular region in the form of a Sommerfeld integral [19].

Substitution of Sommerfeld integrals into the system of boundary conditions gives a system of recurrence functional equations for unknown analytical integrands. The system's coefficients are Fresnel coefficients defining the reflection of plane media or their refraction into the opposite medium. From the system of functional equations, one determines, in a recurrence manner, sequences of integrand poles and residues in these poles.

The edge diffraction field in both media is determined using a pair of Fredholm-type singular integral equations of the second kind which are obtained from the above-indicated systems of functional equations with subsequent computation of Sommerfeld integrals by the saddle-point approximation. The branching points of the integrands condition the presence of creeping waves excited by the edge of the dielectric wedge.

The proposed method is only true of monochromatic waves and of the approximate Leontovich boundary conditions, when the field of the electromagnetic wave slowly varies from point to point on a wavelength scale [20].

We note that the existing approximate Leontovich conditions have a number of other constants and should be used with caution [20].

In actual fact, the proposed calculation method does not work in the presence of, for example, two wedges, when the sharp angles are pointed at each other, that is, an optical knife, or in diffraction of the electromagnetic wave on a system of parallel lobes, when the gap between the lobes is in the region of microns, and the electromagnetic field is strongly “cut” throughout the space with a step much than the wavelength.

(A) Optical Knife. Figure 7 shows the field of an electromagnetic wave in its diffraction on the optical knife. The parameters of the wave at entry and at exit are $E_x = 10^4 \sin(10^{10}t)$, $E_y = 10^4 \cos(10^{10}t)$.

The electrophysical characteristics are as follows. The wedge is manufactured from aluminum: $\varepsilon = 1$; $\mu = 1$; $\sigma = 3.774 \cdot 10^7$ S/m; the ambient medium is air.

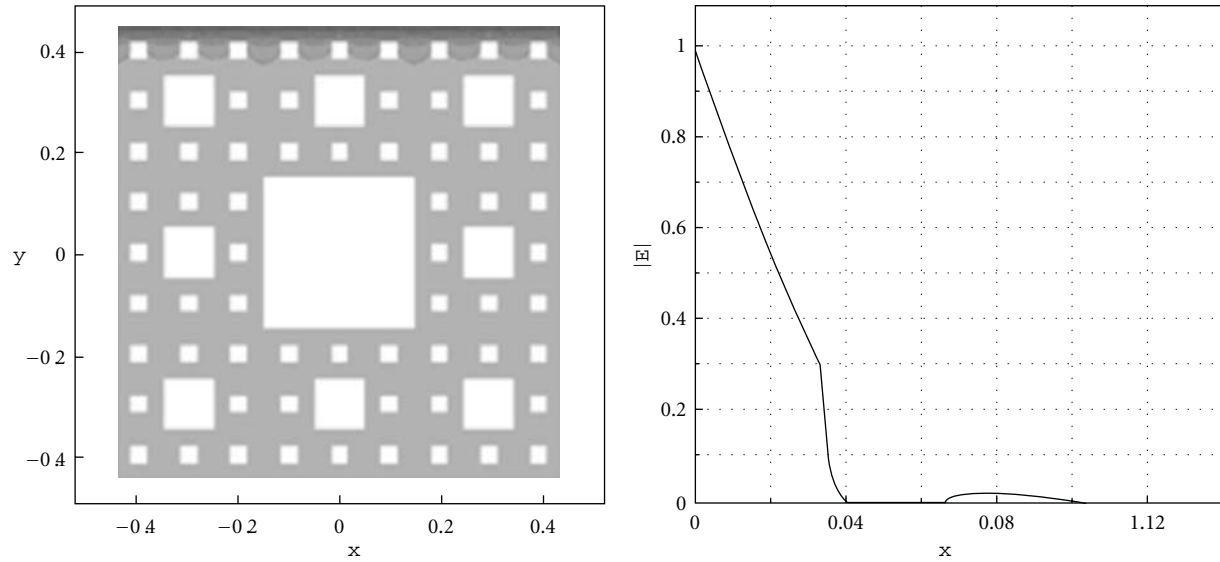
The dimensions of the computational domain are 0.1×0.05 m. The calculation time 10^{-9} sec, and the time step is 10^{-11} sec.

Numerical solution of the system of equations (13) yields the dependences of the distribution E_x , E_y on the optical knife. The calculation results are in good agreement with the existing experimental data and experiments specially conducted at the Department of the Physics and Chemistry of Nonequilibrium Media of the A.V. Luikov Heat and Mass Transfer Institute of the National Academy of Sciences by A. I. Berezhnyak.

The experiments were carried out with an optical-range laser and were tentative in character but the obtained experimental photographs of diffraction fields, and the calculated results turned out to be in good qualitative agreement. The authors express their thanks to A. I. Berezhnyak for the conducting of the experiments.

(B) Diffraction Grating. The parameters of the wave and the interfacial conditions are the same, as those for the case “optical knife.” The electrophysical characteristics are as follows: 2D lobes, $\varepsilon = 12$; and $\sigma = 100$ S/m; the ambient medium is air; the characteristics of the prism and the square are identical to those of the lobes.

Figure 8 corresponds to a calculation time of 10^{-10} sec; the time step is 10^{-12} sec. Figure 9 corresponds to a calculation time of 10^{-9} sec; the time step is 10^{-11} sec.



(a) Distribution of the amplitude of the electric-field strength in the two-dimensional medium (b) Distribution of the amplitude of the electric-field strength in depth

FIGURE 6: Distribution of the amplitude of the electric-field strength in the two-dimensional medium and in depth at $\epsilon_1 = 15$, $\epsilon_2 = 20$, $\lambda_1 = 10^{-6}$, $\lambda_2 = 10$, $\mu_1 = \mu_2 = 1$, and $\omega = 10^9$ Hz (the dark background denotes medium 1, and the light background denotes medium 2). x , y , mm; E , V/m.

It is seen from the modeling results that the proposed “comb” can be used as a filter of a high-frequency signal. Furthermore, we carried out numerical calculations of a modulated signal at a frequency of 20 kHz. The results of the modulated-signal calculations are not given. To analyze the difference scheme for stability was analyzed by the initial data. When the time and space steps are large there appear oscillations of the grid solution and of its “derivatives” (“ripple”) which strongly decrease the accuracy of the scheme. Undoubtedly, this issue calls for separate consideration. The proposed algorithm of solution of Maxwell equations allows circuitry-engineering modeling of high-frequency radio-engineering devices and investigation of the propagation of electromagnetic waves in media of intricate geometry in the presence of strong discontinuities of electromagnetic field.

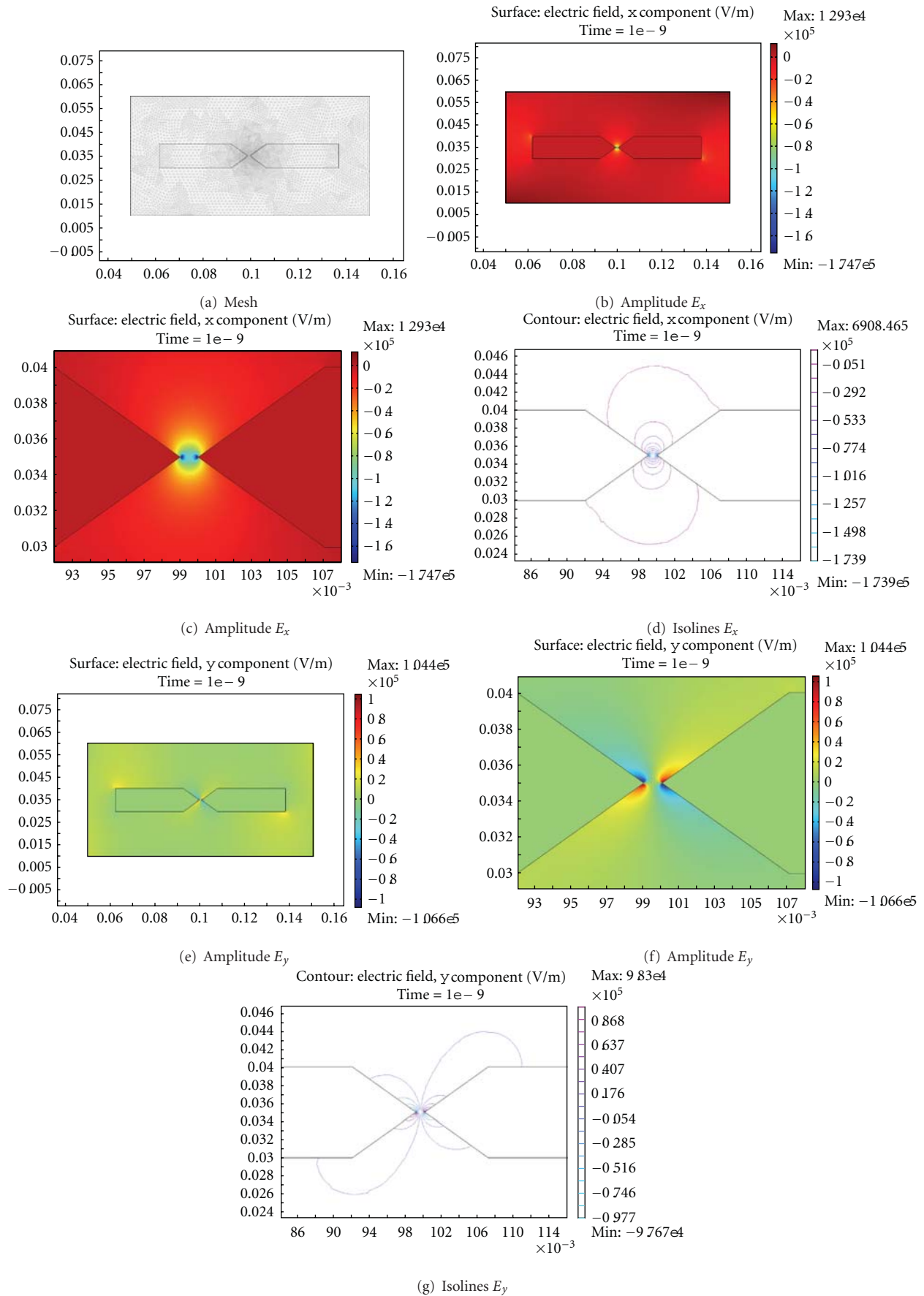
The result of Para 2.1 were published in part [21].

2.1.5. Conclusions. We were the first to construct a consistent physicomathematical model of propagation of electromagnetic waves in layered media without recourse to the matrices of the induced-surface-charge impedances. This model is based on the Maxwell equations, the electric-charge conservation law, the total-current continuity, and the Dirichlet theorem. Our numerical investigations have shown that the physical and mathematical model proposed can be used to advantage for simulation of the propagation of a high-frequency electromagnetic wave in a medium consisting of layers having different electrophysical properties.

2.2. Wave Equation for \vec{H} and Conditions on the Boundaries in the Presence of Strong Discontinuities of the Electromagnetic Field. Numerical Modeling of Electrodynamical Processes in the Surface Layer

2.2.1. Introduction. During the interaction of an external magnetic field and magnetic abrasive particles, the particles are magnetized, and magnetic dipoles with the moment oriented predominantly along the field are formed. “Chains” along the force lines of the field [22, 23] appear that periodically act on the processable surface with a frequency $\omega = l/v$. A fixed elemental area of the material periodically experiences the effect of the magnetic field of one direction. Actually, the frequency and duration of the pulse will be still higher because of the rotation of the magnetic abrasive particle due to the presence of the moment of forces on contact and of the friction of the particle against the processable part. In what follows, we will not take into account the effect of rotation.

We assume that the particle velocity on the polisher is v . If the particle radius is r , then the angular frequency is $\omega = 2\pi v/r$, and precisely this frequency determines the frequency of the effect of the variable magnetic field component due to the fact that for a ferromagnetic $\mu > 1$. The magnetic permeability μ of ferromagnetics, which are usually used in magnetoabrasive polishing, is measured by thousands of units in weak fields. However, in polishing, the constant external magnetic field is strong and amounts to

FIGURE 7: Mesh, amplitude E_x and isolines, and amplitude E_y and isolines of the electromagnetic field strength.

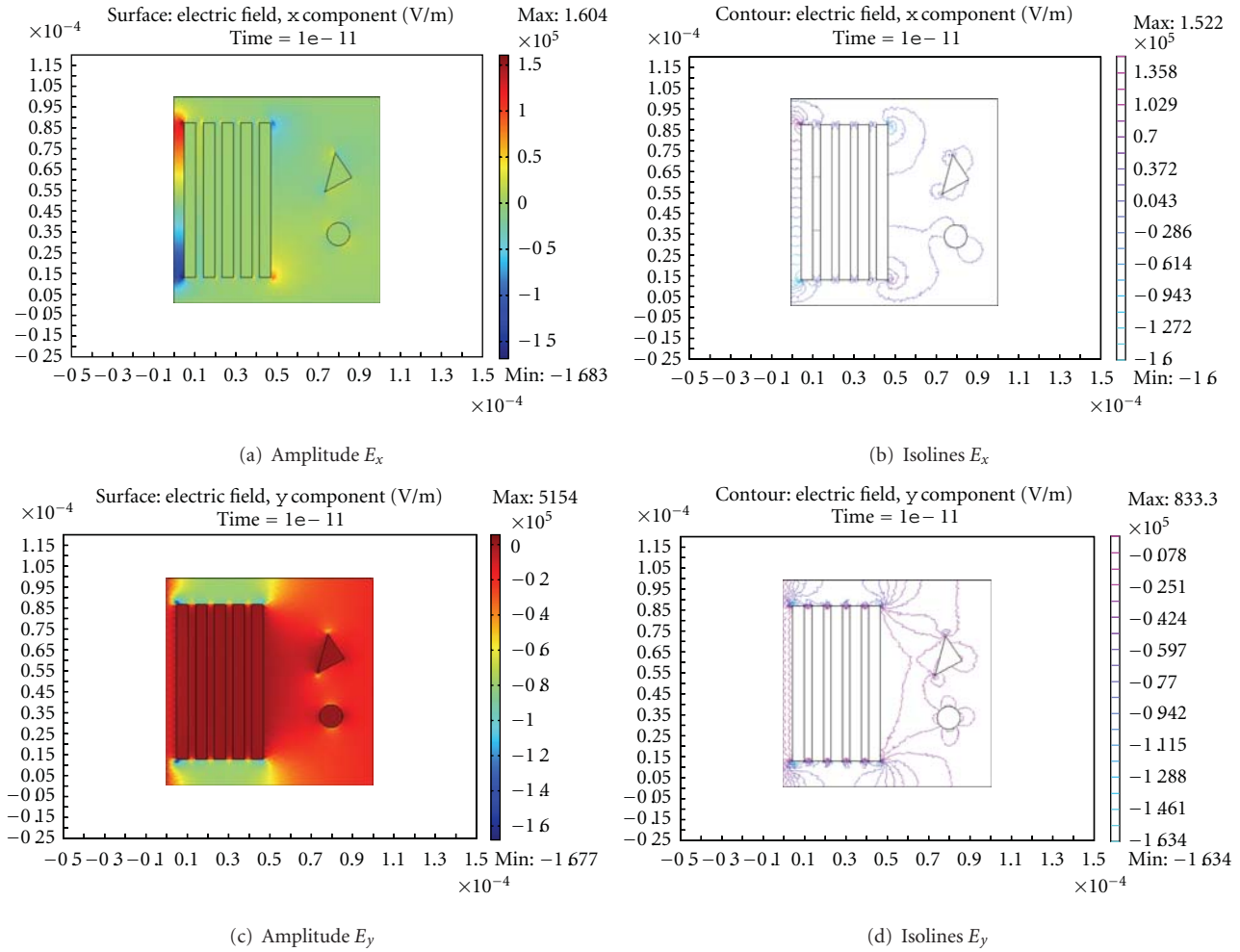


FIGURE 8: Amplitude E_x and isolines and amplitude E_y and isolines of the electromagnetic field strength.

10^5 – 10^6 A/m, and in this case the value of μ for compounds of iron and nickel and for Heusler alloy decreases substantially.

Because of the presence of a strong external magnetic field H_0 the “small” absolute value of μ of an abrasive particle leads to a periodic “increase” and “decrease” in the normal component of the magnetic induction near the processable surface. In the present work we used neodymium magnets (neodymium-iron-boron) with $H_0 > 485,000$ A/m. The magnetic permeability of a magnetic abrasive particle based on carbonyl iron was assumed in this case to be equal to $\mu_1 = 100$.

Due to the continuity of the normal magnetic induction component $B_{n1} = B_{n2}$, where $B_{n1} = \mu_1 \mu_0 H_1$; $B_{n2} = \mu_2 \mu_0 H_2$. For example, in glasses ($\mu_2 = 1$; therefore at the boundary of contact of the glass with the magnetic abrasive particle an additional variable magnetic field of strength $H_1 > H_0$ appears.

In [24–27], magnetic field-induced effects in silicon are considered: a nonmonotonic change in the crystal lattice parameters in the surface layer of silicon, the gettering of defects on the surface, the change in the sorption properties

of the silicon surface, and the change in the mobility of the edge dislocations and in the microhardness of silicon.

In [28–30], the influence of an electromagnetic field on the domain boundaries, plasticity, strengthening, and on the reduction of metals and alloys was established.

In view of the foregoing, it is of interest to find the relationship between the discrete-impulse actions of a magnetic field of one direction on the surface layer of the processable material that contains domains. According to [22], the size of domains is as follows: $0.05 \mu\text{m}$ in iron, $1.5 \mu\text{m}$ in barium ferrite; $8 \mu\text{m}$ in the MnBi compound, and 0.5 – $1 \mu\text{m}$ in the acicular gamma ferric oxide. According to [31], the size of a domain may reach 10^{-6}cm^3 (obtained by the method of magnetic metallography).

As a rule, an abrasive exhibits a distinct shape anisotropy, whereas the frequency of the effect is determined by the concentration of abrasive particles in a hydrophobic solution and by the velocity of its motion. We assume that on the surface of a processable crystal the magnetic field strength $H(t) = H_1 \sin^4(\omega t) + H_0$.

It is required to find the value of the magnetic field strength in the surface layer that has the characteristics λ_1, ϵ_1 ,

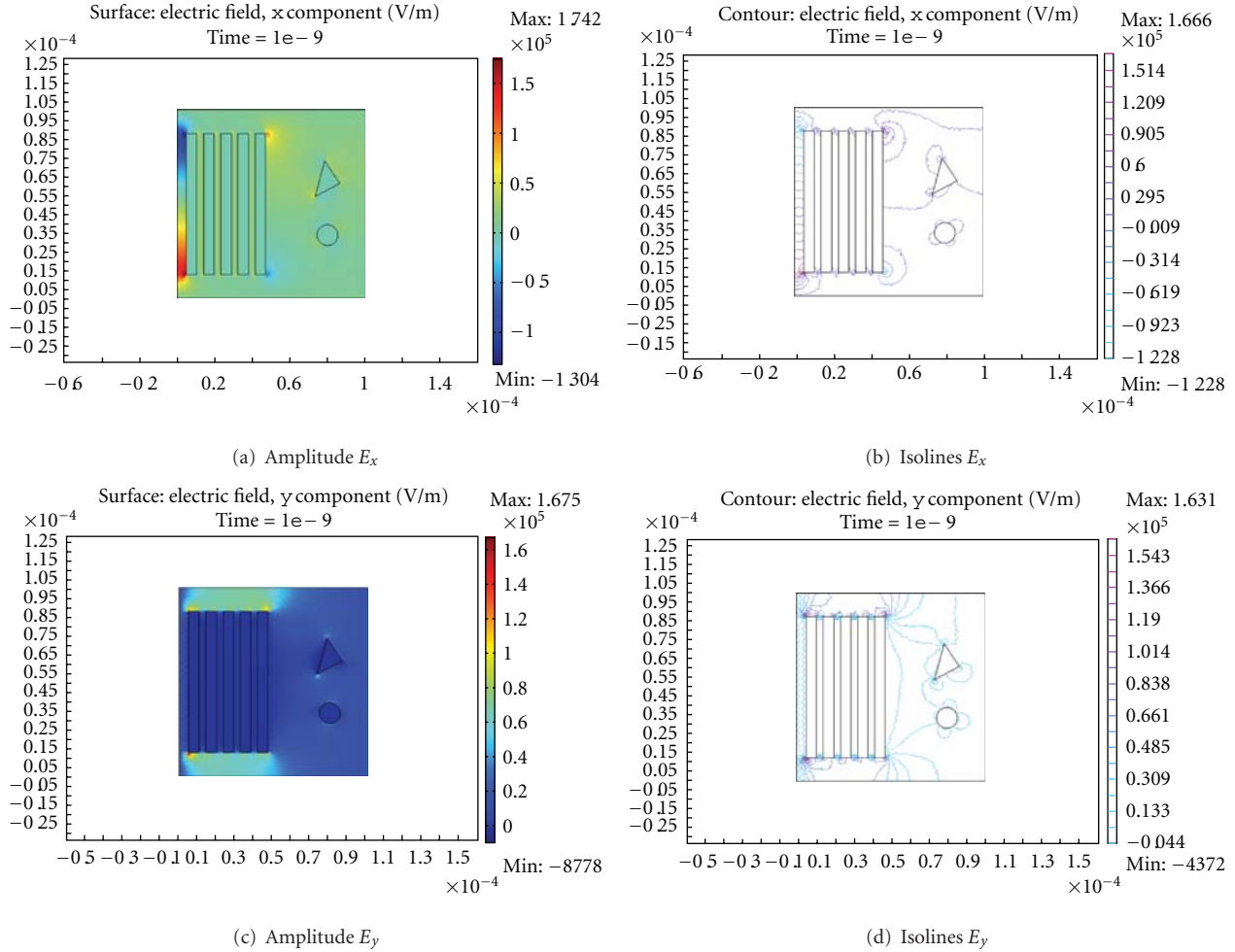


FIGURE 9: Amplitude E_x and isolines and amplitude E_y and isolines of the electromagnetic field strength.

and μ_1 and contains domains with electrophysical properties λ_2 , ε_2 , and μ_2 . The domains may have the form of a triangular prism, a bar, a cylinder, and so forth.

2.2.2. Physicomathematical Model: Wave Equation for \vec{H} . We consider interaction of a nonstationary magnetic field with substance on an example of a specific technology of magneto abrasive polishing based on use of magneto-rheological suspension. We will formulate a physicomathematical model of propagation of electromagnetic waves in a heterogeneous medium. The media in contact are considered homogeneous. We operate with the operator rot on the left- and right-hand sides of the first equation for the total current (6) and multiply by $\mu_0\mu$; then we differentiate the second equation in (7) with respect to time. Taking into consideration the solenoidality of the magnetic field (7) and the rule of repeated application of the operator ∇ to the vector \vec{H} , we obtain

$$\mu_0\varepsilon\varepsilon_0\frac{\partial^2\vec{H}}{\partial t^2} + \lambda\mu_0\frac{\partial\vec{H}}{\partial t} = \frac{1}{\mu}\nabla^2\vec{H}. \quad (35)$$

In the Cartesian coordinates, (35) will have the form

$$\begin{aligned} \varepsilon\varepsilon_0\frac{\partial^2 H_x}{\partial t^2} + \lambda\mu_0\frac{\partial H_x}{\partial t} &= \frac{1}{\mu}\left(\frac{\partial^2 H_x}{\partial x^2} + \frac{\partial^2 H_x}{\partial y^2} + \frac{\partial^2 H_x}{\partial z^2}\right), \\ \varepsilon\varepsilon_0\frac{\partial^2 H_y}{\partial t^2} + \lambda\mu_0\frac{\partial H_y}{\partial t} &= \frac{1}{\mu}\left(\frac{\partial^2 H_y}{\partial x^2} + \frac{\partial^2 H_y}{\partial y^2} + \frac{\partial^2 H_y}{\partial z^2}\right), \\ \varepsilon\varepsilon_0\frac{\partial^2 H_z}{\partial t^2} + \lambda\mu_0\frac{\partial H_z}{\partial t} &= \frac{1}{\mu}\left(\frac{\partial^2 H_z}{\partial x^2} + \frac{\partial^2 H_z}{\partial y^2} + \frac{\partial^2 H_z}{\partial z^2}\right). \end{aligned} \quad (36)$$

One fundamental electromagnetic field equation is the equation $\text{div } \vec{B} = 0$. The use of the Dirichlet theorem for approximation of the value of the magnetic field strength on the boundaries between adjacent media analogously to that of the electric field strength does not necessarily guarantees the observance of the condition of solenoidality of the magnetic field; furthermore, the magnetic properties of heterogeneous media were assumed constant in deriving generalized wave equations. The experience of numerical calculations has shown that when it is necessary to model nonstationary magnetic phenomena it is better in many cases to use a generalized wave equation for \vec{E} , accordingly

expressing $\vec{H}(t, \vec{r})$ by $\vec{E}(t, \vec{r})$ and, if need be, to perform backward recalculation to $\vec{H}(t, \vec{r})$. This approach is difficult to apply to modeling of heterogeneous media with different magnetic properties, when the magnetic permeability μ is dependent on coordinates.

In media with a weak heterogeneity where $\mu(x, y, z)$ is a piecewise continuous quantity, the application of the proposed method of through counting is quite justified. Indeed, the system of (13) and (36) yields that the function's discontinuity on the boundaries between adjacent media is determined by the complexes which will be called the generalized permeability $\varepsilon^* \equiv \varepsilon\mu\varepsilon_0\mu_0$ and the generalized conductivity $\lambda^* \equiv \lambda\mu\mu_0$. Using the Dirichlet theorem for ε^* and λ^* , we obtain their values on the boundaries between adjacent media and the values for the electric field strength at the discontinuity point (see (34)); here, we note that the value of the electric field strength is obtained without solving Maxwell equations. In fact, at the discontinuity point, we use linear interpolation of the function to obtain the values of ε^* , λ^* , and $E_{x=\xi} = (1/2)[E(\xi - 0) + E(\xi + 0)]$. Consequently, for piecewise continuous quantity $\mu(x, y, z)$, the application of the proposed method of through counting is justified. We note that the equality of the derivatives of the electric field strength along the normal to the surface at the discontinuity point according to Equation (32) holds. When the wave equation for \vec{H} is used for media with different magnetic permeabilities the condition of equality of the derivatives fails, that is,

$$\left. \frac{\partial H_x}{\partial x} \right|_{x=\xi-0} \neq \left. \frac{\partial H_x}{\partial x} \right|_{x=\xi+0}, \quad (37)$$

which is a consequence of (10); therefore, the use of through-counting schemes for the wave equation for \vec{H} is difficult.

Moreover, reformulation of the boundary conditions for equations (6) and (7), with electric field strength being eliminated from the boundary conditions, does not even allow prediction of the surface current direction. Indeed, magnetic field strength \vec{H} is an axial vector which on substitution $\vec{r} \rightarrow (-\vec{r})$ must remain constant. The value of the surface current also cannot be determined without knowledge of the polar vector of electric field strength. The generalized wave equation for \vec{E} contains the term $\text{grad div } \vec{E}$ which directly allows for the influence of induced surface charges on the propagation of waves, the right-hand side of the generalized wave equation has the same form as the equations of the linear elasticity theory, hydrodynamics. We note that the proposed method of calculation can be used on condition that there are no built-in space charges and extraneous electromotive forces [13].

By virtue of what has been stated above, for modeling of the propagation of electromagnetic waves in glasses having roughness and defects, we used system (13) with boundary conditions (22)–(31) and (32).

2.2.3. Results of Numerical Simulation. The physicomathematical model developed can also efficiently be used in modeling the propagation of electromagnetic waves in media

with complex geometries and strong electromagnetic field discontinuities.

The transverse cut of a cellular structure represents a set of parallelepipeds and triangular prisms of various cross-sections, as depicted in Figures 10(a) and 11(a). An electromagnetic wave propagates across the direction of parallelepipeds and triangular prisms (channels) along the coordinate x .

The size of the investigated two-dimensional object is $14 \times 20 \cdot 10^{-6}$ m, and the sizes of the domains are $2\text{--}4 \mu\text{m}$. The frequency of the influence of the magnetic field is $\omega = 2\pi \cdot 10^6$, and the strength of the field is

$$H_x = 21 \cdot 10^5 \sin^4(2\pi \cdot 10^6 t) \frac{\text{A}}{\text{m}}. \quad (38)$$

The electrophysical properties are as follows: of the large parallelepiped, $\mu = 1$, $\varepsilon = 8$, $\sigma = 10^{-9} \Omega \cdot \text{m}$; of domains, $\mu = 1$, $\varepsilon = 6$, $\sigma = 10^{-8} \Omega \cdot \text{m}$. They correspond to the electrophysical properties of glasses.

It was assumed that in a layer of thickness $15\text{--}20 \mu\text{m}$ an electromagnetic wave propagates without attenuation; therefore, on all the faces of the large parallelepiped the fulfillment of condition (38) was considered valid. On the faces of the parallelepiped that are parallel to the OX axis condition (38) corresponded to the “transverse” tangential component of the wave; on the faces parallel to OY condition (38) corresponded to the normal component of the field.

The calculations were carried out with a time step of 10^{-13} sec up to a time instant of 10^{-10} sec.

Figures 10(a) and 11(a) present the amplitude values of the magnetic field strength along H_x and H_y with a comparison scale, whereas Figures 11(b) and 11(b) present the corresponding isolines. An analysis of these figures shows that at the places of discontinuity, on the wedges, force lines of the electromagnetic field concentrate. According to [32], precisely wedges are often the sources and sinks of the vacancies that determine, for example, the hardness and plasticity of a solid body.

Also, we modeled the propagation of waves in media, when domains possess magnetic properties. We assumed, in the calculations, that $\mu = 100$; the remaining parameters correspond to the previous example of solution (Figure 12).

Of interest is the interaction of the electromagnetic wave with the rough surface shown in Figures 13 and 14. As in the previous examples, we observe the concentration of electromagnetic energy on angular structures.

From Figures 13 and 14, it is seen that electromagnetic heating of tapered structures may occur in addition to mechanical heating in magnetic abrasive machining.

As we have mentioned above, for investigation of the propagation of electromagnetic waves in nonmagnetic materials, it is more expedient to use the generalized equation for \vec{E} . For the purpose of illustration we give an example of numerical calculation of an optical knife with the wave equation for \vec{H} (Figure 15).

From Figure 15, it is seen that the actual problem of diffraction on the optical knife remains to be solved, that is, there is no “glow” on the optical-knife section, which is inconsistent with experimental data.

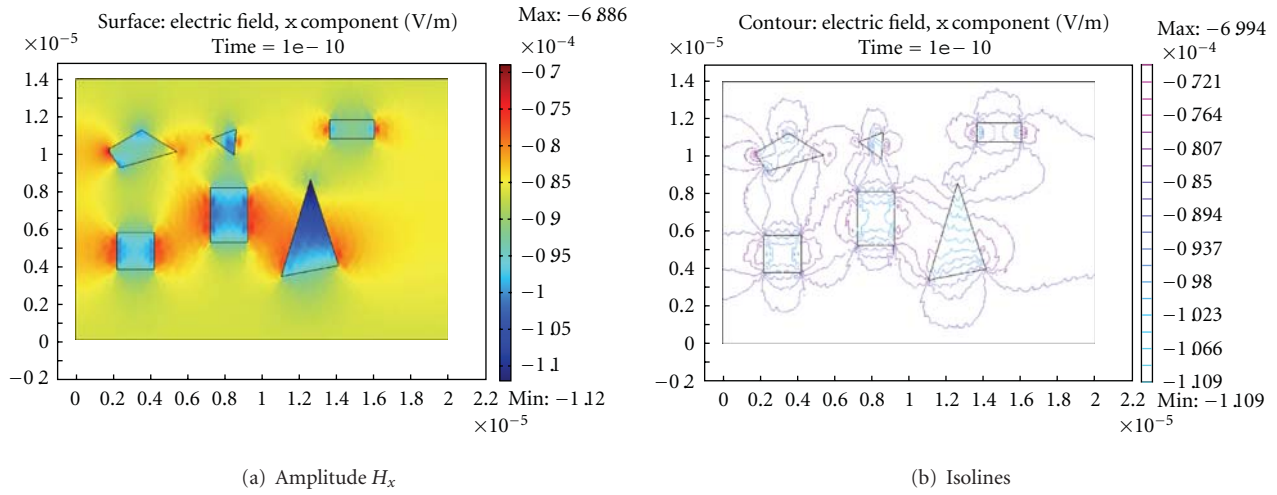


FIGURE 10: Amplitude H_x and isolines of the magnetic field strength.

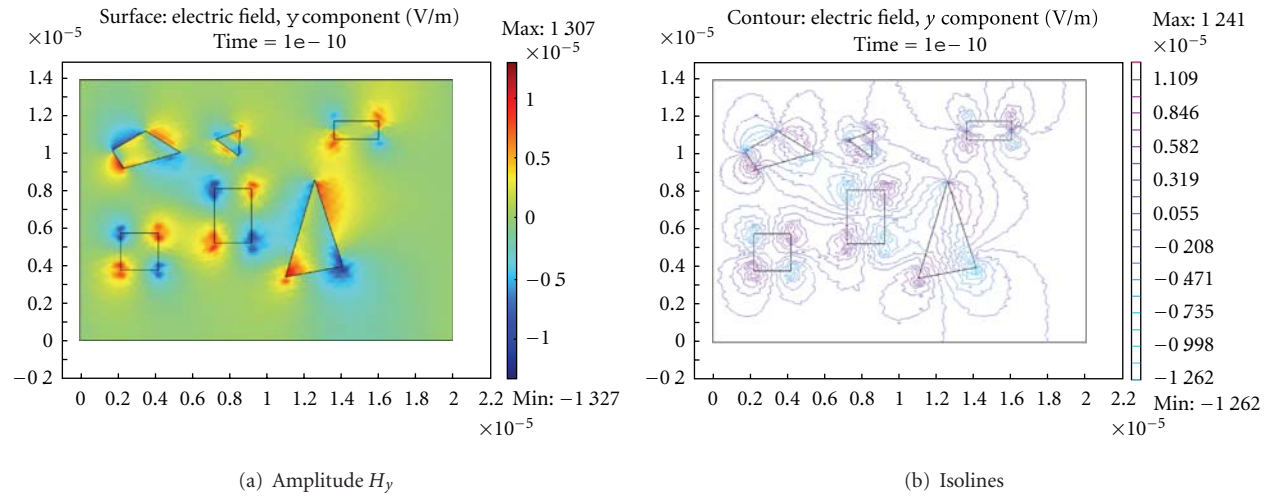


FIGURE 11: Amplitude H_y and isolines of the magnetic field strength.

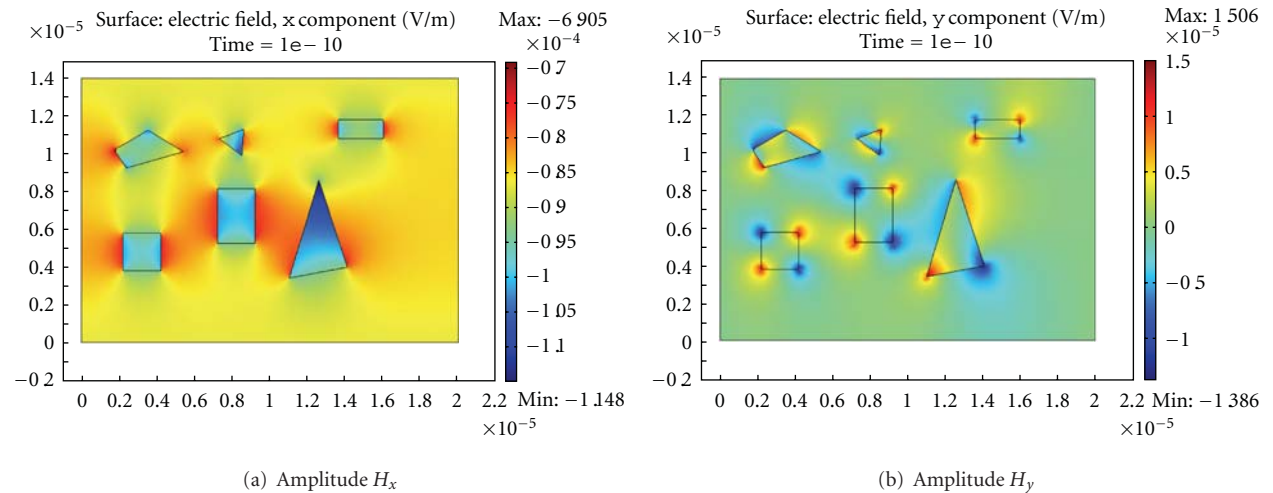
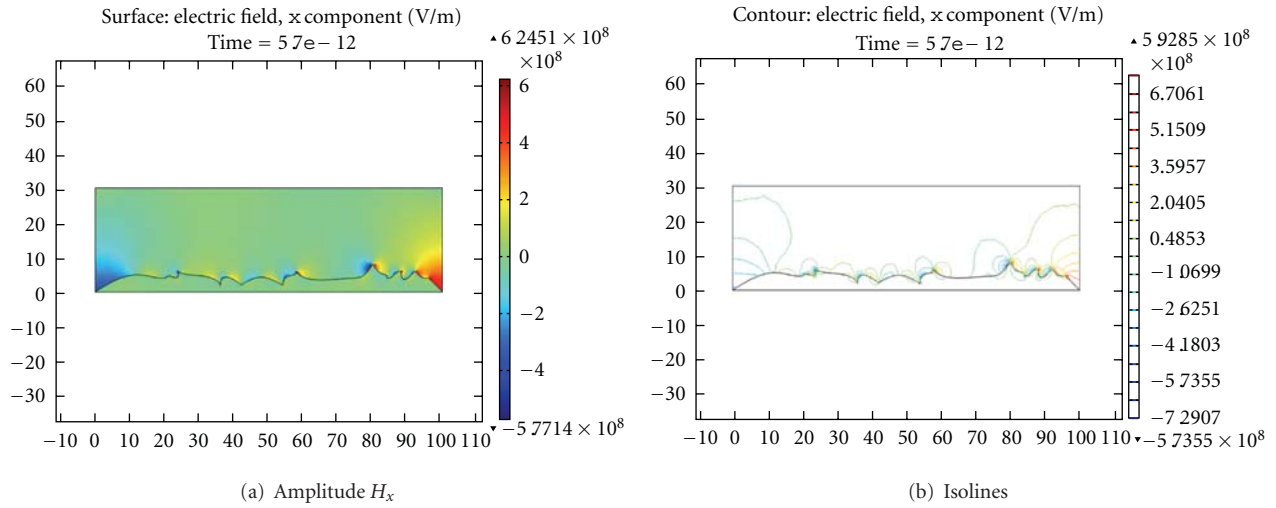
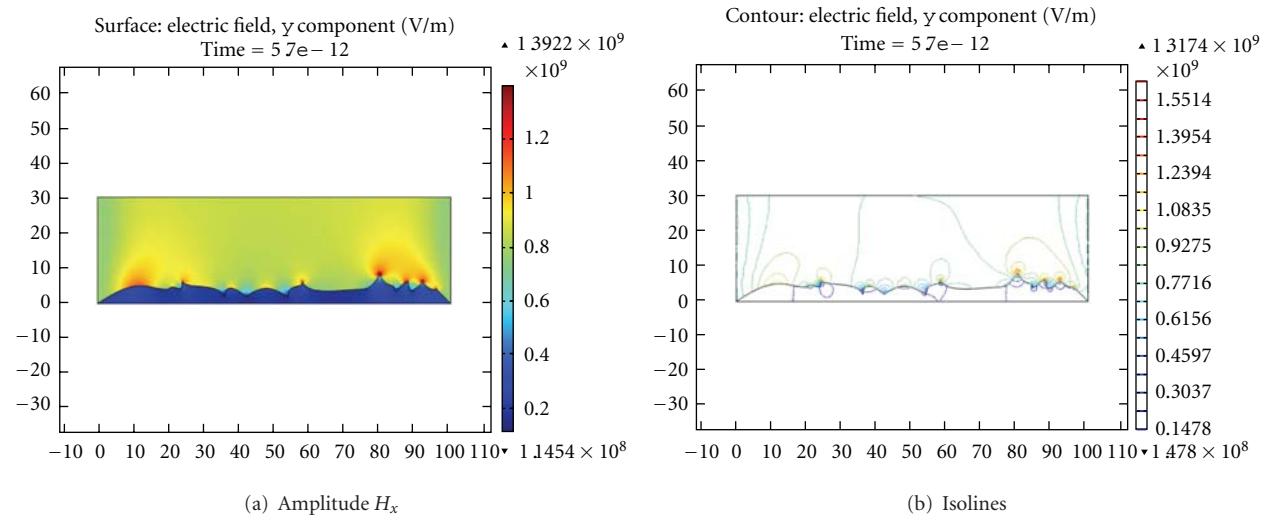
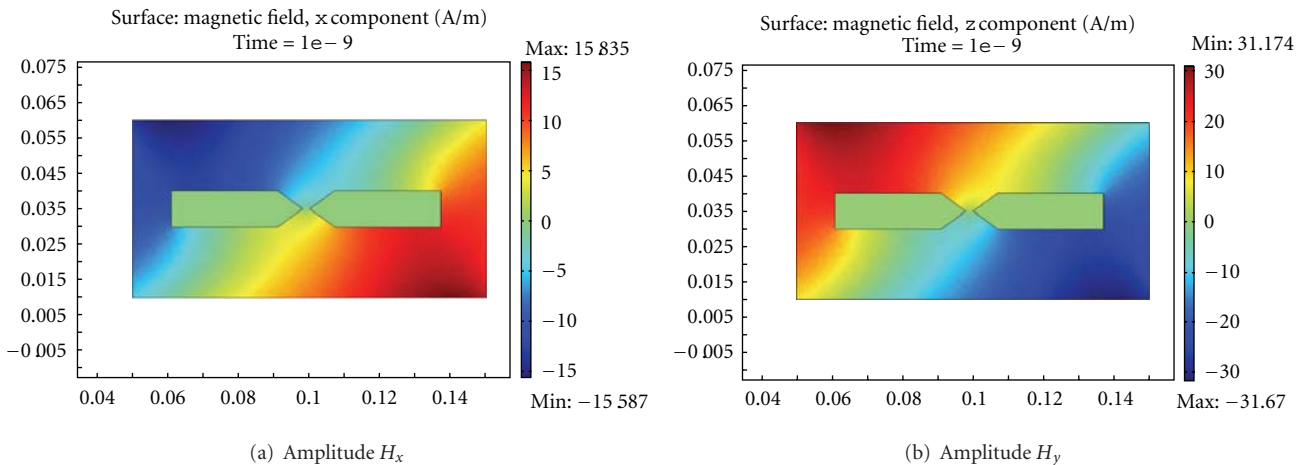


FIGURE 12: Amplitude H_x and H_y of the magnetic field strength.

FIGURE 13: Amplitude H_x and isolines of the magnetic field strength.FIGURE 14: Amplitude H_y and isolines of the magnetic field strength.FIGURE 15: Amplitude H_x and H_y of the magnetic field strength.

As is known [33] in thermodynamically equilibrium systems the temperature T and the electrical φ and chemical μ_c potentials are constant along the entire system:

$$\text{grad } T = 0, \quad \text{grad } \varphi = 0, \quad \text{grad } \mu_c = 0. \quad (39)$$

If these conditions are not fulfilled ($\text{grad } T \neq 0$, $\text{grad } \varphi \neq 0$, $\text{grad } \mu_c \neq 0$), irreversible processes of the transfer of mass, energy, electrical charge, and so forth appear in the system.

The chemical potential of the j th component is determined, for example, as a change of the free energy with a change in the number of moles:

$$\mu_{cj} = \left(\frac{\partial F}{\partial n_j} \right)_{T,V}, \quad (40)$$

where

$$dF = -SdT - PdV + \bar{H} d\bar{B} + EdD. \quad (41)$$

The last term in (41) takes into account the change in the free energy of a dielectric due to the change in the magnetic induction. The free energy of a unit volume of the dielectric in the magnetic field in this case has the form

$$F(T, D) = F_0 + \mu\mu_0 \frac{\bar{H}^2}{2} + \varepsilon\varepsilon_0 \frac{E^2}{2}. \quad (42)$$

We assume that changes in the temperature and volume of the dielectric are small. Then the mass flux is determined by a quantity proportional to the gradient of the chemical potential or, according to (41), we obtain

$$q_i = -D_{\mu_c} \text{grad} \left(\bar{H} d\bar{B} + EdD \right) = -D_{\mu_c} \text{grad } W, \quad (43)$$

where $W = \mu\mu_0(\bar{H}^2/2) + \varepsilon\varepsilon_0(E^2/2)$ is the density of the magnetic field in the unit volume of the dielectric.

In magnetic abrasive polishing on the sharp protrusions of domains the gradients of magnetic energy are great, which can lead to the origination of vacancy flows.

An analysis of the results shows that the nonstationary component of the full electromagnetic energy is also concentrated in the region of fractures and wedges, that is, at the sharp angles of domains, which may lead to the improvement of the structure of the sublayer of the treated surface due to the “micromagnetoplastic” effect. Maximum values of the nonstationary part of the total electromagnetic energy W_{\max} in the sublayer corresponds to a maximum value of the function $\sin(2\pi \cdot 10^6 t)$ and occur for the time instants $t = (n/4)10^{-6}$ sec, where n is the integer, with the value of W_{\max} for a neodymium magnet and a magnetoabrasive particle on the basis of carboxyl iron amounting to a value of the order of $((5)-(6)) \cdot 10^6$ J/m³. Having multiplied W_{\max} by the volume of a domain, vacancy, or atom, we may approximately obtain the corresponding energy. The density of the electromagnetic energy in all of the cases is much smaller than the bonding energy of atoms, $10^{-18}-10^{-19}$ J. However, a periodic change in the magnetic field in one direction leads to a ponderomotive

force that may influence the motion of various defects and dislocations to create a stable and equilibrium structure of atoms and molecules in magnetic abrasive polishing and, on the long run, in obtaining a surface with improved characteristics due to the “micromagnetoplastic” effect. The result of Para 2.2 were published in part [34].

3. Ion Conductors: New Closing Relations on the Boundaries of Adjacent Media

3.1. Diffusion Electric Phenomena in Electrolytes. The medium under discussion is assumed to consist of a non ionized solvent, an electrolyte in the form of ions and uncharged components. At first we consider infinitely diluted electrolytes when molecules are completely dissociated into cations and anions.

In a solution, ions are transferred by convection, diffusion, and migration in the presence of an electric field. Derivation of the equation for ion migration is based on the following considerations. In a solution with molar concentration n and diffusion coefficient D_i let there be ions with charge z_i . When an ion is exposed to an electric field with intensity E applied to the solution, the ion experiences the force $z_i e E$, which brings it into motion. The ion velocity is related to this force by the usual expression known for the motion of particles in a viscous medium:

$$u = \gamma_i^* z_i e E, \quad (44)$$

where γ_i^* is the ion mobility. The latter may be expressed in terms of the diffusion coefficient using the known Einstein relation:

$$\gamma_i^* = \frac{D_i F}{RT}. \quad (45)$$

The total flux of ions of the i th kind in a moving medium in the presence of diffusion and migration is determined by the Nernst-Planck equation:

$$q_i = n_i v - D_i \nabla n_i + \frac{D_i z_i F E}{RT} n_i. \quad (46)$$

Formulas (44) and (45) have, in fact, a limited sphere of applicability. Indeed, Einstein's work [35] is concerned only with the diffusion of a neutral impurity with its small concentration in a solution when the usual relations of hydrodynamics are valid for a flow around a sphere.

In the physics of plasma, formulas (44) and (45) are based on other considerations and provided the plasma is weakly ionized, that is, particles move independently of each other. Here, only the collision of charged particles with neutral ones is taken into account [36].

In [37, 38], for describing the diffusion and migration of ions in a partially dissociated electrolyte it is suggested to take into consideration their transfer by neutral molecules. In the theory developed by Y. Kharkats [37] the expression for the total flux of ions is

$$q_i = n_i v - D_i \nabla n_i + \frac{D_i z_i F E}{RT} n_i - D z_i \nabla n_A. \quad (47)$$

TABLE 1: The degree of HCl electrolytical dissociation in terms of measured electric conductivity α_1 and E.m.f. α_2 .

C_{HCl} , mole/liter	0.003	0.08	0.3	3.0	6.0	16.0
α_1	0.986	0.957	0.903	—	—	—
α_2	0.99	0.88	0.773	1.402	3.4	13.2

The last term in (47) takes into account ion transfer by a flux of neutral molecules; here the concentrations of anions, cations, and neutral dissociated molecules are determined by the chemical equilibrium conditions

$$\beta = \frac{(n^-)^{z^+} (n^+)^{z^-}}{n_A}, \quad (48)$$

where β is the dissociation equilibrium constant. If the degree of dissociation at the prescribed total concentration n is α , then $n_A = (1 - \alpha)n$ and, consequently,

$$\beta = \frac{\alpha^2 n}{1 - \alpha}. \quad (49)$$

The dissociation constant β , unlike the degree of dissociation, must not depend on concentration. However, in real partially dissociated electrolytes those arguments for α and β are in rather poor agreement with experiment. In [39] the dissociation degree for HCl is listed in Table 1 as a function of concentrations, calculated in terms of measured electric conductivity α_1 and e.m.f. α_2 .

Inspection of the table reveals that the dissociation degrees obtained by different experimental methods coincide best in the case of dilute solutions. In the high-concentration range of the electrolyte, α_2 even exceeds unity, which, naturally, has no physical sense.

According to the Arrhenius theory the dissociation constant β for the given electrolyte at the prescribed temperature and pressure must remain constant independently of the solution concentration. In [40], the dissociation constants of some electrolytes are given at their different concentrations. Only for very weak electrolytes (solutions of ammonia and acetic acid) does the dissociation constant remain more or less constant on dilution. For strong electrolytes (potassium chloride and magnesium sulfate), it changes by severalfold and in no way may be considered a constant.

Of course, one may formally take into account the dependence of the dissociation constant on the electrolyte concentration and use it in the modified Nernst-Planck equation (47) and (48) but the main drawback in describing separately the diffusion and migration of ions in an electrolyte, in D. I. Mendelev's opinion, lies in the fact that the interaction of particles of a dissolved substance between each other as well as with solvent molecules is neglected. Also, he has pointed out that not just the processes of formation of new compounds with solvent molecules are of importance for solutions. D. I. Mendelev's viewpoints have been extended by Sakhanov [40], who believed that in addition to the usual dissociation reaction in an electrolyte solution there also proceeds associating of simple molecules. Molecular associations dissociate, in their

turn, into complex and simple ions. In this case (47) will not hold mainly because of the fact that the expressions for diffusion, migration, and nondissociated flows of molecules must be determined relative to some mean liquid velocity. In concentrated solutions, this velocity does not coincide with the solvent velocity and must be determined from the fluid dynamics equations of a multicomponent mixture in which characteristics of its components (physical density, charge, diffusion coefficient of a complex ion) are, in fact, unknown. This is a reason why the theory of diffusion and migration of ions for a partially dissociated electrolyte solution, with a current traversing through it, encounters crucial difficulties. Besides, it is rather difficult to take an account of the force interaction of complex cations and anions between each other and with an external electric field. Therefore Einstein's formula (44) will also change its form.

The main drawbacks of the theory of electrolytic dissociation are fully defined in collected papers "Fundamental Principles of Chemistry" by D. I. Mendelev as well as in [40, 41].

In our opinion, the principal disadvantage of the approaches considered above lies in the fact that the Nernst-Planck equation as well as its modified form for a partially dissociated electrolyte (see (47)) are based on the hydrodynamic theory of diffusion. We shall substantiate below that it is more reasonable to use the equations of thermodynamics of irreversible processes.

When applying the Nernst-Planck equation (see (46)) and its modified forms (see (47)), it is implicitly postulated that cations and anions in the electrolyte solution are different components. The equations of transfer of cations and anions are written separately. On the other hand, the commonly used equation of electroneutrality does not ensure, according to Gibbs [39], the independence of differentials of cations ∂n_i and anions ∂n_e in a volumetric electrolyte solution their changes are functionally related and therefore they are identical, indiscernible components.

3.1.1. The Case of a Current Traversing a Binary Fully Dissociated Electrolyte. Let us write system of equations (see (46)) in the form:

$$\frac{\partial n_e}{\partial \tau} + \mathbf{v} \text{grad } n_e = D_e \Delta n_e + \frac{z_e F D_e}{RT} \text{div}(n_e \mathbf{E}), \quad (50)$$

$$\frac{\partial n_i}{\partial \tau} + \mathbf{v} \text{grad } n_i = D_i \Delta n_i + \frac{z_i F D_i}{RT} \text{div}(n_i \mathbf{E}),$$

$$z_e n_e - z_i n_i = 0. \quad (51)$$

Analogously to [39], instead of concentrations n_e and n_i we introduce the molar concentration related to n_e and n_i by the expressions

$$C = \frac{n_e}{z_i} = \frac{n_i}{z_e}. \quad (52)$$

Expressing n_e and n_i in (50) in terms of the molar concentration, we arrive at the following expression for the function C :

$$\frac{\partial C}{\partial \tau} + \mathbf{v} \nabla C = D_{\text{ef}} \Delta C, \quad (53)$$

where

$$D_{\text{ef}} = \frac{D_e D_i (z_e + z_i)}{z_e D_e + z_i D_i} \quad (54)$$

is the diffusion coefficient of a salt or the effective diffusion coefficient of a binary electrolyte. Expressing the concentrations n_e and n_i in terms of the molar concentration C we find the expression for the vector of current density \mathbf{J} [42]:

$$\mathbf{J} = (D_i - D_e) F z_i z_e \nabla C + \frac{F^2 z_i z_e}{RT} (z_i D_i + z_e D_e) C \mathbf{E}. \quad (55)$$

In [43] it is shown that by its meaning D_{ef} is a coefficient of molecular diffusion. For instance, the diffusion coefficients of copper sulfate have an intermediate value between the diffusion coefficients of copper and sulfate ions; if $D_e = 0.173 \cdot 10^{-9} \text{ m}^2/\text{sec}$ and $D_i = 1.065 \cdot 10^{-9} \text{ m}^2/\text{sec}$, then $D_{\text{ef}} = 0.854 \cdot 10^{-9} \text{ m}^2/\text{sec}$. However, expression (54) does not offer an explanation of the abnormally high mobility of H and OH ions when their displacement proceeds by a croquet-like mechanism [44].

In the system of (53)–(55) no symmetry of cross terms is observed; therefore, it is difficult to take into account “the superposition effects.” Indeed, from (55) it is evident that the molar concentration gradients ∇C exert an influence on the current \mathbf{J} . On the other hand, one can see from (53) that an electric field has no effect on the diffusion of the molecules, and therefore the Onsager reciprocal relation is disturbed.

One may raise the objection that according to the Nernst-Planck equations it follows that the concentration gradients of cations and anions exert an influence on the potential distribution of an electric field [42]:

$$\nabla(\rho_R \nabla \varphi) = -F \sum_i z_i \nabla(D_i \nabla C_i). \quad (56)$$

However, relation (56) itself has been derived by Neumann [43] on the assumption that the resultant current does not depend on the mass flow.

On derivation of the equations for diffusion and migration of ions in a volumetric electrolyte solution we shall employ the relations of the thermodynamics of irreversible processes.

Finally, it is worthy of note that in plasma physics there is also no symmetry of “the superposition effects” in describing the ambipolar diffusion of ions, and the theory is based on the hydrodynamic model [36].

In investigating the dynamics of an electron-hole semiconductor plasma, the hydrodynamic model (50)–(51) is also used.

In our opinion, electric field-induced transfer of charges entails transfer of their kinetic energy as well as of heat and mass, and, conversely, mass or heat transfer may simultaneously cause, if we are concerned with the system of charged particles, charge transfer and give rise to an electromotive force.

3.1.2. Conclusion. To phenomenologically describe diffusional-electrical phenomena in electrolytes it is suggested

to use the methods of the thermodynamics of irreversible processes, rather than the hydrodynamic theory of diffusion of ions, for the experimentally observable thermodynamic flows and forces without clear discernment and identification of *real* ion flows and mobilities.

3.2. Landau Model. In what follows we consider ion conductors that contain the electrolytic plasma with a fairly high concentration of charged particles. The interaction of the charged plasma particles with the external electromagnetic field and their collective interaction can theoretically be investigated completely only on the basis of the Boltzmann kinetic equation with a self-consistent field. In this probabilistic approach to the phenomena under study, one introduces characteristics that are average over a large ensemble of particles and are always related to the introduction of additional hypotheses on the properties of particles and their interactions and to the simplification of these properties and interactions. We note that in many cases, for example, when the electrolytic plasma in liquid electrolytes is considered, there is even no basis for constructing such methods. The developed methods are usually not an efficient means of solving problems by virtue of the excessive complexity of corresponding equations.

Another general method is construction of a phenomenological macroscopic theory based on the general regularities and hypotheses obtained experimentally; this precisely method will be developed in the present work. For many problems of applied character, consideration of a plasma as a conducting gas is sufficient. Such approximation is strictly justified only in the case of a dense plasma when the free path of charged particles is much smaller than the characteristic dimension of the system and particle collisions are of crucial importance. The velocity distribution of particles is Maxwellian; at each point, it is fully determined by the local values of density, temperature, and macroscopic velocity. With these conditions being observed, we can carry out, in a unified context, macroscopic phenomenological description of a gas medium, a metal and dielectric plasma, a plasma in a liquid electrolyte, or an electrolytic plasma.

The necessary condition of existence of the state of local thermodynamic equilibrium (LTE) of a plasma is high frequency of collisions of plasma particles (Maxwellization) so that the plasma state undergoes no marked changes over the period between collisions on the mean free path. The observance of this condition means the following: (1) the electrons have time to transfer the energy received from the electrostatic field to heavy particles; (2) ionization processes are nearly totally counterbalanced by recombination (the Saha equation holds true); (3) the overwhelming part of excited atoms gives up its energy in collisions; (4) energy exchange between particles dominates the processes in which the plasma energy markedly grows or diminishes.

In the LTE plasma state, it is only the radiation field (photons) that is not in equilibrium with the plasma, but the energy loss by radiation is minor in a number of cases compared to other mechanisms of energy transfer. With allowance for the assumptions enumerated above,

the plasma electrodynamics can be described by Maxwell continuity, motion, and energy equations [45]. For macroscopic description of transfer processes in ion conductors, we will use the equations of thermodynamics of irreversible processes without separating explicitly ion carriers.

The possibility of such description was first suggested by L. D. Landau and E. M. Lifshits. This approach which has been substantiated above does not provide for the introduction and determination of the coefficients of molecular diffusion of cations and anions and of the degree of dissociation in an ion conductor. It is conditioned by the interaction of the mass and charge fluxes. The ion fluxes are not determined. The density of the conduction current \mathbf{J}_q , the mass flux \mathbf{J}_m , and the heat flux \mathbf{J}_T for the medium's nonequilibrium state has the form [45]:

$$\begin{aligned} \mathbf{J}_q &= \lambda(\mathbf{E} - \beta \text{grad } n) - \lambda\alpha(T)\text{grad } T, \\ \mathbf{J}_m &= -D_m \text{grad } n - D_A^* \lambda \mathbf{E} - D_T \text{grad } T, \\ \mathbf{J}_T &= -k \text{grad } T - I_q(\Pi + \varphi) - \lambda D_T^* \text{grad } n, \end{aligned} \quad (57)$$

where D_M is the coefficient of molecular diffusion, D_A^* is the coefficient of ambipolar diffusion, D_T^* is the coefficient allowing for heat transfer by the impurity motion, β is the coefficient of specific electrical ambipolar conductivity due to ∇n , and Π is the Peltier coefficient.

To investigate the interaction of electromagnetic impotential fields ($\text{rot } \vec{E} \neq 0$) and heat and mass transfer rates it is advisable to use the system of (57) for polar vectors; if needed, the pseudovector of the magnetic field strength can be calculated from the Maxwell equation (7).

3.3. Interaction of Nonstationary Electric, Thermal, and Diffusion Fields with Allowance for Mass Transfer in a Layered Medium with the Example of an Electrochemical Cell

3.3.1. Introduction. Investigation of the interaction of electric and thermal fields with allowance for mass transfer and contact phenomena is a complex and topical problem of the theory and practice of various fields of natural science and technology.

The work seeks to construct a physicomathematical model of the interaction of nonstationary electric fields in a layered medium with allowance for nonstationary thermal phenomena and mass transfer without explicit separation of charge carriers. The media in contact are considered to be homogeneous. For the sake of clear representation, we will consider two-layer one-dimensional models.

3.3.2. Interaction of Electric and Thermal Fields. In different substances, the processes of transfer of charge and energy are interrelated. The quantity of the released heat is determined by Joule heating and by the effects of Thomson and Peltier. The problem of interaction of nonstationary thermal phenomena has been considered in [46] without taking into account the Thomson effect.

According to [45], the expressions for the conduction-current density and the energy-flux density in the absence of

an external magnetic field or in the case of its slight influence have, respectively, the form

$$\begin{aligned} I_q &= -\lambda(\alpha(T)\text{grad } T + \text{grad } \varphi), \\ I_T &= -k(T)\text{grad } T + I_q(\Pi + \varphi), \end{aligned} \quad (58)$$

where $a(T)$ is the specific thermoelectromotive force, $\Pi = \alpha T$ is the Peltier coefficient, φ is the potential, and $k(T)$ is the thermal-conductivity coefficient. We note that the problem is always nonlinear.

Having eliminated the magnetic-field strength from system (13) according to one method of [47–49], we obtain the equation for the electric-field strength

$$\frac{\varepsilon}{c^2} \frac{\partial^2 \mathbf{E}}{\partial t^2} + \mu_0 \frac{\partial \mathbf{I}_q}{\partial t} = \frac{1}{\mu} \nabla^2 \mathbf{E}. \quad (59)$$

The heat-balance equation has the form [45]

$$\begin{aligned} c_p \rho \frac{\partial T}{\partial t} &= \text{div}(k(T)\text{grad } T) \\ &+ \mathbf{I}_q \cdot (\mathbf{E} - (\alpha(T) + T\beta(T))\text{grad } T). \end{aligned} \quad (60)$$

At the interface, the following relation [50] holds:

$$\text{div } \mathbf{i} + I_{q1} - I_{q2} = -\frac{\partial \sigma}{\partial t}. \quad (61)$$

Here ε is the permittivity, $c^2 = 1/(\varepsilon_0 \cdot \mu_0)$, μ is the magnetic permeability, ε_0 is the electric constant, μ_0 is the magnetic constant, $c_p \rho$ is the product of the specific heat of the medium by its density, and $\beta(T) = \partial\alpha(T)/\partial T$.

In deriving (60), use has been made of the condition of local electroneutrality of the substance. We give a differential formulation of the problem and the method of its solution in greater detail.

Let us investigate, on the segment $[0 \leq x < l] = [0 \leq x < \xi] \cup [\xi \leq x \leq l]$, the contact of homogeneous media 1 and 2 with different electrophysical properties. The quantities ε , λ , μ , E , and φ have discontinuities of the first kind at the point of the interface $x = \xi$. We will consider the case of plane contact where the influence of surface currents can be disregarded and the thickness of the electric double-layer is much smaller than the characteristic dimension of the object. We set $E = -\text{grad } \varphi$. Equations (59) and (60) for the one-dimensional problem will take the form

$$\begin{aligned} \frac{\varepsilon}{c^2} \frac{\partial^2 E}{\partial t^2} + \mu_0 \frac{\partial}{\partial t} \left(-\lambda \left(\alpha(T) \frac{\partial T}{\partial x} - E \right) \right) &= \frac{1}{\mu} \frac{\partial^2 E}{\partial x^2}, \\ c_p \rho \frac{\partial T}{\partial t} &= \frac{\partial}{\partial x} \left(k(T) \frac{\partial T}{\partial x} \right) \\ &- \lambda \left(\alpha(T) \frac{\partial T}{\partial x} - E \right) \left(E - (\alpha(T) + T\beta(T)) \frac{\partial T}{\partial x} \right). \end{aligned} \quad (62)$$

Conditions (39) and (61) will be written, respectively, in the form

$$\varepsilon_1 \varepsilon_0 E_1|_{x=\xi-0} - \varepsilon_2 \varepsilon_0 E_2|_{x=\xi+0} = \sigma|_{x=\xi}, \quad (63)$$

$$\begin{aligned} \lambda_1 \left(E_1 - \alpha_1(T) \frac{\partial T}{\partial x} \right) \Big|_{x=\xi-0} - \lambda_2 \left(E_2 - \alpha_2(T) \frac{\partial T}{\partial x} \right) \Big|_{x=\xi+0} \\ = - \frac{\partial \sigma}{\partial t} \Big|_{x=\xi}, \end{aligned} \quad (64)$$

By differentiating (63) with respect to time and taking into account (64), at the phase boundary we obtain the condition of equality of the total currents:

$$\left[\lambda \left(E - \alpha(T) \frac{\partial T}{\partial x} \right) + \varepsilon \varepsilon_0 \frac{\partial E}{\partial t} \right] \Big|_{x=\xi} = 0. \quad (65)$$

Here and in what follows, for the arbitrary function f we adopt the notation

$$[f]|_{x=\xi} = f|_{x=\xi+0} - f|_{x=\xi-0}. \quad (66)$$

Equality (63) is a corollary of the relation $\lim_{x \rightarrow \xi \pm 0} \operatorname{div} \mathbf{D} = \rho$ [50]. Taking into consideration the finiteness of the value of the space electric charge and the continuity of it, in the one-dimensional case we obtain

$$\left[\varepsilon \varepsilon_0 \frac{\partial E}{\partial x} \right] \Big|_{x=\xi} = 0. \quad (67)$$

Relations (65) and (67) reflect the laws of conservation and continuity of electric charge [45, 50]. At the contact point, we also have the equality of the temperatures and the energy fluxes [45]:

$$[T]|_{x=\xi} = 0, \quad (68)$$

$$\left[k(T) \frac{\partial T}{\partial x} + \lambda \left(\alpha(T) \frac{\partial T}{\partial x} - E \right) (\alpha(T) T + \varphi) \right] \Big|_{x=\xi} = 0. \quad (69)$$

Thus, in the presence of the interaction of the electric and thermal fields in a layered medium, the equality of the charge fluxes (65), the equality of the charges (67) (when the conditions of quasineutrality of the contacting media beyond the electric double-layer are satisfied), the equality of the temperatures (68), and the equality of the energy fluxes must be fulfilled at the interface of the media. In the relations for the charge and energy fluxes, we take into account cross-thermoelectrical phenomena.

The process of charge of the electric field is considered on the finite time interval $[0 \leq t \leq t_0]$. The initial conditions have the form

$$T(x, 0) = T_0(x), \quad E(x, 0) = f_1(x), \quad \frac{\partial E(x, 0)}{\partial t} = f_2(x). \quad (70)$$

We give the boundary conditions, for example, for the value $x = 0$. We set the value of the total-current density to be known

$$\left(\lambda \left(\alpha(T) \frac{\partial T}{\partial x} - E \right) - \varepsilon \varepsilon_0 \frac{\partial E}{\partial t} \right) \Big|_{x=0} = j_1(t), \quad (71)$$

and take into account the heat exchange at the boundary using the Newton relation

$$\begin{aligned} \left(k(T) \frac{\partial T}{\partial x} + \lambda \left(\alpha(T) \frac{\partial T}{\partial x} - E \right) (\alpha(T) T + \varphi) \right) \Big|_{x=0} \\ = \gamma_1 (T - T^*) \Big|_{x=0}, \end{aligned} \quad (72)$$

where γ_1 is the coefficient of heat exchange and T^* is the ambient temperature.

We consider the analogous relations at the right-hand boundary.

3.3.3. Interaction of Electric and Thermal Fields with Allowance for Mass Transfer. Let us consider the nonstationary model of heat and mass transfer for electrochemical systems with the example of electrolysis. For this problem, an electric double-layer occurs at the site of contact of the electrolyte with the metallic anode and cathode. Let us set the density of the space charge beyond the electric double-layer of the metal-electrolyte contact to be zero at the initial instant and hence, according to [51], remain constant in the future while the voltage drop in the electrodes and leads is small. The influence of the electrodes on the temperature field of the electrolyte will be taken into account in terms of the coefficient of heat exchange.

Two approaches to modeling of diffusion-electrical phenomena have currently been developed, each of which has certain disadvantages and advantages. The first approach [37, 38, 42] is characterized by consideration of the flows of ions of the corresponding sort in a completely or partially dissociated electrolyte. The equations derived contain many parameters, the reliable procedure of determination of which is absent in the majority of cases. Furthermore, the proposed theory fails to provide for taking into account the interaction of the cations and the anions of the dissolved substance with each other and with the molecules of the solvent. It must also be borne in mind that, apart from the dissociation reaction, we have the association of simple molecules which in turn are dissociated into complex and simple ions. It is difficult to determine the diffusion coefficients of complex ions; it is also difficult to take into account the force interaction of complex cations and anions with each other and with the external electric field. The difficulties in question become more serious when a multicomponent electrolyte is described. We note that such difficulties also arise in modeling, for example, certain problems of plasma physics.

The second approach [52–56] fails to provide for the introduction and determination of the coefficients of molecular diffusion of cations and anions and the degree of dissociation of the electrolyte. It is based on the interaction of the mass and charge fluxes. The ionic flows are not determined. The model is formulated without explicit separation of the charge carriers and the charge of an electric double layer.

The system of equations describing the electrodynamic processes in the electrolyte is as follows:

$$\begin{aligned}\frac{\varepsilon}{c^2} \frac{\partial^2 \mathbf{E}}{\partial t^2} + \mu_0 \frac{\partial \mathbf{I}_q}{\partial t} &= \frac{1}{\mu} \nabla^2 \mathbf{E}, \\ \frac{\partial n}{\partial t} &= -\operatorname{div}(\mathbf{I}_m), \\ c_0 \rho_0 \frac{\partial T}{\partial t} &= -\operatorname{div}(\mathbf{I}_T).\end{aligned}\quad (73)$$

Here \mathbf{I}_q , \mathbf{I}_m , and \mathbf{I}_T are the densities of the conduction current and of the mass and heat fluxes which (in the case of the nonequilibrium state of the medium) have, respectively, the form (57) [45], where D_M is the molecular diffusion coefficient, D_A^* is the ambipolar diffusion coefficient, D_T is the thermal diffusion coefficient, D_T^* is the coefficient taking into account the transfer of heat due to the motion of the impurity, and n is the concentration of the impurity.

We give the initial

$$\begin{aligned}E(x, 0) &= E_0(x), & \frac{\partial E(x, 0)}{\partial t} &= \tilde{E}(x), \\ T(x, 0) &= T_0(x), & n(x, 0) &= n_0(x),\end{aligned}\quad (74)$$

and boundary conditions (anode-electrolyte, $x = 0$):

$$\begin{aligned}\mathbf{I}_q &= \lambda \left(\lambda_A^* \frac{\partial n}{\partial x} - E \right) + \lambda \alpha(T) \frac{\partial T}{\partial x} - \varepsilon \varepsilon_0 \frac{\partial E}{\partial t}, \\ \gamma_1(T - T^*) &= k \frac{\partial T}{\partial x} - I_q(\Pi + \varphi) + D_T^* \frac{\partial n}{\partial x}, \\ k_a I_q(t) &= D_M \frac{\partial n}{\partial x} - D_A^* \lambda E + D_T \frac{\partial T}{\partial x},\end{aligned}\quad (75)$$

in modeling the one-dimensional problem in the region $G = [0 \leq x \leq l] \times [0 \leq t \leq T]$. Here k_a is the electrochemical equivalent of a substance which deposits at the anode. The analogous conditions hold for $x = l$ as well.

The constructed system of differential equations makes it possible to model the processes of transfer in the electrochemical system with allowance for the influence of an electric double-layer; this influence directly determines the thermoelectrical and ambipolar electrodiffusion phenomena at the boundary of the metal-electrolyte contact.

3.3.4. Numerical Modeling of Electrochemical Systems. Heating of an Electrochemical Cell in the Case of Constant-Current and Pulse Electrolysis. In electrochemical systems, the electrodes are metals as a rule. The electrical conductivity of metals is hundreds of times higher than the specific electrical conductivity of electrolytes; therefore, one can disregard the voltage drop in electrodes and leads. In highly conductive metals, one can also disregard the displacement currents and the coefficients of ambipolar diffusion and thermal diffusion and restrict oneself to consideration of the system of equations (73)–(75) just in the electrolyte itself.

Let us consider the process of heating of an electrochemical medium in the case of passage of an electric current with density $I_q(t)$ through a solution of copper sulfate $\text{CuSO}_4 \cdot 5\text{H}_2\text{O}$. We use copper (99.78%) as the anode.

The copper from the solution is deposited at the cathode. We set the current efficiencies for the copper equal to 100% and the electrochemical equivalent k_e equal to $0.6588 \cdot 10^{-6}$ kg/C. The dependence of the specific electrical conductivity $\lambda(n)$ of the copper-plating electrolyte on the concentration of the copper sulfate in water is given in [57]; the dependence of λ and k on the temperature will be considered to be insignificant. In the calculations for CuSO_4 , we set $D_M = 5 \cdot 10^{-10}$ m²/sec, $D_A^* = 10^{-11}$ λ, $\lambda_A^* = 10^{-4}$ λ, $\varepsilon = 70$, and $\mu = 1$ and disregard the effects of thermal diffusion. The distance between the cathode and the anode is $L = 0.05$ m. The heat capacity, the density, and the thermal-conductivity coefficient of the electrolyte are taken to be $4.2 \cdot 10^3$ J/(kg·K), 10^3 kg/m³, and 0.6 V/(m·K) respectively. We note that the regimes of pulse action have been considered in [58] as applied to the processes of electrodeposition of alloys. This investigation has been carried out on the basis of a separate description of the transport of ions and the employment of the Kirchhoff law for quasistationary currents in a cell. With such an approach, the displacement currents are taken into account indirectly through introduction of the capacitive current of the electrode and determination of the experimental dependence of the polarization capacitance of the electrode on the character of the pulse action. In [58], it has been noted that neglect of the capacitive current in pulse electrolysis involves significant errors. The employment of system (73)–(75) to model the process of copper plating makes it possible to consider the problems without introducing the concepts of inductance and capacitance. The obtained nonlinear system of equations is solved by the finite-difference method analogously to [54].

We have modeled numerically the process of copper plating for a constant current and a pulse current (Figure 16). The density of the constant current was equal to 300 A/m². The maximum density of the pulse current was also 300 A/m², while the period of traversal of the current and the break were equal to 0.01 sec.

Figure 16 gives the results of modeling the distributions of the concentration of CuSO_4 and the temperature for different regimes of electrolysis. The measurements were carried out within 60 sec after switching on the current. It is seen from the figure that the concentration gradients near the cathode surface ($x = 1$) are different and depend on the regime of copper plating. In the case of nonstationary action they are substantially smaller than in the case of electrolysis in the regime of constant current. As has been shown in [58], this tendency also holds in the case where one and the same total charge passes through the electrochemical cell.

The analysis of the temperature field (Figure 16(b)) shows that the temperatures of the electrolyte in the vicinity of the anode and the cathode differ significantly. Nonsymmetric heating of the electrochemical cell attributed to the am-bipolar diffusion and electrical ambipolar conductivity occurs. The modeling results are in agreement with the data of [59].

With the aim of measuring the temperature in the surface layer of the electrolyte solution near the cathode and comparing the results to the calculated data, we developed and manufactured an experimental setup. Copper anode and

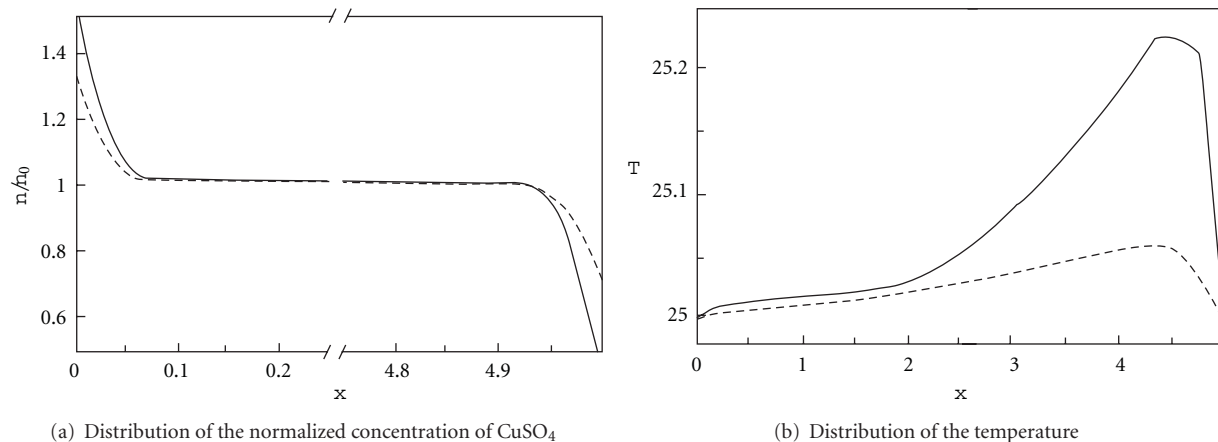


FIGURE 16: Distribution of the normalized concentration of CuSO_4 and the temperature in an electrochemical cell within 60 sec after switching on the current. The solid curve, at constant current; the dashed curve, at pulse current. T , $^{\circ}\text{C}$; x , mm.

cathode were placed in an electroplating bath with a sulfuric-acid copper-plating electrolyte. In the 1 mm thick cathode, a hole was made into which we placed a temperature-sensitive element. As the latter we employed a thermal resistor. The current strength in the bath was prescribed by a variable resistor.

Figure 17 gives the results of numerical modeling and the experimental data on heating of the cathode region in relation to the regime of current. It is seen that the increase in the density of the current (both constant and pulse) causes the temperature near the cathode surface to increase. In the anode, no increase in the temperature was observed either in the calculations or in the experiment, which is in agreement with the data of [59]. The surface temperature obtained in solving (73)–(75) in the regime of constant current is 10–15% higher than the temperature recorded in the experiments.

A more complicated situation occurs when we compare the experimental data and the results of numerical modeling in the regime of pulse electrolysis. The results of the experiments demonstrate that in the regime of pulse current the temperature of the electrolyte in the cathode region increases more than in the regime of constant current. At the same time, the numerical calculations of the pulse electrolysis show that the heating of the cathode region here is smaller than for the regime of constant current. The difference is, apparently, attributed to concentration convection [60], whose influence is substantial for high densities of the current for pulse electrolysis.

In a longer term, one must take into account natural and concentration convection and heat exchange with the ambient medium. Nonetheless, despite the errors in determination of the coefficients and the assumptions made in the model, the calculation results are in qualitative agreement with the experimental data, which makes it possible, in certain cases, to use the proposed approach for modeling of nonstationary processes.

Results were published in part [52, 53, 55, 56, 61].

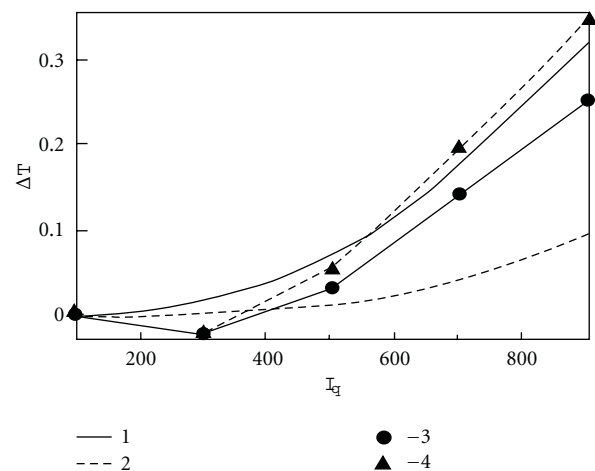


FIGURE 17: Heating of the electrolyte in the cathode region as a function of the value and kind of polarizing current: (1) constant current; (2) pulse current; (3, 4) corresponding experimental data. ΔT , $^{\circ}\text{C}$; I_q , A/m^2 .

4. Interaction of Nonstationary Electric and Thermal Fields with Allowance for Relaxation Processes

We investigate electric and thermal fields created by macroscopic charges and currents in continuous media. Of practical interest is modeling of local heat releases in media on exposure to a high-frequency electromagnetic field. We should take into account the influence of the energy absorption on the propagation of an electromagnetic wave, since the transfer processes are interrelated.

In an oscillatory circuit with continuously distributed parameters, the energy dissipation is linked [62] to the dielectric loss due to the dependence of the relative permittivity $\epsilon(\omega)$ on frequency. In the general case ϵ is also complex,

and the relationship between the electric displacement and electric field vectors has the form $D = \varepsilon(\omega)E$, where $\varepsilon(\omega) = \varepsilon'(\omega) - i\varepsilon''(\omega)$; here, ε' and ε'' are determined experimentally. As of now, the problems of dielectric heating of a continuous medium are reduced in many cases to consideration of an equivalent circuit based on lumped parameters, such as capacitance, inductance, loss angle, and relative-dielectric-loss factor [63, 64], that are established experimentally.

With this approach, there arise substantial difficulties in determining the temperature field of equivalent circuits. Also, we have polarization and the occurrence of an electric double-layer of a prescribed electric moment in contact of media with different properties. Equivalent circuits in lamellar media additionally involve empirical lumped parameters: surface capacitance and surface resistance [65]. The total current can always be separated into a dissipative or conduction current which is in phase with the applied voltage and a displacement current shifted in time relative to the voltage. The exact physical meaning of these components of the current is largely dependent on selection of an equivalent electric circuit. A unique equivalent circuit—series or parallel connection of the capacitor, the resistor, and the inductor—does not exist; it is determined by a more or less adequate agreement with experimental data.

In the case of electrolytic capacitors, the role of one plate is played by the electric double-layer with a specific resistance much higher than the resistance of metallic plates. Therefore, decrease in the capacitance with frequency is observed, for such capacitors, even in the acoustic-frequency range [65]. Circuits equivalent to an electrolytic capacitor are very bulky: up to 12 R , L , and C elements can be counted in them; therefore, it is difficult to obtain a true value of, for example, the electrolyte capacitance. In [65] experimental methods of measurement of the dielectric properties of electrolyte solutions at different frequencies are given and ε' and ε'' are determined. The frequency dependence of dispersion and absorption are essentially different consequences of one phenomenon: “dielectric-polarization inertia” [65]. In actual fact, the dependence $\varepsilon(\omega)$ is attributable to the presence of the resistance of the electric double-layer and to the electrochemical cell in the electrolytic capacitor being a system with continuously distributed parameters, in which the signal velocity is a finite quantity.

Actually, ε' and ε'' are certain integral characteristics of a material at a prescribed constant temperature, which are determined by the geometry of the sample and the properties of the electric double-layer. It is common knowledge that in the case of a field arbitrarily dependent on time any reliable calculation of the absorbed energy in terms of $\varepsilon(\omega)$ turns out to be impossible [45]. This can only be done for a specific dependence of the field E on time. For a quasimonochromatic field, we have [45]

$$\begin{aligned} \mathbf{E}(t) &= \frac{1}{2} [\mathbf{E}_0(t)e^{-i\omega t} + \mathbf{E}_0^*(t)e^{i\omega t}], \\ \mathbf{H}(t) &= \frac{1}{2} [\mathbf{H}_0(t)e^{-i\omega t} + \mathbf{H}_0^*(t)e^{i\omega t}]. \end{aligned} \quad (76)$$

The values of $\mathbf{E}_0(t)$ and $\mathbf{H}_0(t)$, according to [66], must very slowly vary over the period $T = 2\pi/\omega$. Then, for absorbed

energy, on averaging over the frequency ω , we obtain the expression [66]:

$$\begin{aligned} \frac{\partial \mathbf{D}(t)}{\partial t} \cdot \mathbf{E}(t) &= \frac{1}{4} \frac{d(\omega\varepsilon'(\omega))}{d\omega} \frac{\partial}{\partial t} [\mathbf{E}_0(t)\mathbf{E}_0^*(t)] \\ &+ \frac{\omega\varepsilon''}{2} \mathbf{E}_0(t)\mathbf{E}_0^*(t) \\ &+ i \frac{d(\omega\varepsilon''(\omega))}{4d\omega} \left(\frac{\partial \mathbf{E}_0(t)}{\partial t} \mathbf{E}_0^*(t) - \frac{\mathbf{E}_0^*(t)}{\partial t} \mathbf{E}_0(t) \right), \end{aligned} \quad (77)$$

where the derivatives with respect to frequency are taken at the carrier frequency ω . We note that for an arbitrary function $\mathbf{E}(t)$, it is difficult to represent it in the form

$$E(t) = a(t) \cos \varphi(t), \quad (78)$$

since we cannot unambiguously indicate the amplitude $a(t)$ and the phase $\varphi(t)$. The manner in which $E(t)$ is decomposed into factors a and $\cos \varphi$ is not clear. Even greater difficulties appear in the case of going to the complex representation $W(t) = U(t) + iV(t)$ when the real oscillation $E(t)$ is supplemented with the imaginary part $V(t)$. The arising problems have been considered in [67] in detail. In the indicated work, it has been emphasized that certain methods using a complex representation and claiming higher-than-average accuracy become trivial without an unambiguous determination of the amplitude, phase, and frequency.

Summing up the aforesaid, we can state that calculation of the dielectric loss is mainly empirical in character. Construction of the equivalent circuit and allowance for the influence of the electric double-layer and for the dependence of electrophysical properties on the field's frequency are only true of the conditions under which they have been modeled; therefore, these are fundamental difficulties in modeling the propagation and absorption of electromagnetic energy.

As we believe, the release of heat in media on exposure to nonstationary electric fields can be calculated on the basis of allowance for the interaction of electromagnetic and thermal fields as a system with continuously distributed parameters from the field equation and the energy equation which take account of the distinctive features of the boundary between adjacent media. When the electric field interacting with a material medium is considered we use Maxwell equations (6)-(7). We assume that space charges are absent from the continuous medium at the initial instant of time and they do not appear throughout the process. The energy equation will be represented in the form

$$\rho C_p \frac{dT}{dt} = \text{div}[k(T)\text{grad}(T)] + Q, \quad (79)$$

where Q is the dissipation of electromagnetic energy.

According to [68], the electromagnetic energy converted to heat is determined by the expression

$$Q = \rho \left[\mathbf{E} \frac{d}{dt} \left(\frac{\mathbf{D}}{\rho} \right) + H \frac{d}{dt} \left(\frac{\mathbf{B}}{\rho} \right) \right] + \mathbf{J}_q \cdot \mathbf{E}. \quad (80)$$

In deriving this formula, we used the nonrelativistic approximation of Minkowski's theory. If ε , μ , and $\rho = \text{const}$, there is

no heat release; therefore, the intrinsic dielectric loss is linked to the introduction of $\varepsilon'(\omega)$ and $\varepsilon''(\omega)$. The quantity Q is affected by the change in the density of the substance $\rho(T)$.

A characteristic feature of high frequencies is the lag of the polarization field behind the charge in the electric field in time. Therefore, the electric-polarization vector is expediently determined by solution of the equation $\mathbf{P}(t + \tau_e) = (\varepsilon - 1)\varepsilon_0\mathbf{E}(t)$ with allowance for the time of electric relaxation of dipoles τ_e . Restricting ourselves to the first term of the expansion $\mathbf{P}(t + \tau_e)$ in a Taylor series, from this equation, we obtain

$$\mathbf{P}(t) + \tau_e \frac{d\mathbf{P}(t)}{dt} = (\varepsilon - 1)\varepsilon_0\mathbf{E}(t). \quad (81)$$

The solution (81), on condition that $\mathbf{P} = 0$ at the initial instant of time, will take the form

$$\mathbf{P} = \frac{(\varepsilon - 1)\varepsilon_0}{\tau_e} \int_0^t \mathbf{E}(\tau) e^{-(t-\tau)/\tau_e} d\tau. \quad (82)$$

It is noteworthy that (81) is based on the classical Debye model. According to this model, particles of a substance possess a constant electric dipole moment. The indicated polarization mechanism involves partial arrangement of dipoles along the electric field, which is opposed by the process of disorientation of dipoles because of thermal collisions. The restoring “force”, in accordance with (81), does not lead to oscillations of electric polarization. It acts as if constant electric dipoles possessed strong damping.

Molecules of many liquids and solids possess the Debye relaxation polarizability. Initially polarization aggregates of Debye oscillators turn back to the equilibrium state $\mathbf{P}(t) = \mathbf{P}(0) \exp(-t/\tau_e)$.

A dielectric is characterized, as a rule, by a large set of relaxation times with a characteristic distribution function, since the potential barrier limiting the motion of weakly coupled ions may have different values [63]; therefore, the mean relaxation time of the ensemble of interacting dipoles should be meant by τ_e in (81).

To eliminate the influence of initial conditions and transient processes we set $t_0 = -\infty$, $\mathbf{E}(\infty) = 0$, $\mathbf{H}(\infty) = 0$, as it is usually done. If the boundary regime acts for a fairly long time, the influence of initial data becomes weaker with time owing to the friction inherent in every real physical system. Thus, we naturally arrive at the problem without the initial conditions:

$$\mathbf{P} = \frac{(\varepsilon - 1)\varepsilon_0}{\tau_e} \int_{-\infty}^t \mathbf{E}(\tau) e^{-(t-\tau)/\tau_e} d\tau. \quad (83)$$

Let us consider the case of the harmonic field $\mathbf{E} = \mathbf{E}_0 \sin \omega t$; then, using (83) we have, for the electric induction vector

$$\begin{aligned} \mathbf{D} &= \varepsilon_0\mathbf{E} + \mathbf{P} = \frac{(\varepsilon - 1)\varepsilon_0}{\tau_e} \int_{-\infty}^t \mathbf{E}(\tau) e^{-(t-\tau)/\tau_e} d\tau + \varepsilon_0\mathbf{E}_0 \sin \omega t \\ &= \frac{\varepsilon_0(\varepsilon - 1)\varepsilon_0}{1 + \omega^2\tau_e^2} (\sin \omega t - \omega\tau_e \cos \omega t) \\ &\quad + \varepsilon_0\mathbf{E}_0 \sin \omega t. \end{aligned} \quad (84)$$

The electric induction vector is essentially the sum of two absolutely different physical quantities: the field strength and the polarization of a unit volume of the medium.

If the change in the density of the substance is small, we obtain, from formula (80), for the local instantaneous heat release

$$\mathbf{Q} = \mathbf{E} \frac{d\mathbf{D}}{dt} = \frac{E_0^2(\varepsilon - 1)\varepsilon_0}{1 + \omega^2\tau_e^2} (\omega \sin \omega t \cos \omega t + \omega^2\tau_e \sin^2 \omega t), \quad (85)$$

when we write the mean value of Q over the total period T :

$$\mathbf{Q} = \frac{1}{2} \frac{E_0^2(\varepsilon - 1)\varepsilon_0}{1 + \omega^2\tau_e^2} \omega^2\tau_e + \frac{\lambda E^2}{2}. \quad (86)$$

For high frequencies ($\omega \rightarrow \infty$), heat release ceases to be dependent on frequency, which is consistent with formula (86) and experiment [63].

When the relaxation equation for the electric field is used we must also take account of the delay of the magnetic field, when the magnetic polarization lags behind the change in the strength of the external magnetic field:

$$\mathbf{I}(t) + \tau_i \frac{d\mathbf{I}(t)}{dt} = \mu\mu_0\mathbf{H}(t). \quad (87)$$

Formula (86) is well known in the literature; it has been obtained by us without introducing complex parameters. In the case of “strong” heating of a material where the electrophysical properties of the material are dependent on temperature expression (81) will have a more complicated form and the expression for Q can only be computed by numerical methods. Furthermore, in the presence of strong field discontinuities, we cannot in principle obtain the expression for Q because of the absence of closing relations for the induced surface charge and the surface current on the boundaries of adjacent media; therefore, the issue of energy relations in macroscopic electrodynamics is difficult, particularly, with allowance for absorption.

Energy relations in a dispersive medium have repeatedly been considered; nonetheless, in the presence of absorption, the issue seems not clearly understood (or at least not sufficiently known), particularly in the determination of the expression of released heat on the boundaries of adjacent media.

Indeed, it is known from the thermodynamics of dielectrics that the differential of the free energy F has the form

$$dF = -SdT - PdV + EdD. \quad (88)$$

If the relative permittivity and the temperature and volume of the dielectric are constant quantities, from (88) we have

$$F(T, D) = F_0 + \varepsilon\varepsilon_0 \frac{E^2}{2}, \quad (89)$$

where F_0 is the free energy of the dielectrics in the absence of the field.

The change of the internal energy of the dielectrics during its polarization at constant temperature and volume can

be found from the Gibbs-Helmholtz equation. Disregarding F_0 which is independent of the field strength, we can obtain

$$U(T, D) = F(T, D) - T \left(\frac{dF}{dT} \right)_D. \quad (90)$$

If the relative dielectric constant is dependent on temperature ($\varepsilon(T)$), we obtain

$$U(T, D) = \frac{\varepsilon_0 E^2}{2} + \left(\varepsilon + T \left(\frac{d\varepsilon}{dT} \right)_D \right). \quad (91)$$

Expression (91) determines the change in the internal energy of the dielectric in its isothermal polarization but with allowance for the energy transfer to a thermostat, if the polarization causes the dielectric temperature to change. In the works on microwave heating, that we know, (91) is not used.

A characteristic feature of high frequencies is that the polarization field lags behind the change in the external field in time; therefore, the polarization vector is expediently determined by solution of the equation:

$$\mathbf{P}(t + \tau_e) = \left(\varepsilon - 1 + T \left(\frac{d\varepsilon}{dT} \right)_D \right) \varepsilon_0 \mathbf{E}(t). \quad (92)$$

With allowance for the relaxation time, that is, restricting ourselves to the first term of the expansion $\mathbf{P}(t + \tau_e)$ in a Taylor series, we obtain

$$\mathbf{P}(t) + \tau_e \frac{d\mathbf{P}(t)}{dt} = \left(\varepsilon - 1 + T \left(\frac{d\varepsilon}{dT} \right)_D \right) \varepsilon_0 \mathbf{E}(t). \quad (93)$$

In the existing works on microwave heating with the use of complex parameters, they disregard the dependence $\varepsilon''(T)$. In [69], consideration has been given to the incidence of a one-dimensional wave from a medium with arbitrary complex parameters on one or two boundaries of media whose parameters are also arbitrary. The amplitudes of waves reflected from and transmitted by each boundary have been found. The reflection, transmission, and absorption coefficients have been obtained from the wave amplitudes. The well-known proposition that a traditional selection of determinations of the reflection, transmission, and absorption coefficients from energies (reflectivity, transmissivity, and absorptivity) in the case of complex parameters of media comes into conflict with the law of conservation of energy has been confirmed and exemplified. The necessity of allowing for $\varepsilon''(T)$ still further complicates the problem of computation of the dissipation of electromagnetic energy in propagation of waves through the boundaries of media with complex parameters.

The proposed method of computation of local heat release is free of the indicated drawbacks and makes it possible, for the first time, to construct a consistent model of propagation of nonmonochromatic waves in a heterogeneous medium with allowance for frequency dispersion without introducing complex parameters.

In closing, we note that a monochromatic wave is infinite in space and time, has infinitesimal energy absorption in a material medium, and transfers infinitesimal energy, which

is the idealization of real processes. However with these stringent constraints, too, the problem of propagation of waves through the boundary is open and far from being resolved even when the complex parameters of the medium are introduced and used. In reality, the boundary between adjacent media is not infinitely thin and has finite dimensions of the electric double-layers; therefore, approaches based on through-counting schemes for a hyperbolic equation without explicit separation of the boundary between adjacent media are promising.

5. Ponderomotive Forces in Heterogeneous Lamellar Media with Absorption

It is common knowledge that the electric field strength \mathbf{E} is equal to the ponderomotive mechanical force per unit charge acting at a given point of the field on a test charge (charged body). The issue of the force acting on induced surface charges on the boundaries remains to be solved, since there are no closing equations for σ and the charge is not determined on the interface itself. According to [45], the tension tensor of ponderomotive forces for media with dispersion and absorption due to the dipole relaxation cannot be found in general form in a macroscopic manner at all. As we believe, solution of this problem lies in computing the induced surface charge on the boundaries and the resultants of all tensions applied externally to the surface without the necessity of reducing bulk ponderomotive forces to tensions. The reduction of bulk forces to tensions is not necessarily possible; therefore, this issue will be considered in greater detail.

5.1. Reduction of Bulk Ponderomotive Forces to Tensions. If \mathbf{f} is the bulk density of ponderomotive forces, the resultant of all forces applied to the bodies within the volume V is

$$\mathbf{F} = \int_V \mathbf{f} dV. \quad (94)$$

On the other hand, if bulk forces can be reduced to tensions at all, the set of tensions acting externally of a closed surface S must be equal to the same quantity. We denote by T_n a force acting externally per unit surface the external normal to which is directed along \mathbf{n} ; the components of this force along the coordinate axes are T_{xn} , T_{yn} and T_{zn} . Then the resultant of all tensions applied externally to the surface will be

$$\mathbf{F} = \oint_S \mathbf{T}_n dS. \quad (95)$$

Using the Ostrogradsky-Gauss theorem and equating (94) and (95), we obtain

$$\begin{aligned} f_x &= \frac{\partial T_{xx}}{\partial x} + \frac{\partial T_{xy}}{\partial y} + \frac{\partial T_{xz}}{\partial z}, \\ f_y &= \frac{\partial T_{yx}}{\partial x} + \frac{\partial T_{yy}}{\partial y} + \frac{\partial T_{yz}}{\partial z}, \\ f_z &= \frac{\partial T_{zx}}{\partial x} + \frac{\partial T_{zy}}{\partial y} + \frac{\partial T_{zz}}{\partial z}. \end{aligned} \quad (96)$$

For the bulk forces and tensions to be equivalent, it is necessary that not only the resultant of forces applied to an arbitrary volume remains constant but the moment of these forces be invariant as well [70]. This circumstance imposes an additional constraint on the tension-tensor components. The moment of bulk forces applied to an arbitrary volume V is

$$\mathbf{N} = \int_V [\mathbf{R}\mathbf{f}]dV, \quad (97)$$

where \mathbf{R} is the distance from point O for which the moment of forces is determined to the element dV . Consequently, the component N_x must satisfy relation (97):

$$\begin{aligned} N_x &= \int_V (yf_z - zf_y)dV \\ &= \oint_S (yT_{zn} - zT_{yn})dS + \int_V (T_{yz} - T_{zy})dV. \end{aligned} \quad (98)$$

The surface integral on the right is equal to the moment of tension forces T_n applied to the surface S of volume V . The moment of these tension forces will be equal to the moment of bulk forces only in the case where the last integral on the right is equal to zero. In view of the arbitrariness of the volume V , this will occur only when the integrand

$$T_{yz} = T_{zy} \quad (99)$$

is equal to zero.

By repeating the same considerations for N_y and N_z , we obtain $T_{zx} = T_{xz}$, $T_{xy} = T_{yx}$. Consequently, for the bulk forces and surface ponderomotive forces to be equivalent, the tension tensor must be symmetric. In anisotropic media, the tension tensor is asymmetric; therefore, direct computation of the resultant of forces in terms of tensions from formula (95) is expedient. We note that Maxwell was the first to reduce the field's ponderomotive forces to tensions. Replacement of ponderomotive forces by an equivalent system of tensions makes it much easier to determine forces applied to the volume of the electric field.

The force applied to a charged layer, given the uncompensated surface charge, has the form

$$F_{ij}^S = \sigma(E_{ij}^1 - E_{ij}^2). \quad (100)$$

If the layer is not charged, we have $\sigma = 0$ and $F_{ij}^S = 0$. The resultant force applied to the boundary of a cell is

$$\mathbf{F} = \oint \mathbf{F}_{ij}dS. \quad (101)$$

The projections of f_x , f_y , and f_z are determined according to (96), and in a variable electromagnetic field, we must take into account that f_x , f_y , and f_z are expended in changing the density of the momentum flux of the substance and the

electromagnetic field alike. If the forces acting only on the substance are meant by \tilde{f}_x , \tilde{f}_y , \tilde{f}_z , according to [70], we have

$$\begin{aligned} \tilde{f}_x &= f_x - (\epsilon\mu - 1) \frac{\partial}{\partial t} [\mathbf{E} \bar{\mathbf{H}}]_x, \\ \tilde{f}_y &= f_y - (\epsilon\mu - 1) \frac{\partial}{\partial t} [\mathbf{E} \bar{\mathbf{H}}]_y, \\ \tilde{f}_z &= f_z - (\epsilon\mu - 1) \frac{\partial}{\partial t} [\mathbf{E} \bar{\mathbf{H}}]_z. \end{aligned} \quad (102)$$

The expression $(\epsilon\mu - 1)(\partial/\partial t)[\mathbf{E} \bar{\mathbf{H}}]$ is known to be called the Abraham force [70].

If the medium is heterogeneous and the transmission of the electromagnetic wave involves its absorption and heating, we propose the following scheme of calculating ponderomotive forces:

- (1) the domain under study is subdivided into N cells with constant properties;
- (2) by the method presented in Para 1 and Para 2, we compute the surface charge σ and the surface ponderomotive force for each cell.

In this approach, we disregard the influence of striction forces and tensions acting only on the force distribution over the body's volume but exerting no influence on the value of the resultant of all forces and on their moment [70]. Allowance for ponderomotive forces is important, for example, for biomechanics problems.

The history of the problem of ponderomotive forces developed into a paradoxical situation where the issues of certain basic propositions of classical electrodynamics have been discussed to date [66].

6. Conclusion

The consistent physicomathematical model of propagation of an electromagnetic wave in a heterogeneous medium has been constructed using the generalized wave equation and the Dirichlet theorem. Twelve conditions at the interfaces of adjacent media were obtained and justified without using a surface charge and surface current in explicit form. The conditions are fulfilled automatically in each section of the heterogeneous medium and are conjugate, which made it possible to use through-counting schemes for calculations. For the first time the effect of concentration of "medium-frequency" waves with a length of the order of hundreds of meters at the fractures and wedges of domains of size 1–3 μm has been established. Numerical calculations of the total electromagnetic energy on the wedges of domains were obtained. It is shown that the energy density in the region of wedges is maximum and in some cases may exert an influence on the motion, sinks, and the source of dislocations and vacancies and, in the final run, improve the near-surface layer of glass due to the "micromagnetoplastic" effect.

The results of these calculations are of special importance for medicine, in particular, when microwaves are used in the therapy of various diseases. For a small, on the

average, permissible level of electromagnetic irradiation, the concentration of electromagnetic energy in internal angular structures of a human body (cells, membranes, neurons, interlacements of vessels, etc.) is possible.

For the first time, we have constructed a consistent physicomathematical model of interaction of nonstationary electric and thermal fields in a layered medium with allowance for mass transfer. The model is based on the methods of thermodynamics and on the equations of an electromagnetic field and is formulated without explicit separation of the charge carriers and the charge of an electric double-layer. We have obtained the relations for the electric-field strength and the temperature, which take into account the equality of the total currents and the energy fluxes, to describe the electric and thermal phenomena in layered media where the thickness of the electric double-layer is small compared to the dimensions of the object under study.

We have modeled numerically the heating of an electrochemical cell with allowance for the influence of the electric double-layer at the metal-electrolyte interface. The calculation results are in satisfactory agreement with experimental data.

Notation

\vec{B} :	Axial vector of magnetic induction, Wb/m ²
D :	Electric displacement, C/m ²
D_M :	Molecular diffusion coefficient, m ² /sec
D_i :	Diffusion coefficients of anions and cations, m ² /sec
D_A :	Ambipolar diffusion coefficient, A/(m·kg)
D_A^* :	Ambipolar diffusion coefficient, kg/(A·sec)
E :	Electric field strength, V/m
F :	Free energy of the unit volume of a dielectric, J/m ³
F :	Faraday's constant, 96.985 C/eq.
F_0 :	Free energy of a dielectric in the absence of a field, J/m ³
J :	Current density, A/m ²
\vec{H} :	Magnetic field strength, A/m
h :	Thickness of the electric double-layer, m
I_q, I_q :	Normal components of the conduction current in media 1 and 2, C/(m ² ·sec)
i_r :	Surface current, A/m
i, j, k :	Unit vectors of the orthonormalized basis
j_{tot} :	Total current, A/m
L :	Length, m
l :	Average distance between ferroparticles, m

n :	Unit vector normal to the interface
n :	Concentration, kg/m ³
n_A :	Concentration of neutral molecules, kg/m ³
n_i :	Concentration of dissociated molecules, kg/m ³
n_m :	Molar concentration, g·eq./liter
R :	Universal gas constant
R :	Resistance, $\Omega \cdot m$
P :	Pressure, Pa
q :	Mass flux, kg/(m ² ·sec)
r :	Radius of a particle, μm
S :	Interface between adjacent media
T :	Temperature, °C
t :	Time, sec
V :	Volume, m ³
v :	Velocity of the slip of a ferroparticle over the treated surface, m/sec
U :	Voltage, V
W :	Magnetic field density, J/m ³
x, y, z :	Cartesian coordinates;
β :	Equilibrium constant
α :	Degree of dissociation
ϵ :	Relative permittivity
ϵ_0 :	Electric constant equal to $8.58 \cdot 10^{-12}$ F/m
φ :	Electric potential, V
k :	Boltzmann constant;
λ :	Electrical conductivity, $\Omega \cdot m$
k_e :	Electrochemical equivalent of copper, kg/C
$\lambda_A^*(n)$:	Coefficient of specific electrical ambipolar conductivity, V·m ³ /kg
$\bar{\lambda}$:	Average value of electrical conductivity, $\Omega \cdot m$
μ :	Relative permeability
μ_0 :	Magnetic constant equal to $4\pi \cdot 10^{-7}$ gf/m
μ_e :	Chemical potential
ξ :	Discontinuity point
ρ :	Specific electric charge, C/m ²
ρ_R :	Conductance
σ :	Surface density of a charge, C/m ²
ω :	Angular frequency, 1/sec
$\nabla \equiv \frac{\partial}{\partial x} + \frac{\partial}{\partial y} + \frac{\partial}{\partial z}$:	Symbolic operator
$[f] _{x=\xi} = f_1 _{x=\xi+0} - f_2 _{x=\xi-0}$:	Subscripts: 0, constant component of a magnetic field H
1:	First medium
2:	Second medium
n :	Normal

q :	Charge
m :	Impurity mass
a :	Anode
A :	Ambipolar
M :	Molecular
e :	Equivalent
c :	Concentration
i :	Number of the grid node
j :	Component
max:	Maximum
n, τ :	Directions normal and tangential to the interface
x :	Normal component of a vector
y, z :	Tangential components of a vector at the interface between adjacent media
tot:	Total.

Acknowledgments

The authors express their gratitude to Corresponding Member of the National Academy of Sciences of Belarus N.V. Pavlyukevich, Corresponding Member of the National Academy of Sciences of Belarus Professor V.I. Korzyuk for a useful discussion of the work. This work was carried out with financial support from the Belarusian Republic Foundation for Basic Research and from the Science Support Foundation of Poland "Kassa im. Myanowski" (2005).

References

- [1] I. Monzon, T. Yonte, and L. Sanchez-Soto, "Characterizing the reflectance of periodic lasered media," *Characterizing the reflectance of periodic lasered media*, vol. 218, pp. 43–47, 2003.
- [2] Y. Eremin and T. Wriedt, "Large dielectric non-spherical particle in an evanescent wave field near a plane surface," *Optics Communications*, vol. 214, no. 1–6, pp. 39–45, 2003.
- [3] W. Hu and H. Guo, "Ultrashort pulsed Bessel beams and spatially induced group-velocity dispersio," *Journal of the Optical Society of America A*, vol. 19, no. 1, pp. 49–52, 2002.
- [4] D. Danae, P. Bienstman, R. Bockstaele, and R. Baets, "Rigorous electromagnetic analysis of dipole emission in periodically corrugated layers: the grating-assisted resonant-cavity light-emitting diode," *Journal of the Optical Society of America A*, vol. 19, no. 5, pp. 871–880, 2002.
- [5] J. I. Larruquert, "Reflectance enhancement with sub-quarterwave multilayers of highly absorbing materials," *Journal of the Optical Society of America A*, vol. 18, no. 6, pp. 1406–1414, 2001.
- [6] B. M. Kolundzija, "Electromagnetic modeling of composite metallic and dielectric structures," *IEEE Transactions on Microwave Theory and Techniques*, vol. 47, no. 7, pp. 1021–1032, 1999.
- [7] R. A. Ehlers and A. C. R. Metaxas, "3-D FE discontinuous sheet for microwave heating," *IEEE Transactions on Microwave Theory and Techniques*, vol. 51, no. 3, pp. 718–726, 2003.
- [8] O. Bárta, J. Pištora, J. Vlček, F. Staněk, and T. Kreml, "Magnetooptics in bi-gyrotropic garnet waveguide," *Opto-Electronics Review*, vol. 9, no. 3, pp. 320–325, 2001.
- [9] J. Broe and O. Keller, "Quantum-well enhancement of the Goos-Hänchen shift for p-polarized beams in a two-prism configuration," *Journal of the Optical Society of America A*, vol. 19, no. 6, pp. 1212–1222, 2002.
- [10] O. Keller, "Optical response of a quantum-well sheet: internal electrodynamics," *Journal of the Optical Society of America B*, vol. 12, no. 6, pp. 997–1005, 1995.
- [11] O. Keller, "Sheet-model description of the linear optical response of quantum wells," *Journal of the Optical Society of America B*, vol. 12, no. 6, pp. 987–997, 1995.
- [12] O. Keller, "V: local fields in linear and nonlinear optics of mesoscopic system," *Progress in Optics*, vol. 37, pp. 257–343, 1997.
- [13] G. A. Grinberg and V. A. Fok, "On the theory of Coastal Refraction of Electromagnetic Waves," in *Investigations on Propagation of Radio Waves*, B. A. Vvedenskii, Ed., M-L. AN SSSR, 1948.
- [14] N. N. Grinchik and A. P. Dostanko, "Influence of Thermal and Diffusional Processes on the Propagation of Electromagnetic Waves in Layered Materials," Minsk: ITMO im. A. V. Luikova, NAN Belarusi, 2005.
- [15] M. Born, *Principles of Optics*, Mir, Moscow, Russia, 1970.
- [16] L. Kudryavtsev, *Mathematical Analysis*, Mir, Moscow, Russia, 1970.
- [17] A. Frumkin, *Electrode Processes*, Nauka, Moscow, Russia, 1987.
- [18] A. N. Tikhonov and A. A. Samarskii, *Equations of Mathematical Physics*, Nauka, Moscow, Russia, 1977.
- [19] A. F. Kryachko et al., *Theory of Scattering of Electromagnetic Waves in the Angular Structure*, Nauka, Moscow, Russia, 2009.
- [20] M. Leontovich, *On the Approximate Boundary Conditions for the Electromagnetic Field on the Surface of Well Conducting Bodies*, On the approximate boundary conditions for the electromagnetic field on the surface of well conducting bodies, Moscow, Russia, 1948.
- [21] N. N. Grinchik, A. P. Dostanko, I. A. Gishkelyuk, and Y. N. Grinchik, "Electrodynamics of layered media with boundary conditions corresponding to the total-current continuum," *Journal of Engineering Physics and Thermophysics*, vol. 82, no. 4, pp. 810–819, 2009.
- [22] Z. P. Shul'man and V. I. Kordonskii, *Magnetorheological Effect*, Nauka i Tekhnika, Minsk, Russia, 1982.
- [23] M. Khomich, *Magnetic-Abrasive Machining of the Manufactured Articles*, BNTU, Minsk, Russia, 2006.
- [24] M. N. Levin et al., "Activation of the surface of semiconductors by the effect of a pulsed magnetic field," *Zh. Tekh. Fiz.*, vol. 73, no. 10, pp. 85–87, 2003.
- [25] A. M. Orlov et al., "Magnetic-stimulated alteration of the mobility of dislocations in the plastically deformed silicon of n-type," *Fiz. Tverd. Tela*, vol. 43, no. 7, pp. 1207–1210, 2001.
- [26] V. A. Makara et al., "On the influence of a constant magnetic field on the electroplastic effect in silicon crystals," *Fiz. Tverd. Tela*, no. 3, pp. 462–465, 2001.
- [27] A. P. Rakomsin, *Strengthening and Restoration of Items in an Electromagnetic Field*, Paradoks, Minsk, Russia, 2000.
- [28] Yu. I. Golovin et al., "Influence of weak magnetic fields on the dynamics of changes in the microhardness of silicon initiated by low-intensity beta-irradiation," *Fiz. Tverd. Tela*, vol. 49, no. 5, 2001.
- [29] V. A. Makara et al., "Magnetic field-induced changes in the impurity composition and microhardness of the near-surface layers of silicon crystals," *Fiz. Tekh. Poluprovodn.*, vol. 42, no. 9, pp. 1061–1064, 2008.
- [30] A. M. Orlov et al., "Dynamics of the surface dislocation ensembles in silicon in the presence of mechanical and

- magnetic perturbation," *Fiz. Tverd. Tela*, vol. 45, no. 4, pp. 613–617, 2003.
- [31] N. S. Akulov, *Dislocations and Plasticity*, Izd. AN BSSR, Minsk, Russia, 1961.
 - [32] N. S. Akulov, *Ferromagnetism*, ONTI, Leningrad, Russia, 1939.
 - [33] I. P. Bazarov, *Thermodynamics: Textbook for Higher Educational Establishments*, Vysshaya Shkola, Moscow, Russia, 1991.
 - [34] N. N. Grinchik et al., "Electrodynamic processes in a surface layer in magnetoabrasive polishing," *Journal of Engineering Physics and Thermodynamics*, vol. 83, no. 3, pp. 638–649, 2010.
 - [35] A. Einstein, *Elementary Theory of Brownian Motion*, Collected Papers (3), 1966.
 - [36] V. E. Golant et al., *Fundamental Principles of Plasma Physics*, Moscow, Russia, 1977.
 - [37] Y. Kharkats, "Dependence of the limiting diffusion-migration current on the degree of electrolyte dissociation," *Elektrokhimiya*, vol. 24, no. 4, pp. 539–541, 1988.
 - [38] A. Sokirko and Yu. Kharkats, "the limiting diffusion and migration currents as functions of the rate constants of electrolyte dissociation and recombination," *Elektrokhimiya*, vol. 25, no. 3, pp. 331–335, 1989.
 - [39] D. V. Gibbs, *Thermodynamics. Statistical Mechanics*, Moscow, Russia, 1982.
 - [40] L. N. Antropov, *Theoretical Electrochemistry*, Moscow, Russia, 1984.
 - [41] H. G. Hertz, *Electrochemistry*, New York, NY, USA, 1980.
 - [42] V. Levich et al., *Physicochemical Hydrodynamics*, Moscow, Russia, 1959.
 - [43] J. Neumann, *Electrochemical Systems*, Moscow, Russia, 1977.
 - [44] V. Skorcheletti, *Theoretical Electrochemistry*, Leningrad, Russia, 1969.
 - [45] L. D. Landau and E. M. Lifshits, *Theoretical Physics. Vol. 8. Electrodynamics of Continuous Media*, Moscow, Russia, 1982.
 - [46] V. Tsurko, *Tr. Inst. Mat. Nats. Akad. Nauk Belarusi*, vol. 3, pp. 128–133, 1999.
 - [47] A. I. Shvab, *Elektrichestvo*, no. 4, pp. 59–67, 1994.
 - [48] A. I. Shvab and F. Imo, *Elektrichestvo*, no. 5, pp. 55–59, 1994.
 - [49] N. N. Grinchik et al., *Vesti Nats. Akad. Nauk Belarusi, Ser. Fiz.-Mat. Navuk*, vol. 2, pp. 66–70, 1997.
 - [50] I. E. Tamm, *Principles of the Theory of Electricity*, Moscow, Russia, 1976.
 - [51] J. A. Stratton, *The Theory of Electromagnetism*, Leningrad, Russia, 1938.
 - [52] N. N. Grinchik, "Diffusional-electrical phenomena in electrolytes," *Journal of Engineering Physics and Thermophysics*, vol. 64, no. 5, pp. 497–504, 1993.
 - [53] N. N. Grinchik, "Electrodiffusion phenomena in electrolytes," *Inzhenerno-Fizicheskii Zhurnal*, vol. 64, no. 5, pp. 610–618, 1993.
 - [54] N. N. Grinchik et al., "Interaction of thermal and electric phenomena in polarized media," *Mat. Modelir*, vol. 12, no. 11, pp. 67–76, 2000.
 - [55] N. N. Grinchik, *Modeling of Electrical and Thermophysical Processes in Layered Medium*, Belorusskaya Nauka Press, Minsk, Russia, 2008.
 - [56] N. N. Grinchik, A. N. Muchynski, A. A. Khmyl, and V. A. Tsurkob, "Finite-differences method for modeling electric diffusion phenomena," *Matematicheskoe Modelirovanie*, vol. 10, no. 8, pp. 55–66, 1998.
 - [57] L. N. Antropov, *Theoretical Electrochemistry*, Moscow, Russia, 1989.
 - [58] N. A. Kostin and O. V. Labyak, *Elektrokhimiya*, vol. 31, no. 5, pp. 510–516, 1995.
 - [59] A. I. Dikumar et al., *Thermokinetic Phenomena in High-Frequency Processes*, Kishinev, 1989.
 - [60] F. Bark, Yu. Kharkats, and R. Vedin, *Elektrokhimiya*, vol. 34, no. 4, pp. 434–44, 1998.
 - [61] N. N. Grinchik and V. A. Tsurko, "Problem of modeling of the interaction of nonstationary electric, thermal, and diffusion field in layered media," *Journal of Engineering Physics and Thermodynamics*, vol. 75, no. 3, pp. 693–699, 2002.
 - [62] P. Kolesnikov, *Theory and Calculation of Waveguides, light-guides, and integral-optoelectronics elements. Electrodynamics and Theory of Waveguides*, ITMO NAN Belarusi, Minsk, Russia, 2001.
 - [63] T. Skanavi, *Dielectric Physics (Region of Weak Fields)*, Gostekhizdat, Moscow, Russia, 1949.
 - [64] P. Perre and I. W. Turner, "A complete coupled model of the combined microwave and convective drying of softwood in an oversized waveguide," in *Proceedings of the 10th International Drying Symposium (IDS'96)*, vol. A, pp. 183–194, Krakow, Poland, 1996.
 - [65] J. Jaeger, *Methods of Measurement in Electrochemistry*, Moscow, Russia, 1977.
 - [66] Y. Barash and V. L. Ginzburg, "On the expressions of energy density and the release of heat in electrodynamics of a dispersing and absorbing medium," *Uspekhi Fizicheskikh Nauk*, vol. 118, no. 3, p. 523, 1976.
 - [67] D. E. Vakman and L. A. Vanshtein, "Amplitude, phase, frequency are the principal notions in the theory of oscillations," *Uspekhi Fizicheskikh Nauk*, vol. 123, no. 4, p. 657, 1977.
 - [68] B.-T. Choo, *Plasma in a Magnetic Field and Direct Thermal-to-Electric Energy Conversion*, Moscow, Russia, 1962.
 - [69] I. V. Antonets, L. N. Kotov, V. G. Shavrov, and V. I. Shcheglov, "Energy characteristics of propagation of a wave through the boundaries of media with complex parameters," *Radiotekhnika i Elektronika*, vol. 54, no. 10, pp. 1171–1183, 2009.
 - [70] I. E. Tamm, *Foundations of Electricity Theory*, Nauka, Moscow, Russia, 2003.

Research Article

Magneto-Optical and Magnetic Studies of Co-Rich Glass-Covered Microwires

Alexander Chizhik and Valentina Zhukova

Departamento de Física de Materiales, Facultad de Química, Universidad del País Vasco, UPV/EHU, 1072, 20080 San Sebastian, Spain

Correspondence should be addressed to Alexander Chizhik, oleksandr.chyzyk@ehu.es

Received 22 July 2011; Revised 10 January 2012; Accepted 18 January 2012

Academic Editor: Mitsuteru Inoue

Copyright © 2012 A. Chizhik and V. Zhukova. This is an open access article distributed under the Creative Commons Attribution License, which permits unrestricted use, distribution, and reproduction in any medium, provided the original work is properly cited.

The magnetization reversal process in the surface and volume areas of Co-rich glass-covered microwires has been investigated. The study has been performed in the wide series of microwires with chemical composition, geometry (thickness of glass coating) with the purpose of the tailoring of the giant magnetoimpedance effect. The comparative analysis of the magnetoelectric, magnetic, and magneto-optical experiments permits to optimise the giant magnetoimpedance ratio and elucidate the main properties of the magnetization reversal process in the different parts of the Co-rich microwire.

1. Introduction

The investigation of the magnetization reversal process in amorphous wires and microwires is one of the most important tasks related to the use of these magnetic wires in different technological devices. In particular, the intensive studies of magnetic properties of nearly zero magnetostriction Co-rich wires and glass-covered microwires have been performed in relation with the giant magnetoimpedance (GMI) effect [1]. This GMI effect is of great interest in sensor application. As is well known, the origin of the GMI effect is related with the penetration depth of the skin effect. Consequently, the investigation and comparison on the magnetization reversal in the surface and volume areas of the wire become a particular importance.

The present paper is devoted to the recent results on magneto-optical Kerreffect and fluxmetric investigations of the magnetization reversal and domain structure in glass-coated microwires. Having in our laboratory the wide line of the magnetic, magnetoelectric, and magneto-optic experimental techniques, we have created the new direction of the complex study of glass covered microwires. During last years, we have performed series of the magneto-optical investigations of different types of the glass covered microwires. Kerr effect and fluxmetric methods as two complementary

methods provide the complex information relatively on the magnetization reversal and magnetic domain structure in the volume and in the surface of the microwires. Analyzing the experimental results obtained by these two methods we could model and predict the time and space distribution and transformation of the tree-dimensional magnetic structure of the cylindrical-shaped microwires.

In turn, the magneto-optical set-up which we use to study the microwires consists of two complementary parts: Kerr effect magnetometer and Kerr effect microscopy. Taking into account non-plane surface of the studied microwires the application of the Kerr effect technique is accompanied by the specific difficulties which were successfully overcome during the experiments performed in our laboratory. First, the doubt relatively possible application of Kerr effect was related to the possible interference which could be produced by the glass covering. This doubt was resolved: because of extremely thin thickness the glass covering does not present noticeable contribution. Second, the difficult related to the light reflection from the cylindrical surface of the microwire was resolved by the application of the system of lenses and diaphragms. In the same time, application of the Kerr effect microscopy to the study of the non-plane surface of the microwire gave unexpected result: the series of the original

images of surface domain structure has been obtained. Applying the polar configuration of the Kerr microscopy which is sensitive to magnetization perpendicular to the studied surface, we have obtained unusual, very informative images of bamboo-type domains.

Following originally to the technological task of the optimization and miniaturization of the active elements of the magnetic sensors, we nevertheless focused also our attention on such fundamental problems as magnetic domain formation and transformation and domain walls motion. This duality also reflected in the present paper.

2. Correlation between the GMI Effect and Bulk and Surface Hysteresis Loops

Magnetically soft Co-rich glass-coated microwires have been fabricated by the Taylor-Ulitovsky method. Among the Co-rich compositions a $\text{Co}_{69-x}\text{Mn}_{6+x}\text{Si}_{10}\text{B}_{15}$ series varying the chemical composition ($x = 0; 0.5; 0.75$, and 1) of the metallic nucleus and $\text{Co}_{67}\text{Fe}_{3.85}\text{Ni}_{1.45}\text{B}_{11.5}\text{Si}_{14.5}\text{Mo}_{1.7}$ microwires of different geometric ratio, ρ , of metallic core diameter to total microwire diameter $0.789 \leq \rho \leq 0.98$ have been fabricated [2, 3]. The chemical composition has been selected taking into account the studies on the effect of chemical composition on magnetic softness of amorphous alloys [4, 5].

The sample composition has been selected among the series of $\text{Co}_{69-x}\text{Mn}_{6+x}\text{Si}_{10}\text{B}_{15}$ ($0 < x < 1$) compositions in order to achieve the best combination of soft magnetic properties (high magnetic permeability, low magnetic anisotropy field, and low coercivity). An increasing of the magnetic permeability and coercivity and decreasing of the magnetic anisotropy field were observed in glass-coated amorphous $\text{Co}_{69-x}\text{Mn}_{6+x}\text{Si}_{10}\text{B}_{15}$ ($0 < x < 1$) compositions with x at $x < 0.75$ [6]. The magnetostriction constant of $\text{Co}_{69-x}\text{Mn}_{6+x}\text{Si}_{10}\text{B}_{15}$ samples changes its sign at around $x = 0.75$ [7], being of negative character at $x < 0.75$. Small negative magnetostriction constant can be assumed for the sample with 6.5% at Mn. Accordingly, it is expected that the outer domain structure changes its circular easy magnetization axis (very favourable for the GMI effect) to the radial one at $x \approx 0.75$.

Conventional and surface hysteresis loops have been measured by fluxmetric and Kerr effect (MOKE) [8] methods, respectively. An axial DC-field with intensity up to 200 Oe was supplied by a magnetization coils.

The electrical impedance of the microwire was evaluated by means of the four-point technique. The magnetoimpedance ratio, $\Delta Z/Z$, has been defined as:

$$\frac{\Delta Z}{Z} = \frac{[Z(H) - Z(H_{\max})]}{Z(H_{\max})}. \quad (1)$$

Bulk hysteresis loops of three magnetically soft glass-coated $\text{Co}_{67}\text{Fe}_{3.85}\text{Ni}_{1.45}\text{B}_{11.5}\text{Si}_{14.5}\text{Mo}_{1.7}$ microwires with different geometric ratio $0.78 \leq \rho \leq 0.98$ are shown in Figure 1. As can be observed from this figure, the magnetic anisotropy field, H_k , increases with decreasing ratio ρ , that is, with the increase of the glass coating thickness.

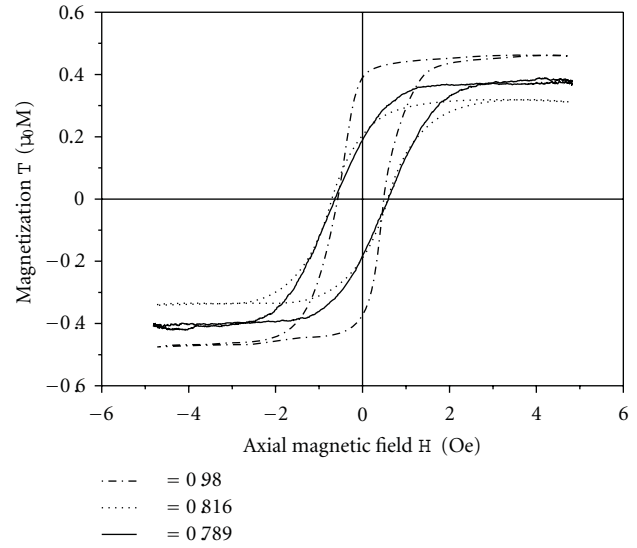


FIGURE 1: Bulk hysteresis loop of three samples with ρ as a parameter.

Strong dependence of the hysteresis loops on the parameter ρ should be attributed to the magnetoelastic energy. The values of the internal stresses in glass coated microwires arises from the difference in the thermal expansion coefficients of metallic nucleus and glass coating, depending strongly on the ratio between the glass coating thickness and metallic core diameter, increasing with the increasing of the glass coating thickness. Large internal stresses give rise to a drastic change of the magnetoelastic energy, even for small changes of the glass-coating thickness at fixed metallic core diameter. Additionally, such a change of the ρ ratio should be related to the change of the magnetostriction constant with applied stress.

The dependence of the magnetoimpedance ratio on the axial field at the driving AC-current ranging from 0.75 up to 5 mA of the frequency, both treated as the parameters have been investigated. The electrical impedance of the microwire was evaluated by means of the four-point technique.

The $(\Delta Z/Z)(H)$ dependences measured at $f = 10$ MHz and $I = 0.75$ mA for the samples with ratio $\rho = 0.98, 0.816$, and 0.789 are presented in the Figure 2.

A maximum relative change in the GMI ratio, $\Delta Z/Z$, up to around 615% is observed at $f = 10$ MHz and $I = 0.75$ mA in the sample with $\rho \approx 0.98$ (see Figure 2).

As may be seen from Figure 2, the field corresponding to the maximum of the GMI ratio, H_m increases, and $(\Delta Z/Z)_m$ decreases with ρ . Such $H_m(\rho)$ dependence should be attributed to the effect of internal stresses, σ , on the magnetic anisotropy field. Indeed, the value of the DC axial field corresponding to the maximum of the GMI ratio, H_m , should be attributed to the static circular anisotropy field, H_k [1, 9]. The estimated values of the internal stresses in these amorphous microwires are of the order of 1000 MPa, depending strongly on the thickness of glass coating and metallic nucleus radius [10].

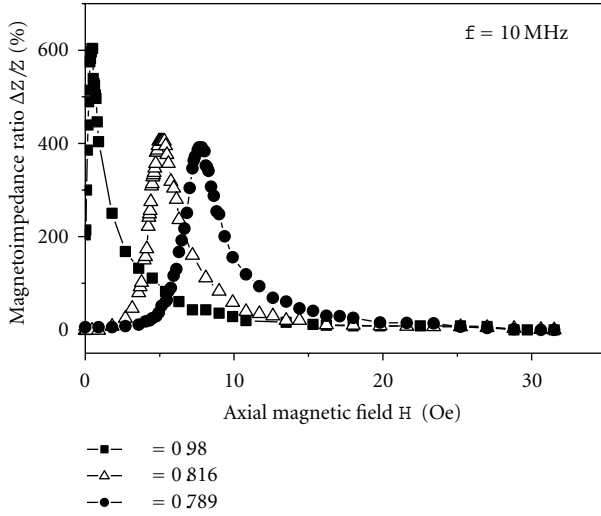


FIGURE 2: Axial field dependence of $\Delta Z/Z$ at $f = 10$ MHz and $I = 0.75$ mA in microwire with ρ as a parameter.

It has been demonstrated that the spatial magnetization distribution close to the surface is very sensitive to the internal or applied stresses [11, 12].

It was shown that the $(\Delta Z/Z)(H)$ dependence is mainly determined by the type of magnetic anisotropy [12]. Circumferential anisotropy leads to the observation of the maximum of the real component of wire impedance (and consequently of the GMI ratio) as a function of the external magnetic field. In the case of axial magnetic anisotropy, the maximum value of the GMI ratio corresponds to zero magnetic field [12], that is, results in monotonic decay of GMI ratio with H . Therefore, the important contribution of the non-diagonal components of the permeability tensor is expected for the samples with well-defined maximum in the axial field dependence of GMI ratio [12].

The MOKE hysteresis loop reflects the axial field dependence of circular magnetization (see Figure 3) in the outer shell of the wire. The transverse configuration of MOKE has been used. The polarized light of a He-Ne laser was reflected from the microwire to the detector. The beam diameter was 0.8 mm. For the transverse configuration of MOKE, the intensity of the reflected light was proportional to the magnetization, which was perpendicular to the plane of incident light.

Observed MOKE hysteresis loops can be interpreted in the following way: the absence of the circular magnetization under axial magnetic field above 2 Oe reflects the axial alignment of the magnetization in the surface layer at this magnetic field range. The monotonic increase of the magnetization with decreasing the field below 2 Oe is related to the magnetization rotation from the axial to the circular direction. The relatively sharp change of magnetization (at around ± 0.7 Oe) could be attributed to the nucleation of new domains with the opposite circular magnetization (appearance of bamboo-like domain structure), and growth of these new domains through the domain walls propagation, until

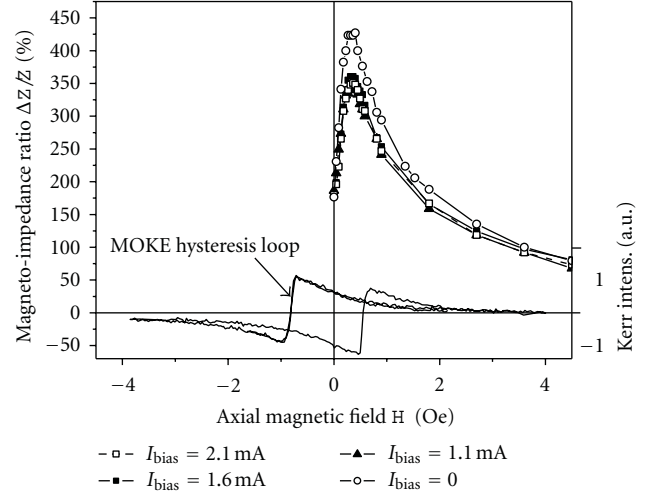


FIGURE 3: $\Delta Z/Z$ and MOKE hysteresis loop of microwire with $\rho = 0.98$.

the single circular domain structure with the opposite circular magnetization is appeared. Further increase of H results in the magnetization rotation towards the axial direction.

A correlation has been observed between the $(\Delta Z/Z)(H)$ and the surface axial hysteresis loops: a maximum of GMI ratio occurs approximately at the same axial magnetic field as the sharp change of magnetization on the MOKE loop (see Figure 3).

3. Effect of the Sample Composition and Geometry on the Bulk Hysteresis Loops

Hysteresis loops of Co-rich glass-coated microwires with sample composition as the parameter ($\text{Co}_{69-x}\text{Mn}_{6+x}\text{Si}_{10}\text{B}_{15}$) are shown in Figure 4 [3].

As can be observed, hysteresis loops are quite sensible to both parameters chemical composition and sample geometry (Figure 1).

Such strong dependence of the hysteresis loops on these parameters can be related with the magnetoelastic energy. In fact the magnetoelastic energy is given by

$$K_{me} \approx 3/2 \lambda_s \sigma_i, \quad (2)$$

where λ_s is the saturation magnetostriction, and σ_i are the internal stresses.

The magnetostriction constant depends on the chemical composition achieving nearly zero value in amorphous Fe-Co-based alloys at about %Co/%Fe $\approx 70/5$ [4, 5]. On the other hand, the estimated values of the internal stresses in these amorphous microwires arising from the difference in the thermal expansion coefficients of metallic nucleus and glass coating are of the order of 100–1000 MPa, depending strongly on the thickness of glass coating and metallic core diameter [13]. It was established that the strength of such internal stresses increase with increasing the glass coating thickness. Such large internal stresses give rise to a drastic change of the magnetoelastic energy, K_{mei} , even for small

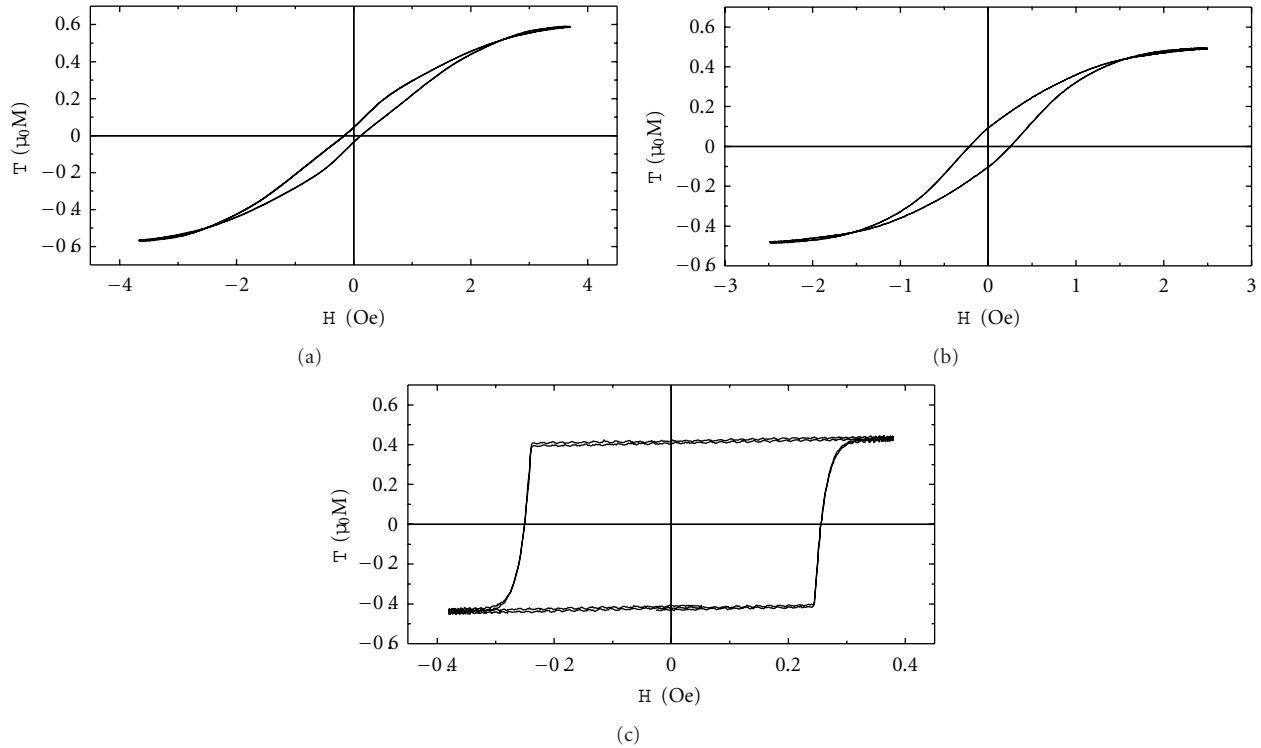


FIGURE 4: Hysteresis loops of the $\text{Co}_{69-x}\text{Mn}_{6+x}\text{Si}_{10}\text{B}_{15}$ microwires. $x = 1$ (a); $x = 0, 5$ (b); $x = 0$ (c).

changes of the glass-coating thickness at fixed metallic core diameter. Additionally, such change of the ρ -ratio should be related to the change of the magnetostriction constant with applied stress [14]:

$$\lambda_s = \left(\frac{\mu_0 M_s}{3} \right) \left(\frac{dH_k}{d\sigma} \right), \quad (3)$$

where μ_0 is the free space permeability equals $4\pi \times 10^{-7}$ H/m and M_s —the saturation magnetization.

These considerations allow us to predict that any method to change the internal stresses (by using thermal treatment, chemical etching, etc.) can change drastically magnetic anisotropy and consequently the hysteresis loops and the GMI behaviour.

Thermal treatment has been realized either by Joule heating passing along the microwire sample a DC-current of 30 and 40 mA, at various times of this treatment or by conventional furnace annealing. This Joule heating has been performed without additional external field (CA) and under axial applied magnetic field of about 100 Oe (MFA). Electrical contacts were made removing mechanically the glass insulating layer at the sample edges and soldering them with the Cu cables.

Consequently, the hysteresis loops of $\text{Co}_{69-x}\text{Mn}_{6+x}\text{Si}_{10}\text{B}_{15}$ ($x = 0.5$) has been changed after MFA treatment (see Figure 5), and the GMI response has been improved.

Similarly, in the case of $\text{Co}_{69-x}\text{Mn}_{6+x}\text{Si}_{10}\text{B}_{15}$ ($x = 0.5$) microwire, the MFA treatment of $\text{Co}_{67}\text{Fe}_{3.85}\text{Ni}_{1.45}\text{B}_{11.5}\text{Si}_{14.5}\text{Mo}_{1.7}$ microwire also induces changes in hysteresis (see Figure 6). In this case, the external axial magnetic field applied during

the MFA treatment induces axial magnetic anisotropy, like what can be appreciated from Figure 6.

It is worth mentioning that appearance of Large and single Barkhausen jump takes place under magnetic field above some critical value (denominated as switching field) and also if the sample length is above some critical value denominated also as critical length. The switching field depends on magnetoelastic energy determined by the strength of the internal stresses, applied stresses and magnetostriction constant. The critical length first increases with stress, but then again decreases.

Conventional annealing performed at $T_{\text{ann}} = 400^\circ\text{C}$ in $\text{Fe}_{74}\text{B}_{13}\text{Si}_{11}\text{C}_2$ does not affect significantly the magnetic properties of studied sample (see Figure 7): some decrease of H_c has been observed, while the squared character of the hysteresis loop remains unchanged (Figure 7(b)). On the other hand, stress annealing, (SA), is performed at the same annealing conditions ($T_{\text{ann}} = 400^\circ\text{C}$) but under applied stress, $\sigma = 458$ MPa, results in drastic changes of the hysteresis loop (see Figure 7(c)): hysteresis loop becomes inclined with a magnetic anisotropy field about 1000 A/m. A transverse magnetic anisotropy induced by the SA allows us to predict the existence of the magnetoimpedance effect in such samples.

Above-mentioned results allow us to assume that there are few factors which can affect the GMI behaviour of the glass coated microwires such as-following:

- (a) metallic nucleus chemical composition;
- (b) samples geometry;
- (c) thermal treatments.

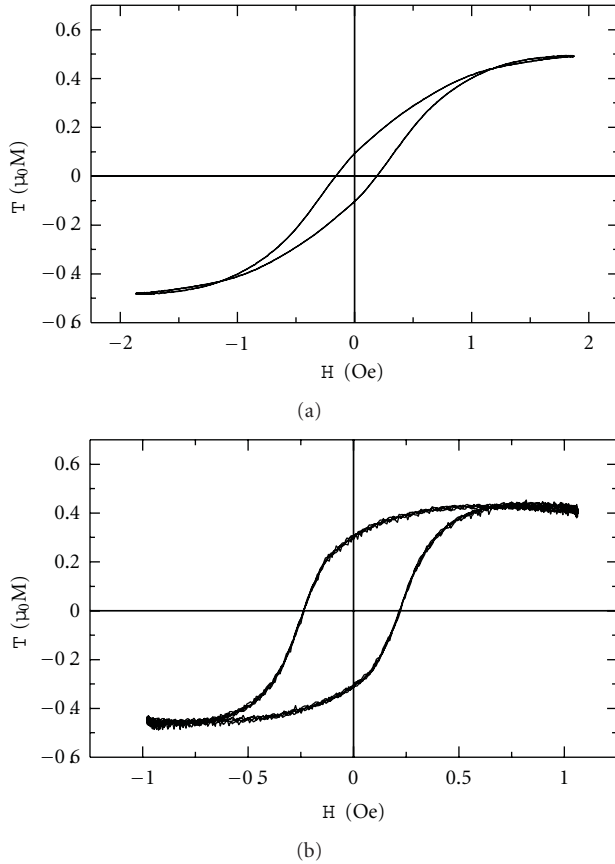


FIGURE 5: Effect of the MFA (current annealing under axial applied magnetic field) treatment on hysteresis loops of $\text{Co}_{9-x}\text{Mn}_{6+x}\text{Si}_{10}\text{B}_{15}$ ($x = 0.5$) microwires: (a) as-cast; (b) MFA.

4. Effect of the Sample Composition on the Surface Hysteresis Loops

The Kerr effect experiments have been performed in microwires of nominal composition $(\text{Co}_{1-x}\text{Mn}_x)_{75}\text{Si}_{10}\text{B}_{15}$ (diameter around $20\text{ }\mu\text{m}$) with different content of Mn ($0.07 < x < 0.11$) [15].

There were four schemes of the experiments, depending on the combination of magnetic field combination and the type of Kerr effect:

- (1) transverse Kerr effect at sweeping of circular field (+ axial bias field);
- (2) longitudinal Kerr effect at sweeping of circular field (+ axial bias field);
- (3) transverse Kerr effect at sweeping of axial field (+ circular bias field);
- (4) longitudinal Kerr effect at sweeping of axial field (+ circular bias field).

The obtained Kerr effect loops show different shape, which can be attributed to different type of domain structure and difference in the magnetization reversal process (Figure 8).

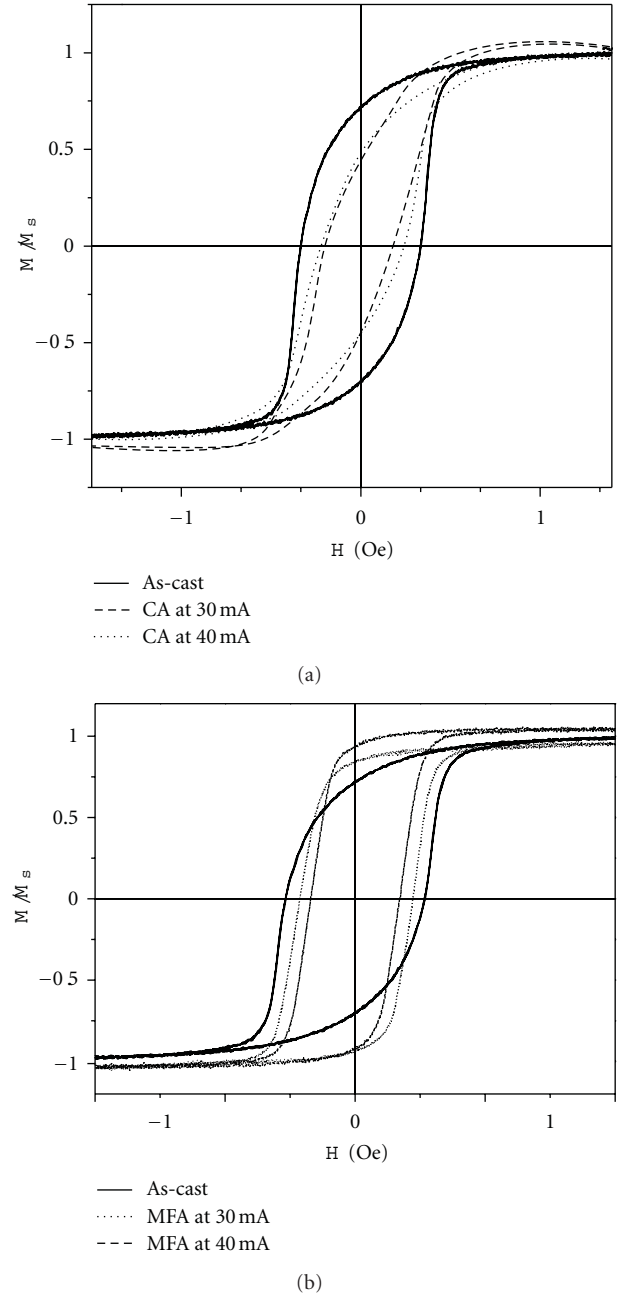


FIGURE 6: Effect of CA (current annealing without additional external magnetic field) (a) and MFA (b) treatments on bulk hysteresis loops of $\text{Co}_{67}\text{Fe}_{3.85}\text{Ni}_{1.45}\text{B}_{11.5}\text{Si}_{14.5}\text{Mo}_{1.7}$ microwires.

The transverse and longitudinal Kerr effect loops obtained in ac circular field for the microwire with $x = 0.07$ are presented in the Figures 8(a) and 8(b). From the analysis of these curves, it is possible to conclude that jumps of circular magnetization take place. The rectangular shape of transverse curve and the peaks in the longitudinal curve are related to quick rotation of magnetization in circular surface domain similar to large Barkhausen jump.

For the microwire with content of Mn $x = 0.11$, the rectangular shape of the magnetization reversal curve was found

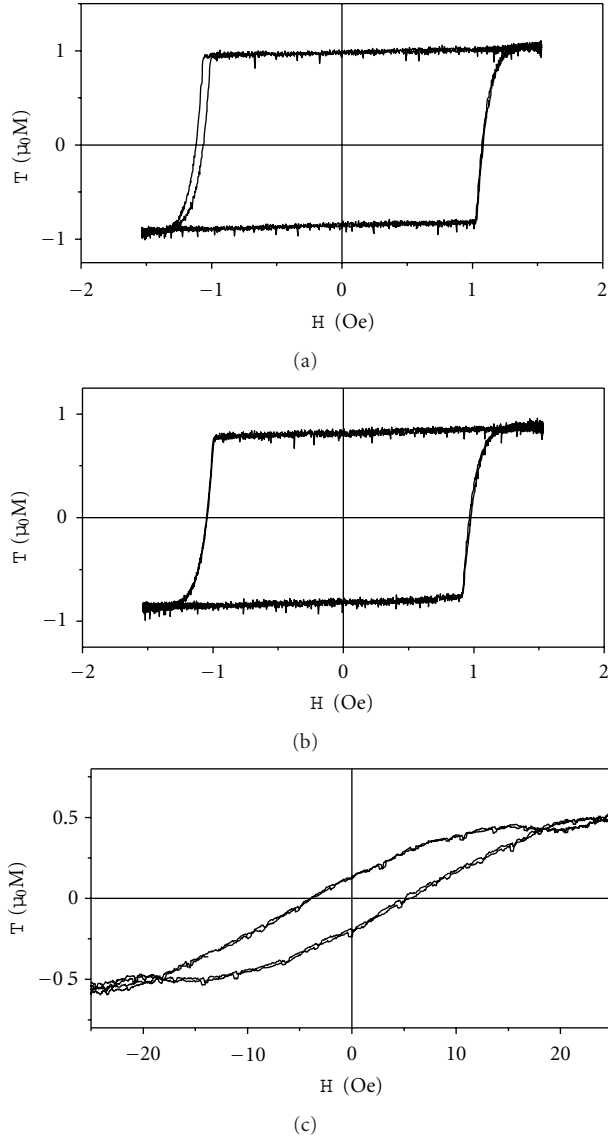


FIGURE 7: Effect of CA and SA (stress annealing) on bulk hysteresis loops of Fe₇₄B₁₃Si₁₁C₂ microwire: (a) as cast; (b) conventional annealing; (c) stress annealing.

in *ac* axial field (Figures 8(c) and 8(d)). The longitudinal Kerr loop reflects the change of the axial projection of the magnetization inside the surface area of the wire. Therefore, the sharp change of longitudinal Kerr effect (Figure 8(c)) could be attributed to a quick change of the axial magnetization.

The transformation of transverse loops in presence of *dc* circular field could clarify the details of the magnetization process (Figure 8(d)). The absence of signal when the axial field is zero can be explained taking into account the absence of a circular projection during magnetization reversal. That is, the magnetization reversal occurs only by domain walls motion between the axial domains. Under the application of the *dc* circular field, the magnetization inside the domain deviates from the axial direction, the transverse projection

appears, and the transverse Kerr loops are observed. In this way, the magnetization reversal process can occur by the domain wall motion owing to the rotation of the magnetization.

The magnetization reversal for the microwire with $x = 0.09$ is close to that of the microwire $x = 0.11$, but some peculiarities are observed (Figures 8(e) and 8(f)). The longitudinal loop obtained in *ac* axial field presents a rectangular shape related to the change of the axial magnetization similarly to the case of $x = 0.11$. At the same time, the transverse loop has the shape, which can be attributed to successive rotation of magnetization and nucleation of new domains.

The modification of the domain structure of glass-coated amorphous microwires (Co_{1-x}Mn_x)₇₅Si₁₀B₁₅ could be ascribed to the change of the value and the sign of the magnetostriction constant. As was shown in [16], the λ_s is positive for the wires with $x \geq 0.1$ and negative for the wires with $x < 0.1$. Taking into account that the circular magnetization process in the outer shell is attributed to the negative sign of the magnetostriction, and axial magnetization in outer shell is attributed to positive magnetostriction, our magneto-optical investigation for the wire with $x = 0.07$ and for $x = 0.11$ is in agreement with independent examination of the magnetostriction constant value. It is necessary to note that the quick magnetization reversal discovered in wire with $x = 0.07$ can be considered like large Barkhausen jump in the circular magnetic structure. This effect was observed in Co-rich amorphous wire when an electric current is flowing along the wire to produce a circular magnetic field.

In spite of that for the microwire with $x = 0.09$ λ_s is negative, the axial domain structure exists in this wire. Significant contribution of rotation of the magnetization is found in this wire together with domain nucleation, which suggests that this wire occupies intermediate place between wires with $x = 0.07$ and $x = 0.11$.

Therefore, Co-rich microwires with different content in Mn demonstrate the variety of the shape of magnetization reversal loop, which similarly can be attributed to the change of sign and value of the magnetostriction. The rectangular shape of the hysteresis loop in circular magnetic field of the microwire with $x = 0.07$ can be interpreted by considering that the magnetization process in the outer shell takes place by large Barkhausen jumps of circular domain structure, while the rectangular shape of the Kerr hysteresis loop in axial magnetic field of the microwire with $x = 0.11$ could be connected to large Barkhausen jumps in the axial domain structure in the outer shell.

5. Surface Circular Bistability

Glass-covered microwires of nominal composition Co₆₇Fe_{3.85}Ni_{1.45}B_{11.5}Si_{14.5}Mo_{1.7} (metallic nucleus radius $R = 11.2 \mu\text{m}$, glass coating thickness $T = 0.2 \mu\text{m}$) have been studied using transverse MOKE in axial and circular magnetic field [17].

Figure 9 presents the transverse Kerr effect dependence on the *ac* electric current I flowing with the frequency of

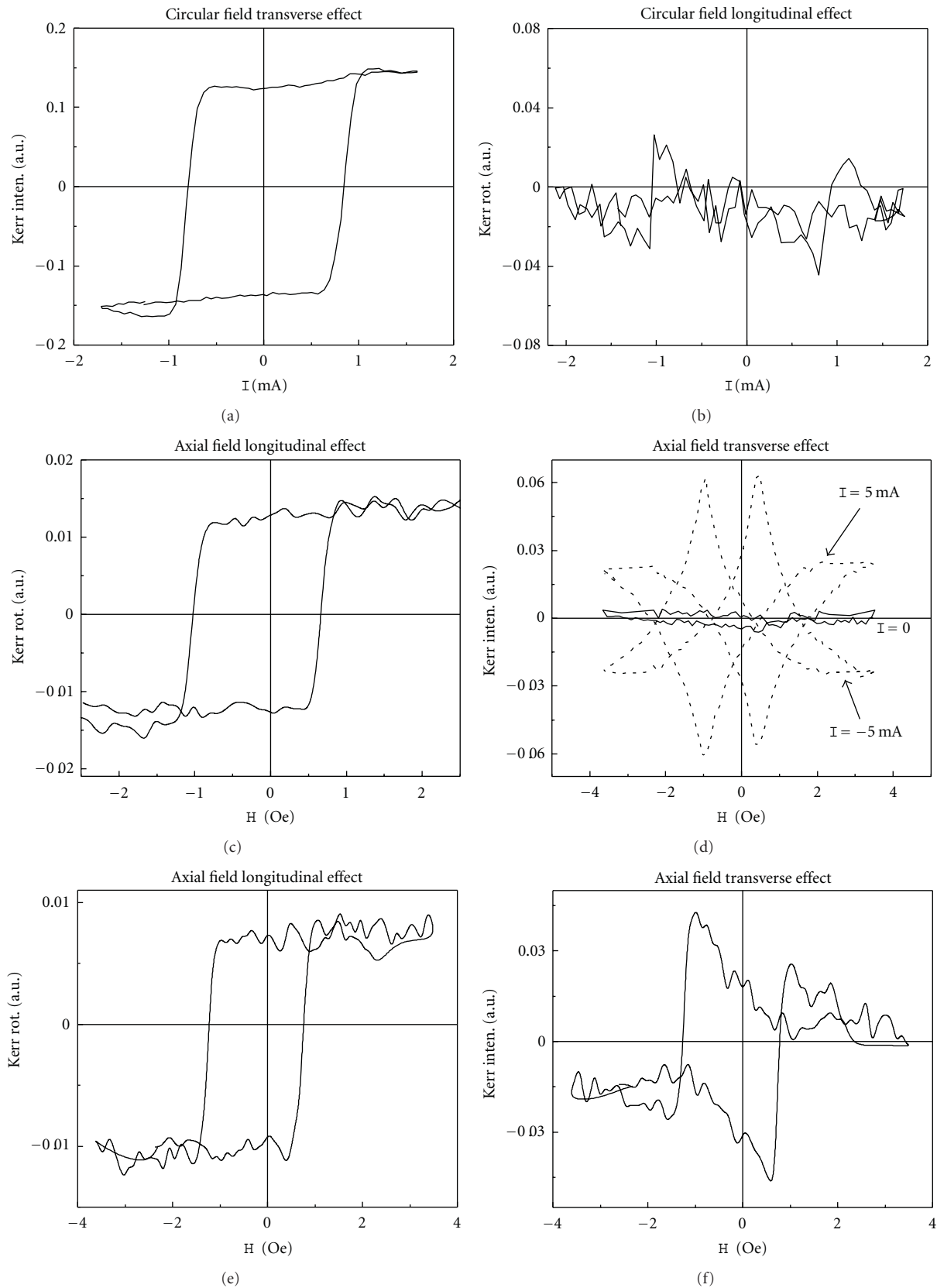


FIGURE 8: Longitudinal and transverse Kerr effect loops of the glass-coated $(\text{Co}_{1-x}\text{Mn}_x)_{75}\text{Si}_{10}\text{B}_{15}$ amorphous microwires for different Mn content: (a)-(b) $x = 0.07$; (c)-(d) $x = 0.11$; (e)-(f) $x = 0.09$.

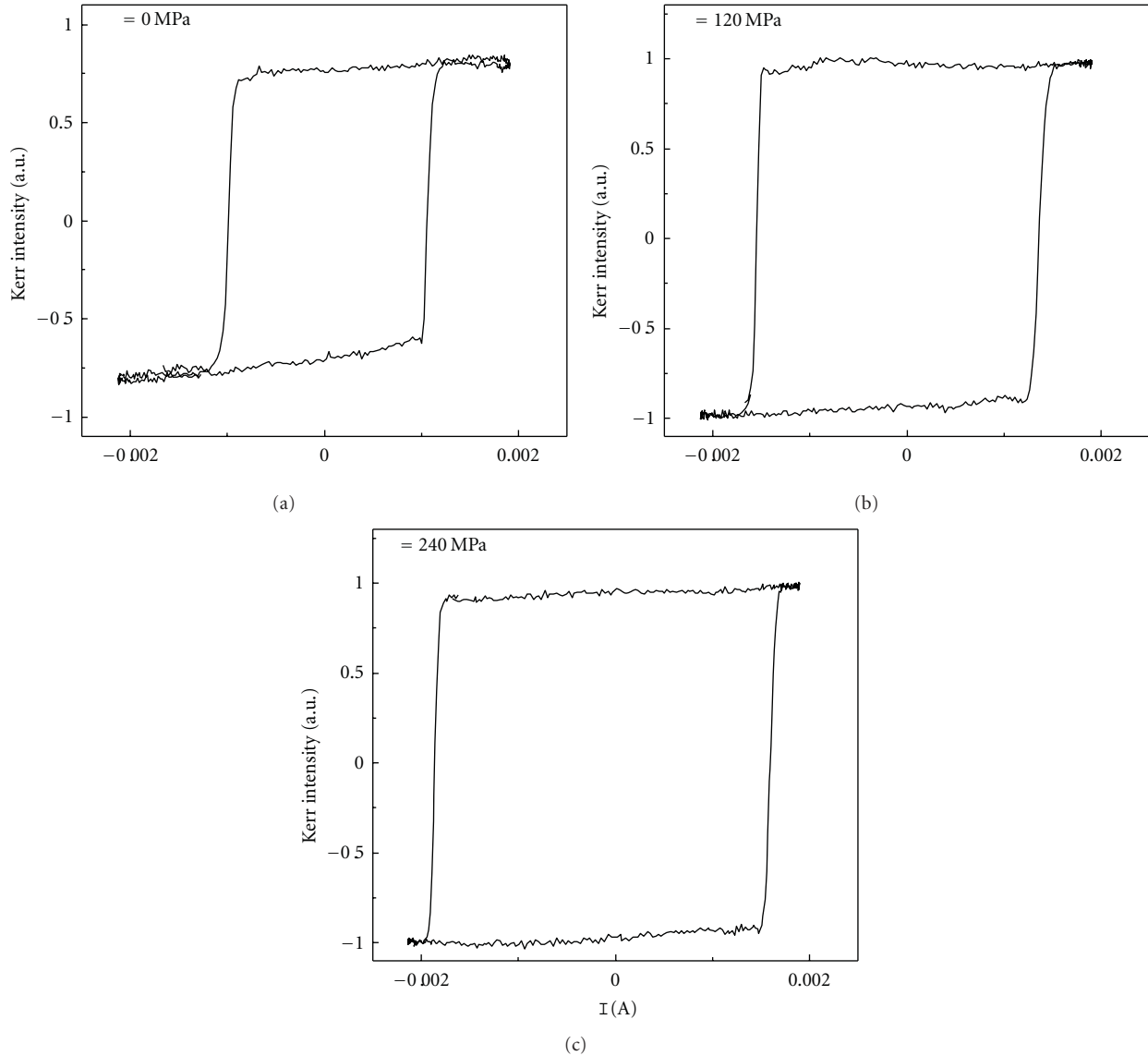


FIGURE 9: Transverse Kerr effect dependence on ac electric current flowing with the frequency of 50 Hz through the wire for different tensile stresses: (a) 0 MPa; (b) 120 MPa; (c) 240 MPa.

50 Hz along the sample with an external tensile stress σ as a parameter. The shape of hysteresis loop is perfectly rectangular with sharp vertical areas associated with quick enough reversal of circular magnetization in the absence of external tensile stress (Figure 9(a)). This reversal is a realization of circular magnetic bistability in the form of large Barkhausen jumps between two states with opposite directions of circular magnetization. The external tensile stress causes the change of switching field, H_{SW} , (associated with the switching current).

The change of the I_R/I_S ratio under the tensile stress is also observed (I_R is the intensity of the Kerr signal in the remanent state, and I_S is the intensity of the Kerr signal in the saturation state). The Kerr intensity is proportional to transverse magnetization M in the surface area of the wire. There-

fore, it is possible to consider that $I_R/I_S = M_R/M_S$, where M_R is the transverse saturation magnetization, and M_S is the transverse remanent magnetization.

The circular magnetic bistability is related to the magnetoelastic anisotropy in the circular direction, as the classical longitudinal magnetic bistability [18, 19]. The circular magnetoelastic anisotropy results in the appearance of circular monodomain structure in the outer shell. It is known that in negative magnetostrictive wires the axial tensile stress produces circular anisotropy in the outer shell. In the presented experiments, this effect is reflected in the increase of circular remanence magnetization and in the increase of the squariness of the hysteresis loops in presence of tensile stress.

The tensile stress-induced increase of circular switching field could be explained taking into account the strong

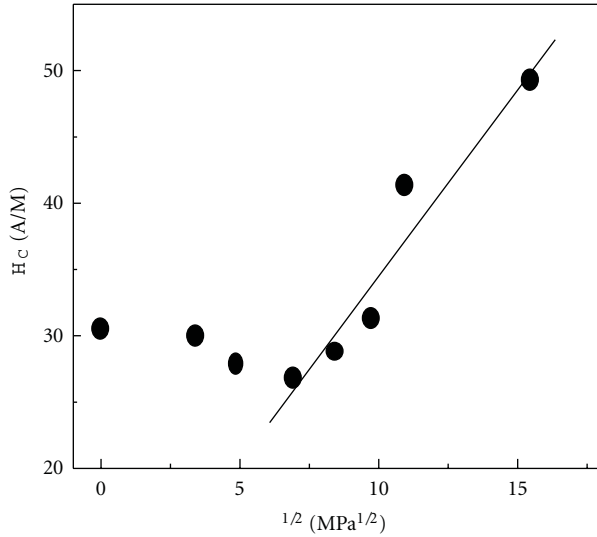


FIGURE 10: The circular switching field as a function of the square root external tensile stress.

influence of the magnetostriction on the domain structure in the amorphous wires. The circular bistability effect is related to formation of circular domain walls. The circular switching field should be proportional to the energy γ required to form the circular domain wall. The circular switching field is related to the magnetoelastic anisotropy as given by [20, 21]:

$$H_{SW} \propto \gamma \propto \left[\frac{3}{2A\lambda_s(\sigma_a + \sigma_r)} \right]^{1/2}, \quad (4)$$

where A is the exchange energy constant, σ_a is applied tensile stress, σ_r is the internal tensile stress, and λ_s is magnetostrictive constant. The switching field must be proportional to $\sigma_a^{1/2}$ for the applied stress σ_a larger than the internal stress σ_r , that is, when the remanence has reached the saturation value. The magnetostriction constant of this microwire is negative, so it is expected that the volume of outer shell will increase with the circular anisotropy. Due to the increase of circular anisotropy region with the stress at the expense of the reduction of the axial anisotropy volume, the circular remanence increases as a function of the applied stress. For high value of σ_a , there will be no contributions from the axial volume, and the circular remanence reaches its saturation value.

The experimental H_{SW} dependence on the tensile stress has been plotted as a function of the square root applied stress σ_a (Figure 10). Good fitting of the experimental points by the linear dependence take place for the $\sigma_a > 50$ MPa, when the circular remanence reaches the saturation. Consequently, we can estimate the value of the σ_r internal stress as about 50 MPa. Such small value of the internal stress seems to be acceptable taking into account the extremely small value of glass coating in the studied wire. The observed decrease of H_{SW} for low-applied tensile stress is probably a result of the tensor character of internal stresses with an important contribution of radial and circular stresses components.

6. Tensile Stress Influence on Surface Magnetization Reversal

Figure 11 shows the stress-induced changes of surface hysteresis loop in the microwire of nominal composition $\text{Co}_{67}\text{Fe}_{3.85}\text{Ni}_{1.45}\text{B}_{11.5}\text{Si}_{14.5}\text{Mo}_{1.7}$ (metallic nucleus radius $R = 11.2 \mu\text{m}$, glass coating thickness $T = 3 \mu\text{m}$). The experimental results have been obtained using MOKE magnetometer. The monotonic hysteresis loop is observed with $\sigma = 0$ (Figure 11(a)). The sharp jumps of magneto-optical signal arising in the presence of the tensile stress (Figure 11(c)) should be attributed to circular bistability. Another significant feature is the increase of the value of the circular switching field with increasing tensile stress. This indicates the change of coercivity of circular domain structure under the tensile stress.

The transverse Kerr effect experiments in ac axial field (Figures 11(d)-11(f)) give additional information about the formation of circular domain structure and open new details of the magnetization reversal process. It is worth mentioning that these three graphs were plotted in the same scale of Kerr intensity. Figures 11(e) and 11(f) represent the typical behavior of circular domain structure in axial field. The monotonic increase of the Kerr signal with increase of field could be related to the rotation of magnetization from axial to circular direction. Sharp jump of the signal, which is followed by the change of the sign of the signal, is associated with nucleation of new circular domain with the opposite direction of the magnetization. The last part of the loop is the monotonic decrease of the signal reflected the magnetization rotation from circular into the axial direction.

The transverse hysteresis loop with perfectly squared shape appears step by step under the applied tensile stress (Figure 11). In the intermediate stage (tensile stress of 30 MPa), the Kerr effect curve contains monotonic parts and jumps (Figure 11(b)), which could be associated with the rotation of magnetization and the motion of domain walls between circular domains. Also the minor loop is observed at this tensile stress.

The existence of such hysteresis loop permits us to suppose the existence of a multidomain circular bamboo structure in the studied microwires. The Kerr microscopy experiments confirm this supposition.

The results obtained have been explained taking into account the strong correlation between the magnetostriction and the domain structure in the amorphous microwires. This correlation is based on the competition between the magnetostatic and magnetoelastic energies. The magnetostatic energy depends on the demagnetizing field. We consider, in our experimental results, the supposition that one of the reasons for the observed transformation of the hysteresis loops is the change of the sign of the magnetostriction constant. The large Barkhausen jump of the axial magnetization in the outer shell could be attributed to positive value of magnetostrictive constant, while the large Barkhausen jump of the circular magnetization in the outer shell for could be attributed to negative value of magnetostrictive constant.

Considering that $\lambda_s(\sigma) = 0$ for tensile stress of about 30 MPa, we could estimate the value of phenomenological

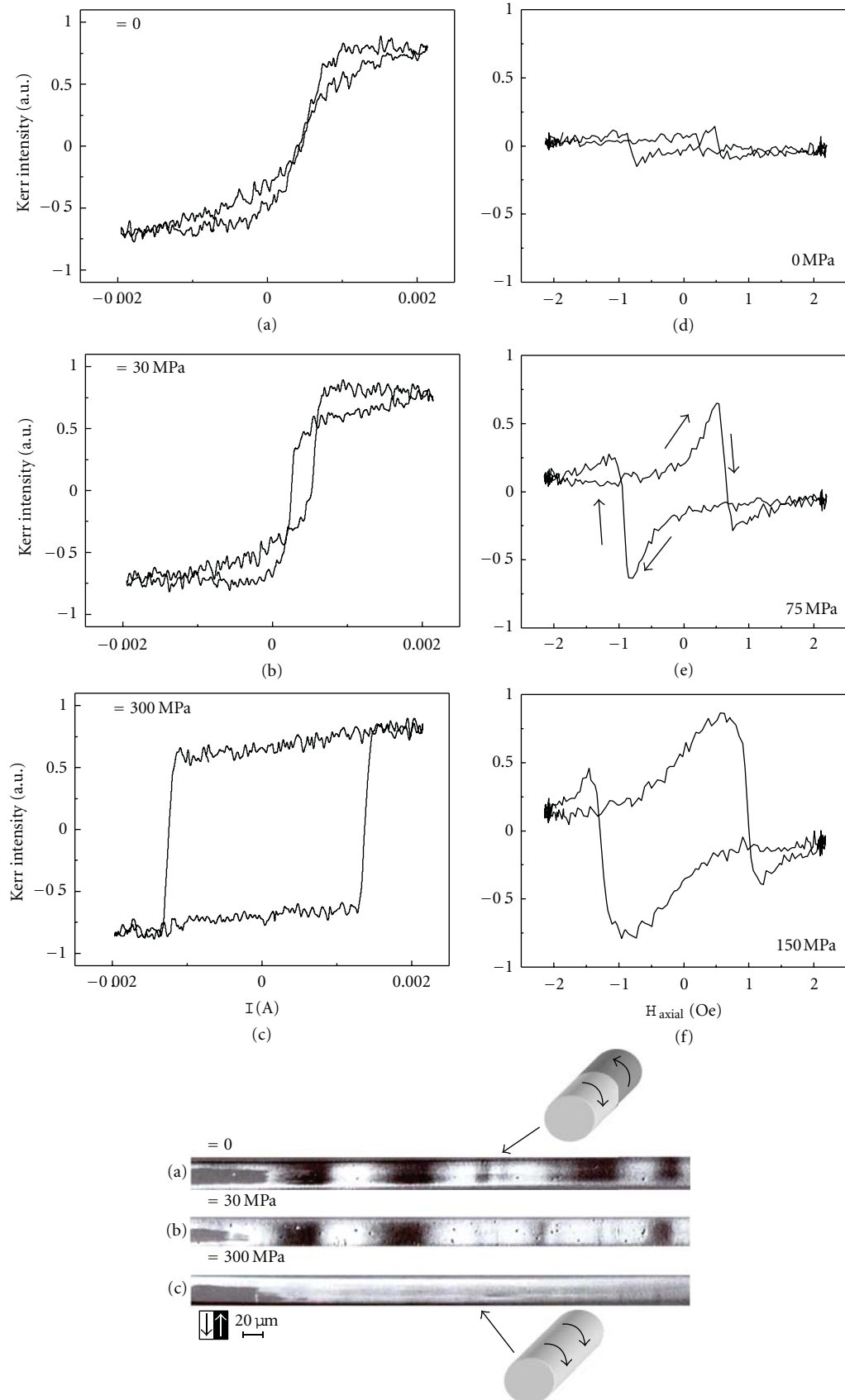


FIGURE 11: Transverse Kerr-effect dependencies: (a)-(c) on the electric current flowing through the wire in the presence of tensile stress; (d)-(f) on the axial magnetic field in the presence of tensile stress. Inset: circular domain structure in presence of external tensile stress in microwire.

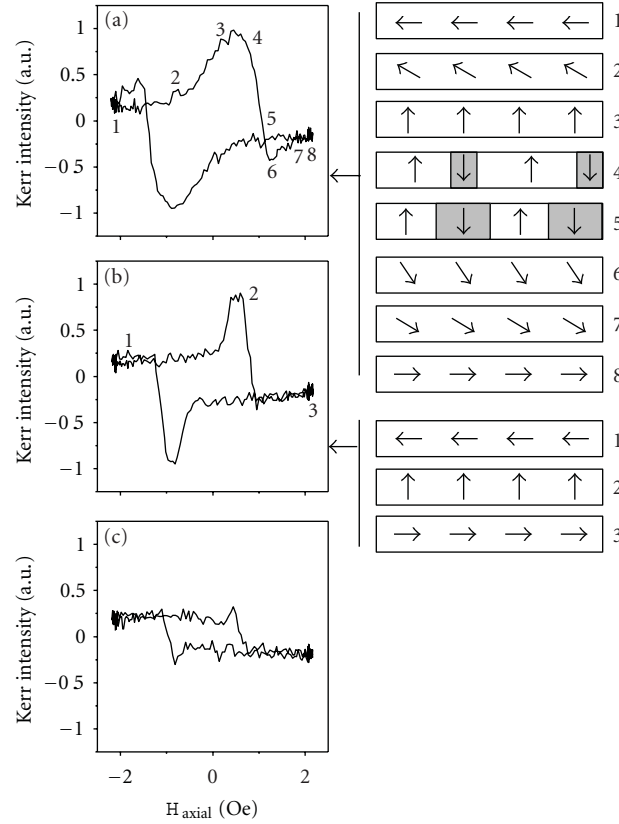


FIGURE 12: Transverse Kerr effect dependence on the axial magnetic field under the presence of HF electric current (4 kHz) (a)—(c): (a) 0 mA, (b) 0.76 mA, and (c) 1.35 mA.

A constant for glass-covered wires to be about 3×10^{-9} MPa. This value differs from the value of A for conventional wires and ribbons (10^{-10} MPa). The possible reason for this difference is additional internal stress introduced by glass coating.

The increase of the tensile stress causes the increase of the value of the circular projection of the magnetization in the outer shell of the microwire, which reflects on the coercive properties of the domain structure. The change of the sign of the magnetostriction constant and its small value are crucial for the observation of changes of the type of the domain structure and for its high sensitivity to external stresses.

For the analysis of our results, we used the core-shell model developed for Co-rich amorphous wires of a finite length [22]. The demagnetizing field of surface magnetic charges can arise near the wire ends for the case of finite length wires. The magnetostatic energy of the magnetic charges could be reduced by twisting, of magnetization near the wire ends. Due to this twisting the intermediate area with circular and axial projections of magnetization could exist between the inner core and the outer shell. Taking into account the strong correlation between the magnetization in the inner core and the outer shell the appearance of domain walls between circular domains could be energetically favorable in order to diminish the magnetostatic energy in whole volume of the wire.

The stability of multidomain circular structure in the nearly zero magnetostrictive composition could be reasonable when the external stresses are small enough because of

the competition between the magnetostatic and the magnetoelastic energy at the condition, when the magnetoelastic energy is low enough. The increase of the external tensile stress makes the multidomain structure nonstable, due to the increase of the domain wall energy. Applying additional external stress, we increase the magnetoelastic energy and, consequently, the domain wall energy. At such conditions the bamboo domain structure disappears, and single circular domain state is observed (see domain images in Figure 11).

7. Influence of High-Frequency Electric Current on Surface Magnetization Reversal

Figure 12 shows the influence of HF electric current ($f = 4$ kHz) flowing along the microwire on the MOKE dependence on the axial magnetic field in the microwire of nominal composition $\text{Co}_{67}\text{Fe}_{3.85}\text{Ni}_{1.45}\text{B}_{11.5}\text{Si}_{14.5}\text{Mo}_{1.7}$ (metallic nucleus radius $R = 8.6 \mu\text{m}$, glass coating thickness $T = 0.6 \mu\text{m}$).

The value of the circular magnetic field on the surface of the wire could be obtained using the formula for circumferential field $H_{\text{circ}} = Ir/2\pi R^2$ (for $r = R$). The value of H_{circ} is 0.3 Oe for the value of the ac electric current of 1.35 mA. The experimental setup was tuned in such a way, that the high-frequency signal has been cut by the special filter and therefore we observed only the low-frequency changes of the circular magnetization. Our experiments show that the

electric current of such amplitude does not produce essential Joule heating.

The insets show how the magnetization in the surface area of the microwire changes during the magnetization reversal. The magnetization reversal in the absence of HF current is demonstrated in Figure 12(a). As mentioned above, at the first stage of the surface magnetization reversal, when the external axial magnetic field H_{AX} increases, a rotation of the magnetization from axial to circular direction in the outer shell of the wire is observed (schematic pictures (1)–(3)). At the second stage, the jump of the circular magnetization takes place (schematic pictures (4)–(6)). During this jump, the direction of the circular magnetization reverses (picture (6)). This jump is related to the circular magnetic bistability effect. At the third stage, the magnetization rotation from the circular to the axial direction is observed (pictures (6)–(8)).

The HF current causes the transformation of axial hysteresis loop (Figures 12(b)–12(c)). A decrease of the coercive field, H_{C-AX} and I_{MAX} (I_{MAX} is the maximum value of the intensity of the Kerr signal during the magnetization reversal in axial magnetic field) takes place. The coercive field H_{C-AX} should be considered as the field, at which the drastic change of the circular magnetization starts in the presence of the axial magnetic field.

The Kerr effect loops presented in the Figure 12 demonstrate the change of the mechanism of the magnetization reversal that is reflected in the change of the shape of the hysteresis curve. The sharp jump (Figure 12(c), pictures (1)–(2)) replaces the monotonic change of the Kerr signal on the first stage of the magnetization reversal (Figures 12(a), pictures (1)–(3)). The HF circular magnetic field induces the jump of magnetization from the axial direction (Figure 12(c), picture (1)) to the circular direction (Figure 12(c), picture (2)) suppressing the process of the rotation of the magnetization.

The HF current has the opposite effect on the surface magnetization reversal as compared with the tensile stress influence: the tensile stress causes the increase of circular magnetization, and the HF current causes the decrease of circular magnetization. It is interesting to compare two intermediate curves presented in the Figures 11(e) and 12(b). Being quite similar, these hysteresis loops have a difference in the magnetization reversal process. The question is about the presence (Figure 11(e) or absence (Figure 12(b)) of the small peak. This difference confirms that the HF electric current not only suppresses the circular magnetization but also changes the mechanism of the surface magnetization reversal.

8. Surface and Bulk Magnetic Hysteresis Loops of Co-Rich Microwires with Helical Anisotropy

Two microwires of nominal composition $\text{Co}_{69.5}\text{Fe}_{3.9}\text{Ni}_{1.8}\text{Si}_{10.8}\text{Mo}_2$ and with different geometric ratio ρ of metallic nucleus diameter d to total microwire diameter D , $\rho = 0.785$ (metallic nucleus diameter $d = 19 \mu\text{m}$) and $\rho = 0.885$ (metallic nucleus diameter $d = 20 \mu\text{m}$) have

been studied by transversal MOKE and fluxmetric methods [23].

Experimental Kerr effect hysteresis loops obtained in the axial magnetic field are presented in the Figures 13(a) and 13(b). The surface magnetization reversal in Co-rich amorphous microwires in presence of an axial magnetic field consists of a rotation of the magnetization and a jump of the circular magnetization. For the wire with $\rho = 0.785$, the magnetization reversal consists mainly of the rotation of the magnetization, and the jump of the magnetization is quite small, while for the wire with $\rho = 0.885$ the jump is large.

The bulk hysteresis loops obtained for the two studied wires in axial magnetic field are presented in Figures 14(a) and 14(b). Just as the experimental curves presented in Figure 13, these loops also have the parts related to the rotation of the magnetization and jumps of the magnetization.

The transverse Kerr effect curves and the conventional curves reflect the change of the circular and axial projection of the magnetization, respectively. Therefore, they could be considered as complement date. From another side, the Kerr effect loops contain information about the surface magnetization reversal when the conventional loops present the magnetization reversal of the whole volume of the wire. Consequently, this complement could not be considered as a complete one.

We believe that the observed difference in surface and bulk hysteresis curves is related to the existence of helical magnetic structure in the studied wires. Generally, the magnetic structure of Co-based amorphous wires was considered in frame of the core-shell model: a Co-based amorphous wire has an inner core with the longitudinal easy magnetization axis and an outer shell with the circular or helical anisotropy [24]. In the glass-covered microwires, the helical magnetic anisotropy originates from the magnetoelastic anisotropy associated with the internal stresses. The internal stresses are produced due to the contraction of the metal and glass having different thermal expansion coefficients [13].

The calculation of the hysteresis loops has been performed taking into account the existence of a helical magnetic anisotropy in the wire. The expression of the energy of the system has the form:

$$U = -K_U \cos^2(\theta - \varphi) - h \cdot m \quad (5)$$

$$= -K_U \cos^2(\theta - \varphi) - h_{\text{axial}} \cos(\theta),$$

where h_{axial} is the applied magnetic field, K_U is the uniaxial anisotropy constant, m is the saturation magnetization, φ is the angle between the anisotropy axis, and the wire axis and θ is the angle between the magnetic moment and the wire axis.

The result of the numerical analysis of (5) is presented in Figure 15. There is the calculated dependence of the jump of the circular magnetization ΔM_{CIRC} (Figure 13(d)) on the angle of helical anisotropy. This dependence has a maximum for the angle of 62° . The maximum is not sharp, but for the angles close to 0° and 90° the change of the ΔM_{CIRC} is strong enough. For the angles close to 90° , the magnetization reversal is determined mainly by a fluent rotation of the magnetization, and this rotation continues after the moment when the magnetization reaches the exact circular

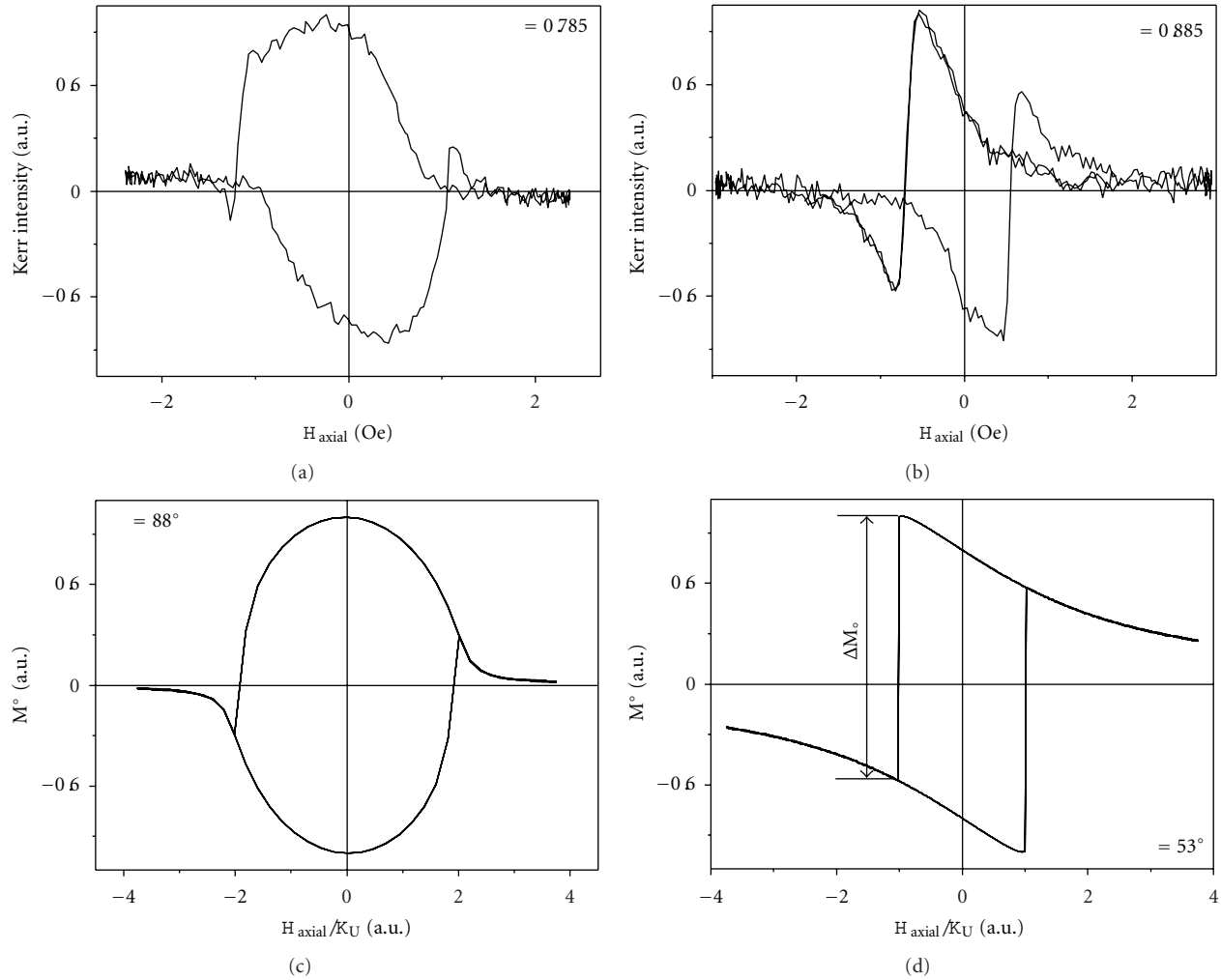


FIGURE 13: (a)-(b) experimental transverse Kerr effect dependencies on axial magnetic field for two wires with different thickness of glass covering. (c)-(d) calculated dependencies of circular magnetization on normalized axial magnetic field for two angles of the anisotropy direction ϕ .

direction. For the angles close to 60° the jump of the magnetization occurs at the moment when the direction of the magnetization is close to the circular magnetization. Because of that the value of the ΔM_{CIRC} is large for these angles. When the angle of helicity approximates to 0° , the inclination of the magnetization decreases. The Kerr effect experimental results and the results of the calculation have been compared taking into account the value and position of the jump of the circular magnetization ΔM_{CIRC} . This jump is related to the overcoming of the helical hard axis. The shape of the calculated hysteresis curves, and, in particular, the value of the jump ΔM_{CIRC} is very sensitive to the value of the angle of the anisotropy. We can conclude that the angle of the helical anisotropy in the surface of the studied microwires is $88^\circ \pm 1^\circ$ for the wire with $\rho = 0.785$ and $53^\circ \pm 1^\circ$ for the wire with $\rho = 0.885$. The results of the comparison are presented in Figures 13(c) and 13(d) (transversal projection).

Based on the same calculation, we have analysed the bulk hysteresis curves (Figure 14), taking into account that these

curves have the information about the axial magnetization reversal in the whole volume of the wire. Following the above-mentioned criteria, we have determined the angles of the helical anisotropy which could be attributed to the experimental volume hysteresis: $70^\circ \pm 1^\circ$ for the wire with $\rho = 0.785$ and $45^\circ \pm 1^\circ$ for the wire with $\rho = 0.885$.

As it is possible to see, the angles gotten from the analysis of the experimental results obtained by Kerr effect and the conventional method for the same microwires are different. The conventional curves present information about the magnetization reversal averaged through the wire volume, and the Kerr effect curves reflect the magnetization reversal in the thin surface layer of the wire. Based on the comparison of the obtained results, we can say that there is some distribution of the anisotropy angle in the wire, and that this angle increases in the approximation to the surface. The difference Δ between the averaged and the surface values of the angle is different for the two studied wires: 18 for the wire with $\rho = 0.785$ and 8 for the wire with $\rho = 0.885$.

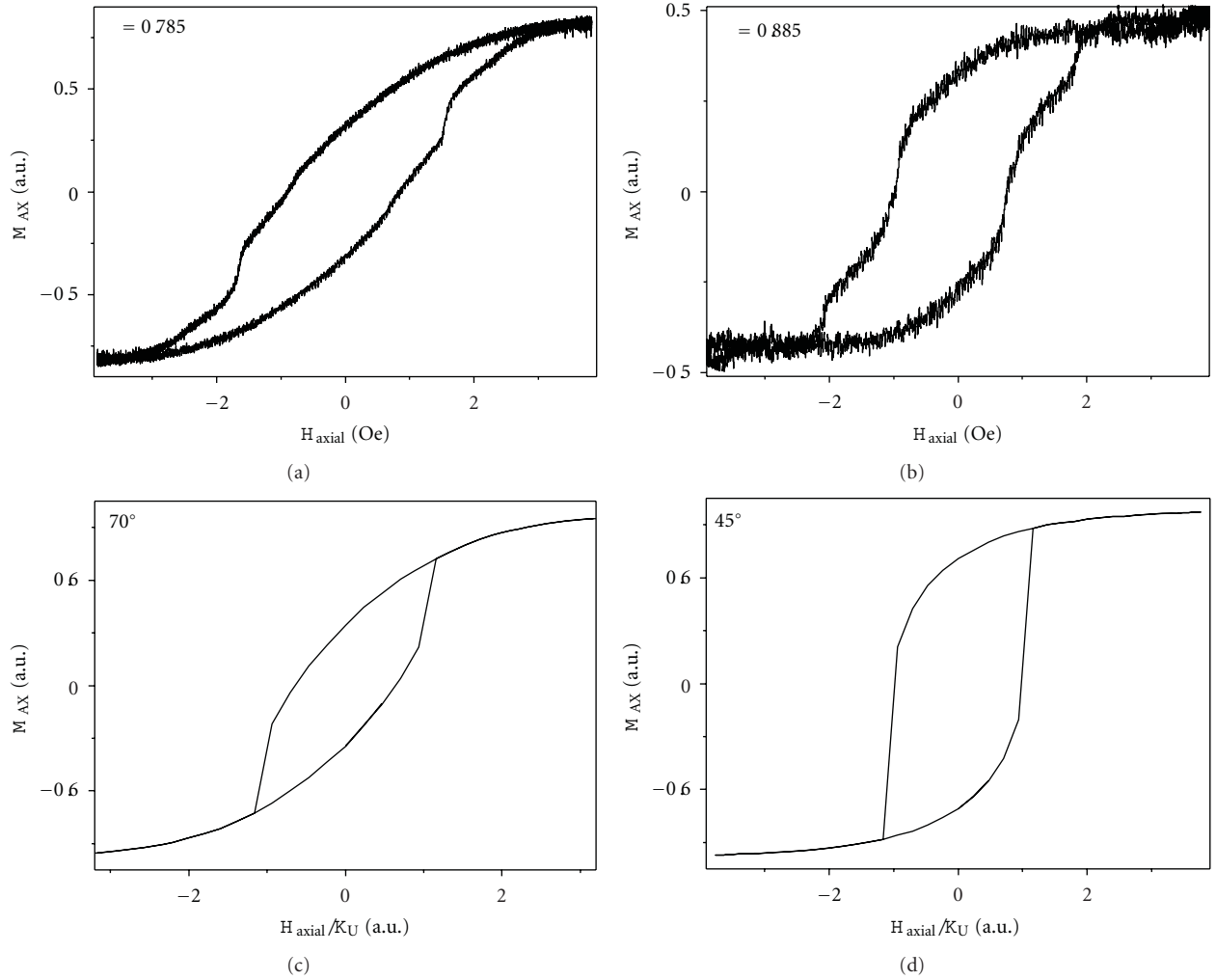


FIGURE 14: (a)-(b) experimental bulk dependencies on axial magnetic field for the two wires with different thickness of glass covering. (c)-(d) calculated dependencies of axial magnetization on normalized axial magnetic field for two angles of anisotropy direction ϕ .

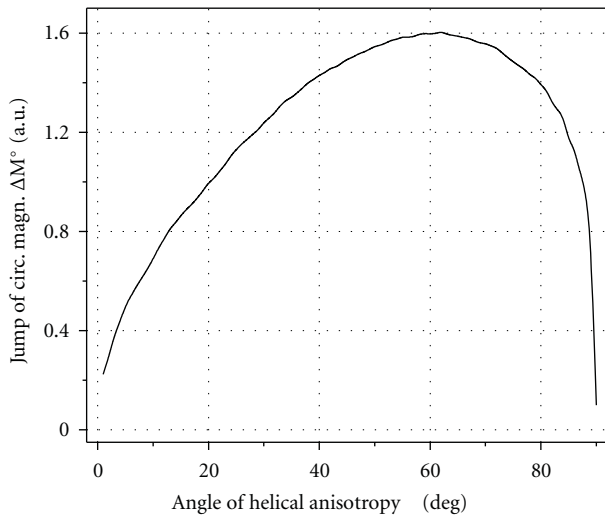


FIGURE 15: Calculated dependence of the jump of the circular magnetization ΔM_{CIRC} on the angle of helical anisotropy ϕ .

It could mean that the distribution of the anisotropy angle is more inhomogeneous for the wire with $\rho = 0.785$. In turn, it is related to the different distribution of the internal stress inside the wire.

Frequency dependence of the coercive field has been studied for the wire with $\rho = 0.885$ using the conventional and Kerr effect techniques. The results of the conventional experiments are presented in Figure 16. Frequency dependence of the coercive field H_C has been analyzed using the calculations presented in [25]. It was shown that the result of the solution of the equation of domain wall motion in the following relation has been obtained [26]:

$$H_{CD} = H_{CO} + \frac{4fH_0(L + 2I_sA)}{K}, \quad (6)$$

where H_{CD} is the dynamic switching field, H_{CO} is the static coercive field, f is the frequency of the magnetic field, H_0 is the amplitude of the magnetic field, L is the damping coefficient, I_s is the saturation magnetization, K is the elastic

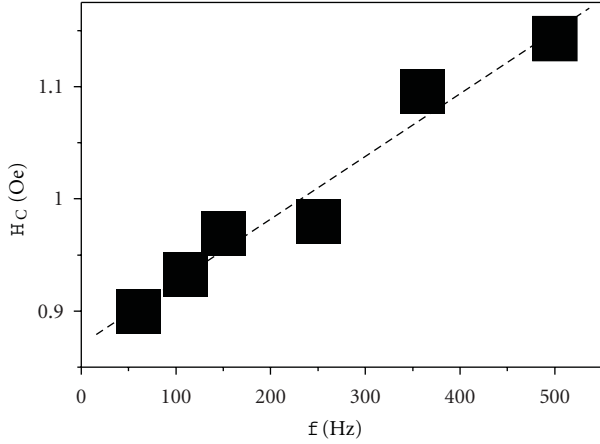


FIGURE 16: Dependence of the volume coercive field on the frequency of magnetic field for the wire with $\rho = 0.885$.

coefficient, and A is a proportionality constant. This linear dependence of the coercive field on frequency could be described in terms of domain nucleation mechanism. The nucleation process is associated with the overcoming of the energy barrier. Thermoactivation mechanism of the overcoming was satisfactorily employed for the explanation of the coercive field fluctuations observed in amorphous wires. Frequency of the applied field in this way affects the value of the coercive field. The experimental dependence of the coercive field on the frequency fits well the linear function that gives us possibility to conclude that the above mechanism of magnetization reversal could be applied to this experiment.

Kerr effect dependencies also changed when the frequency of the axial magnetic field increased. But the transformation of the surface curves differs from the transformation of the bulk curves. Figure 17(a) demonstrates the observed decrease of H_{C-MO} and the increase of I_{MAX} (H_{C-MO} should be considered as the field at which the drastic change of the circular magnetization starts, I_{MAX} is the maximal intensity of the Kerr signal during the magnetization reversal). Taking into account that the Kerr intensity is proportional to the transverse magnetization in the surface area of the wire, $I_{MAX} \sim M_{MAX}$, where M_{MAX} is the maximal value of the transverse (circular) magnetization.

Analyzing the results obtained in the Kerr effect experiments, we consider that the magnetization reversal process in the surface area of the wire occurs as the formation of a circular domain in the outer shell. The coercive field H_{C-MO} is, respectively, determined by the circular domain nucleation. The expression for H_{C-MO} can be presented as [26]

$$H_{C-MO} = \frac{\alpha}{M_{MAX}} - NM_{MAX}, \quad (7)$$

where the first term is related to losses of energy at nucleation process and the second term to the demagnetizing field of the nucleus (N is the demagnetizing factor). We consider, within numerical factor, that $\alpha = \sigma/v^{1/3}$, where σ is energy of domain wall, v is critical volume of the nucleus.

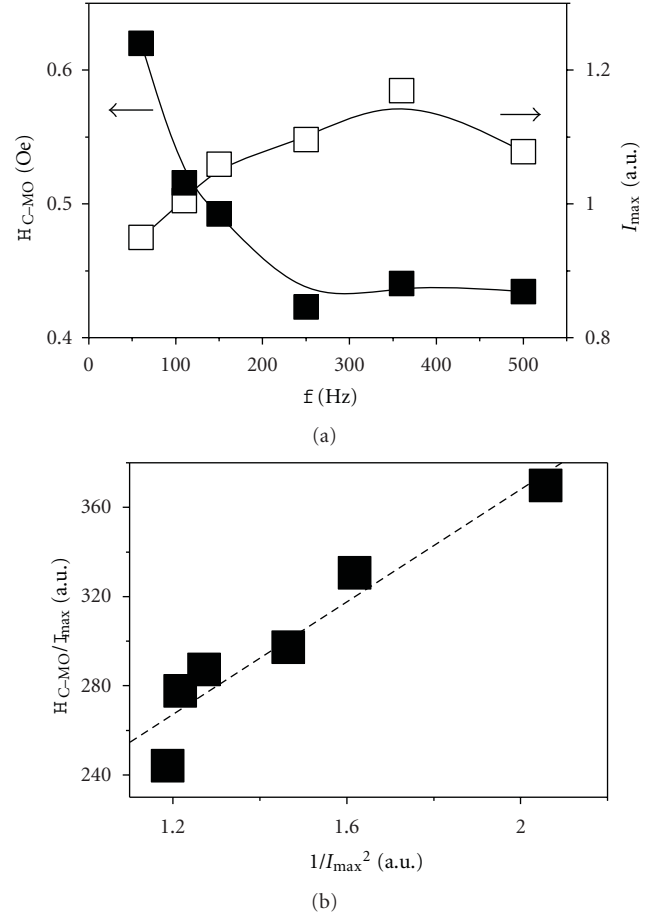


FIGURE 17: (a) H_{C-MO} and I_{MAX} dependencies on frequency of magnetic field for $\rho = 0.885$; (b) H_{C-MO}/M_{MAX} dependence on $1/M_{MAX}^2$.

To verify the above-mentioned assumption regarding the mechanism of the magnetization reversal in the outer shell of the microwire, the H_{C-MO}/I_{MAX} dependence on $1/I_{MAX}^2$ has been plotted (Figure 17(b)). Taking into account that $I_{MAX} \sim M_{MAX}$, this dependence could be considered as the analogy of H_{C-MO}/M_{MAX} ($1/M_{MAX}^2$) dependence. Good fitting of the experimental points by the linear function demonstrates the strong relation between the H_{C-MO} and the M_{CIRC} .

The strong difference of the frequency dependence of the H_C and H_{C-MO} means that the magnetization reversal happens independently enough in the surface and in the volume of the wire. H_{C-MO} is smaller than H_C . Therefore, the nucleation starts in the surface in the moment when the circular projection of the magnetization reaches the sufficient value. This value of this circular projection is the key parameter which changes with the magnetic field frequency. We suppose that one of the possible reasons of this change is the following one. The increase of the frequency means the growth of the velocity of the increase of the magnetic field dH/dt . Therefore, the magnetic field increases more quickly for the higher frequency. The quicker increase of magnetic field causes the quicker increase of the circular magnetization. Therefore, for the higher frequency

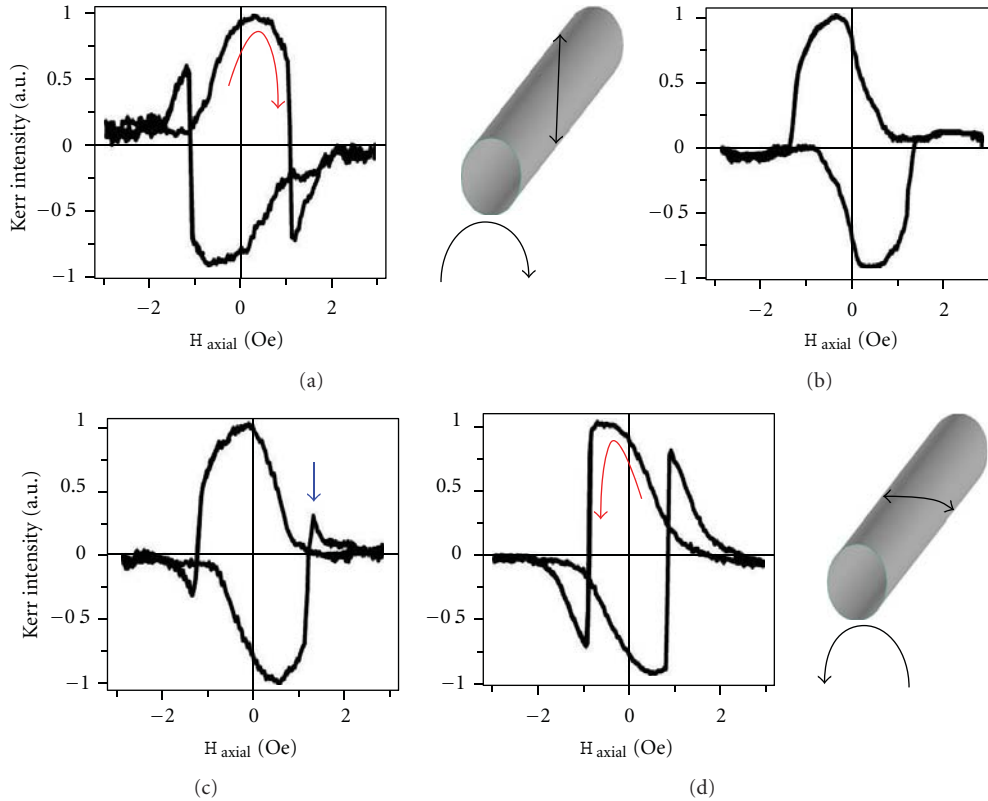


FIGURE 18: Transverse Kerr effect dependence on the magnetic field applied along the microwire axis in the presence of torsion stress. (a) $\tau = -22 \pi \text{ rad m}^{-1}$, (b) $\tau = -2.2 \pi \text{ rad m}^{-1}$, (c) $\tau = 0$, and (d) $\tau = 8.9 \pi \text{ rad m}^{-1}$. Insets: schematically pictures of the inclination of the axis of helical anisotropy induced by the torsion stress.

the magnetization could reach the larger value in the moment when the domain nucleus becomes the stable one, that is, in the moment close to the nucleation. Finally, the relation of the dH/dt and the probability of the nucleation are realized in the decrease of the H_{C-MO} with frequency.

We consider that the surface magnetization reversal is determined mainly by the nucleation mechanism. The sharpness of the ΔM_{CIRC} jump (Figure 13(b)) and our early Kerr microscopy study of the magnetization reversal in amorphous wires [27] permit us to make such conclusion.

Equation (7) is used in general for the temperature dependence of the coercive field. Earlier we have used it for the frequency dependence of the coercive field [28], and we believe that this application is reasonable taking into account the similar character of the influence of the temperature and frequency on the probability of the domain nucleation.

For the determination of the angle of helical anisotropy, we applied the calculation which did not include the domain wall motion, while for the frequency experiments we use the equation which takes into account the nucleation and domain wall motion. For the studied case, the shape of the hysteresis curve and, particularly, the value and the position of the ΔM_{CIRC} jump, which is the value we used in the analysis, are determined mainly by the direction of the helical anisotropy and to a lesser degree, by the details of the domain wall motion. But for the dependencies of the coercive field

on the frequency, the features of the magnetization reversal become important. Such as known [25], the change of the frequency of the external magnet field influences strongly on the mechanism of the magnetic reversal in the wires.

9. Torsion Stress-Induced Transformation of Surface Magnetic Structure

The process of surface magnetization reversal in the presence of torsion stress of different amplitudes and directions has been studied in microwire of nominal composition of $\text{Co}_{69.5}\text{Fe}_{3.9}\text{Ni}_{11.8}\text{Si}_{10.8}\text{Mo}_2$ ($\rho = 0.79$) (Figure 18) [29].

The magnetization reversal in the surface area of the wires has been studied by transverse magneto-optical Kerr effect method in the presence of axial magnetic field. The torsion stress up to $40 \pi \text{ rad m}^{-1}$ has been applied during the experiments.

The surface magnetization reversal consists of two steps: the magnetization rotation from axial to circular direction in the outer shell following by the magnetization jump between two states with opposite directions of surface circular magnetization. The applied torsion stress induces strong transformation of the surface hysteresis loops. The most essential feature of this transformation is a stress-induced change

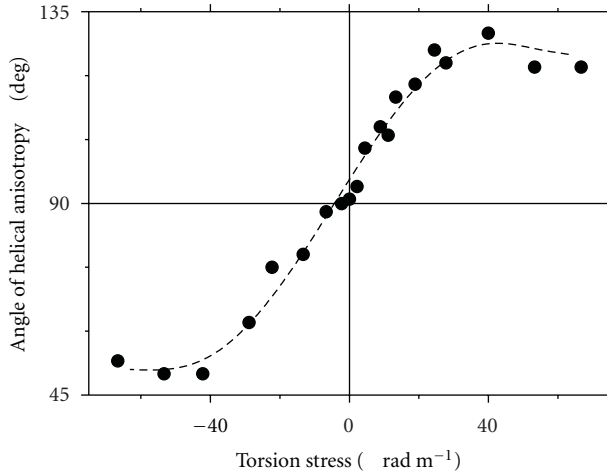


FIGURE 19: Dependence of angle of helical anisotropy on applied torsion stress.

in the value and direction (sign) of the jump of Kerr intensity ΔI (the circular magnetization ΔM_{CIRC}).

It was experimentally confirmed, as predicted, that the torsion stress-induced inclination does not exceed the value of 45° . This inclination along with the growth of the value of the helical anisotropy is the key phenomenon determining the main mechanism of the surface magnetization reversal. As a helical anisotropy increases, this mechanism greatly changes.

The value of jump of the circular magnetization ΔM_{CIRC} for different values of torsion stress was obtained experimentally, and also, by calculating the dependence of the circular magnetization jump ΔM_{CIRC} on the angle of helical anisotropy. Based on numerical analysis of the obtained experimental results, the dependence of helical anisotropy angle on the torsion stress has been obtained for the first time in amorphous wires (Figure 19).

10. Surface Magnetic Domains Nucleation and Transformation

The evolution of the domain structure during the magnetization reversal processes was studied in microwires with nominal composition $\text{Co}_{67}\text{Fe}_{3.85}\text{Ni}_{1.45}\text{B}_{11.5}\text{Si}_{14.5}\text{Mo}_{1.7}$ with geometric ratio $\rho = 0.79$ in the presence of circular magnetic field [30].

The circular magnetic domains could be observed because of the out-of-plane components of the surface magnetization that transforms to black-white contrast when the polarized light reflects from the cylindrical-shape surface of the microwire. The observations of circular magnetic domain images structures were performed by optical polarizing microscope using polar magneto-optical Kerr effect geometry. In this configuration, we can observe the magnetic areas with out-of-plane component magnetization concerning an optical axis of objective and identify domains with the magnetization of opposite directions. “Leica” microscope was

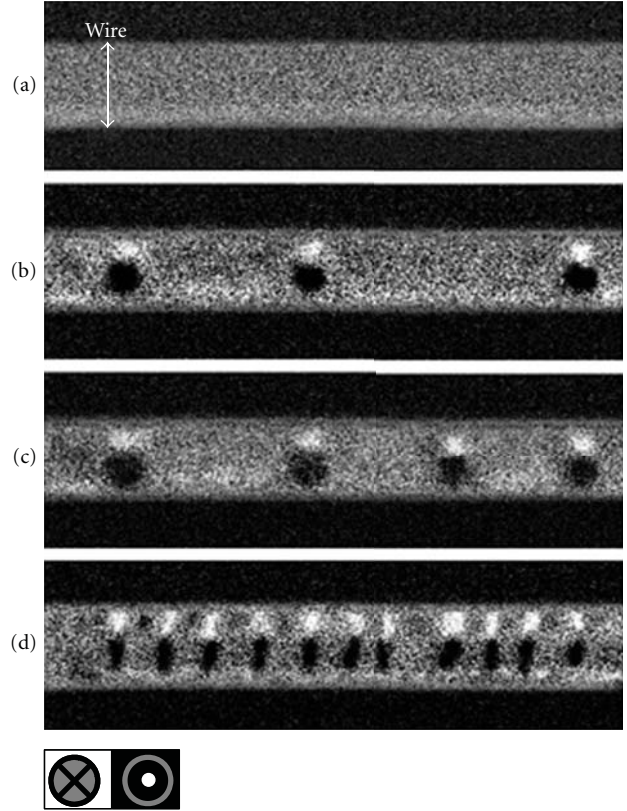


FIGURE 20: The images of magnetic domain structure registered in different values of circular magnetic field: (a) 0, (b) 0.3 Oe, (c) 0.36 Oe, and (d) 0.45 Oe. Image size is $170 \times 50 \mu\text{m}^2$.

equipped with halogen lamp and high-sensitivity “Hamamatsu” digital charge-coupled device (CCD) camera. The following procedure was used for the registration of the surface magnetic domain image: the microwire was saturated in circular magnetic field, then the field was reduced to zero, and the reference image was recorded. In the next step, images in real time during the increase of the magnetic field were registered. After image processing, each image was a result of difference between two images: domain structure at various times and the reference image.

The results of the polar MOKE microscopy experiments are presented in Figure 20. The magnetization reversal starts from a single-domain state (Figure 20(a)). We noticed that the magnetization reversal could be originated at any part of the microwire. At the first stage of the magnetization reversal, the nucleation and fast domain wall motion cause the formation of relatively small circular domains Figure 20(b). Increasing the circular magnetic field leads to the increase in the number of domains with practically equal width Figure 20(c). At the next stage, a strong rearrangement of the domain structure takes place: the number of domains increases sharply Figure 7(d). The magnetization reversal finishes with the formation of a reversed single-domain state.

The magnetization reversal occurs mainly by domain nucleation that is determined basically by the local nucleation sites distribution. The irregular rearrangement of

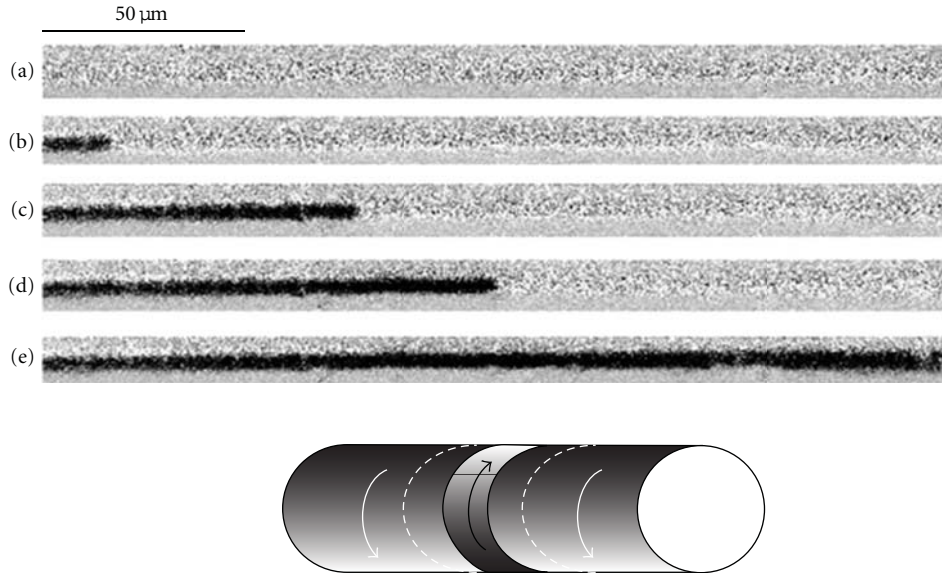


FIGURE 21: Photographs of circular domain formation and domain walls propagation in the presence of circular field of constant amplitude and increasing time duration, $I = 0.38$ mA, $H_{AX} = 0.27$ Oe. (a) $t = 0$, (b) $t = 310$ msec, (c) $t = 372$ msec, (d) $t = 434$ msec, and (e) $t = 496$ msec.

the circular domain structure takes place during the magnetization reversal that was not observed earlier in amorphous magnetic microwires. The circular magnetic domain nucleation in amorphous microwires could be described successfully by the thermoactivated mechanism.

11. Observation of Circular Giant Barkhausen Jumps

First, surface magnetization reversal has been studied using MOKE magnetometer as a function of circular magnetic field in the presence of axial DC bias field in microwire with nominal composition $\text{Co}_{67}\text{Fe}_{3.85}\text{Ni}_{1.45}\text{B}_{11.5}\text{Si}_{14.5}\text{Mo}_{1.7}$ ($\rho = 0.79$) [31]. The jumps of the circular magnetization, associated with Barkhausen jumps, have been observed. These jumps are related to the mentioned effect of circular magnetic bistability. It was found that the application of the axial magnetic field transforms the hysteresis curve in such a way, that the jump of the circular magnetization becomes sharper. Observed change of the hysteresis loop is related to the transformation of the helical magnetic structure induced by the axial magnetic field. In the presence of the axial field of some special value, the jump occurs between two circularly magnetized states.

We have two processes with different velocities of the magnetization reversal. We assume that this difference in velocity reflects the difference in the process of domain nucleation and domain walls propagation. To verify this supposition and to elucidate the details of the Barkhausen jumps, we have performed the MOKE microscope experiments (Figure 21).

Observation of the circular magnetic domain structures in microwires was performed by an optical polarizing microscope to detect the longitudinal MOKE. A Carl Zeiss Jenapol

microscope was equipped with Xe-lamp and a Cool SNAP (Princeton Instruments) high-sensitivity camera having a 1300×1030 pixels, cooled CCD element. The magnetic contrast of the domain structure was improved by image processing software based on LABVIEW.

Figure 21 shows the surface magnetization reversal for the case of $H_{AX} \neq 0$. The successive increase of the time duration of the constant circular magnetic field induces the nucleation of solitary circular domain following by the propagation of the domain wall moving for a long distance along the microwire. This scenario could be considered as classical realization of the giant Barkhausen jump.

Using the axial magnetic field as a unique external parameter, we have achieved that the surface magnetization reversal realizes in the form of sharp giant Barkhausen jump magnetic microwires. We have demonstrated for the first time that this jump is characterized by the quick motion of the solitary domain wall which overpasses long distances of about hundreds of micrometers. We have shown that the extensive motion of the solitary domain wall really exists in magnetic wires, and that it is the determinative constituent of the surface giant Barkhausen jump.

12. Conclusions

The high GMI ratio can be observed in thin glass-coated ferromagnetic microwires with adequate chemical composition and geometry. Changing both parameters, we are able to tailor the GMI ration in Co-rich microwires. It was found that the induced transverse magnetic anisotropy allows us to predict the existence of the magneto-impedance effect. Application of the MOKE method allowed to correlate the axial magnetic field dependences of GMI ratio and MOKE hysteresis loops: a maximum of GMI ratio occurs

approximately at the same field as the sharp change of the circular magnetization on the surface loop.

Taking into account the essential role of the helical magnetic anisotropy in the GMI effect, the magnetization reversal has been studied in the Co-rich microwires with helical magnetic structure. The value of the angle of the helical anisotropy in the surface and in the volume of the wires was determined. Also, it was found that the increase of the frequency of the external axial magnetic field induces the change of the coercive properties in the volume and in the surface of the microwire: the coercive field of the surface magnetic structure decreases with the frequency of the magnetic field when the volume coercive field increases. The surface coercive field is mainly determined by the value of the magnetization in the outer shell of the wire.

The surface and bulk measurements of Co-rich microwires with different chemical composition (especially, the different Mn content) demonstrate the variety of the shapes of magnetization reversal loops, that can be attributed to the change of sign of the magnetostriction. The rectangular shape of the surface hysteresis loop in circular magnetic field of the microwire with $x = 0.07$ can be interpreted by considering that the magnetization process takes place by large Barkhausen jump of circular domain structure, while the rectangular shape of the hysteresis loop in axial magnetic field of the microwire with $x = 0.11$ could be attributed to the large Barkhausen jump within the axial domain structure.

The circular bistability and related circular giant Barkhausen jump are the basic effects which determine the character of the surface magnetization reversal. The giant Barkhausen jump is followed by the formation of the circular domain structure at the surface of the microwire. At the special conditions the long-distance motion of the solitary circular domain wall is observed as a classical realization of the giant Barkhausen jump.

The strong transformation of the surface domain structure takes place in the presence of tensile and torsion external stresses. The direct relation between the angle of helical anisotropy and the value of the torsion stress has been established. The limit values of the angle of the helical anisotropy have been experimentally determined.

References

- [1] L. V. Panina and K. Mohri, "Magneto-impedance effect in amorphous wires," *Applied Physics Letters*, vol. 65, no. 9, pp. 1189–1191, 1994.
- [2] V. Zhukova, A. Chizhik, A. Zhukov, A. Torcunov, V. Larin, and J. Gonzalez, "Optimization of giant magnetoimpedance in Co-rich amorphous microwires," *IEEE Transactions on Magnetics*, vol. 38, no. 5 I, pp. 3090–3092, 2002.
- [3] A. Zhukov, V. Zhukova, J. M. Blanco, and J. Gonzalez, "Recent research on magnetic properties of glass-coated microwires," *Journal of Magnetism and Magnetic Materials*, vol. 294, no. 2, pp. 182–192, 2005.
- [4] A. Zhukov, J. González, M. Vázquez, V. Larin, and A. Torcunov, "Nanocrystalline and amorphous magnetic microwires," in *Encyclopedia of Nanoscience and Nanotechnology*, H. S. Nalwa, Ed., vol. 23, chapter 62, pp. 1–22, American Scientific Publishers, 2004.
- [5] R. Hasegawa, "Nonmagnetostrictive glassy Co-Fe-Ni-Mo-B-Si alloys," *Journal of Applied Physics*, vol. 53, no. 11, pp. 7819–7821, 1982.
- [6] A. Zhukov, J. M. Blanco, J. González, M. J. G. Prieto, E. Pina, and M. Vázquez, "Induced magnetic anisotropy in Co-Mn-Si-B amorphous microwires," *Journal of Applied Physics*, vol. 87, no. 3, pp. 1402–1409, 2000.
- [7] A. F. Cobeño, A. Zhukov, A. R. De Arellano-López et al., "Physical properties of nearly zero magnetostriction Co-rich glass-coated amorphous microwires," *Journal of Materials Research*, vol. 14, no. 9, pp. 3775–3783, 1999.
- [8] A. Chizhik, J. Gonzalez, A. Zhukov, and J. M. Blanco, "Magnetization reversal of Co-rich wires in circular magnetic field," *Journal of Applied Physics*, vol. 91, no. 1, pp. 537–539, 2002.
- [9] M. Knobela, C. Gómez-Polo, and M. Vázquez, "Evaluation of the linear magnetostriction in amorphous wires using the giant magneto-impedance effect," *Journal of Magnetism and Magnetic Materials*, vol. 160, pp. 243–244, 1996.
- [10] J. Velázquez, M. Vázquez, and A. P. Zhukov, "Magnetoelastic anisotropy distribution in glass-coated microwires," *Journal of Materials Research*, vol. 11, no. 10, pp. 2499–2505, 1996.
- [11] A. F. Cobeño, A. Zhukov, J. M. Blanco, and J. Gonzalez, "Giant magneto-impedance effect in CoMnSiB amorphous microwires," *Journal of Magnetism and Magnetic Materials*, vol. 234, no. 3, pp. L359–L365, 2001.
- [12] N. A. Usov, A. S. Antonov, and A. N. Lagar'kov, "Theory of giant magneto-impedance effect in amorphous wires with different types of magnetic anisotropy," *Journal of Magnetism and Magnetic Materials*, vol. 185, no. 2, pp. 159–173, 1998.
- [13] J. Velázquez, M. Vázquez, and A. P. Zhukov, "Magnetoelastic anisotropy distribution in glass-coated microwires," *Journal of Materials Research*, vol. 11, no. 10, pp. 2499–2505, 1996.
- [14] J. González, K. Kułakowski, P. Aragonese, J. M. Blanco, and E. Irurieta, "Stress dependence of bistability in a zero-magnetostrictive amorphous wire," *Journal of Materials Science*, vol. 30, no. 20, pp. 5173–5177, 1995.
- [15] J. González, A. Chizhik, A. Zhukov, and J. M. Blanco, "Surface magnetic behavior of nearly zero magnetostrictive Co-rich amorphous microwires," *Journal of Magnetism and Magnetic Materials*, vol. 258–259, pp. 177–182, 2003.
- [16] F. B. Humphrey, K. Mohri, J. Yamasaki, H. Kawamura, R. Malmhäll, and I. Ogasawara, "Large barkhausen discontinuities in co-based amorphous wires with negative magnetostriction," in *Magnetic Properties of Amorphous Metals*, A. Hernando, V. Madurga, M. C. Sánchez-Trujillo, and M. Vázquez, Eds., p. 110, North-Holland, Amsterdam, The Netherlands, 1987.
- [17] A. Chizhik, C. Garcia, J. Gonzalez, A. Zhukov, and J. M. Blanco, "Study of surface magnetic properties in Co-rich amorphous microwires," *Journal of Magnetism and Magnetic Materials*, vol. 300, no. 1, pp. e93–e97, 2006.
- [18] B. K. Ponomarev and A. P. Zhukov, "Fluctuations of start field exhibited by amorphous alloy," *Soviet Physics, Solid State*, vol. 26, p. 2974, 1984.
- [19] K. Mohri and S. Takeuchi, "Sensitive bistable magnetic sensors using twisted amorphous magnetostrictive ribbons due to Matteucci effect," *Journal of Applied Physics*, vol. 53, no. 11, pp. 8386–8388, 1982.
- [20] L. Kraus, S. N. Kane, M. Vázquez et al., "Tensor components of the magnetization in a twisted Fe-rich amorphous wire," *Journal of Applied Physics*, vol. 75, no. 10, pp. 6952–6954, 1994.

- [21] J. González, N. Murillo, V. Larin, J. M. Barandiarán, M. Vázquez, and A. Hernando, "Magnetoelastic behavior of glass-covered amorphous ferromagnetic microwire," *IEEE Transactions on Magnetics*, vol. 33, no. 3, pp. 2362–2365, 1997.
- [22] V. Zhukova, N. A. Usov, A. Zhukov, and J. Gonzalez, "Length effect in a Co-rich amorphous wire," *Physical Review B*, vol. 65, no. 13, Article ID 134407, 7 pages, 2002.
- [23] A. Chizhik, J. M. Blanco, A. Zhukov et al., "Surface and bulk magnetic hysteresis loops of Co-rich glass covered microwires," *IEEE Transactions on Magnetics*, vol. 42, no. 12, pp. 3889–3892, 2006.
- [24] M. Vázquez and A. Hernando, "A soft magnetic wire for sensor applications," *Journal of Physics D*, vol. 29, no. 4, pp. 939–949, 1996.
- [25] A. Zhukov, M. Vázquez, J. Velázquez, C. García, R. Valenzuela, and B. Ponomarev, "Frequency dependence of coercivity in rapidly quenched amorphous materials," *Materials Science and Engineering A*, vol. 226–228, pp. 753–756, 1997.
- [26] H. Kronmüller, "Micromagnetic background of hard magnetic materials," in *Supermagnets, Hard Magnetic Materials*, G. J. Long and F. Grandjean, Eds., p. 461, Kluwer Academic, Dordrecht, The Netherlands, 1991.
- [27] A. Chizhik, J. Gonzalez, J. Yamasaki, A. Zhukov, and J. M. Blanco, "Vortex-type domain structure in Co-rich amorphous wires," *Journal of Applied Physics*, vol. 95, no. 5, pp. 2933–2935, 2004.
- [28] A. Chizhik, A. Zhukov, J. Gonzalez, and J. M. Blanco, "Magneto-optical investigation of high-frequency electric current influence on surface magnetization reversal in Co-rich amorphous microwires," *Journal of Applied Physics*, vol. 97, no. 7, Article ID 073912, pp. 1–6, 2005.
- [29] A. Chizhik, J. Gonzalez, P. Gawronski, K. Kulakowski, A. Zhukov, and J. M. Blanco, "Torsion and tension stress induced transformation of surface magnetic structure in Co-rich amorphous microwires," *Journal of Non-Crystalline Solids*, vol. 353, no. 8–10, pp. 935–937, 2007.
- [30] A. Chizhik, A. Zhukov, A. Stupakiewicz, A. Maziewski, J. M. Blanco, and J. Gonzalez, "Kerr microscopy study of magnetic domain structure changes in amorphous microwires," *IEEE Transactions on Magnetics*, vol. 45, no. 10, Article ID 5257388, pp. 4279–4281, 2009.
- [31] A. Chizhik, A. Stupakiewicz, A. Maziewski, A. Zhukov, J. Gonzalez, and J. M. Blanco, "Direct observation of giant Barkhausen jumps in magnetic microwires," *Applied Physics Letters*, vol. 97, no. 1, Article ID 012502, 2010.

Research Article

Sintering of Soft Magnetic Material under Microwave Magnetic Field

Sadatsugu Takayama,¹ Jun Fukushima,¹ Junichi Nishijo,² Midori Saito,² Saburo Sano,³ and Motoyasu Sato¹

¹National Institute for Fusion Science, 322-6 Orochi-cho, Toki-shi, Gifu 509-5292, Japan

²Institute for Molecular Science, 38 Nishigo-Naka, Myodaiji, Okazaki-shi, Aichi 444-8585, Japan

³National Institute of Advanced Industrial Science and Technology, 2266-98 Anagahora, Shimoshidami, Moriyama-ku, Nagoya, Aichi 463-8560, Japan

Correspondence should be addressed to Sadatsugu Takayama, takayama.sadatsugu@nifs.ac.jp

Received 1 August 2011; Revised 2 January 2012; Accepted 12 January 2012

Academic Editor: Arcady Zhukov

Copyright © 2012 Sadatsugu Takayama et al. This is an open access article distributed under the Creative Commons Attribution License, which permits unrestricted use, distribution, and reproduction in any medium, provided the original work is properly cited.

We have developed a simple process for sintering of soft magnetization materials using microwave sintering. The saturated magnetization (M_s) of sintered magnetite was 85.6 emu/g, which was as high as 95% of magnetite before heating (90.4 emu/g). On the other hand, the averaged remanence (M_r) and coercivity (H_c) of the magnetite after heating were 0.17 emu/g and 1.12 Oe under measuring limit of SQUID, respectively. For the sintering process of soft magnetic materials, magnetic fields of microwave have been performed in nitrogen atmosphere. Therefore, a microwave single-mode system operating at a frequency of 2.45 GHz and with a maximum power level of 1.5 kW was used. We can sinter the good soft magnetic material in microwave magnetic field. The sample shrank to 82% theoretical density (TD) from 45%TD of green body. The sintered sample was observed the microstructure by TEM and the crystal size was estimated the approximate average size is 10 nm.

1. Introduction

Sintering of magnetite (Fe_3O_4) with nanocrystals has long been of great interest because of their immense technological applications especially in the magnet, motor, and electric parts. Nanoparticles with superparamagnetic properties have great potential to achieve such desirable properties.

Recently, various methods have been developed to synthesize Fe_3O_4 particles in nanometer size range. These methods were the electrochemical synthesis [1], the reactive magnetron sputtering [2], chemical reaction [3], and so on. However, the magnetic properties of magnetite-based nanoparticles or films highly depend upon the synthesis procedure.

Microwave irradiation to materials is a new comer for our civilization with a history of only half century. The temperatures of the surroundings are colder than that of targets, that can easily be imagined by a home microwave oven. It clearly suggests that the energy transfer mechanism

in microwave heating is quite different from the traditional heating process. Roy et al. reported sintering of metal powders by microwave in 1999 [4] and decrystallization of ferrite magnetic materials by microwave magnetic field heating in 2002 [5]. Therefore, we have studied the sintering of soft magnetization under microwave heating.

2. Experimental Setup

The samples had been heated by magnetic field of microwave. Figure 1 shows a schematic drawing of experimental setup of magnetic field heating of 2.45 GHz microwave. The magnetic or electric fields of microwave can be separated on positions in the single-mode cavity. High-frequency alternated magnetic field was applied to a sample placed on the magnetic field node in the TE₁₀₃ single-mode cavity with the cross-section of 27.2 mm × 85 mm. The generator, PRJ-1000L, Ewig Co., Ltd., supplied microwave to the cavity at the frequency 2.45 GHz. The microwave power

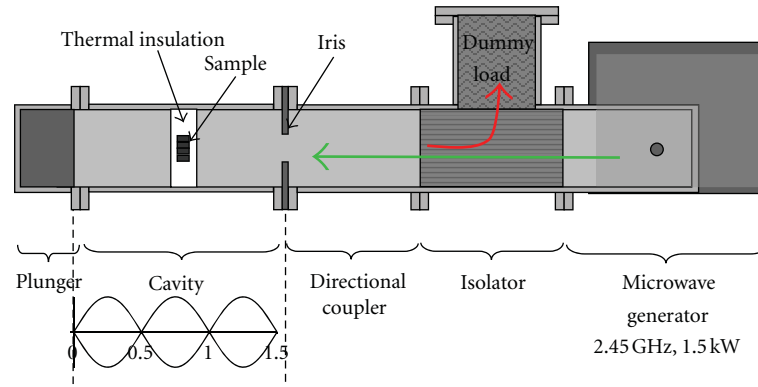


FIGURE 1: The schematic drawing of experimental setup of microwave heating.

varied from 50 to 1500 watts controlling by the DC power supply which consisted of AC-DC inverter. The infrared pyrometer, IGAR12-LO, IMPAC Infrared Co., Ltd., measured the temperature of the sample through the 6 mm hole drilled through the end plunger of cavity. The waveguide was evacuated to 10^{-4} Pa by turbo molecular pump with 100 L/s pumping speed and changed to nitrogen gas in the cavity. During the heating, nitrogen gas was flowing in cavity.

The samples were prepared by uniaxial pressing of magnetite powder (FEO07PB) with the purity of 99 weight% from Kojundo Chemical Laboratory Co., Ltd., Japan. The sample density was up to 45% of the theoretical density (TD) by geometrical method. The grain size of the magnetite was less than 1 micrometer. The size of the sample was 8 mm diameter and 4 mm thick pellet of 0.5 (g) that was small enough not to disturb the criterion for fundamental resonance in the cavity. The four samples were put in the magnetic field maxima in the cavity supported by thermal insulator made of a lightweight alumina silica fiber board.

3. Experimental

The graphs in Figure 2 show a typical progress of process temperatures measured during microwave heating of magnetite samples. The microwave power was controlled manually. The microwave power shows remainder of input power and reflex power. For sintering experiments, the magnetite powder compacts were heated to the sintering temperature of 1000°C for 10 min followed by 70 min soak time. In initial step heating during the first 30 min, the sample temperature was dramatically changing. Thereafter, the sample temperature was settling and microwave power was lower as 270 watt.

Figure 3 shows a magnetite sample sintered by using H-filed of microwaves at 1000°C . The sample shrank to 6.2 mm diameter from 8 mm diameter for sintering. The sintered sample was found to be oxidized on the only surface. The linear shrinkage of the sample was 17% and no remarkable change in the shape was observed. The sample shrank to 82% theoretical density (TD) from 45%TD of green body.

Figure 4 shows the X-ray diffraction profile of the magnetite after heating at 1000°C . It shows Bragg reflections of

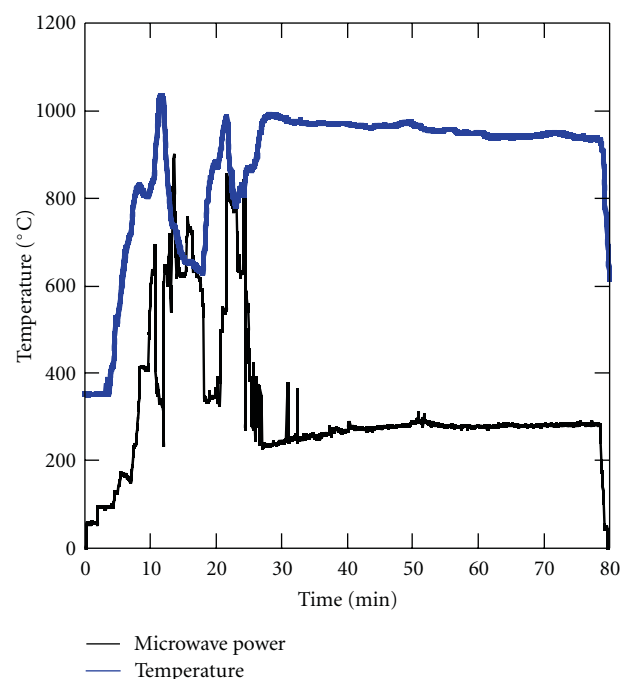


FIGURE 2: The typical progress of process temperature measured during microwave heating.

both magnetite and hematite. The surface of sample was oxidized because the nitrogen gas was flowing in cavity during heating.

The high-resolution transmission electron microscope (TEM; a JEOL JEM-3200) observed the images of the original magnetite powder before heating and those excited in the selected magnetic field. The original crystal can see the well-ordered lattice patterns over the whole crystal; therefore the original crystal has flat and homogeneous surfaces. Figure 5 shows TEM image and selected area electron diffraction pattern. The sample heated in the magnetic field exhibits the presence of randomly oriented nano-crystal. The crystal sizes of this sample are of approximate average size 10 nm. The randomness of the lattice orientation indicates that the particle-particle magnetic interaction is negligible in



FIGURE 3: The picture of magnetite sintered by using magnetic field of microwave at 1000°C.

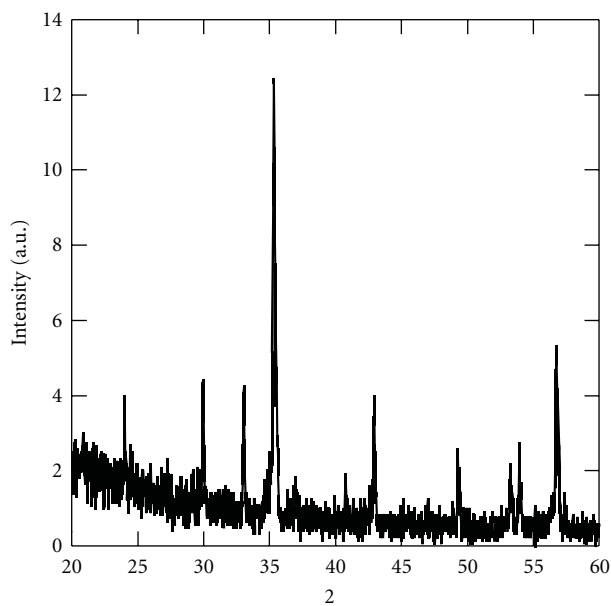
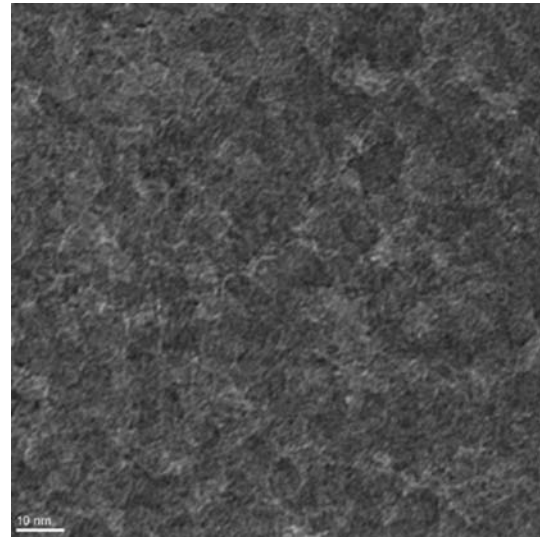


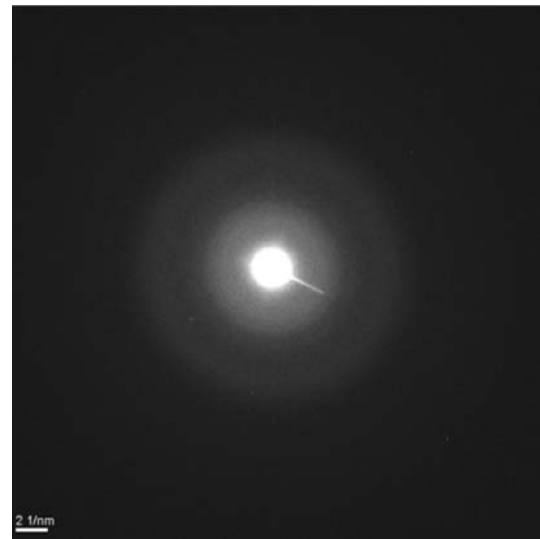
FIGURE 4: X-ray diffraction of samples heated by magnetic field at 1000°C.

the heating cooling process. If each magnetic domain should be highly excited by application of the oscillating magnetic field, cohesive rotation of the domains can be induced synchronously with the oscillating field. It is very interesting that the temperature increase in the sample is accelerated at a temperature close to the Curie point and never rises above 1000°C but it is well below the melting point of 1535°C.

The macroscopic magnetizations of samples were measured by SQUID without zero correction (Quantum Design MPMS-XL7). Figure 6 shows the hysteresis loop of magnetite at 300 K. As can be seen in Figure 6, the saturated magnetization (M_s) of sintered magnetite was 85.6 emu/g, which was as high as 95% of magnetite before heating (90.4 emu/g).



(a)



(b)

FIGURE 5: TEM image of magnetite sintered by using magnetic field of microwave at 1000°C.

The averaged remanence (M_r) and coercivity (H_c) of the magnetite before heating were 11.74 emu/g and 108.9 Oe, respectively. On the other hand, the averaged remanence (M_r) and coercivity (H_c) of the magnetite after heating were 0.17 emu/g and 1.12 Oe under measuring limit of SQUID, respectively. Their M_r value and H_c value of sintered sample became two digits smaller than raw sample for heating by magnetic field of microwave.

4. Conclusion

We have developed a simple process for sintering of soft magnetization materials. For the sintering process of soft magnetic materials, magnetic fields of microwave have been performed in nitrogen atmosphere. Therefore, a microwave

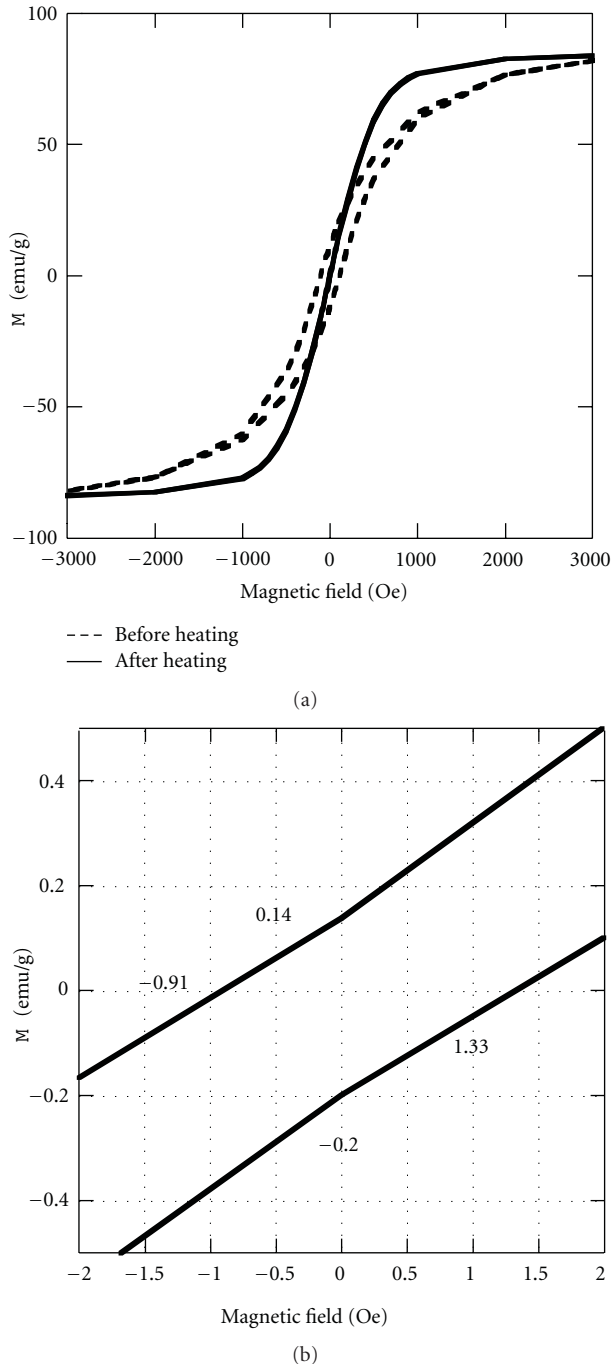


FIGURE 6: (a) The hysteresis loop of the magnetite sintered by using magnetic field of microwave at 1000°C. (b) The M_r and H_c of the magnetite sintered by using magnetic field of microwave at 1000°C.

single-mode system operating at a frequency of 2.45 GHz and with a maximum power level of 1.5 kW was used. We can sinter the good soft magnetic material in microwave magnetic field. The sample shrank to 82% theoretical density (TD) from 45%TD of green body. The sintered sample was observed the microstructure by TEM and the crystal size was estimated the approximate average size is 10 nm.

Using microwave sintering, the M_s of sintered magnetite was 85.6 emu/g, which was as high as 95% of raw magnetite with 90.4 emu/g. On the other hand, the M_r and H_c of the magnetite after heating were 0.17 emu/g and 1.12 Oe under measuring limit of SQUID, respectively.

From TEM and SQUID data, it is suggested that the sintered magnetite under magnetic field of microwave has super-ferrimagnetism.

We expect that it is used in transformer or electromagnetic cores. The macroscopic magnetization of sintered body using microwave can easily reverse direction without dissipating much energy, that is, hysteresis losses. Because of their comparatively low losses, they are extensively used in the cores of transformers and electromagnetic cores in applications such as car industrials.

References

- [1] L. Cabrera, S. Gutierrez, N. Menendez, M. P. Morales, and P. Herrasti, "Magnetite nanoparticles: electrochemical synthesis and characterization," *Electrochimica Acta*, vol. 53, no. 8, pp. 3436–3441, 2008.
- [2] L. Pan, G. Zhang, C. Fan et al., "Fabrication and characterization of Fe_3O_4 thin films deposited by reactive magnetron sputtering," *Thin Solid Films*, vol. 473, no. 1, pp. 63–67, 2005.
- [3] H. K. Lee, S. H. Do, S. H. Kong et al., "The role of magnetite nano particle (MNP) to oxidize nitrobenzene using heterogeneous fenton reaction," in *Proceedings of the World Congress on Engineering and Computer Science (WCECS '10)*, vol. 2, 2010.
- [4] R. Roy, D. Agrawal, J. Cheng, and S. Gedevanishvili, "Full sintering of powdered-metal bodies in a microwave field," *Nature*, vol. 399, no. 6737, pp. 668–670, 1999.
- [5] R. Roy, R. Peelamedu, L. Hurtt, J. Cheng, and D. Agrawal, "Definitive experimental evidence for *Microwave Effects*: radically new effects of separated E and H fields, such as decrystallization of oxides in seconds," *Materials Research Innovations*, vol. 6, no. 3, pp. 128–140, 2002.

Research Article

Metamagnetic Phase Transitions in $(\text{Sm}_{0.5}\text{Gd}_{0.5})_{0.55}\text{Sr}_{0.45}\text{MnO}_3$ Ceramics

Fedor N. Bukhanko

Department of Electronic Properties of Metals, Donetsk Physical and Technical Institute NASU, Donetsk 83114, Ukraine

Correspondence should be addressed to Fedor N. Bukhanko, buhanko@mail.fti.ac.donetsk.ua

Received 4 August 2011; Revised 18 January 2012; Accepted 18 January 2012

Academic Editor: Manh-Huong Phan

Copyright © 2012 Fedor N. Bukhanko. This is an open access article distributed under the Creative Commons Attribution License, which permits unrestricted use, distribution, and reproduction in any medium, provided the original work is properly cited.

The temperature dependences of *ac* magnetic susceptibility of the $(\text{Sm}_{0.5}\text{Gd}_{0.5})_{0.55}\text{Sr}_{0.45}\text{MnO}_3$ ceramics provide evidence of the formation of a mixed insulating state with a specific quantum-disordered phase, in which the domains with a long-range antiferromagnetic order dominate at temperatures below $T_N \cong 48,5$ K. Irreversible metamagnetic phase transition in the ferromagnetically ordered state is carried out at the critical field $H_{c1} \sim 25$ kOe which remains constant in the temperature range from 4.2 K to 60 K. From the analysis of the magnetization isotherms, the conclusion can be made about a spontaneous phase transition into the state with charge and orbital ordering at temperatures below the critical value $T_{CO} \sim 60$ K. It is supposed that short-range charge correlations exist in unusually large interval of temperatures ~ 90 K at temperatures above T_{CO} that considerably exceeds the area of existence of local orbital correlations ~ 50 K.

1. Introduction

Change of the average radius $\langle r_A \rangle$ of a rare-earth ion replacing lanthanum in A-positions of perovskite-like matrixes in $R_{0.55}\text{Sr}_{0.45}\text{MnO}_3$ ($R = \text{Sm}, \text{Eu}, \text{Gd}$) manganites leads to the bicritical phase diagram where the metallic ferromagnetic phase is separated from the dielectric antiferromagnetic phase with charge/orbital (CO/OO) ordering by the first order phase transition [1, 2]. Prominent features which should be observed in experiment close to bicritical point have been predicted: (1) phase transition from a paramagnetic state in the ferromagnetic should be the of first order; (2) the critical temperatures of phase transitions T_{CO} and T_c close to bicritical point should decrease sharply; (3) high sensibility of the sample to external magnetic field near to interphase boundary. These effects arise because of huge fluctuation of several order parameters related to bicritical behavior, which sharply amplifies near to boundary of two phases, where more than two order parameters meet. As a result of the local lattice distortion in $R_{0.55}\text{Sr}_{0.45}\text{MnO}_3$, large structural disorder enhances the phase fluctuation between ferromagnetic metal and charge/orbital-ordered insulator and suppresses their long-range orders [3–5].

The transition between a ferromagnetic (FM) metal and an insulator with short-range charge/orbital correlation induced by the change of average radius $\langle r_A \rangle$ has been investigated for the single crystals $(\text{Sm}_{1-y}\text{Gd}_y)_{0.55}\text{Sr}_{0.45}\text{MnO}_3$ ($0 \leq y \leq 1$) [6]. A systematic study indicates that the long-range ferromagnetic order is kept up to $y \sim 0.5$ (corresponding to $R = \text{Eu}$) with T_c reduced from ~ 130 K to ~ 50 K, while it changes to a spin-glass-like insulator for $y \geq 0.6$. Strong competition was found between long-range ferromagnetic order and paramagnetic disorder or a spin-glass-like insulator with short-range charge/orbital correlation, being controlled by changes of the average radius $\langle r_A \rangle$ or the external magnetic field. No macroscopic phase separation is discerned when high-quality single-crystal specimens are used.

The results of measurements of magnetic susceptibility $\chi(T)$ and magnetization isotherms $M(H)$ in the samples of ceramics of $(\text{Sm}_{0.5}\text{Gd}_{0.5})_{0.55}\text{Sr}_{0.45}\text{MnO}_3$ in strong static and pulse magnetic fields essentially differ from the same measurements made earlier on the single crystals. It is supposed that the reason of a significant disparity of magnetic properties of these systems is the various nature of the ground state in single crystals and the ceramics, related to different values of the structural disorder.

2. Experimental Procedures

In this work, the ceramic samples of $(\text{Sm}_{1-y}\text{Gd}_y)_{0.55}\text{Sr}_{0.45}\text{MnO}_3$ ($0 \leq y \leq 1$) were prepared using the standard solid-state reaction technique. In brief description, homogeneous powders were heat treated during three stages at temperatures of 1000, 1100°C for 10 h, and 1150°C for 24 h with intermediate grinding of as-obtained products. Compacted under pressure of 10 kbar, pellets were sintered in air at 1150°C for 10 h with succeeding temperature drop to the room temperature at the rate of 70°C/hour. Temperature dependences of magnetic susceptibility $\chi(T)$ were measured by induction method at frequencies of 1, 5, 7, and 10 kHz in the temperature range of 4,2–100 K with the help of PPMS-10. Field dependences of magnetization $M(H)$ have been measured in an interval of temperatures of 4,2–200 K in the strong pulse and static magnetic fields. Measurements in pulse fields to 300 kOe at temperatures varied from 20 to 200 K were made by nonindustrial pulse magnetometer, and measurements in static fields to 80 kOe at 4,2 K have been carried out by application of vibrating magnetometer VSM EGG, Princeton Applied Reserch.

3. Experimental Results and Discussion

According to [6], in the $(\text{Sm}_{1-y}\text{Gd}_y)_{0.55}\text{Sr}_{0.45}\text{MnO}_3$ single crystals, the metal ferromagnetic ground state is saved with growth of Gd content only in the range of concentration of $0 \leq y \leq 0.5$. The further increase of y results in the first-order phase transition in dielectric low-temperature state with characteristic signs of spin-glass phase. Unlike the results of article [2], in the given work, the metal ferromagnetic phase was destroyed completely already for $y = 0.5$, that is, associated apparently with larger structural disorder of ceramic samples. Results of measurement of the temperature dependence of *ac* magnetic susceptibility of $(\text{Sm}_{0.5}\text{Gd}_{0.5})_{0.55}\text{Sr}_{0.45}\text{MnO}_3$ gave evidences of formation of long-range antiferromagnetic structure in the samples with the critical temperature $T_N \cong 48,5$ K. The sharp peak of *ac* magnetic susceptibility close to 48,5 K is observed independently of the frequency of measurement (Figure 1) and with a small temperature hysteresis ~ 2 K, which strongly differs from a wide peak $\chi(T)$ in the vicinity of $T_G \approx 45$ K for single crystals [6]. The same sharp peak of magnetic susceptibility had been observed earlier in various antiferromagnets with Heisenberg, XY and Ising type of interaction, on magnetic lattices of dimensionality 1, 2, and 3 [7]. At decrease of the temperature, there is fast growth of $\chi(T)$ for $T \geq T_N$ and then a sharp drop of the susceptibility was found for $T \leq T_N$. As shown in Figure 1, sharp peak of magnetic susceptibility is imposed on continuous paramagnetic increase of a susceptibility with the temperature drop in the wide temperature interval. The magnetic susceptibility intensively rises with fall of temperature of the sample and diverges near to absolute zero of temperatures, that is, characteristic for quantum phase transitions in low-dimensional quantum Heisenberg antiferromagnets with the structural disorder [8–10]. In this phase, low-temperature

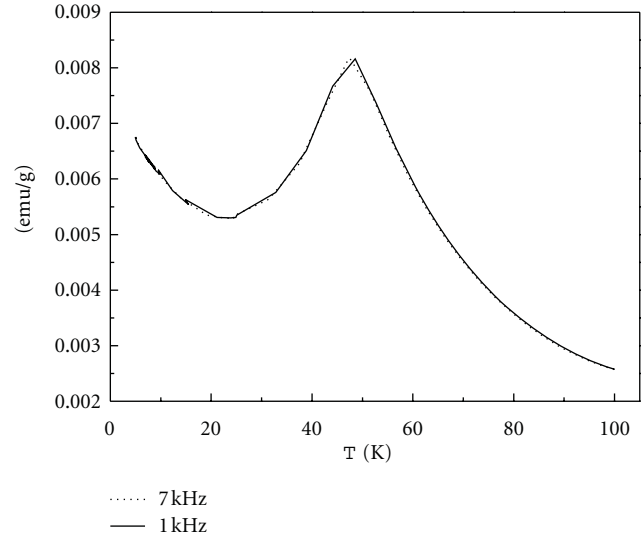


FIGURE 1: Initial *ac* magnetic susceptibility curves $\chi(T)$ in the $(\text{Sm}_{0.5}\text{Gd}_{0.5})_{0.55}\text{Sr}_{0.45}\text{MnO}_3$ ceramics in zero external magnetic field.

uniform susceptibility diverges algebraically with nonuniversal exponents. This is a signature that the quantum-disordered phase is a *quantum Griffiths phase*. Superposition of two various contributions to a low-temperature magnetic susceptibility testifies to the inhomogeneity nature of the ground state of the $(\text{Sm}_{0.5}\text{Gd}_{0.5})_{0.55}\text{Sr}_{0.45}\text{MnO}_3$ ceramics in a zero external magnetic field. Apparently, in these ceramic samples, long-range antiferromagnetism coexists with short-range magnetic correlations in the large temperature interval near absolute zero. It is supposed that the mixed insulating state with a special feature of a quantum-disordered phase with dominating domains of long-range antiferromagnetism is found in the $(\text{Sm}_{0.5}\text{Gd}_{0.5})_{0.55}\text{Sr}_{0.45}\text{MnO}_3$ ceramics at the temperatures below $T_N \cong 48,5$ K. Similar mixed state close to quantum critical point had been discovered recently in the $\text{La}_{2/3}\text{Ca}_{1/3}\text{Mn}_{1-x}\text{Ga}_x\text{O}_3$ manganites in the vicinity of a metal-insulator transition [11, 12].

The variation of an external static magnetic field in an interval ± 6 T at 4,2 K had led to irreversible destruction of mixed phase accompanied by formation of the steady ferromagnetic phase (Figure 2). Field-induced stable FM phase was formed as a result of continuous metamagnetic phase transition induced by growth of an external magnetic field to extremely small critical value $H_{c1} = 25$ kOe with a sharp increase in magnetization $M(H)$ in the form of a step in height ΔM . The further increase of the field to 60 kOe resulted only in insignificant growth of magnetization. At the magnetic field reduction, the induced ferromagnetic phase is saved up to zero field. The subsequent variation field in an interval ± 15 kOe has allowed receiving of a wide hysteresis loop corresponding apparently to an anisotropic ferromagnetic state of the sample at 4,2 K. A distinction of the received magnetization curve $M(H)$ at 4,2 K is large width of the hysteresis loop ($\sim 4,4$ kOe), which corresponds to coercive field $H_c \cong 2,2$ kOe, and rather small size of magnetization of saturation in the field of 60 kOe ~ 60 emu/g, related evidently with the canted state of the manganese spins.

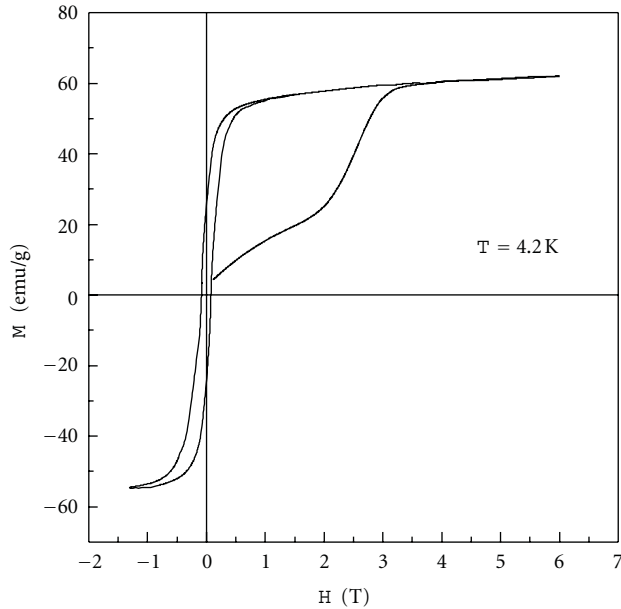


FIGURE 2: Evolution of a magnetization isotherm $M(H)$ of the $(\text{Sm}_{0.5}\text{Gd}_{0.5})_{0.55}\text{Sr}_{0.45}\text{MnO}_3$ sample at 4.2 K induced by metamagnetic phase transition.

Similar behavior of the field dependence of the magnetization was observed in $\text{Pr}_{0.7}\text{Ca}_{0.3}\text{MnO}_3$ at 5.0 K [13]. According to neutron-diffraction experiments, without a magnetic field, $\text{Pr}_{0.7}\text{Ca}_{0.3}\text{MnO}_3$ demonstrates three phase transitions: change of the lattice symmetry at $T_B = 200$ K, antiferromagnetic ordering at $T_N = 140$ K, and canted antiferromagnetism at $T_{CA} = 110$ K. It shows a canted ferromagnetic structure accompanied with antiferromagnetic (AF) components of so-called pseudo-CE-type antiferromagnetic structure at the temperatures below T_{CA} . Furthermore, the charge ordering of Mn^{3+} and Mn^{4+} ions takes place simultaneously with a lattice distortion described as buckling, where MnO_6 octahedra show alternating tilting and cause a doubling of the periodicity of the the lattice along the [010] direction. Although the resistivity of $\text{Pr}_{0.7}\text{Ca}_{0.3}\text{MnO}_3$ shows insulating behavior at zero field, it exhibits an insulator-metal transition at around 4.0 T. An applied field enforces an alignment of the AF components towards the field direction and drives $\text{Pr}_{0.7}\text{Ca}_{0.3}\text{MnO}_3$ into the metallic state by actuating the double-exchange mechanism and destroying the charge ordering. This an insulator-metal transition induced by external magnetic field is accompanied also by a large magnetic hysteresis, that indicates a strong coupling between spins and charges. It has been suggested that irreversible metamagnetic phase transition in $\text{Pr}_{0.7}\text{Ca}_{0.3}\text{MnO}_3$ can be viewed as a melting of the charge ordering.

It is well known that the field-induced insulator-metal phase transition in half-doped manganites occurs at relatively small magnetic fields $\sim 10\text{--}40$ T. Rather little value of the critical magnetic field necessary for generation of a ferromagnetic metal state is explained within the framework of double-fluid model [14, 15] by the competition between canting induced metallicity and inhomogeneity arising from the trapping of carriers by the Jahn-Teller defects. It has been

found that with growth of intensity of an external magnetic field basic state sharply leaves from the JT-distorted canted insulator state and is seized in a metal phase with the optimal (high) canting angle. In the given work, metamagnetic phase transitions in the $(\text{Sm}_{0.5}\text{Gd}_{0.5})_{0.55}\text{Sr}_{0.45}\text{MnO}_3$ ceramics located in immediate vicinity of the insulator-metal transition take place at extremely small value of the critical external magnetic field. This suggests that the phase transitions in a ferromagnetic state in $(\text{Sm}_{0.5}\text{Gd}_{0.5})_{0.55}\text{Sr}_{0.45}\text{MnO}_3$ are induced by a delocalization of self-trapped e_g -electrons of Mn accompanied by disappearance of the local JT distortions and the locking in a metal ferromagnetic phase.

As shown in Figure 3, at temperatures smaller 60 K, isotherms of $M(H)$ in pulse fields practically coincide in form with the curves of the magnetization obtained in static fields at 4,2 K. Size of magnetization step ΔM produced by transition in the metal ferromagnetic state practically did not change with temperature growth. Metamagnetic phase transitions occur at the critical field $H_{c1} \cong 25$ kOe which remains constant up to the temperature of 60 K. Stability of the induced ferromagnetic phase in the range of temperatures of 4,2–60 K is confirmed also by the temperature dependence of ac magnetic susceptibility $\chi(T)$ (Figure 4) received at heating of the sample in zero dc field where the ferromagnetic phase has been induced by strong magnetic field at 18 K. The temperature dependence of susceptibility corresponds to phase transition from the induced ordered ferromagnetic state to the disordered paramagnetic state with critical temperature of $T_c \approx 48$ K. The temperature of 60 K in this figure corresponds to full destruction of long-range ferromagnetic ordering of Mn spins and can be considered as a boundary of stability of the induced ferromagnetic phase, which considerably exceeds the area of existence of the mixed state in zero magnetic field. Unusual feature of metamagnetic phase transitions in the range of temperatures of 4.2–60 K is the constancy of critical field H_{c1} , that is, an evidence of absence of effect of temperature changes on generation of ferromagnetic phase in the $(\text{Sm}_{0.5}\text{Gd}_{0.5})_{0.55}\text{Sr}_{0.45}\text{MnO}_3$ ceramics. It is necessary also to notice that irreversible metamagnetic phase transitions investigated in the given paper do not contain strong discontinuities of isotherms of $M(H)$ that are characteristic of earlier investigated irreversible metamagnetic phase transitions in the manganites [16, 17] both in static, and in pulse magnetic fields, and exist at sufficiently elevated temperatures. Therefore, the mechanisms of the irreversible transitions offered in these papers cannot fully explain the given experimental results.

At temperatures above 60 K, behaviour of magnetization in a strong pulse magnetic field essentially varies. As shown in Figure 3, the isotherms of magnetization in high-temperature paramagnetic phase agrees with well-known behaviour of $M(T)$ curves in a Griffiths-like phase and strongly differs from the isotherms received in low-temperature phase with the mixed insulating ground state with dominating domains of long-range antiferromagnetism. At growth of intensity of external magnetic field to the critical value H_{c1} , there is a reversible metamagnetic-like transition from paramagnetic to a ferromagnetic state in the form of a narrow step on

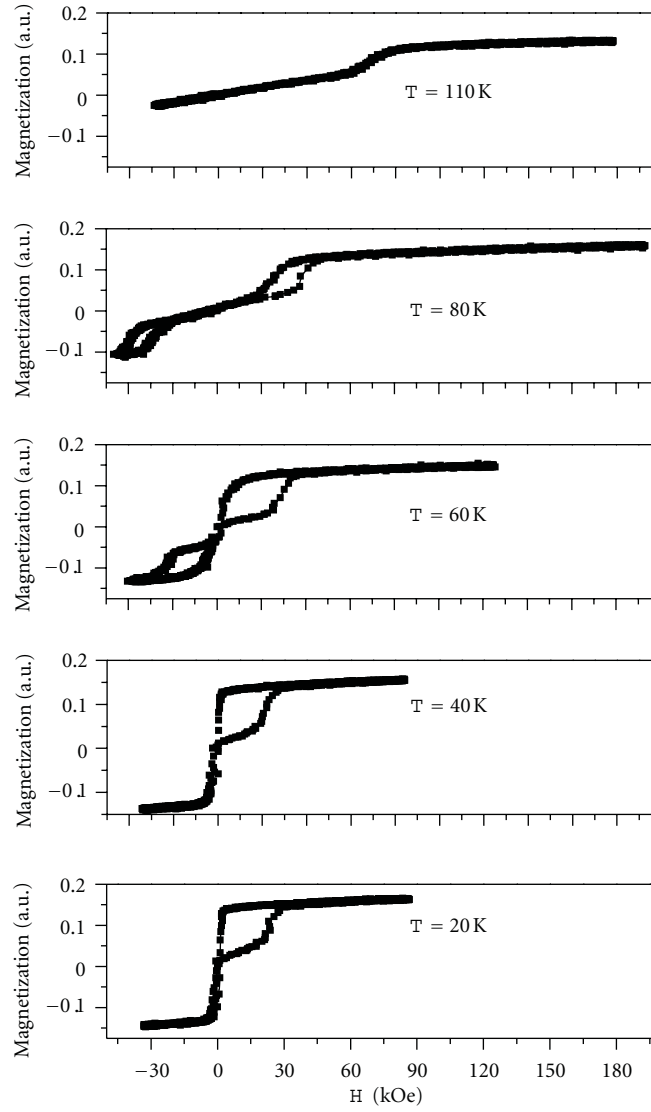


FIGURE 3: Evolution of magnetization isotherms $M(H)$ of the $(\text{Sm}_{0.5}\text{Gd}_{0.5})_{0.55}\text{Sr}_{0.45}\text{MnO}_3$ ceramics in the pulse magnetic fields for temperatures of 20–110 K.

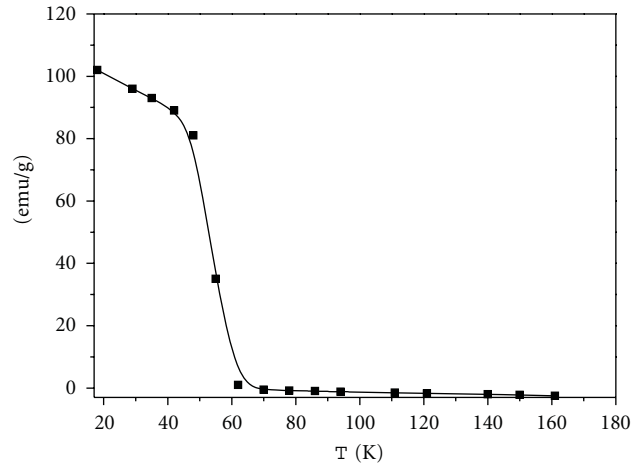


FIGURE 4: Temperature dependence of the ac magnetic susceptibility $\chi(T)$ of the ceramics $(\text{Sm}_{0.5}\text{Gd}_{0.5})_{0.55}\text{Sr}_{0.45}\text{MnO}_3$ obtained after metamagnetic phase transition at 18 K.

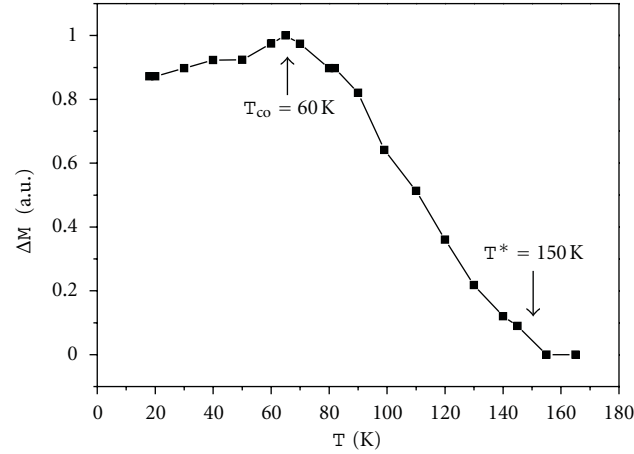


FIGURE 5: Temperature dependence of magnetization step height $\Delta M(T)$ at the metamagnetic phase transitions in the $(\text{Sm}_{0.5}\text{Gd}_{0.5})_{0.55}\text{Sr}_{0.45}\text{MnO}_3$ ceramics induced in the temperature interval of 18–165 K.

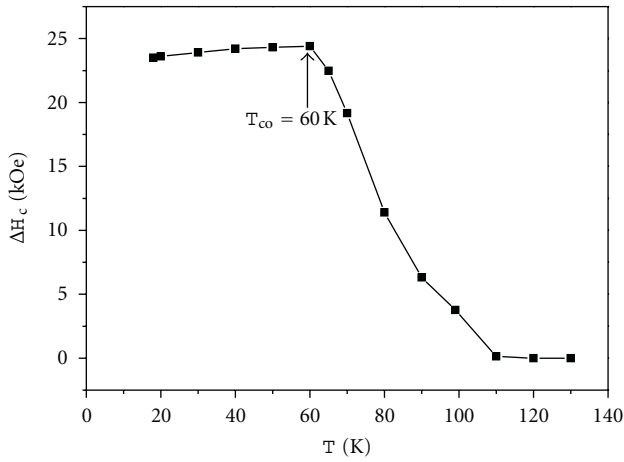


FIGURE 6: Temperature dependence of field hysteresis width ΔH_c of the metamagnetic phase transitions in the $(\text{Sm}_{0.5}\text{Gd}_{0.5})_{0.55}\text{Sr}_{0.45}\text{MnO}_3$ ceramics induced in the temperature interval of 18–165 K.

$M(H)$ curve accompanied by field hysteresis at reduction of magnetic field intensity with critical field $H_{c2} \neq 0$ below which the sample comes back to the initial paramagnetic state. The values of critical fields H_{c1} and H_{c2} practically linearly increase at temperatures above 80 K, whereas a difference of critical fields $\Delta H_c = H_{c1} - H_{c2}$ decreases with the temperature rising and reaches zero near 110 K. At the further rise in temperature, the field-induced phase transition looked like a narrow step of magnetization $\Delta M(T)$ without field hysteresis, which was displaced linearly on temperature towards stronger fields and disappeared at temperatures above 150 K (Figure 5). At temperatures above 150 K corresponding to top boundary T^* of Griffiths-like phase, we observed only linear increase in magnetization with field growth, characteristic for a usual paramagnetic phase. Unusual behaviour of magnetization isotherms at temperatures above 60 K apparently is caused by growth of local charge/orbital correlations with the temperature drop

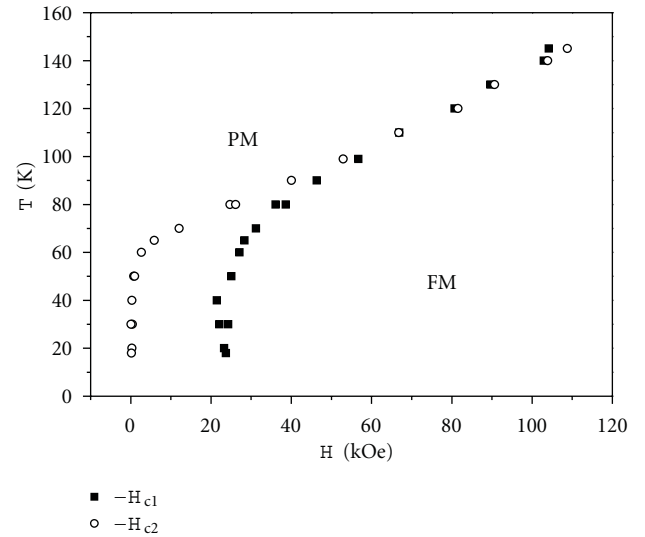


FIGURE 7: Magnetic H - T phase diagram of the $(\text{Sm}_{0.5}\text{Gd}_{0.5})_{0.55}\text{Sr}_{0.45}\text{MnO}_3$ ceramics, received in strong pulse magnetic fields.

to the critical value $T_{CO} \cong 60$ K associated with transition of the sample to a state with long-range charge-ordering. The strong magnetic field destroys both long-range charge-ordering state ($T < T_{CO}$) and the state with short-range charge/orbital correlation ($T > T_{CO}$) that results in field-induced phase transitions found in this work. It is possible to assume that sharp falling to zero of width of a hysteresis ΔH_c of the critical fields of metamagnetic phase transition with growth of temperature (Figure 6) is related to destruction of local correlations of orbital order $\xi_{OO}(T)$ at temperatures above 110 K, whereas field-induced magnetization step ΔM , falling to zero in the range of temperatures of 60–150 K, implies destruction of local charge-order and reduction to zero of the correlation length $\xi_{CO}(T)$ at the temperature $T^* \cong 150$ K. Magnetic H - T phase diagramme of the $(\text{Sm}_{0.5}\text{Gd}_{0.5})_{0.55}\text{Sr}_{0.45}\text{MnO}_3$ ceramics had been received in strong pulse magnetic fields (Figure 7).

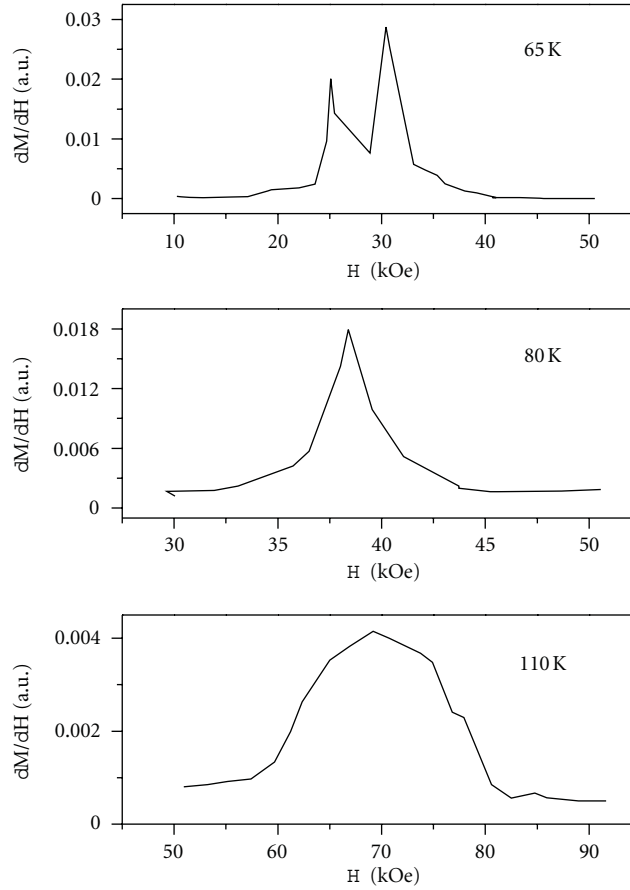


FIGURE 8: Field dependences of derivative of magnetization dM/dH received near to critical field H_{c1} of transition in a ferromagnetic state at temperatures above $T_{CO} \cong 60$ K.

Special interest is represented by additional step structure of magnetization isotherms $M(H)$ close to critical field H_{c1} where charge/orbital correlations are broken, received only in the rapid pulse fields with sweep rate of magnetic field ≥ 2 T/ μ s. In experiment, an existence of one or two small narrow steps of the magnetization was shown, which arise with growth of magnetic field near to critical value H_{c1} and are absent in hysteresis curves at field reduction close to H_{c2} . More clearly, this feature is shown in field dependences of magnetization derivative dM/dH close to H_{c1} in the form of additional narrow peaks of the derivative, having by the basis peak in width ~ 20 kOe (Figure 8). These steps of isotherms of magnetization exist only at temperatures lower 110 K that allows us to assume that the reason of their occurrence is destruction of short-range orbital correlations forming the domain structure of JT distortions of a crystal lattice for $T < 110$ K. In vicinity of $T_{CO} \cong 60$ K, there is a splitting of dM/dH single peak evidently connected with existence of close T_{CO} incommensurate lattice modulation of an elastic field JT distortions with wave number incommensurate with the lattice constant.

4. Conclusion

The results of measurement of the temperature dependences of *ac* magnetic susceptibility $\chi(T)$ of the $(\text{Sm}_{0.5}\text{Gd}_{0.5})_{0.55}\text{Sr}_{0.45}\text{MnO}_3$ ceramics illustrate formation of the mixed insulating state with a special feature of a quantum-disordered phase with dominating domains with a long-range antiferromagnetism at the temperatures below $T_N \cong 48,5$ K. In extremely weak magnetic field $H_{c1} \cong 25$ kOe, field-induced irreversible metamagnetic phase transition from a mixed insulating state to metallic ferromagnetic one was found out, being related to destroy of long-range charge/orbital correlation which amplifies the local antiferromagnetic correlations of Mn spins. From the analysis of isotherms of magnetization, the conclusion was made about spontaneous phase transition with charge/orbital ordering at temperatures below the critical value $T_{CO} \cong 60$ K. At temperatures above 60 K, there are reversible field-induced metamagnetic-like transitions in the ferromagnetic state, related to destroy of short-range charge/orbital correlations. It is supposed that nanoscale correlations of a charge exist in unusually large interval of

temperatures ~ 90 K at temperatures above T_{CO} that considerably surpasses area of existence of short-range orbital correlations ~ 50 K, creating an elastic field Jahn-Teller deformations of the crystal lattice. An additional steps structure of magnetization isotherms close to H_{c1} was found, which exist only at magnetization in very fast pulse fields with sweep rate of magnetic field ≥ 2 T/ μ s. It is supposed the existence of close to T_{CO} incommensurate lattice modulation of elastic field JT distortions with wave number incommensurate with the lattice constant.

References

- [1] Y. Tokura, "Critical features of colossal magnetoresistive manganites," *Reports on Progress in Physics*, vol. 69, no. 3, pp. 797–851, 2006.
- [2] S. Murakami and N. Nagaosa, "Colossal magnetoresistance in manganites as a multicritical phenomenon," *Physical Review Letters*, vol. 90, no. 19, Article ID 197201, 4 pages, 2003.
- [3] Y. Motome, N. Furukawa, and N. Nagaosa, "Competing orders and disorder-induced insulator to metal transition in manganites," *Physical Review Letters*, vol. 91, no. 16, Article ID 167204, 4 pages, 2003.
- [4] H. Aliaga, D. Magnoux, A. Moreo, D. Poilblanc, S. Yunoki, and E. Dagotto, "Theoretical study of half-doped models for manganites: fragility of CE phase with disorder, two types of colossal magnetoresistance, and charge-ordered states for electron-doped materials," *Physical Review B*, vol. 68, no. 10, Article ID 104405, 14 pages, 2003.
- [5] J. Burgi, M. Mayr, V. Martin-Mayor, A. Moreo, and E. Dagotto, "Colossal effects in transition metal oxides caused by intrinsic inhomogeneities," *Physical Review Letters*, vol. 87, no. 27, Article ID 277202, 4 pages, 2001.
- [6] Y. Tomioka, Y. Okimoto, J. H. Jung, R. Kumai, and Y. Tokura, "Critical control of competition between metallic ferromagnetism and charge/orbital correlation in single crystals of perovskite manganites," *Physical Review B*, vol. 68, no. 9, Article ID 094417, 7 pages, 2003.
- [7] L. J. de Jongh and A. R. Miedema, "Experiments on simple magnetic model systems," *Advances in Physics*, vol. 23, no. 1, pp. 1–260, 1974.
- [8] T. Vojta and J. Schmalian, "Quantum Griffiths effects in itinerant Heisenberg magnets," *Physical Review B*, vol. 72, no. 4, Article ID 045438, 6 pages, 2005.
- [9] A. A. Zvyagin, "Quantum phase transitions in low-dimensional quantum spin systems with incommensurate magnetic structures," *Physical Review B*, vol. 72, no. 6, Article ID 064419, 8 pages, 2005.
- [10] A. W. Sandvik, "Quantum criticality and percolation in dimer-diluted two-dimensional antiferromagnets," *Physical Review Letters*, vol. 96, no. 20, Article ID 207201, 4 pages, 2006.
- [11] J. L. Alonso, L. A. Fernandez, F. Guinea, V. Laliena, and V. Martin-Mayor, "Interplay between double-exchange, superexchange, and Lifshitz localization in doped manganites," *Physical Review B*, vol. 66, no. 10, Article ID 104430, 6 pages, 2002.
- [12] J. M. de Teresa, P. A. Algarabel, C. Ritter et al., "Possible quantum critical point in $\text{La}_{2/3}\text{Ca}_{1/3}\text{Mn}_{1-x}\text{Ga}_x\text{O}_3$," *Physical Review Letters*, vol. 94, no. 20, Article ID 207205, 4 pages, 2005.
- [13] H. Yoshizawa, H. Kawano, Y. Tomioka, and Y. Tokura, "Neutron-diffraction study of the magnetic-field-induced metal-insulator transition in $\text{Pr}_{0.7}\text{Ca}_{0.3}\text{MnO}_3$," *Physical Review B*, vol. 52, no. 18, pp. R13145–R13148, 1995.
- [14] T. V. Ramakrishnan, H. R. Krishnamurthy, S. R. Hassan, and G. V. Pai, "Theory of insulator metal transition and colossal magnetoresistance in doped manganites," *Physical Review Letters*, vol. 92, no. 15, Article ID 157203, 4 pages, 2004.
- [15] O. Cepas, H. R. Krishnamurthy, and T. V. Ramakrishnan, "Doping and field-induced insulator-metal transitions in half-doped manganites," *Physical Review Letters*, vol. 94, no. 24, Article ID 247207, 4 pages, 2005.
- [16] L. Ghivelder, R. S. Freitas, M. G. das Virgens et al., "Abrupt field-induced transition triggered by magnetocaloric effect in phase-separated manganites," *Physical Review B*, vol. 69, no. 21, Article ID 214414, 5 pages, 2004.
- [17] D. S. Rana, D. G. Kuberkar, and S. K. Malik, "Field-induced abrupt change in magnetization of the manganite compounds $(\text{LaR})_{0.45}(\text{CaSr})_{0.55}\text{MnO}_3$ (R = Eu and Tb)," *Physical Review B*, vol. 73, no. 6, Article ID 064407, 6 pages, 2006.

Review Article

Novel Applications of Ferrites

Raúl Valenzuela

*Departamento de Materiales Metálicos y Cerámicos, Instituto de Investigaciones en Materiales,
Universidad Nacional Autónoma de México, P.O. Box 70360, Coyoacán 04510, México City, DF, Mexico*

Correspondence should be addressed to Raúl Valenzuela, raulvale@yahoo.com

Received 26 July 2011; Accepted 21 December 2011

Academic Editor: Arcady Zhukov

Copyright © 2012 Raúl Valenzuela. This is an open access article distributed under the Creative Commons Attribution License, which permits unrestricted use, distribution, and reproduction in any medium, provided the original work is properly cited.

The applications of ferrimagnetic oxides, or ferrites, in the last 10 years are reviewed, including thin films and nanoparticles. The general features of the three basic crystal systems and their magnetic structures are briefly discussed, followed by the most interesting applications in electronic circuits as inductors, in high-frequency systems, in power delivering devices, in electromagnetic interference suppression, and in biotechnology. As the field is considerably large, an effort has been made to include the original references discussing each particular application on a more detailed manner.

1. Introduction

Ferrites are a large class of oxides with remarkable magnetic properties, which have been investigated and applied during the last ~50 years [1]. Their applications encompass an impressive range extending from millimeter wave integrated circuitry to power handling, simple permanent magnets, and magnetic recording. These applications are based upon the very basic properties of ferrites: a significant saturation magnetization, a high electrical resistivity, low electrical losses, and a very good chemical stability. Ferrites can be obtained in three different crystal systems by many methods, and the feasibility to prepare a virtually unlimited number of solid solutions opens the means to tailor their properties for many applications. For many applications, ferrites cannot be substituted by ferromagnetic metals; for other, ferrites often compete with metals on economic reasons.

The possibility of preparing ferrites in the form of nanoparticles has open a new and exciting research field, with revolutionary applications not only in the electronic technology but also in the field of biotechnology.

In this paper, the applications of ferrites developed in the last 10 years are briefly described.

2. Ferrites

2.1. Spinel. Spinel ferrites possess the crystal structure of the natural spinel MgAl_2O_4 , first determined by Bragg [2]. This

structure is particularly stable, since there is an extremely large variety of oxides which adopt it, fulfilling the conditions of overall cation-to-anion ratio of 3/4, a total cation valency of 8, and relatively small cation radii. Spinel structure is shown in Figure 1. Cation valency combinations known are 2, 3 (as in $\text{Ni}^{2+}\text{Fe}_2^{3+}\text{O}_4$); 2, 4 (as in Co_2GeO_4); 1, 3, 4 (as in LiFeTiO_4); 1, 3 (as in $\text{Li}_{0.5}\text{Fe}_{2.5}\text{O}_4$); 1, 2, 5 (as in LiNiVO_4); 1, 6 (as in Na_2WO_4). In ferrites with applications as magnetic materials, Al^{3+} has usually been substituted by Fe^{3+} . An important ferrite is magnetite, $\text{Fe}^{2+}\text{Fe}_2^{3+}\text{O}_4$ (typically referred as Fe_3O_4), probably the oldest magnetic solid with practical applications and currently a very active research field, due to the fascinating properties associated with the coexistence of ferrous and ferric cations. Another important material by its structure, as well as by its applications in audio recording media, is maghemite or $\gamma\text{-Fe}_2\text{O}_3$, which can be considered as a defective spinel $\square_{1/3}\text{Fe}_{8/3}^{3+}\text{O}_4$, where \square represents vacancies on cation sites.

The overall symmetry of oxygens is fcc (face centered cubic), which defines two types of interstitial sites: 64 tetrahedral sites and 32 octahedral sites, for a unit cell containing 8 times the basic formula AB_2O_4 . Only one-eighth of tetrahedral sites and half of octahedral sites are occupied by cations. The space group is $\text{Fd}\bar{3}\text{m}$.

In MgAl_2O_4 , Al and Mg cations occupy the octahedral and tetrahedral sites, respectively. This cation distribution, known as a *normal* spinel, is usually indicated as

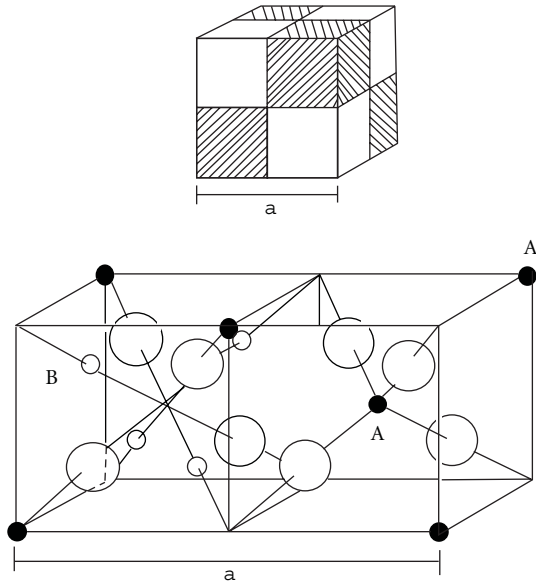


FIGURE 1: The unit cell of the spinel structure, divided into octants to show the tetrahedral (small, black spheres A) and octahedral (small white spheres B) sites. Oxygens are the large white spheres [1].

(Mg)[Al₂]O₄; that is, square brackets contain the octahedral sites occupancy (“B” sites), while parenthesis show the cations in tetrahedral sites (“A” sites). A radically different cation distribution, where half of trivalent cations (denoted by T³⁺) occupy A sites and B sites are shared by divalent cations (denoted by D²⁺) and the remaining trivalent cations (T³⁺)[T³⁺D²⁺]O₄, is known as the *inverse* spinel. An intermediate cation distribution can be expressed as (D_{1-δ}T_δ)[D_δT_{2-δ}]O₄, where δ is the degree of inversion. In many intermediate spinels, δ depends on the preparation technique and, more specifically, on the cooling rate after sintering or annealing.

A remarkable characteristic of spinel structure is that it is able to form an extremely wide variety of *total solid solutions*. This means that the composition of a given ferrite can be strongly modified, while the basic crystalline structure remains the same. An example is the Zn-Ni system, with general formula Zn_xNi_{1-x}Fe₂O₄, where 0 ≤ x ≤ 1. In the present example, the end compositions NiFe₂O₄ (for x = 0) and ZnFe₂O₄ (x = 1) can be obtained. NiFe₂O₄ is an inverse spinel: in contrast, ZnFe₂O₄ is a normal spinel. The properties of these compounds are very different: Ni ferrite is ferrimagnetic with a Curie temperature ≈ 858 K, while Zn ferrite is antiferromagnetic, with a Néel temperature about 9 K. This means that the general properties of the ferrite (as discussed in the following section) can be easily “tailored” just by varying the composition. Cations forming spinel solid solutions appear in Table 1.

The cation distribution in spinels was an interesting problem for some time; currently, it has been established that it depends essentially on various factors. First the *elastic energy* (the lattice deformation produced by cation radii differences) has to be considered. It refers to the degree of

TABLE 1: Some cations forming spinel solid solutions.

1+	2+	3+	4+
Li	Mg	Al	Ti
Cu	Ca	Ti	V
Ag	Mn	V	Mn
	Fe	Cr	Ge
	Co	Mn	Sn
	Ni	Fe	
	Cu	Ga	
	Zn	Rh	
	Cd	In	

From [1].

distortion of the crystal structure, as a result of differences in dimensions of the several cations within the specific spinel. In principle, small cations should occupy the smallest sites (tetrahedral sites), while larger cations should locate on the larger octahedral sites. However, trivalent cations are generally smaller than divalent ones, leading to some tendency to the inverse structure. The next factor to be considered is *electrostatic energy* (Madelung energy), which has to do with the electrical charge distribution. In a simple way, cations with high electrical charge should occupy the sites with larger coordination number (octahedral), and cations with smaller valency should be more stable when occupying the tetrahedral sites. The *crystal field* stabilization energy comes next to account for cation site “preference.” This energy has to do with the geometry of *d* orbitals and the arrangements these orbitals can established within the crystal structure. The five *d* orbitals no longer have the same energy but are split according to the electric field distribution established by anions on the particular crystal site. The physical basis for this differences in energy is simply the electrostatic repulsion between the *d* electrons and the orbitals of the surrounding *p* orbitals of anions.

Since bonding in most ferrites has an ionic character, cations are surrounded by anions, and conversely anions have cations as nearest neighbors. Magnetic ordering in ferrites (as in many oxides) tends to form antiferromagnetic arrangements, as interactions between cations have to be established through the anions. However, in most cases a resulting magnetic moment remains due to the fact that magnetic lattices contain different numbers of cations. In the case of spinels, the magnetic structure can be inferred from a small part of the structure, as shown in Figure 2 Superexchange interactions can then be schematized as a triangular arrangement. The strongest interactions are AOB, which occur between tetrahedral and octahedral cations, followed by BOB (cations on neighboring octahedral sites).

The relative strength of these interactions can be illustrated by the Curie temperature of Li and Zn ferrites (both Li and Zn are paramagnetic cations). Li_{0.5}Fe_{2.5}O₄ is an inverse spinel, with a cation distribution that can be expressed as Fe [Li_{0.5}Fe_{1.5}] O₄, while Zn ferrite is a normal spinel, (Zn)[Fe₂]O₄. Iron ions have an antiparallel order in both

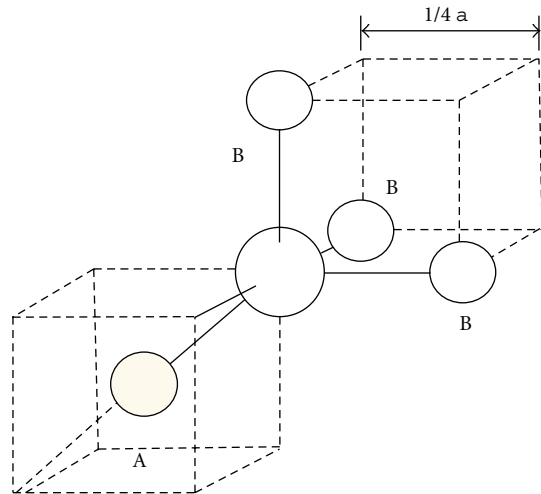


FIGURE 2: Detail of the A and B sites around an oxygen, to show AB and BB interactions.

ferrites, but as they both occupy octahedral sites, they compensate completely in Zn ferrite. In the case of Li ferrite, they have also an antiparallel order, but they belong to different sublattices, with different number. As a result, Zn ferrite is anti-ferromagnetic (with zero resulting magnetization), and Li ferrite is ferromagnetic, with a magnetization (per formula unit) of about 0.5 Bohr magneton (close to 0 K). The strength of interactions is apparent in the transition temperatures: the Curie point for Li ferrite is the highest observed in spinels 958 K, while Néel temperature for Zn ferrite is the lowest in spinels 9 K.

An interesting system is $\text{Zn}_x\text{Ni}_{1-x}\text{Fe}_2\text{O}_4$, which is normal for Zn and inverse for Ni. The general site occupancy can be expressed as: $(\text{Zn}_x\text{Fe}_{1-x})[\text{Ni}_{1-x}\text{Fe}_{1+x}]\text{O}_4$. The composition varies from Ni ferrite ($x = 0$) to Zn ferrite ($x = 1$). Starting with Ni ferrite, the decrease in x occurs as if Zn entering in A sites “push” Fe toward B sites, filling the octahedral sites left by the decreasing Ni ions. As in all inverse ferrites, the low-temperature global magnetization depends on the divalent cation (as Fe ions are antiparallel). The presence of Zn decreases the magnetization in A sublattice and increases the B sublattices. The addition of a paramagnetic cation thus leads to an increase in total magnetization! However, as Zn increases in A sites, AOB interaction weakens, and for $x \approx 0.65$, BOB interaction is comparable to AOB interaction leading to a triangular structure (known as Yafet-Kittel [3]).

The Curie temperature shows also a large variation with composition for ZnNi ferrites, $T_C = 858$ K for $x = 0$ (Ni ferrite), and as mentioned above, Zn ferrite is antiferromagnetic, with $T_N = 9$ K.

2.2. Garnets. The crystal structure is that of the garnet mineral, $\text{Mn}_3\text{Al}_2\text{Si}_3\text{O}_{12}$. The magnetic garnets include Fe^{3+} instead of Al and Si, and a rare earth cation (R) substitutes Mn, to give the general formula $\text{R}_3\text{Fe}_5\text{O}_{12}$ for ferromagnetic garnets [4, 5]. The crystal structure has cubic symmetry and is relatively complex; the unit cell has 8 formula units (160 atoms) and belongs to the space group O_h^{10} -Ia3d. In

contrast with spinels, the oxygen sublattice is not a close-packed arrangement, but it is better described as a polyhedra combination. Three kinds of cation sites exist in this structure: dodecahedral (eightfold), octahedral (sixfold), and tetrahedral (fourfold) sites. Rare earth cations, R, occupy the largest, dodecahedral sites, while Fe^{3+} cations distribute among the tetra- and octahedral places. The cation distribution is generally expressed as $\{\text{R}_3\}(\text{Fe}_3)[\text{Fe}_2]\text{O}_{12}$; $\{\}$ bracket denotes dodecahedral sites, $()$ parenthesis are used for tetrahedral site occupancy, and octahedral sites are indicated by square brackets $[\]$. Rare earth cations (from La^{3+} to Lu^{3+}) enter the dodecahedral sites, and as spinels, garnets can form total solid solutions. A wide variety of cation substitutions has been reported [6]. Yttrium iron garnet, $\text{Y}_3\text{Fe}_5\text{O}_{12}$ also known as “YIG,” has remarkable magnetic properties.

The magnetic structure of garnets can be described by three magnetic sublattices, with a superexchange interaction through oxygens. Dodecahedral and octahedral ions are parallel, while tetrahedral cations adopt an antiparallel orientation. At very low temperatures, global magnetization (per formula unit) is roughly $(3\mu_R - \mu_{\text{Fe}})$, where μ_R and μ_{Fe} are the rare earth and the iron magnetic moments, respectively. The differences in thermal behavior among the three sublattices lead to the *compensation* of magnetic moments. As temperature increases, the magnetization in each sublattice is affected by the thermal agitation and decreases. This reduction in magnetization is slow in iron sublattices, but, due to its larger size, the decrease is quite steeply in the dodecahedral sublattice. At a certain temperature, the reduction in magnetization in rare earth sublattice exactly compensates the difference between octa- and tetrahedral sublattice, and global magnetization exhibits a zero value. For GdIG, this temperature is 300 K. The fact that magnetic structure is dominated by iron sublattices can also be observed in the Curie temperature: virtually all iron garnets show the same transition point (~ 560 K).

2.3. Hexaferrites. All of hexagonal ferrites are synthetic; barium hexaferrite ($\text{BaFe}_{12}\text{O}_{19}$) possesses the same structure as the natural mineral magnetoplumbite, of approximate formula $\text{PbFe}_{7.5}\text{Mn}_{3.5}\text{Al}_{0.5}\text{Ti}_{0.5}\text{O}_{19}$. Rather than sharing a common crystal structure, hexaferrites are a family of related compounds with hexagonal and rhombohedral symmetry. The main compositions can be represented in the upper section of the $\text{MeO}-\text{Fe}_2\text{O}_3-\text{BaO}$ ternary phase diagram. Me is a divalent cation such as Ni, Mg, Co, Fe, Zn, Cu, for instance. All the magnetic hexaferrites are found on the $\text{BaFe}_{12}\text{O}_{19}-\text{Me}_2\text{Fe}_4\text{O}_8$ and $\text{BaFe}_{12}\text{O}_{19}-\text{Me}_2\text{BaFe}_{12}\text{O}_{22}$ joins (Figure 3). If the end members are designated as M ($\text{BaFe}_{12}\text{O}_{19}$), S ($\text{Me}_2\text{Fe}_4\text{O}_8$), and Y ($\text{Me}_2\text{BaFe}_{12}\text{O}_{22}$); the joins are M-S and M-Y, respectively. Some of the main compositions are found in Table 2.

Hexaferrites can also form an extensive variety of solid solutions. Ba can be substituted by Sr, Ca, and Pb. Fe^{3+} can be substituted by trivalent cations such as Al, Ga, In, Sc [8], or by a combination of divalent + tetravalent cations, such as $\text{Co}^{2+} + \text{Ti}^{4+}$. A more complete account of these solid solutions can be found in [1].

TABLE 2: Formulae of some hexaferrites and their formation from end members of the ternary phase diagram.

Designation	Formula
M	$\text{BaFe}_{12}\text{O}_{19}$
Y	$\text{Ba}_2\text{Me}_2\text{Fe}_{12}\text{O}_{22}$
W (MS)	$\text{BaMe}_2\text{Fe}_{16}\text{O}_{27}$
X (M_2S)	$\text{Ba}_2\text{Me}_2\text{Fe}_{28}\text{O}_{46}$
U (M_2Y)	$\text{Ba}_4\text{Me}_2\text{Fe}_{36}\text{O}_{60}$
Z (M_2Y_2)	$\text{Ba}_6\text{Me}_4\text{Fe}_{48}\text{O}_{82}$

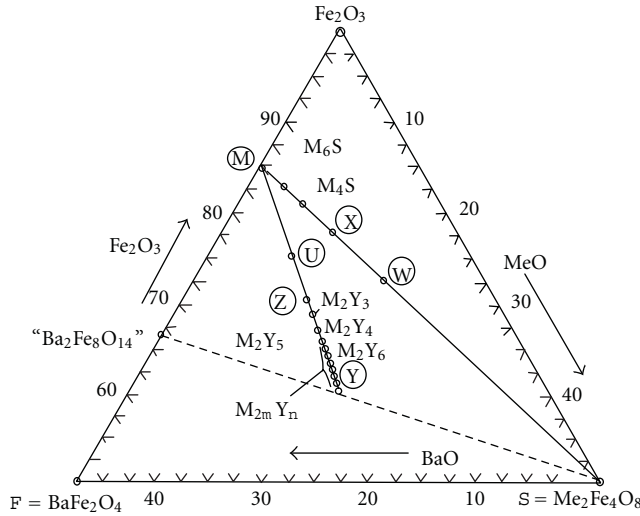


FIGURE 3: Upper triangle of the Fe_2O_3 -BaO-MeO phase diagram showing the several compositions of hexaferrites [7].

The magnetic structure in hexaferrites is complex, as a consequence of their complex crystal structure. In $\text{BaFe}_{12}\text{O}_{19}$, iron ions occupy five different sublattices, with a total magnetization $20\mu_B$ per formula unit, at low T . A detailed analysis of magnetic and crystal structures can be found in (9). The most interesting feature of hexaferrites is their high coercivity.

2.4. Preparation of Ferrites. Ferrites were first prepared by ceramic methods, involving milling, mixing, pressing, sintering, and finishing as basic operations, to obtain bulk materials with grains in the micrometric scale. However, as a result of the general current tendency to circuit integration and miniaturization, ferrites are prepared in the form of thick and thin films and, more recently, as nanostructured materials.

Ferrite thin films can be polycrystalline or epitaxial films. Major methods to obtain ferrite thin films are electroplating (or ferrite plating) [9], magnetron sputtering (single and multitarget) [10], pulsed laser deposition [11], and molecular beam epitaxy [12]. A detailed account of epitaxial ferrite films can be found in [13].

An additional route to tuning ferrite properties for specific applications is the production of heterostructures, that is,

the artificial layering of ferrites with isostructural and non-isostructural materials, such as $\text{Fe}_3\text{O}_4/\text{NiO}$ (53), $\text{Fe}_3\text{O}_4/\text{CoO}$ (56), and $(\text{Mn,Zn})\text{Fe}_2\text{O}_4/\text{Co Fe}_2\text{O}_4$ [14], and incorporating them into planar devices. The combination of ferrite layers with piezoelectric layers is leading to new and exciting applications, as reported below.

By reducing the scale to the nanometric size, new and technologically interesting properties have been obtained. Nanocrystalline magnetic materials have been obtained by a variety of methods, such as coprecipitation [15], hydrothermal [16], sonochemical [17], citrate precursor [18], sol-gel [19], mechanical alloying [20], shock wave [21], reverse micelle [22], forced hydrolysis in a polyol [23], and even by using egg white as an aqueous medium [24].

The preparation methods of ferrites for applications in biotechnology are reported below.

3. Novel Applications of Ferrites

3.1. Inductors. Ferrites are primarily used as inductive components in a large variety of electronic circuits such as low-noise amplifiers, filters, voltage-controlled oscillators, impedance matching networks, for instance. Their recent applications as inductors obey, among other tendencies, to the general trend of miniaturization and integration as ferrite multilayers for passive functional electronic devices. The multilayer technology has become a key technology for mass production of integrated devices; multilayers allow a high degree of integration density. Multilayer capacitors penetrated the market a few decades ago, while inductors started in the 1980s. The basic components to produce the inductance are a very soft ferrite and a metallic coil.

In addition, to provide a high permeability at the operation frequency, the ferrite film should be prepared by a process compatible with the integrated circuit manufacturing process. Sputtering provides films with high density, but the composition is sometimes difficult to control with accuracy, and the annealing processes can attain high temperatures. Pulsed laser deposition leads to high-quality films; however, a method involving the preparation of the ferrite film by a combination of sol-gel and spin-coating seems easier and with a lower cost [25].

Layered samples of ferrites with piezoelectric oxides can lead to a new generation of magnetic field sensors. The basis of their performance is the capability of converting magnetic fields into electrical voltages by a two-step process. First, the magnetic field produces a mechanical strain on the magnetic material (due to its magnetostriction); this strain then induces a voltage in the piezoelectric layer. These sensors can provide a high sensitivity, miniature size, and virtually zero power consumption. Sensors for ac and dc magnetic fields, ac and dc electric currents, can be fabricated. Sensors based on nickel ferrite ($\text{Ni}_{1-x}\text{Zn}_x\text{Fe}_2\text{O}_4$ with $x = 1-0.5$)/lead zirconate-titanate ($\text{PbZr}_{0.52}\text{Ti}_{0.48}\text{O}_3$) have shown an excellent performance [26]. Both ferrite and zirconate-titanate films are prepared by tape casting; typically, 11 ferrite layers were combined with 10 piezoelectric layers (both layers $18\mu\text{m}$ thick, $3 \times 6\text{ mm}^2$ area).

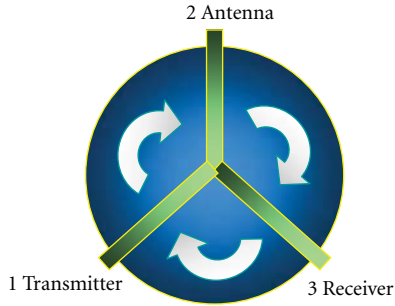


FIGURE 4: Schematic representation of a circulator.

3.2. High Frequency. There has been an increasing demand of magnetic materials for high-frequency applications such as telecommunications and radar systems, as microwave technology requires higher frequencies and bandwidths up to 100 GHz. Ferrites are nonconducting oxides and therefore allow total penetration of electromagnetic fields, in contrast with metals, where the skin effect severely limits the penetration of high-frequency fields [27]. At such frequencies, domain walls are unable to follow the fields (dispersion of domain walls typically occurs about 10 GHz), and absorption of microwave power takes place by spin dynamics. The usual geometry is to align spins first with a DC magnetic field H and apply the microwave field perpendicular to H . The spins precess around their equilibrium orientation at the frequency of the microwave field. The classical description of this dynamics is the Landau-Lifshitz equation [28] of motion, which can be written in its undamped form:

$$\frac{dM}{dt} = \gamma M \times H_i, \quad (1)$$

where M is the magnetization, γ is the gyromagnetic ratio (ratio of mechanical to magnetic moment, $\gamma = ge/2mc = 2.8 \text{ MHz/G}$), and H_i is the total internal field acting upon the spin. The magnetization and the field terms can be separated in the static and time-dependent parts as

$$H = H_i + h e^{i\omega t}, \quad M = M_s + m e^{i\omega t} \quad (2)$$

These equations show a singularity at

$$\omega = \omega_0 = \gamma H_0 \quad (3)$$

H_0 is the total field on the spins (external and internal); (3) expresses the ferromagnetic resonance (FMR) conditions and is known as the Larmor equation. FMR is associated with the uniform (in phase) precession of spins. The upper limit of applications of ferrites is FMR, since the interaction with the microwave field becomes negligible as $\omega > \omega_0$. Spinels are therefore applied at frequencies up to 30 GHz, while this limit is about 10 GHz for garnets and can attain 100 GHz for hexaferrites.

The absorption of microwaves by ferrites involves losses; a damping or relaxation term is normally added to (3). In polycrystalline ferrites, losses are associated with defects and the anisotropy field distribution, and with electrical conduction a common problem, especially in spinels, is the presence

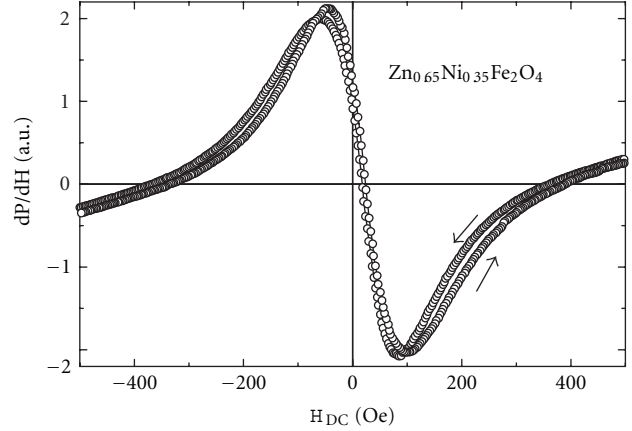


FIGURE 5: Low-field microwave absorption (LFA) of a Ni-Zn ferrite at 9.4 GHz room temperature and room temperature. A small hysteresis is observed for increasing and decreasing applied field.

of Fe^{2+} , which promotes a hopping conduction process in combination with Fe^{3+} . The physical origin of losses in polycrystalline ferrites, through its effects on the linewidth, has been recently investigated in detail; the dominant role of grain boundaries is apparent [29, 30].

Some of ferrite applications rely on the fact that the spin rotation depends on the orientation of the external field, which allows the control of the interaction with the microwave field. For one direction of the field, the ferrite transmits the microwave field; for the opposite, it strongly absorbs it. This is the basis of nonreciprocal devices.

Typical devices are circulators, isolators, phase shifters, and antennas. Circulators were developed for radar systems and are now used in mobile phones. They allow the use of the same device for transmission and reception of the response signal. As shown schematically in Figure 4, any signal entering through port 1 exits by port 2, with no connection with port 3. If the generator is connected to port 1 and the antenna to port 2, this is the path of the outgoing signal. The incoming signal enters through port 2 (the antenna) and is directed to port 3, to the receiver. This allows the handling of a strong outgoing signal (ports 1-2) together with a very sensitive detector (ports 2-3), with no risk of damaging the receiver and using the same antenna. Circulators are usually fabricated with garnets.

Recently, a nonresonant absorption of microwave power at very low magnetic fields has been receiving attention. This absorption, known as LFA (for low-field microwave Absorption), has shown to be clearly dominated by the anisotropy field, H_K , of the ferro- or ferrimagnetic material [31]. Recent results obtained in a Ni-Zn ferrite are shown in Figure 5 in many respects, this absorption is similar to giant magnetoimpedance, GMI [32], that is, the change in electric impedance of a material when subjected to a DC magnetic field [33]. A significant difference with GMI is that LFA does not need that the electrical conductivity of the sample be

of metallic type. No practical applications of LFA have been proposed, so far; however, it is possible to expect that similar applications to GMI can be made (sensors for magnetic field, DC electric current, mechanical stress, etc.), with the additional advantages over classic GMI of high frequencies and insulator magnetic materials.

3.3. Power. Power applications of ferrites are dominated by the power supplies for a large variety of devices such as computers, all kinds of peripherals, TV and video systems, and all types of small and medium instruments. The main application is in the systems known as switched-mode power supplies (SMPs). In this application, the mains power signal is first rectified it is then switched as regular pulses (typically rectangular) at a high frequency to feed into a ferrite transformer, and finally it is rectified again to provide the required power to the instrument. An increase in power delivery and efficiency can be obtained by increasing the working frequency of the transformer.

A recent approach to increase efficiency of the ferrite cores is based on the decrease of eddy currents, by increasing resistivity. Beside the use of nonconducting additives that locate preferentially on grain boundaries (and limit the intergrain conductivity), MnZn and NiZn are combined as $\text{Mn}_x\text{Ni}_{0.5-x}\text{Zn}_{0.5}\text{Fe}_2\text{O}_4$ and obtained through a citrate precursor method [34].

An additional difficulty appears in the case of power applications at high temperature, as is the case of some automotive power devices. Due to the closeness to the car engine, the working temperature increases from the usual 80–100°C for standard applications, to 140°C. A proposed solution involves the modification of the MnZn ferrites (used previously for these applications) in order to produce a higher fraction of Fe^{2+} [35], such as $(\text{Mn}_{0.76}\text{Zn}_{0.17}\text{Fe}_{0.07}^{2+})\text{Fe}_2\text{O}_4$. This ferrous concentration presents a minimum in the magnetocrystalline anisotropy close to 140°C, and therefore, a minimum in losses appears at this temperature. The change is obtained through a careful control of the oxidation atmosphere during sintering and cooling.

As in all other applications, a strong need for miniaturization has also marked the developments in this area in the last few years. In addition to standard methods to obtain ferrite thin films (such as sputtering, laser ablation, sol-gel), screen or stencil printed ceramic-polymer composites have been investigated [36], combining the remarkable magnetic properties of ferrites with the processability of polymer thick films. These polymer thick films can be cured at temperatures about 200°C or less, leaving only the polymer binder and the ferrite filler. This technique allows the fabrication of highly integrated power circuits. The coil is obtained by patterning copper on a flexible polyimide substrate; the ferrite-polymer composite film is then printed above and below the plane of the coil. The magnetic ceramic filler is formed by MnZn ferrite particles about 10 μm , obtained by a standard method. The inductance value remains stable up to 124 MHz.

A different method based on a batch-fabrication method of 3D transformers and inductors has also been proposed [37]. The magnetic core is made of two half magnetic pieces and a printed circuit board (or flexi foil) carrying the

electric windings around the core. The 3D ferrite cores are microstructured out of a 1 mm thick ferrite wafer using a newly developed batch-type micropowder blasting process [38]. These transformers are well suited for low-power applications at working frequencies up to 1 MHz.

Losses in ferrites depend essentially on hysteresis loss at low frequencies, conductivity (or eddy current) loss, and relaxation-resonance loss at high frequencies; their modeling is complex. A model based on the Preisach theory [39] has been applied to predict the hysteretic behavior of soft ferrites for applications in power electronics [40], with good results at low frequencies. On the other hand, by using a network model based on the total energy loss (not only hysteresis loss), a good agreement with experimental results for power, signal, and electromagnetic interference has been found [41]. The approach offers a mechanism for the inclusion of parameters such as temperature or stress variations.

3.4. Electromagnetic Interference (EMI) Suppression. The significant increase in the amount of electronic equipment such as high-speed digital interfaces in notebooks and computers, digital cameras, scanners, and so forth, in small areas, has seriously enhanced the possibility of disturbing each other by electromagnetic interference (EMI). In particular, the fast development of wireless communications has led to interference induced by electric and magnetic fields. Electromagnetic interference can be defined as the degradation in performance of an electronic system caused by an electromagnetic disturbance [42]. The noise from electric devices is usually produced at frequencies higher than circuit signals. To avoid, or at least reduce EMI, suppressors should work as low-pass filters, that is, circuits that block signals with frequencies higher than a given frequency value.

There are several approaches to build EMI suppressors: soft ferrites [43], ferromagnetic metals [44], ferromagnetic metal/hexaferrite composites [45], encapsulated magnetic particles [46], and carbon nanotube composites [47].

Ferrite components for EMI suppressors have been used for decades. In the recent years, however, there have been special needs for these materials as a consequence of the miniaturization trends, increase in integration density, and increase in higher clock frequency, especially in communication, computing, and information technologies. Ferrite multilayer components have been developed as a response to these needs, formed essentially by a highly conductive layer embedded in a ferrite monolithic structure, produced by ceramic coprocessing technologies. Typically, Ni-Zn ferrites are used for the 20–200 MHz frequency range. Multilayer suppressors behave like a frequency-dependent resistor; at low frequencies, losses in the ferrite are negligible. As frequency increases, losses increase also, and, as ferromagnetic resonance is approached, the inductor behaves as a frequency-independent resistor and no longer as an inductor.

Hexaferrites represent an interesting alternative to cubic ferrites as EMI suppressor components; they possess higher resonance frequencies, relatively high permeabilities (at microwave frequencies), and high electrical resistivities. Metallic ferromagnets, in contrast, show a larger saturation

magnetization, but, as frequency increases, they exhibit a strong decrease in permeability due to eddy currents. However, in combination with hexaferrites, they have shown a strong potential for EMI suppressor devices [45]. Co_2Z and Zn_2Y hexaferrite particles ($10\text{--}30\text{ }\mu\text{m}$), mixed with metallic Ni particles ($2\text{--}3\text{ }\mu\text{m}$), and prepared with a polymer (polyvinylidene fluoride) by hot pressing at low temperature led to high shield effectiveness.

Carbon nanotube-polystyrene foam composites have shown a high EMI shielding effectiveness based on a mechanism associated with the reflection of electromagnetic radiation [48]; no magnetic material is used.

Ferrite nanoparticles in combination with carbon nanotubes can efficiently absorb microwave radiation. Carbon nanotubes/ CoFe_2O_4 spinel nanocomposite was fabricated by a chemical vapor deposition method using CoFe_2O_4 nanoparticles as catalysts [46]. The microwave absorption ($2\text{--}18\text{ GHz}$ range) was enhanced. For carbon nanotubes, dielectric loss contributes to the energy loss of electromagnetic waves, while, for pure Co ferrite, the effects of microwave absorption are associated with magnetic losses, but both isolated mechanisms are poor absorbers. For the nanocomposites, however, the microwave absorption improves because of a better match between the dielectric loss and the magnetic loss, which originates from the combination of paramagnetic nanotubes and ferromagnetic material. The dispersed CoFe_2O_4 nanoparticles absorb the microwave signals by resonance effects due to shape anisotropy and dipolar interactions between particles. Such effects are weakened in congregated particles.

3.5. Biosciences. Magnetic materials in the form of nanoparticles, mainly magnetite (Fe_3O_4), are present in various living organisms [49] and can be used in a number of applications. Magnetic nanoparticles can, of course, be prepared in the laboratory by means of the well-known methods; however, magnetic biogenic particles have better properties than synthetic ones: they have a definite size range and width/length ratio and high chemical purity, they are almost perfect crystallographically, and sometimes they possess unusual crystallographic morphologies. Extracellular production of nanometer magnetite particles by various types of bacteria has been described [50]. In many cases, the biogenic particles retain a lipid layer which makes them very stable and easily biocompatible.

Many biotechnological applications have been developed based on biogenic and synthetic magnetic micro- and nanoparticles [51]. Magnetic nanoparticles have been used to guide radionuclides to specific tissues. An approach has been developed to directly label a radioisotope with ferrite particles [52] in *in vivo* liver tissue in rats. Therapeutic applications are feasible by further conjugation with other medicals.

In magnetic resonance imaging (MRI), magnetite superparamagnetic particles are selectively associated with healthy regions of some tissues (liver, for instance); since these particles change the rate of proton decay from the excited to the ground state (which is the basis of MRI), a different, dark-

er contrast is obtained from these healthy regions of tissue [53, 54].

Thermal energy from hysteresis loss of ferrites can be used in hyperthermia, that is, the heating of specific tissues or organs for treatment of cancer. The temperature in tumor tissues rises and becomes more sensitive to radio- or chemotherapy. In addition of magnetite [55], several spinel ferrites (M-Zn , with $\text{M} = \text{Mn}, \text{Co}, \text{Fe}^{2+}$, and $\text{Fe}^{2+}\text{--Mn}$) are under investigation [56] as well as hexaferrites [57].

Enzymes, oligonucleotides, antibodies, and other biologically active compounds can be immobilized, as an important technique used in biotechnology. Such immobilized compounds can be targeted to a specific place or can be removed from the system by using an external magnetic field. The compounds can exert their activity on the specific place or tissue or can be used as affinity ligands to trap the cells or target molecules [58].

Magnetic nanoparticles can also be used in a variety of applications: modification, detection, isolation, and study of cells [59], and isolation of biologically active compounds [60], for instance.

4. Conclusions

Ferrites have been studied and applied for more than 50 years and are considered as well-known materials with “mature” technologies ranging from hard magnets to magnetic recording and to microwave devices. However, the advances in applications and fabrication technologies in the last 10 years have been impressive. Bulk ferrites remain a key group of magnetic materials, while nanostructured ferrites show a dramatic promise for applications in even significantly wider fields.

References

- [1] R. Valenzuela, *Magnetic Ceramics*, Cambridge University Press, 2005.
- [2] W. H. Bragg, “The structure of the spinel group of crystals,” *Philosophical Magazine*, vol. 30, no. 176, pp. 305–315, 1915.
- [3] Y. Yafet and C. Kittel, “Antiferromagnetic arrangements in ferrites,” *Physical Review*, vol. 87, no. 2, pp. 290–294, 1952.
- [4] F. Bertaut and F. Forrat, “Structure des ferrites ferrimagnétiques des terres rares,” *Comptes Rendus de l’Académie des Sciences*, vol. 242, pp. 382–384, 1956.
- [5] S. Geller and M. A. Gilleo, “The crystal structure and ferrimagnetism of yttrium-iron garnet, $\text{Y}_3\text{Fe}_2(\text{FeO}_4)_3$,” *Journal of Physics and Chemistry of Solids*, vol. 3, no. 1-2, pp. 30–36, 1957.
- [6] M. A. Gilleo, “Ferromagnetic Insulators: garnets,” in *Ferromagnetic Materials*, E. R. Wohlfarth, Ed., vol. 2, North Holland, The Netherlands, 1980.
- [7] G. Wrinkler, “Crystallography, chemistry and technology of ferrites,” in *Magnetic Properties of Materials*, J. Smit, Ed., p. 20, McGraw-Hill, London, UK, 1971.
- [8] G. Albanese, M. Carbuicchio, and A. Deriu, “Substitution of Fe^{3+} by Al^{3+} in the trigonal sites of M-type hexagonal ferrites,” *Il Nuovo Cimento B*, vol. 15, no. 2, pp. 147–158, 1973.
- [9] M. Abe, Y. Kitamoto, K. Matsumoto, M. Zhang, and P. Li, “Ultrasound enhanced ferrite plating; bringing breakthrough in ferrite coating synthesized from aqueous solution,” *IEEE Transactions on Magnetics*, vol. 33, no. 5, pp. 3649–3651, 1997.

- [10] J. J. Cuomo, R. J. Gambino, J. M. E. Harper, J. D. Kuptsis, and J. C. Webber, "Significance of negative ion formation in sputtering and sims analysis," *Journal of Vacuum Science & Technology*, vol. 15, no. 2, pp. 281–287, 1978.
- [11] D. Dijkkamp, T. Venkatesan, X. D. Wu et al., "Preparation of Y-Ba-Cu oxide superconductor thin films using pulsed laser evaporation from high T_c bulk material," *Applied Physics Letters*, vol. 51, no. 8, pp. 619–621, 1987.
- [12] D. M. Lind, S. D. Berry, G. Chern, H. Mathias, and L. R. Testardi, "Growth and structural characterization of Fe₃O₄ and NiO thin films and superlattices grown by oxygen-plasma-assisted molecular-beam epitaxy," *Physical Review B*, vol. 45, no. 4, pp. 1838–1850, 1992.
- [13] Y. Suzuki, "Epitaxial spinel ferrite thin films," *Annual Review of Materials Science*, vol. 31, pp. 265–289, 2001.
- [14] Y. Suzuki, R. B. Van Dover, E. M. Gyorgy, J. M. Phillips, and R. J. Felder, "Exchange coupling in single-crystalline spinel-structure (Mn,Zn)Fe₂O₄/CoFe₂O₄ bilayers," *Physical Review B*, vol. 53, no. 21, pp. 14016–14019, 1996.
- [15] J. M. Yang, W. J. Tsuo, and F. S. Yen, "Preparation of ultrafine nickel ferrite powders using mixed Ni and Fe tartrates," *Journal of Solid State Chemistry*, vol. 145, no. 1, pp. 50–57, 1999.
- [16] J. Zhou, J. Ma, C. Sun et al., "Low-temperature synthesis of NiFe₂O₄ by a hydrothermal method," *Journal of the American Ceramic Society*, vol. 88, no. 12, pp. 3535–3537, 2005.
- [17] K. V. P. M. Shafi, Y. Koltypin, A. Gedanken et al., "Sonochemical preparation of nanosized amorphous NiFe₂O₄ particles," *Journal of Physical Chemistry B*, vol. 101, no. 33, pp. 6409–6414, 1997.
- [18] S. Prasad and N. S. Gajbhiye, "Magnetic studies of nanosized nickel ferrite particles synthesized by the citrate precursor technique," *Journal of Alloys and Compounds*, vol. 265, no. 1–2, pp. 87–92, 1998.
- [19] D. -H. Chen and X. -R. He, "Synthesis of nickel ferrite nanoparticles by sol-gel method," *Materials Research Bulletin*, vol. 36, no. 7–8, pp. 1369–1377, 2001.
- [20] Y. Shi, J. Ding, X. Liu, and J. Wang, "NiFe₂O₄ ultrafine particles prepared by co-precipitation/mechanical alloying," *Journal of Magnetism and Magnetic Materials*, vol. 205, no. 2, pp. 249–254, 1999.
- [21] J. Liu, H. He, X. Jin, Z. Hao, and Z. Hu, "Synthesis of nanosized nickel ferrites by shock waves and their magnetic properties," *Materials Research Bulletin*, vol. 36, no. 13–14, pp. 2357–2363, 2001.
- [22] A. Kale, S. Gubbala, and R. D. K. Misra, "Magnetic behavior of nanocrystalline nickel ferrite synthesized by the reverse micelle technique," *Journal of Magnetism and Magnetic Materials*, vol. 277, no. 3, pp. 350–358, 2004.
- [23] Z. Beji, T. Ben Chaabane, L. S. Smiri et al., "Synthesis of nickel-zinc ferrite nanoparticles in polyol: morphological, structural and magnetic studies," *Physica Status Solidi A*, vol. 203, no. 3, pp. 504–512, 2006.
- [24] S. Maensiri, C. Masingboon, B. Boonchom, and S. Seraphin, "A simple route to synthesize nickel ferrite (NiFe₂O₄) nanoparticles using egg white," *Scripta Materialia*, vol. 56, no. 9, pp. 797–800, 2007.
- [25] C. Yang, F. Liu, T. Ren et al., "Fully integrated ferrite-based inductors for RF ICs," *Sensors and Actuators A*, vol. 130–131, pp. 365–370, 2006.
- [26] Y. K. Fetisov, A. A. Bush, K. E. Kametsev, A. Y. Ostashchenko, and G. Srinivasan, "Ferrite-piezoelectric multilayers for magnetic field sensors," *IEEE Sensors Journal*, vol. 6, no. 4, Article ID 1661574, pp. 935–938, 2006.
- [27] M. Pardavi-Horvath, "Microwave applications of soft ferrites," *Journal of Magnetism and Magnetic Materials*, vol. 215, pp. 171–183, 2000.
- [28] L. D. Landau and E. Lifshitz, "On the theory of the dispersion of magnetic permeability in ferromagnetic bodies," *Physik Z. Sowjetunion*, vol. 8, pp. 153–169, 1935.
- [29] N. Mo, Y. Y. Song, and C. E. Patton, "High-field microwave effective linewidth in polycrystalline ferrites: physical origins and intrinsic limits," *Journal of Applied Physics*, vol. 97, no. 9, Article ID 093901, pp. 1–9, 2005.
- [30] N. Mo, J. J. Green, P. Krivosik, and C. E. Patton, "The low field microwave effective linewidth in polycrystalline ferrites," *Journal of Applied Physics*, vol. 101, no. 2, Article ID 023914, 2007.
- [31] R. Valenzuela, R. Zamorano, G. Alvarez, M. P. Gutiérrez, and H. Montiel, "Magnetoimpedance, ferromagnetic resonance, and low field microwave absorption in amorphous ferromagnets," *Journal of Non-Crystalline Solids*, vol. 353, no. 8–10, pp. 768–772, 2007.
- [32] H. Montiel, G. Alvarez, I. Betancourt, R. Zamorano, and R. Valenzuela, "Correlations between low-field microwave absorption and magnetoimpedance in Co-based amorphous ribbons," *Applied Physics Letters*, vol. 86, no. 7, Article ID 072503, pp. 1–3, 2005.
- [33] M. Knobel, M. Vazquez, and L. Kraus, "Giant Magnetoimpedance," in *Handbook of Magnetic Materials*, K. H. J. Buschow, Ed., vol. 15, p. 497, Elsevier Science, 2003.
- [34] A. Verma, M. I. Alam, R. Chatterjee, T. C. Goel, and R. G. Mendiratta, "Development of a new soft ferrite core for power applications," *Journal of Magnetism and Magnetic Materials*, vol. 300, no. 2, pp. 500–505, 2006.
- [35] V. Zaspalis, V. Tsakaloudi, E. Papazoglou, M. Kolenbrander, R. Guenther, and P. V. D. Valk, "Development of a new MnZn-ferrite soft magnetic material for high temperature power applications," *Journal of Electroceramics*, vol. 13, no. 1–3, pp. 585–591, 2004.
- [36] E. J. Brandon, E. E. Wesseling, V. Chang, and W. B. Kuhn, "Printed microinductors on flexible substrates for power applications," *IEEE Transactions on Components and Packaging Technologies*, vol. 26, no. 3, pp. 517–523, 2003.
- [37] F. Amalou, E. L. Bornand, and M. A. M. Gijs, "Batch-type millimeter-size transformers for miniaturized power applications," *IEEE Transactions on Magnetics*, vol. 37, no. 4, pp. 2999–3003, 2001.
- [38] E. Belloy, S. Thurre, E. Walckiers, A. Sayah, and M. A. M. Gijs, "Introduction of powder blasting for sensor and microsystem applications," *Sensors and Actuators. A*, vol. 84, no. 3, pp. 330–337, 2000.
- [39] F. Preisach, "Über die magnetische Nachwirkung," *Zeitschrift für Physik*, vol. 94, no. 5–6, pp. 277–302, 1935.
- [40] M. Angeli, E. Cardelli, and E. Della Torre, "Modelling of magnetic cores for power electronics applications," *Physica B*, vol. 275, no. 1–3, pp. 154–158, 2000.
- [41] P. R. Wilson, J. N. Ross, and A. D. Brown, "Modeling frequency-dependent losses in ferrite cores," *IEEE Transactions on Magnetics*, vol. 40, no. 3, pp. 1537–1541, 2004.
- [42] G. Stojanovic, M. Damnjanovic, V. Desnica et al., "High-performance zig-zag and meander inductors embedded in ferrite material," *Journal of Magnetism and Magnetic Materials*, vol. 297, no. 2, pp. 76–83, 2006.
- [43] Z. W. Li, L. Guoqing, L. Chen, W. Yuping, and C. K. Ong, "Co²⁺Ti⁴⁺ substituted Z-type barium ferrite with enhanced imaginary permeability and resonance frequency," *Journal of Applied Physics*, vol. 99, no. 6, Article ID 063905, 2006.

- [44] Y. B. Feng, T. Qiu, C. Y. Shen, and X. -Y. Li, "Electromagnetic and absorption properties of carbonyl iron/rubber radar absorbing materials," *IEEE Transactions on Magnetics*, vol. 42, no. 3, pp. 363–368, 2006.
- [45] B. W. Li, Y. Shen, Z.-X. Yue, and C.-W. Nan, "Enhanced microwave absorption in nickel/hexagonal-ferrite/polymer composites," *Applied Physics Letters*, vol. 89, no. 13, Article ID 132504, 2006.
- [46] R. C. Che, C. Y. Zhi, C. Y. Liang, and X. G. Zhou, "Fabrication and microwave absorption of carbon nanotubes CoFe_2O_4 spinel nanocomposite," *Applied Physics Letters*, vol. 88, no. 3, Article ID 033105, pp. 1–3, 2006.
- [47] C. Xiang, Y. Pan, X. Liu, X. Sun, X. Shi, and J. Guo, "Microwave attenuation of multiwalled carbon nanotube-fused silica composites," *Applied Physics Letters*, vol. 87, no. 12, Article ID 123103, pp. 1–3, 2005.
- [48] Y. Yang, M. C. Gupta, K. L. Dudley, and R. W. Lawrence, "Novel carbon nanotube—Polystyrene foam composites for electromagnetic interference shielding," *Nano Letters*, vol. 5, no. 11, pp. 2131–2134, 2005.
- [49] H. A. Lowenstam, "Magnetite in denticle capping in recent chitons (Polyplacophora)," *Bulletin Geological Society of America*, vol. 73, no. 4, pp. 435–438, 1962.
- [50] C. Zhang, H. Vali, C. S. Romaner, T. J. Phelps, and S. V. Liu, "Formation of single-domain magnetite by a thermophilic bacterium," *American Mineralogist*, vol. 83, no. 11-12, pp. 1409–1418, 1998.
- [51] I. Šafařík and M. Šafaříková, "Magnetic nanoparticles and biosciences," *Monatshefte für Chemie*, vol. 133, no. 6, pp. 737–759, 2002.
- [52] C. M. Fu, Y. F. Wang, Y. F. Guo, T. Y. Lin, and J. S. Chiu, "In vivo bio-distribution of intravenously injected Tc-99 m labeled ferrite nanoparticles bounded with biocompatible medicals," *IEEE Transactions on Magnetics*, vol. 41, no. 10, pp. 4120–4122, 2005.
- [53] C. R. Martin and D. T. Mitchell, "Nanomaterials in analytical chemistry," *Analytical Chemistry*, vol. 70, no. 9, pp. 322A–327A, 1998.
- [54] T. C. Yeh, W. Zhang, S. T. Ildstad, and C. Ho, "In vivo dynamic MRI tracking of rat T-cells labeled with superparamagnetic iron-oxide particles," *Magnetic Resonance in Medicine*, vol. 33, no. 2, pp. 200–208, 1995.
- [55] A. Jordan, R. Scholz, K. Maier-Hauff et al., "Presentation of a new magnetic field therapy system for the treatment of human solid tumors with magnetic fluid hyperthermia," *Journal of Magnetism and Magnetic Materials*, vol. 225, no. 1-2, pp. 118–126, 2001.
- [56] J. Giri, P. Pradhan, T. Sriharsha, and D. Bahadur, "Preparation and investigation of potentiality of different soft ferrites for hyperthermia applications," *Journal of Applied Physics*, vol. 97, no. 10, Article ID 10Q916, pp. 1–3, 2005.
- [57] D. H. Kim, S. H. Lee, K. N. Kim, K. M. Kim, I. B. Shim, and Y. K. Lee, "Temperature change of various ferrite particles with alternating magnetic field for hyperthermic application," *Journal of Magnetism and Magnetic Materials*, vol. 293, no. 1, pp. 320–327, 2005.
- [58] T. Matsunaga and S. Kamiya, "Use of magnetic particles isolated from magnetotactic bacteria for enzyme immobilization," *Applied Microbiology and Biotechnology*, vol. 26, no. 4, pp. 328–332, 1987.
- [59] I. Šafařík and M. Šafaříková, "Use of magnetic techniques for the isolation of cells," *Journal of Chromatography B*, vol. 722, no. 1-2, pp. 33–53, 1999.
- [60] K. Sode, S. Kudo, T. Sakaguchi, N. Nakamura, and T. Matsunaga, "Application of bacterial magnetic particles for highly selective mRNA recovery system," *Biotechnology Techniques*, vol. 7, no. 9, pp. 688–694, 1993.

Research Article

Investigation of Multicritical Phenomena in ANNNI Model by Monte Carlo Methods

A. K. Murtazaev^{1,2} and J. G. Ibaev¹

¹ *Institute of Physics, Daghestan Scientific Center of RAS, Yaragskogo Street 94, Makhachkala 367003, Russia*

² *Daghestan State University, Gadzhieva Street 43a, Makhachkala 367025, Russia*

Correspondence should be addressed to J. G. Ibaev, ibaev77@mail.ru

Received 20 July 2011; Accepted 16 December 2011

Academic Editor: Vladimir Shavrov

Copyright © 2012 A. K. Murtazaev and J. G. Ibaev. This is an open access article distributed under the Creative Commons Attribution License, which permits unrestricted use, distribution, and reproduction in any medium, provided the original work is properly cited.

The anisotropic Ising model with competing interactions is investigated in wide temperature range and $|J_1/J|$ parameters by means of Monte Carlo methods. Static critical exponents of the magnetization, susceptibility, heat capacity, and correlation radius are calculated in the neighborhood of Lifshitz point. According to obtained results, a phase diagram is plotted, the coordinates of Lifshitz point are defined, and a character of multicritical behavior of the system is detected.

1. Introduction

Apart from problems of critical phenomena, more complex phenomena observed near the diagram special points of system states, where the lines of different order phase transitions cross, are heavily emphasized [1]. These phenomena, conditionally named “multicritical,” are possible in those systems, where a symmetry and interparticle interaction assumes several types of ordering. Similar phenomena are observed in a mixture of gases, liquids, ferroelectrics, magnetics, and so forth.

An experimental investigation of the multicritical phenomena is more complex than theoretical. This complexity has to do with the fact that in the neighborhood of multicritical point, a region with different strongly developed fluctuations broadens, and the crossovers are probable [2].

A theoretical study of multicritical phenomena results in complex nonlinear differential equations. Exact analytical solution of these equations also entails great difficulties [3]. In this connection the methods of computational physics (Monte Carlo method (MC)) and molecular dynamics (MD) became basic techniques to study those equations at present. In practice, for description of such complex systems, different models are used. The simplest and effective one among them is anisotropic Ising model with competing interactions with second nearest neighbors (ANNNI model,

Figure 1). We plot a phase diagram for this model and study a character of the critical behavior in Lifshitz point using the standard method of Monte Carlo.

2. Model

ANNNI model appeared in the static physics in the second half of XX century for explanation of the spiral magnetic order in heavy rear-earth metals [4]. Its Hamiltonian in perfect cubic lattice has the following form:

$$H_{\text{ANNNI}} = -J \sum_{i,j} s_i s_j + J_1 \sum_i s_i s_{i+1}, \quad (1)$$

where $s_i = \pm 1$, J denotes the parameter of exchange interaction of neighboring spin pairs, and $J_1 > 0$ is the parameter of antiferromagnetic exchange of neighbors following the nearest neighbor along Z axis.

A topology of $T - |J_1/J|$ phase diagram includes three regions for three-dimensional case (3D), which are crossing in multicritical Lifshitz point [5]. The system is paramagnetic at high temperatures and is ferromagnetic at low T and small $|J_1/J|$; when $|J_1/J|$ has sufficiently large values, the modulated phases are generated (Figure 2).

According to the literature data when temperature decreasing ANNNI model undergoes the second-order phase

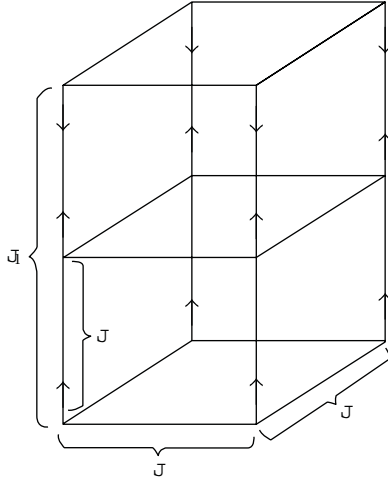


FIGURE 1: Anisotropic model with competing interactions.

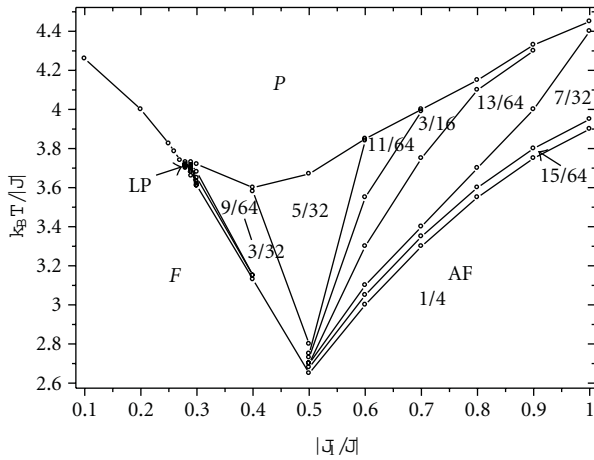


FIGURE 2: Phase diagram of anisotropic Ising model with competing interactions (by the data of [6]).

transition from paramagnetic state to the nearest ordered state, and a transition “ferromagnetic-modulated state” is the first-order transition [7].

For description of a phase behavior of studied model, we used approximated theoretical methods including high- and low-temperature expansions [8], the mean-field theory [9], and other theoretical approximations [10].

The Monte Carlo modeling [11] mainly was carried out in a region of “ferromagnetic-paramagnetic” transition up to the Lifshitz point [12], but a precise determination of the transition in the point and its nearest neighborhood remains unsolved.

According to data in [6, 12], a critical behavior of the systems with modulated structures at small values of $|J_1/J|$ is described by the Ising universality class of the critical behavior. When increasing $|J_1/J|$ a crossover to the critical behavior typical for the Lifshitz point occurs and from it to XY-critical behavior.

3. Method of Investigation

The cubic systems with periodic boundary conditions and sizes $L \times L \times L$, $L = 12 \div 64$ were used for investigation of multicritical phenomena in the vicinity of the Lifshitz point. Spin number in studied systems was $N_{\text{eff}} = 512 \div 262144$. Markov chains of $\tau = 1000\tau_0$ length ($\tau_0 = 10^4$ MC-step/spin is a length of nonequilibrium part) were generated on the computer. The thermodynamic parameters of the system were calculated by averaging along this chain. Moreover, the averaging was carried out by 1000 different initial configurations. An error of obtained results does not exceed the sizes of symbols used in Figures.

The temperature dependences of the heat capacity and susceptibility were derived by means of expressions [9]

$$C = (NK^2)(\langle U^2 \rangle - \langle U \rangle^2),$$

$$\chi = (NK)(\langle m^2 \rangle - \langle m \rangle^2),$$
(2)

where $K = |J|/k_B T$; U denotes the intrinsic energy; m indicates the magnetization.

The critical temperature was estimated by the Binder cumulant method. According to the finite-size scaling theory (FSS) [13], the cumulants

$$U_L = 1 - \frac{\langle m^4 \rangle}{3\langle m^2 \rangle^2},$$
(3)

for systems with different sizes L , cross in a critical point T_c . Plotting the U_L temperature dependences for systems with different sizes L , one can estimate the critical temperatures of systems. Critical temperatures values calculated by this method for different values of $|J_1/J|$ are presented in Table 1.

The critical parameters of the magnetization, susceptibility, and correlation radius were estimated from a ratio of FSS theory [14].

For calculation of the magnetic properties of modulated region, we used a value

$$M_Z = \frac{1}{L^2} \sum_{x,y}^L S_{x,y,z},$$
(4)

being the averaged magnetization of the layer, which is perpendicular to Z axis.

The values of a wave number and a character of amplitude and phase modulation were detected by means of mathematical apparatus of the spectral analysis based on the Fourier transformations [15].

4. Results and Discussion

Using Fourier transformations, we succeeded, with sufficiently high accuracy, to calculate the existence domains of modulated phases with different values of the wave length and estimate a stability of the modulated phases. If on their Fourier transforms, there are observed clearly defined peaks at a value of k , one can consider with confidence that the structure is stable in the given temperature range and ratio of interaction constants. The appearance of side

TABLE 1: Critical parameters of the ANNNI model.

$ J_1/J $	T_c	α/ν	β/ν	γ/ν	$1/\nu$	α	β	γ	ν
0,271	3,736(1)	0,352	0,431	2,499	1,799	0,196(4)	0,240(4)	1,389(6)	0,556(6)
0,272	3,732	0,379	0,429	2,719	1,903	0,199	0,225	1,427	0,525
0,273	3,728	0,420	0,422	2,880	2,055	0,203	0,206	1,403	0,487
0,274	3,724	0,460	0,421	3,053	2,183	0,211	0,193	1,398	0,458
0,275	3,726	0,449	0,422	3,002	2,125	0,211	0,199	1,414	0,471
0,276	3,727	0,461	0,422	3,117	2,225	0,207	0,189	1,400	0,449
Ising	4,511					0,113	0,3258	1,239	0,63

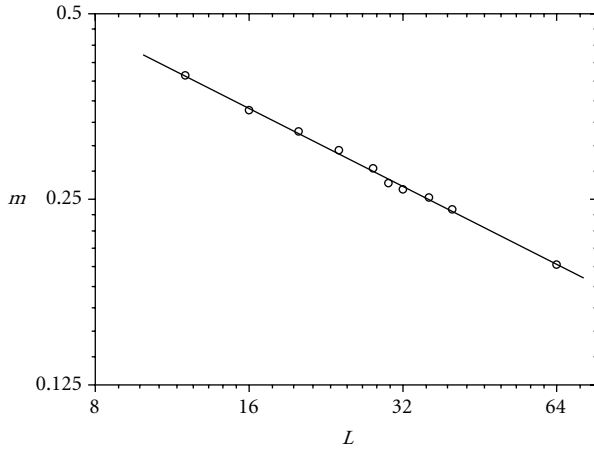


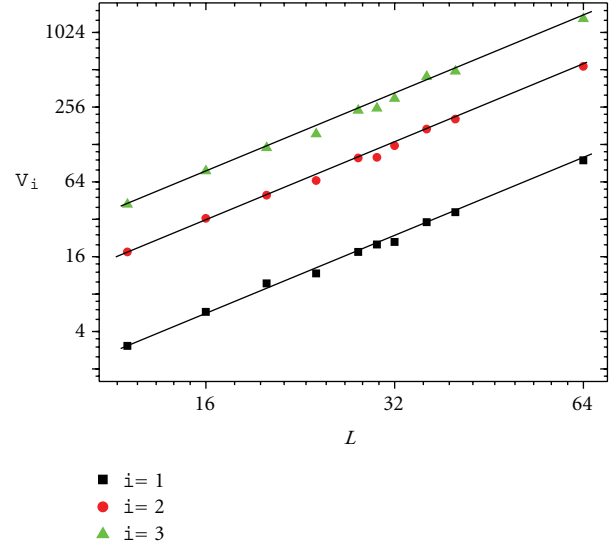
FIGURE 3: Log-log scale dependence of the magnetization.

peaks above and below the main maximum on the Fourier transformations indicates that the system is in a region of transition from one modulated structure to another. A transition of the system from a modulated phase into the paramagnetic phase can be detected by a sharp increase of peaks on the Fourier transformations, what confirms the continuity of its spectrum.

Generalizing the obtained results, we plotted a $|J_1/J|$, $k_B T/|J|$ phase diagram (Figure 2). The second-order phase transition dependences were calculated by the Binder cumulants method, and lines of transitions in the modulated region were derived by the results of Fourier analysis. A temperature in which uneven change in wave number of modulated structures occurs was taken as a transition temperature.

As it is evident from plotted phase diagram, the multicritical Lifshitz point is revealed in the intervals $0,27 < |J_1/J| < 0,28$ and $3,74 < T < 3,72$. Therefore, all experimental data of the critical parameters presented in the work belong to the given range of parameter change of $|J_1/J|$ and T .

To determine the critical exponents, we plotted the log-log scale curves for the dependences of thermodynamic parameters on system linear sizes at $T = T_c$. Figures 3 and 4 present the characteristic dependences of magnetization and parameters of V_i at $i = 1, 2, 3$ on linear sizes at $|J_1/J| = 0,273$. As it is clear from Figures, all points on curves lie down a straight line within an error. The inclination of line detects

FIGURE 4: Log-log scale dependence of V_i on the system linear sizes.

the values of β/ν in Figure 3 and of $1/\nu$ in Figure 4. By the same dependences the values of α/ν and γ/ν were defined. The obtained values of the critical exponents are shown in Table 1.

According to data in the Table 1, a character of change of critical parameters up to $|J_1/J| < 0,274$ is the same as in work [6]. Such a behavior is connected with the crossover from the critical behavior to the multicritical and inversely. Obviously, behavior of critical parameters at $|J_1/J| > 0,274$ is due to the fact that our system starts to aberrate from multicritical behavior, and, consequently, the Lifshitz point is localized in range of $|J_1/J| = 0,274$ and $T = 3,724$.

It should be observed that, in this work, unlike previous work [6], the critical exponents of correlation radius are estimated. A change of ν values with increase in $|J_1/J|$, probably, has to do with the region that with strongly developed fluctuations widens at approximation to the multicritical point.

In conclusion, let us note that a critical behavior of majority of crystals in the vicinity of phase transitions differs from being predicted for corresponding universality classes. A reason for such behavior is various anisotropic and competitive interactions existing in real systems. A consideration of all possible kinds of anisotropy and interactions can

lead to the multicritical phenomena, which appear on the phase diagrams as intersection point of phase transitions curves (a typical example—the Lifshitz point). Therefore, the investigation of similar phenomena is also important condition for studying the critical phenomena. A design of new methods of investigation and algorithms of modeling for estimation of multicritical phenomena can favour the study not only of the Lifshitz point neighborhoods but amplify the application of Monte Carlo methods for research of more complex systems.

Acknowledgment

Support by RFBR (no. 09-02-96506), and PHCP (no. II554 and no. 02.740.11.03.97) is acknowledged.

References

- [1] P. A. Fleury, “Phase transitions, critical phenomena, and instabilities,” *Science*, vol. 211, no. 4478, pp. 125–131, 1981.
- [2] M. A. Anisimov, E. E. Gorodetskii, and V. M. Zaprudskii, “Phase transitions with coupled order parameters,” *Soviet physics, Uspekhi*, vol. 24, pp. 57–75, 1981.
- [3] Yu. A. Izumov and V. M. Siromyatnikov, *Phase Transitions and Crystal Symmetry*, Springer, 1984.
- [4] W. Selke, “The ANNNI model—theoretical analysis and experimental application,” *Physics Reports*, vol. 170, no. 4, pp. 213–264, 1988.
- [5] R. M. Hornreich, M. Luban, and S. Shtrikman, “Critical behavior at the onset of $k \rightarrow -$ space instability on the λ line,” *Physical Review Letters*, vol. 35, no. 25, pp. 1678–1681, 1975.
- [6] A. K. Murtazaev and Z. G. Ibaev, “Critical properties of the anisotropic Ising model with competing interactions,” *Journal of Experimental and Theoretical Physics*, vol. 113, no. 1, pp. 106–112, 2011.
- [7] A. Gendiar and T. Nishino, “Phase diagram of the three-dimensional axial next-nearest-neighbor Ising model,” *Physical Review B*, vol. 71, no. 2, Article ID 024404, 7 pages, 2005.
- [8] S. Redner and H. E. Stanley, “Helical order and its onset at the Lifshitz point,” *Physical Review B*, vol. 16, no. 11, pp. 4901–4906, 1977.
- [9] P. Peczak, A. M. Ferrenberg, and D. P. Landau, “High-accuracy Monte Carlo study of the three-dimensional classical Heisenberg ferromagnet,” *Physical Review B*, vol. 43, no. 7, pp. 6087–6093, 1991.
- [10] P. Bak and J. Von Boehm, “Ising model with solitons, phasons, and ‘the devil’s staircase,’” *Physical Review B*, vol. 21, no. 11, pp. 5297–5308, 1980.
- [11] K. Kaski and W. Selke, “Monte Carlo coarse graining for the three-dimensional axial next-nearest-neighbor Ising model,” *Physical Review B*, vol. 31, no. 5, pp. 3128–3130, 1985.
- [12] M. Pleimling and M. Henkel, “Anisotropic scaling and generalized conformal invariance at Lifshitz points,” *Physical Review Letters*, vol. 87, no. 12, Article ID 125702, 4 pages, 2001.
- [13] K. Binder, “Critical properties from Monte Carlo Coarse graining and renormalization,” *Physical Review Letters*, vol. 47, no. 9, pp. 693–696, 1981.
- [14] A. K. Murtazaev, I. K. Kamilov, and K. K. Aliev, “Finite-size scaling and critical exponents of the real antiferromagnetic model,” *Journal of Magnetism and Magnetic Materials*, vol. 204, no. 1, pp. 151–158, 1999.
- [15] R. J. Elliott, “Phenomenological discussion of magnetic ordering in the heavy rare-earth metals,” *Physical Review*, vol. 124, no. 2, pp. 346–353, 1961.

Review Article

Softening the “Crystal Scaffold” for Life’s Emergence

Gargi Mitra-Delmotte¹ and Asoke Nath Mitra²

¹ 39 Cite de l’Ocean, Montgaillard, 97400 St. Denis, Reunion

² Department of Physics, Delhi University, 244 Tagore Park, Delhi 110009, India

Correspondence should be addressed to Gargi Mitra-Delmotte, gargijj@orange.fr
and Asoke Nath Mitra, ganmitra@nde.vsnl.net.in

Received 1 August 2011; Accepted 13 November 2011

Academic Editor: Manh-Huong Phan

Copyright © 2012 G. Mitra-Delmotte and A. N. Mitra. This is an open access article distributed under the Creative Commons Attribution License, which permits unrestricted use, distribution, and reproduction in any medium, provided the original work is properly cited.

Del Giudice’s group studies how water can organize on hydrophilic surfaces forming coherent domains (loaning energy from the quantum vacuum), plus quasifree electrons, whose excitations produce cold vortices, aligning to ambient fields. Their electric and magnetic dipolar modes can couple to oscillatory (electric-organic dipoles) and/or rotary (magnetic-mineral dipoles), besides responding to magnetic potentials. Thus, imprinted electromagnetic patterns of catalytic colloids—compared with Cairns-Smith’s “crystal scaffold”—on their structured water partners could have equipped the latter with a selection basis for “choosing” their context-based “soft-matter” (de Gennes) replacements. We consider the potential of the scenario of an external control on magnetic colloids forming in the Hadean hydrothermal setting (of Russell and coworkers)—via a magnetic rock field—conceptually enabling self-assembly, induction of asymmetries, response effects towards close-to-equilibrium dynamics, and associative networks, besides providing a coherent environment for stabilizing associated symmetry-broken quanta and their feedback interactions with those of coherent water domains, to address the emergence of metabolism and replication.

1. Introduction

1.1. Revisiting Cairns-Smith’s “Arch” Metaphor for Soft Living Systems. Life’s efficient use of the colloid-gel state, combining the best from the structured world of solids with the softness and fluidity of the liquid state, strongly supports its origins in such a setting [1–4]. Again as the cell’s synthetic machinery reveals a hierarchy of organic compounds of progressively increasing complexity, approaches to the emergence of life have traditionally centered on organic-based assemblies. These approaches can broadly be distinguished in terms of the targeted location on the machinery: the core comprising simpler organics woven in cycles of small metabolic reactions, or the periphery, consisting of organics with specialized functions. Typically, theories proposing that the metabolic wing of life had preceded the replicating one focus on the simpler core reactions that could have been hosted on assemblies of either organics [5] or colloidal inorganic compounds [6], as running the simple (core) cycles in the reverse (reductive) mode can shed light on the plausible links between the transfer of electrons from higher

to lower states of energy and the emergence of life in the Hadean conditions of disequilibrium [7–9]. “Replicators” in “metabolism-first” approaches are thought to have gradually emerged as feedback type correlations emerged between networks, eventually leading to the code [10, 11]. These scenarios are based on the sound premise that the efficient capture of energy, released from the primordial reaction networks, would have awaited the emergence of order in the hosting surfaces [12]. Still, plausible stages as to how this came about and enabled the quantitative reproduction of information do need to be chartered. At the other extreme, theories proposing that the replicating wing appeared first focus on the complex organics on the periphery of the reaction nets. Although their principle of targeting the function is a sound one, these proposals face a dilemma on account of the assumed association of these functions with complex organic structures (whose synthesis they attempt) as their peripheral location indicates that they must have arisen later. And even if it were possible to accomplish the Herculean task of construing a suitable geochemical setting in the Hadean that could be argued to meet the requirements

for producing ample amounts of the complex building blocks, directly from very basic organic units, the conceptual bridge as to how the complex biomolecules associated with biofunctions came to be formed from the simpler organics in the core would remain unaddressed. By uncoupling the organic structure-function association, Cairns-Smith [13] proposes the analogy to the “arch” metaphor as a way out of this impasse, suggesting that in the Hadean, available nonorganic predecessors that could have accomplished these functions may have started the cycle and thus offered a functional basis of selection for takeover by the bio-organics. His novel theory posits that clay minerals were the first self-replicating living forms where genetic information was encoded in patterns like random sequences of stacked mineral layers (instead of nucleotide bases), crystal growth defects, aperiodic distributions of ions, and so forth. Its main hurdle is that the rigid framework of hard crystals is seen as conceptually incompatible with evolving dissipative dynamical structures.

Nevertheless, the intuitive argument of a “readily available” mineral scaffold [13] could be expanded in the sense of a lowest common denominator (LCD) template having the basic functional attributes of living systems in their simplest form, where a synthesis of mineral-based approaches could explain how energy (associated with metabolism) and information (associated with replication) became synonymous in complex biomatter [14]. For instance, although crystalline order is typically associated with rigid geometrical patterns, we need to study the carriers of its information, to look for an aspect of its ordering that could be compatible with motion, towards the dynamical interception of energy by catalytic colloidal surfaces. It is therefore pertinent to look at the correspondence between the “global motions” of enzyme components and the collective vibrations of the crystal lattice [15]. Also, the capacity to capture the released energy and stretch its residence time and prevent its fast dissipation to the sink is difficult to imagine in terms of far-from-equilibrium examples, such as turbulent flows that have no obvious coherent connection between the microscopic and macroscopic flows. Now, a coherent-ordering mechanism associated with an inorganic colloidal scaffold could have compatibility with both requirements, and this extended soft template (c.f. [13]), *with an essential role for structured water* as a fountainhead for life, forms our premise. For meeting this demand, we need a mechanism providing long-range correlations as in condensed matter physics (CMP) via association of ordered structures with the colloidal-gel state.

1.2. QFT/QED: A Basis for Correlated Components and Interaction Space. A glimpse of a kind of stable yet dynamic order in an open system that could have enabled such interception can be from the many-body model proposed by Umezawa et al. [16, 17] which states [18] that “in any material in CMP any particular information is carried by certain ordered patterns maintained by certain long range correlations mediated by massless quanta. It looked to me (Umezawa) that this is the only way to memorize

some information; memory is a particular pattern of order supported by long range correlations.” Indeed, Fröhlich’s [19] landmark proposal suggests how a continuous supply of energy should lead to the establishment of coherent order over macroscopic distances via long-range phase correlations between molecules. Upon pumping, excitations of the densely packed particles with electric and elastic interactions are expected to lead to vibrations building up into collective modes of photons, phonons, and so forth this generates a coherent dipolar wave motion which exchanges energy with the surrounding electromagnetic field. And, being coherent, this energy gets stored in an ordered manner (not thermalized). Importantly, the electromagnetic field coupled to the dipolar biomolecules plays a key role in mediating their coupled interactions.

Now, this picture of correlated components connected via an environmental (electromagnetic) field obviously calls for a paradigm shift from the conventional picture of independent system parts that could be isolated from each other, and also the environment to keep thermal effects at bay. Traditionally complex biosystems are dealt with either thermodynamic or causal-dynamical approaches. Now, while holistic approaches like the former miss out on microscopic details in their search for global principles, reductionist ones like the latter lose sight of holistic features like coherence. Furthermore, features like coherence demand a knowledge of the underlying manifolds of the interactions, that is, the structure of the space in which the components are interacting. Although causal-dynamical approaches can provide such a description, too much “reductionism” associated with them interferes with a holistic formulation; in contrast, thermodynamics is way too macroscopic for adequate descriptions of underlying interacting fields. In this context, quantum electrodynamics (QED)—the acknowledged “Queen” of all quantum field theories (QFTs)—has a natural in-built holistic feature without losing out on causality which is needed to address hierarchical description all the way from microscopic to macroscopic domains [20] (For a flavour of this vast subject, the reader is referred to a tutorial [21] elsewhere). As noted by the Del Giudice group, the field environment, crucial for the dynamics of the correlated particles, finds a powerful representation in the QFT language of “vacuum” (originally formulated for empty space). Now, while a modern form of QFT predicts the existence of infinitely many minima (degenerate vacuum), the former nevertheless owes its origin to its simplest form, namely the so-called unique vacuum—the single state of lowest energy. The time evolution of these degenerate vacua on the other hand follows a more complex pattern of symmetry principles than the one followed by system components in empty space (governed by Euler-Lagrangian equation). And different patterns of time evolution of the vacua, characterized by breaking of conventional symmetries—especially time reversal—as compared to that of the system components in empty space, allow for a description of the evolution of the system across its vacua in an irreversible (biolike) fashion [22–24]. In this scenario, the “phase transitions” of the system are seen as typical QED symmetry-breaking effects corresponding to the

different vacua that are imprinted on the dynamics of its components [25].

Del Giudice and Tedeschi [26] further argue that the archetypal framework of a crowded chemical reactor of randomly colliding independent molecules (range of few angstroms only) cannot explain how, despite crowding, living matter components detect each other from afar and interact via long sequences of biochemical reactions, with sharply defined space-time order. Also, in a chemical reactor, released energy gets dissipated as heat, that is, increased kinetic energy of randomly moving molecules, leading to increase in entropy and wild temperature fluctuations. In contrast, in living matter, where energy gets stored for carrying out different functions, its supply seems to fit in with a wave-like QED scenario (see Section 2) of a moving electromagnetic field whose frequency depends on the coherence strength of the medium and therefore can attract “coresonating” molecules. In this way, as energy gets captured in a coherent medium, its coherent domain expands (by adding more and more field-coupled molecules), while fresh electromagnetic oscillations are added to the existing ones; thus, by mutual feedback, the process multiplies rapidly. This scenario ensures growth and order at very low entropy [27] at almost constant temperature (Section 2). And by virtue of the fact that the intensity of the coupled electromagnetic field is inversely proportional to the difference of their oscillation frequencies, so that only molecules whose oscillation frequencies are nearly resonant attract themselves strongly, a dynamic basis to the origin of the selective-recognition codes orchestrating the bioreactions (hitherto accepted as dogma) is achieved [28].

1.3. Outline of Paper. These insights lead to the intriguing possibility that the colloidal state can also show properties associated with crystal lattices, and when seen from this angle, the two approaches seem to converge, with colloidal minerals participating in a functional template as a basis for selection of biomolecules—from simpler building units to increasingly complex ones (like membrane phospholipids, proteins, carbohydrates, nucleic acids, etc.)—and also their mutual interactions. Indeed, this is in addition to their capacity to act as catalytic soft surfaces, compatible with dynamics. Thus, the following may be outlined:

- (1) we briefly review the scenario of water domains organized on hydrophilic colloidal surfaces envisaged by Del Giudice and coworkers [29] as to how these dissipative structures forming by coherent dynamics can show a reducing nature and effects electromagnetic potentials (instead of fields) can exert on a system with long-range phase correlations, before concluding this section with a brief historical perspective on QED developments (Section 2);
- (2) water being the common denominator in the hypothesized Hadean scenario and in the present day life forms, we consider how mineral colloids can provide a correspondence with the collective response behaviour [30] of complex biological molecules. Analogous to H-field induced associative networks

with ferrofluids, we look at the “mound scenario” [7] where magnetic iron-sulphur colloids can be similarly controlled with a (spatially varying) field from magnetic rocks [31, 32]. In a thermodynamic description, the symmetry-broken patterns of hypothesized field-driven mineral colloid assemblies and ATP-driven soft biomatter are compared (Section 3);

- (3) we point out how the presence of two different dipolar modes could have implications for water CDs to have acted as the “scaffold” enabling “takeover” (Section 4);
- (4) we consider how the paradigm of a soft “scaffold” (cf. [13]) of field-controlled catalytic-mineral colloids enrobed in organized water [26] could address the entangled emergence of both (metabolic and replicating) wings of life (Section 5);
- (5) conclusions and scope (Section 6).

2. Dissipative Coherent Domains and Vector Potential Effects

Having appreciated the relevance of a coherent system of phase-correlated components, for being in a position to intercept energy as in life processes, one also sees the huge jump needed for a molecular assembly (as in conventional origin-of-life approaches)—an uncorrelated ensemble—to make, in order to achieve that status. To that end, Del Giudice and coworkers [25, 27–29] consider the unique role of water in living systems (that accounts for 70% in weight and 99% in molar weight). In fact, the ordering of water, leading to what is called exclusion zones in the presence of structure makers like PEG or natural ones like carbohydrates, has for long been exploited for the stabilization of biomolecules for *in vitro* and *in vivo* purposes [33]. In contrast to ordinary water, interfacial water close to hydrophilic biosurfaces, studied in detail by Pollack’s group, has been found to have a number of anomalous properties. Apart from resisting penetration of solutes, this exclusion zone (EZ) is associated with charge separation; the structured zone itself is negatively charged, while protons concentrated in the region beyond are free to diffuse, as dictated by the local electric gradient [3]. The boundary between EZ and normal water forms a redox pile thanks to the negative electric potential of the former of the order of 100 mV relative to the latter. Remarkably, the growth of this zone has been found to be induced upon exposure to light radiation, thus making this energetic pathway a central protagonist for the origin of life. What is more, fluorescing exclusion zones show the possibility of electronic transitions, with implications for protometabolic processes; recall that energy of the order of soft X-rays is required to ionize a water molecule (ionization potential 12.60 eV [29]). And the diffusing protons—a by-product of the thus built-up exclusion zone—enable the process of coalescence by balancing the inter particle repulsion (owing to negatively charged structured water envelopes on the biomolecules), forming ordered arrays. This is indeed consistent with the

observation that increasing the light intensity diminishes the distance between microparticles [3]. But this scenario of orderly motion is at variance with the conventional picture of water with uncorrelated rotations and thermal effects [34], which is typically described with two-body interactions at relatively large distances. On the other hand, at much smaller relative distances, the opposite scenario dominates. Namely, the N-body interactions become increasingly dominant as r becomes smaller, when radiative corrections acquire increasing dominance giving rise to time-dependent e.m. fluctuations (necessarily coherent as against thermal effects).

These observations therefore have a natural interpretation in terms of the QED-based “coherence domain” (CD) theory [26, 35] in which charged system components are coupled to the e.m. field. CD theory makes use of a new collective ground state of the structured water (with entrapped e.m. fields) whose features differ from those of the isolated molecular ground state water (the incoherent gas phase). The noncoherent and coherent states are separated by an energy gap ($\lambda_{CD} = \hbar c/E_{ex} = 0.1$ m), corresponding to the infrared region, where $E_{ex} = 12.06$ eV is the energy of the excited state of water molecules. In this manner, this ubiquitous molecule gives rise to a “coherence trap,” eventually leading to a larger coherence unit [26, 34], where the water CD offers a reservoir of almost free electrons that are excitable at each step of metabolism with a concomitant reduction of entropy. Now, QFT, as distinguished from mere (single-particle) quantum mechanics, is characterized by an uncertainty relation connecting the number N of field quanta (unspecified) and a “phase” Φ which—unlike the usual phase of wave-like motion in quantum mechanics—describes something more subtle, namely the (coherent) “rhythm” (*a la* Del Giudice) of the field oscillations as a whole. This uncertainty relation [36] in QFT which reads as

$$\Delta N \Delta \Phi \geq \frac{\hbar}{2} \quad (1)$$

plays an important part in determining the collective coherence measure (Φ) of the aggregate of the bioparticles (*vis-a-vis* their number N) under the influence of the ambient e.m. field. A second uncertainty relation brings in the zero-point energy, or the energy of the quantum vacuum, which is best illustrated by the harmonic oscillator problem in quantum mechanics, namely, $\hbar\omega/2$, plays a subtle but crucial role in energy book keeping in the physics of biosystems. This concept shows up rather dramatically when a large number of (incoherent) particles undergo a “phase transition” down to an ordered state with a decrease in entropy. This process must be accompanied by the release of a certain amount of heat energy (so as not to violate the second law of thermodynamics). And the source of this energy is precisely the zero point quantum vacuum energy noted above.

As another interesting observation, Ho [37] has inferred the presence of coherent domains in embryos serving as detectors for the Aharonov-Bohm effect in a suitably designed setup. The abnormality profiles of these embryos match those exposed to weak static magnetic fields, pointing to the sensitivity of the former batch to the *vector potential* in an essentially field-free region. The significance of this subtle

effect has been interpreted by Brizhik et al. [38] in terms of *nonlinearity* of the corresponding Schrodinger equation. For a quick derivation, reinterpret the usual momentum p as *kinetic momentum*, on the lines of its energy counterpart which admits of a division in terms of kinetic and potential energies. Now, the corresponding “potential momentum” involves the e.m. *vector potential* A in the form eA where e is the charge of the concerned particle, so that the kinetic momentum becomes $(p - eA)$, and the usual kinetic energy term $p^2/2m$ term gets replaced by $(p - eA)^2/2m$. Now, for a linear (perturbative or 1st order) dependence on A , the phase ϕ can be simply “gauged away” (i.e., trivially eliminated), so that only a noncoherent description of the state remains! But with a more complete (nonlinear) dependence on A , one has the more interesting possibility that the phase ϕ can no longer be eliminated and depends directly on A , thus producing a coherence effect, while the “mundane” amplitude Ψ_0 has a more or less “classical” (noncoherent like) dependence on the fields E and H [38]. Note also that the phase ϕ is directly connected to the Aharonov-Bohm effect (recall the definition of its characteristic phase shift)!

To sum up the findings with a historical perspective, it is good to recall that the unique vacuum was the source of fundamental discoveries in the middle of the last century, such as the “Lamb shift,” which had generated novel ideas of renormalization of the vacuum, as well as second- and higher-order electromagnetic corrections, leading to incredible agreement with experiment up to one in 10^{12} ! In the excitement of these dramatic discoveries however, the potential powers of the e.m. field for impacting other (less exotic) phenomena somehow got lost sight (due to lack of immediate motivation?). In this respect, an important phenomenon—first recognized by the Italian group of Del Giudice and coworkers—concerns the role of QED as an (ubiquitous) *ambient field* making its impact on biomatter at the more earthly “first-order level” itself, even without going into such fancy second-order corrections! What Del Giudice’s group recognized was that in the ambient interaction of the e.m. field with biomatter, its vacuum is already in a highly degenerate form, together with its features of symmetry breaking and the presence of long-range Nambu-Goldstone (NG) bosons [27, 28, 39]. This interaction is best expressed in terms of the e.m. potentials A , ϕ (which have longer ranges than the corresponding field quantities E and H). It seems surprising that this elementary form of e.m. interaction with biomatter which is otherwise quite basic was not considered earlier in the literature in such a “holistic” form.

3. Water Organized on Biomatter versus Field-Controlled Mineral Colloids

The above framework for stable dissipative structure formation and storage of energy in coherent form brings about a synthesis of energy and information (!) that seems highly relevant for water, which is capable of changing its supramolecular organization depending upon its interaction with the environment. This is thanks to the special properties

of the electronic spectrum of the ubiquitous molecule—their proposed candidate providing the “hardware.” As discussed above [38], the vector potential A —the “brain” behind the coherent arrays (of e.m. field-entrapped CDs)—already offers a “switch” for controlling the phase of the coherent system, with a range of implications for living organisms, such as global selection mechanisms and communication networks. But, as water in the coherent organized state requires a hydrophilic surface for its structuring, this may well also hold the key to how the “takeover” from minerals by organics [13] had come about, its collaborating presence being a common factor in both scenarios—hypothesized mineral colloids in the Hadean and organic living systems today. In particular, we refer to the dynamical basis of selection via the e.m.f. mediated resonance basis of attraction of molecules ([24, 26–28], Section 2). Now, since life is a historical phenomenon, the question of how the phase of the coherent water system could have been manipulated must hence be intimately entangled with the properties, the nature, and the workings of these “eccentric” biomolecules that “took over” from their inorganic ancestors. In addition, noncovalent interactions between the complex molecules, like lipids, proteins, carbohydrates, and nucleic acids, via a variety of recognition modes—that underlie biological language—frequently appear in myriad conserved patterns for propagating information observable across kingdoms of life. Instead of life’s emergence based on the single origins of only one of these complex forms in a suitable geochemical setting (where the issue of how these associations might have happened would have to be either postponed or skipped), the picture gels with that of gradually building up organic networks within a special microenvironment that could allow time for associations between molecules and later between types of molecular networks to occur [10, 11]. And a dynamic superscaffold comprising organized water domains (see Section 2) could have selected different kinds of specialized organics to replace its components carrying out different functional roles; this scenario entails that associations between complex biomolecules came about by these substitutions.

3.1. Soft-Matter and Large Response Functions: A “Thermodynamic” Description. We start with a phenomenological (a *la* statistical mechanics) description urging that the attributes of what has come to be known as “soft matter” coined by de Gennes [30] be reviewed in the light of the “principle of biological continuity” (see, e.g., [40]). One could ask if mineral-like clusters (iron sulphur, etc.) have been around for “more reasons” than the huge list already compiled hitherto [41] (see Section 3.2 next). Had a soft mineral-containing scaffold given residence to a quasiparticle/s, which was equally comfortable in association with its organic successor, providing the same pattern of dynamic functional “goods”? Again, the huge advances in the materials sciences sector show couplings between different d.o.fs (magnetic, elastic, thermal, etc.), as in those of biomolecular systems [42] and raise the possibility of similar patterns in mineral colloidal particles [43]. In fact, thermally stable mineral

liquid crystalline phases are of interest as they can be electronrich in contrast to organic ones and therefore possess pronounced electrical, optical, and magnetic properties [44]. Now, the collective nature of the “large response functions” [30] underlies the susceptibility of complex biomatter to small external perturbations. In fact, the main aspects of soft matter: response functions, noncovalent weak interactions, and entropic forces, play a key role in biological organization and close-to-equilibrium dynamics. Its emergence seems hard to imagine from very simple organics at the core (that could be traced to primordial abiogenics) unless this transition can be in principle addressed in a continuous deterministic manner. Guided by Cairns-Smith’s paradigm that any material with this potential was fine so long as it was readily available, we suggest that a template comprising mineral colloids [32] could have realized these functions. In particular, one may recall that *fields* can carry signatures such as sensitive material responses, indicating how a coherent source can supply energy to matter to sustain an isothermal, symmetry-broken aperiodic assembly subject to random fluctuations. At a macroscopic level, a good example was provided by Breivik [45] who showed how magnetic information transfer (via self-assembled 3 mm-sized magnets) helps encode a sequence of independent and identically distributed random variables [46], underlying life’s information-rich aperiodic order [47]. For an extension of this to the nanoscale, consider field-induced aggregates observed in ferrofluid dispersions [48, 49], described as a phase separation of a particle-concentrated phase from a dilute one [50]. These close-to-equilibrium structures (requiring about tens of milli Tesla fields for their formation) are dissipative in nature, breaking up when the field is switched off, and offer a basis for slowly changing patterns as in soft biomatter. The external H-field breaks the rotational symmetry of the dispersed and disoriented single-domain particles that are subject to thermal fluctuations from the bath and imposes a directional order. Again, Dyson’s [51] use of field-accreted matter for simulating “analog life,” gives an instructive edge to magnetism-based proposals, for example, implementation of Boltzmann machine type of neural network based on interspin exchange interactions in a spin glass [52] and associative memory simulations, using particle-particle dipolar interactions in nanocolloids [53].

3.2. Rock Magnetism and Magnetic Colloids in “Mound Scenario”. Similarly, as magnetic rocks are a good provider of moderate H-fields for accretion of nanoparticles forming on the Hadean Ocean Floor [31], this brings us to the alkaline seepage site mound scenario [6, 54, 55], illustrated in Figure 1 (reproduced with permission from Russell and Martin [7]; Russell et al. [54]). Here, negatively charged colloidal mineral greigite forming under alkaline mound conditions (as pH well above 3 [56]) does resemble an aqueous-based ferrofluid. Significantly, the key to stabilizing its colloidal-gel state lies with organics [57]. And the strong structural similarities between iron-sulphur clusters in enzymes and their mineral counterparts that were likely to have been present on the primordial ocean floor under the interest in

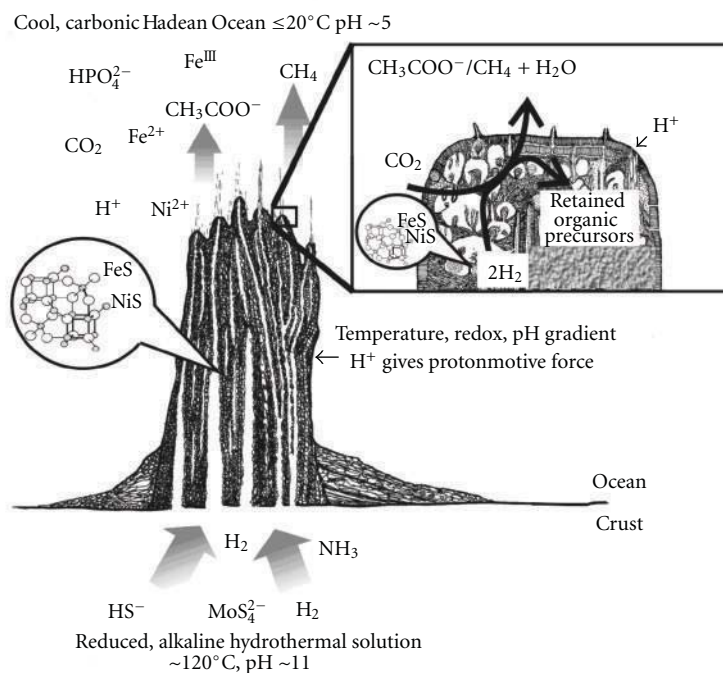


FIGURE 1: The hydrothermal mound as an acetate and methane generator. Steep physicochemical gradients are focused at the margin of the mound (see text also [54] for details). The inset (cross-section of the surface) illustrates the sites where anionic-organic molecules are produced, constrained, react, and automatically organize to emerge as protolife (from Russell and Martin [7] and Russell et al. [54], with permission).

sea-floor hydrothermal systems [7]. Clusters of iron-sulphur are seen ubiquitously across living systems (despite their predominantly organic basis) and carry out a variety of roles, such as electron transfer, radical generation, sulfur donation, and control of protein conformational changes associated with signal transduction, to name some [58–61]. In fact, spin polarization and spin coupling are key characteristics of the sulphur-bridged complexes, embedded within these ancient bioconstructs [62]. The spins on metal sites in di- to polynuclear iron sulphur clusters are coupled via what is called Heisenberg exchange coupling, which typically favors antiferromagnetic alignment of neighbor spins. This in combination with valence delocalization within the cluster helps bring about coupling of different degrees of freedom and add to the complexity of the system [62]. Ligand binding can thus affect not only the electronic distribution, but also the pattern of spin alignment, and hence the net total spin state [63]. The complex web of interactions—orbital interactions, electron delocalization, and spin coupling—in the iron-sulphur clusters [64] shows the likelihood of a similar profile for magnetic mineral colloids in the mound membranes.

In the mound scenario, colloidal membrane surfaces, envisaged as hosting simple metabolic cycles, comprise of iron-sulphide minerals, such as mackinawite and greigite, which along with some other transition metal compounds could have been geochemically available for carrying out

similar catalytic type of functions and acted as protometabolically relevant catalysts [7, 55, 65]. Not only that, but also the confrontation of geofluids at different pH across precipitating colloidal FeS membranes also provides insights into the essential dependence of biological processes on a proton-motive force (chemiosmotic gradient) across cell membranes, which is a more or less invariant mechanism of energy conversion across living forms [66].

The “mound scenario” thus weaves together the key material patterns highly relevant to life processes—soft colloid gel state, catalytic enzyme-like iron-sulphur clusters (for primordial metabolism), plausible abiogenic reactions (with passage of electrons to lower energy states), and natural gradients (of redox, pH, and temperature), to name some—into a persuasive geochemical location on the Hadean Ocean Floor. It gives a plausible account of how key abiogenics could have accumulated [67] and coordinated with each other [10] in membranous inorganic compartments, as well as dynamically ordered framboidal reaction sacs [68], the latter forming through interplay of attractive and repulsive forces (cf. [69]). Indeed, spherical, ordered aggregates of framboidal pyrite about $5\mu\text{m}$ in diameter were found in fossil hydrothermal chimneys [70–73], see Figures 2(a) and 2(b), that seemed to have grown inorganically from the spherical shells of FeS gel. Furthermore, Russell and coworkers [70] have noted the size similarities of the magnetosome crystals to that of pyrite crystallites ($\sim 100\text{ nm}$ in diameter)

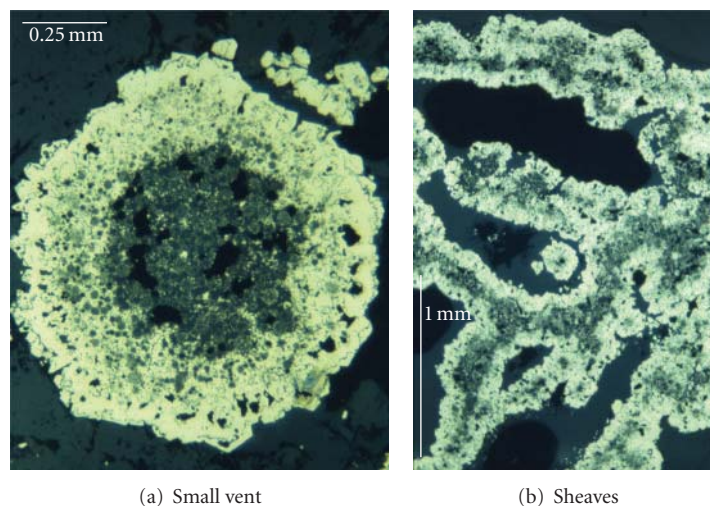


FIGURE 2: Framboids in chimneys: (a) small pyrite vent structure: reflected ore microscopy of transverse section shows a central area of empty black spaces plus (grey) fine framboidal pyrite and a fine euhedral authigenic rim surrounded by baryte, with minor pyrite; (b) Sheaf system, formed from coalescing rods of anastomosing microcrystalline pyrite. Black areas are empty spaces; central regions are framboidal pyrite with an exterior of crystalline pyrite. (Labelled pictures given by Dr. Adrian Boyce are reproduced with his kind permission; source: Boyce et al. [71, 72, 80]).

comprising the interior of framboids that appeared to have grown inorganically from spherical shells of iron-sulphide gel; their earlier stages would have comprised reduced forms of framboidal iron sulphide, just as in iron-sulphide-bearing bacteria. Here, the quasiperiodic organization associated with naturally formed framboids [74] is intriguing in view of their resemblance to the well-studied dynamic order in laboratory-made quasicrystals. These form via an accretion-based mechanism [75] and show unusual combinations of properties (resembling living matter). Thus, the observation of scale-free framboids rekindles the long-standing interest in these forms for the origins of life [76], providing as they do, an opportunity to study the surface-minimized packing of colloidal spheres as independent dynamical components [46]. Wilkin and Barnes [56] explain the formation/stability of micro meter-sized framboids, using an interplay of negatively charged repulsive and magnetically attractive forces, where a size >100 nm would orient crystals to the weak geomagnetic field ~ 70 microTesla. Extrapolation of this to the milli-Tesla scale (via a local field from magnetic rocks) shows the feasibility of *nanoscale aggregates*, analogous to ferrofluid ones. This conjecture [31], inspired by chimneys showing framboids (plate 2 of [73]), gets support from observations of fractal greigite framboids [77] which independently affirm the natural propensity of this mineral towards an aperiodic, nested organization.

As to the possible relevance of these observations to the coherent dynamics discussed in the previous sections, we note in passing that a correspondence exists between fractal structures and the algebra of “q-deformed” coherent states (Fock-Bargmann Representation); see Vitiello [78, 79] for details. While this is beyond the scope of the present paper,

this is an interesting way to describe the emergence of long-range correlations at the global (mesoscopic/macro) level from local (microscopic) deformation patterns.

3.3. Environment as a Field: “Taming the Noisy Shrew”. Now, the scenario of a magnetic template for “soft biomatter” unfolds a *novel role* for the *environment*. Here, far from being solely a harbinger of perturbative influences, the environment holds the *controls* for the assembly process itself: the field enables the superparamagnetic particles to overcome thermal fluctuations so that in the resulting aggregates, the components are held together by reversible weak dipolar interactions. Thus, in contrast to crystal lattices, the soft assemblies seem conceptually compatible with dynamics and would have remained intact, even if the “layers” of the aggregates were used as surfaces for adsorption (e.g., by abiogenics) or as passages to diffusively migrating particles. For an H-field can connect the response-to-field variations (i.e., susceptibility) and the correlators between interacting spins via the fluctuation-dissipation theorem (FDT). And, for gradual flux changes to be consistent with effectively isotropic local surroundings for particles (diffusing through the field-induced aggregates), moderate gradients in the mound may have sufficed (cf. [55]). Sure enough, the weak magnetic dipolar interactions between the latter and those forming the “layers” have a striking resemblance to the recognition-based movement in transcription and translational processes. Note that the same patterns of diffusive migration through assemblies also map with the ATP-driven migration of biomolecular motors on cytoskeletal protein networks. Next, to consider coupling of scalar chemical reactions with vector processes like diffusion [81], let us

extend surface-transfer reactions envisaged in ligand shells of adjacent transition metal elements on crystal surfaces [82] to “template” layers of magnetically ordered particles (cf. [10]). Now, within a common FDT framework for *asymmetric* movements, binding to nonmagnetic ligands (e.g., organics) would increase the net potential energy barrier of the particles for interacting with their “template” partners compared to their unbound counterparts. Thus, greater diffusive exploration of the organic bound particles (as in biomolecular motors) contrasts with the entrapment of the unshielded ones into an expanding network of dipolar interactions (as in growth phenomena). Note that the isothermal, cyclic switching between different entropic states in molecular motors is pictured here using a gentle flux gradient (nonhomogeneous rock H-field) periodically perturbed by local H-fields of “template” partners, leading to alternating high- and low-“template” affinity states due to the dipole’s magnetic degree of freedom [31]. In contrast to these first-order-like phase transitions, the superimposition of a gentle temperature gradient on field-induced structures results in a decrease in magnetization (a second-order phase transition) of a diffusing dipole (cf. [83]). Here, changes in susceptibility seem a plausible response mechanism for harnessing various fluxes in the mound, enveloped by further colloidal/mineral precipitates. In this context, the coupled d.o.fs in biomatter ([42], see Section 3.1) have a strong resemblance to the secondary effects of magnetism in a substance arising as a consequence of couplings between its different physical properties: magnetocaloric, magnetoelectric, magnetooptic, and magnetostriction [84]. Hence similarly, via the fluctuation-dissipation response mechanism, these couplings could have enabled the environment to harness any gentle gradients using its field as a “switch.” In addition, the passage of charges is expected owing to gradients in the mound, which would induce a magnetic field. The scenario of the latter interacting with the rock field at the base of the mound, and leading to a (reversible) homopolar-motor-like rotation of conducting assembly components, does seem reminiscent of the rotatory ATP-driven pumps that are thought to be amongst the early-evolved mechanisms.

3.3.1. Chirality (Naaman and Rosenberg): Mound Scenario. All along, the constructive use of noise (via FDT) is possible thanks to the magnetic asymmetry of the assembly. Their ATP-driven soft-matter counterparts in living systems, however, employ chiral molecules for achieving ratchet effects. A causal connection to understand this correspondence could be given in terms of spin-polarized electrons (as in [85]). This is also consistent with the geochemical-based view of life’s origin [54], which posits that life emerged on the surface of a wet planet (likely earth) once the early evolved mechanisms were set in place (mechanisms requiring light, such as photosynthesis, therefore evolved later in this scenario, which makes it relevant to consider interactions with chirality ingredients like circularly polarized light for later stages of evolution). Briefly, the work of Naaman and coworkers [85, 86] reveals how co-operative effects can endow assemblies of chiral dipolar molecules with the

capacity to selectively discriminate between spins pointing “up” or “down.” A similar spin-filtering effect is achieved in spintronics by applying an external field to induce magnetization in ferromagnetic thin films. On the other hand, the magnetization in its biological counterpart—layered organization of dipolar chiral molecules—is based on two stages: (1) the magnetic field created by transfer of charge (electron or hole) through chiral molecules aligns the magnetic dipole of the charge transferred; (2) then exchange interactions in the layered domain keeps them aligned (the spin-orbit interaction is negligible here). Furthermore, in an important study, Rosenberg [87] has shown how chirality can affect reactions in the presence of spin-polarized electrons, provided by radiating the magnetic substrate binding the organics. The requirements for producing low-energy spin-polarized electrons—ionizing radiation and a magnetic substrate—seem to match with the “infrastructure” available at the base of the mound. In addition to the presence of high levels of radioactivity and the reducing conditions prevailing in the Hadean Earth’s crust, Ostro and Russell (unpublished results 2008) have described how iron and iron-nickel particles derived from the subhypervelocity flux of iron and NiFe-metal containing chondritic meteorites and micrometeorites, and distributed on the ocean floor, would be partially scattered throughout the mound (see [31]). The invasion of the mound by magnetized extraterrestrial materials would have been further reinforced by secondary magnetization of the magnetite produced as an alteration product at the base of the mound [31] as a consequence of serpentinization [88]. The plausibility of having spin-polarized electrons in the mound then throws up the intriguing correspondence between the available carriers of the spin-polarized electrons—the field-ordered magnetic dipolar colloids [31, 32] and structured water [3, 24, 27–29]—and the assemblies of chiral dipolar biological replacements which show magnetic behaviour upon polarized charge transfer [86]. Indeed, recent results demonstrate that mackinawite, which is isostructural with high-temperature Fe-based superconductors, also shows similar magnetic profiles, thus leading to the conjecture that this important component of the “mound scenario” may well be one of the simplest among Fe-based superconductors [89].

4. QFT Scenario: Two Modes of Water CD “Scaffold”

Albeit described above (Section 3) at a “stat mech” (thermodynamic) level, one repeatedly encounters analogies of collective behaviour (many coupled spins versus many coupled atoms), where symmetry-broken patterns in inorganic colloids show matching correspondences with their biological counterparts. This scenario is fully compatible with a QFT description, with merely a change from imaginary (Matsubara) “time” to real time, *a la* Feynman, the system, as the carriers of ordering information. With the “ordering,” there is effectively a freezing of the d.o.fs of some elementary (microscopic) components, leading to a coherent, collective (macroscopic) quantum behaviour called the ordered pattern (see [21, 24, 39]). One can also check that the rotational

symmetry-broken N-G-bosons (magnons) seem to be more relevant to dynamical biological systems (see the application of rotational symmetry breaking via electric dipoles in the dissipative brain model of Vitiello [90]), rather than the translational symmetry-broken phonons—N-G bosons in the crystal context. Nevertheless, the quasiparticles associated with the symmetry-broken organization patterns could hold the key to how the “takeover” [15] from inorganic-magnetic dipolar to organic-electric dipolar nature came about, the association with interfacial water CDs being common to both scenarios.

We have already seen in Section 2 how organized water can exhibit crystal-like collective properties, where a deep reshuffling of its electron clouds allows it to act as an electron donor. Water CDs can act like machines and collect energy—even noncoherent sources like thermal noise—and store in a coherent form and even include “guest molecules” [26]. Further, the association of coherent water CDs with a reservoir of quasifree electrons enables the production of metastable coherent-excited states [91]. Thus, when excited by some externally supplied energy, the ensemble of quasifree electrons executes rotational motion (as cold vortices) with quantized magnetic moments that can align to ambient magnetic fields; their stability is ensured by their “cold” coherent nature, preventing thermal decay [26]. Thus, the water CDs can be associated with both electric (oscillatory) and magnetic (rotatory) dipoles. Now, the criterion for a “guest” molecule to gain entry into the CD “machine” is that of a matching frequency to that of the CD host via its (lowest order) radiative dipole. And interfacial water CDs—capable of both kinds of absorption/emission exchanges—can provide a powerful scaffold mechanism for swapping between inorganic (magnetic-rotatory dipolar) and organic (electric-oscillatory dipolar) colloidal organizations. This is since being coherent systems, their phase can be tuned by an external e.m. potential [35, 38]. Thus, for consistency with the principle of biological continuity, e.m. potentials associated with quasiparticles, arising from the various symmetry-breaking contexts in biological organization today, had to be similarly linked to mineral-based ancestors in the Hadean, for enabling the envisaged “takeover” [13]. Again, the correspondences between the hypothetical Hadean and biological scenarios (Section 3) provide functional contexts for energy dissipation; here, the thermodynamic-FDT basis of description can be checked for their compatibility with coherent exchanges with water CDs. The latter can increase their coherent stores even by accepting incoherent thermal noise, the requirement for release being that the “guest” provides a matching frequency (see above). Evidently though, the organics could not “takeover” all the functions, such as electron transfers and sensing (see below).

5. Metabolism, Replication, and Sensing

Magnetic networks also provide a conceptual platform for bringing together a variety of mechanisms—such as harnessing different fluxes (since further colloidal/mineral precipitates could envelop the mound)—as an alternative

to say, awaiting the emergence of the elaborate genetic setup enabling lateral gene transfers. For in principle the presence of magnetic-dipolar modes in water CDs offers a mechanism for a framboid-like scalingup of magnetic assemblies, permitting their navigation to zones with weaker field intensities. And we speculate that once the weak geomagnetic field started to develop, similarly organized organic replacements could have disembarked from the mound. The former also offers a plausible response-based mechanism for navigation. Note the similarity between the passage of a mag-netosome-containing bacterium, moving in response to the extremely low-frequency geomagnetic field [92] (although by sensing changes in the inclination magnitude increasing from the equator to the poles) and the *scaled-down scenario* of ligand-bound superparamagnetic particles traversing a field-induced aggregate in response to (gentle changes in flux lines due to) an external moderate H-field [31]. For bacteria do use these cell components as compasses [93–95] that help to orient them to the geomagnetic field, as they navigate through waters. Interestingly, magnetosomes are composed of ordered magnetite crystals, as well as greigite ones, albeit less frequently [96, 97]. Their ancient origins can be appreciated from the conjecture that “Magnetoreception may well have been among the first sensory systems to evolve” based on the universal presence of single-domain crystals of magnetite across many species and groups of organisms, ranging from bacteria through higher vertebrates that exploit the geo-magnetic field for orientation, navigation, and homing [98, 99]. In addition, different magnetite-based models of biological magnetic-torque transducers have been proposed as a basis for sensing and transducing magnetic-field changes via direct/indirect coupling to mechanosensitive ionchannels [100]. Indeed, to quote from Kopp and Kirschvink [101], “The magnetosome battery hypothesis suggests the possibility that the magnetosome arose first as an iron sulfide-based energy storage mechanism that was later exapted for magnetotaxis and still later adapted for the use of magnetite.”

The gradual substitutions of colloidal magnetic networks bound by weak dipolar interactions could conceptually explain how recognition-based communication language (e.g., complementary base pairing, enzyme substrate, etc.) may have arisen in water-coated bionetworks bound by noncovalent, weak recurring bonds (H-bonds, van der Waals); note the capacity of the latter to undergo sol-gel transformations, like reversible magnetic gels. Further, as structure (shape, polarity, etc.) dictates interactions, one wonders if incorporation of substitutes had not been an information-registering mechanism of a coherent ancestor leading to the structure-function associations across biology, the “contents” being different functions in different structural (memory) addresses. Now, the emergence of a digital form of storing information in this scenario—where associative networks were available [31]—is likely to have been a later development that can be understood in terms of connections developing between networks [10, 11]. Nevertheless, a magnetic environment proposed by us (see [102]) can provide a basis [32] for Patel’s [103] proposal of a quantum search leading to a digital mechanism

if a coherent ancestor indeed brought forth life, that is. Other workers have also provided arguments involving iron-sulphur minerals [104] and the colloid state [105] that support a quantum basis for the origins of life.

6. Conclusions and Scope

Cairns-Smith's crystal scaffold is softened via field-responsive colloids to conceptually access the "replicator" in two stages: (1) an environmental field enabled the assembly, induction of asymmetries, response effects for close-to-equilibrium dynamics, and associative networks of magnetic colloids, besides providing a coherent environment for stabilizing associated (a variety of) symmetry-broken quanta and their feedback-interactions with those of the coherent water domains; (2) analogue processes in a coherent water-mineral-colloid assembly are speculated to have enabled the "leap" to digital form of information processing. In this new scenario, the catalytic activity and soft-matter patterns arose from field-responsive mineral colloids, whereas energy capture (from protometabolic reactions and a variety of fluxes) and storage in far-from-equilibrium dissipative structures was throughout associated with the coherent water domains organized on the colloidal inorganic or organic surfaces. This might provide insights into the entangled origins of the replicating and metabolic wings of life.

Indeed, in this manner, Nobel Laureate Albert Szent-Gyorgyi's view of life being "an electron looking for a place to rest" can be seen to be consistent with CO₂ as its eventual destination [55] and the essentially organic nature of life. Again, in the words of the father of modern biochemistry, if "water was dancing to the tune of solids"—with tunes as the associated e.m. potentials—this "dance" would have continued uninterrupted if organic replacements of the inorganic ancestors had played the same "tune."

Acknowledgments

The authors are grateful to Professors Michael Russell and Kirt Robinson for bringing the work of the Naaman's group to their notice and Dr. Adrian Boyce for kindly providing his labeled frambooid pictures. They are grateful to the referee for his careful reading of the paper, leading to precise insertions of appropriate references. They thank Professor Michael Russell for inspiration and support (data and figures plus key references, e.g., Brizhik et al. [38]; Carmeli et al. [85]; Kwon et al. [89]). They also are grateful to Dr. Jean-Jacques Delmotte for providing financial and infrastructural support.

References

- [1] M. J. Russell, R. M. Daniel, A. J. Hall, and J. A. Sherrington, "A hydrothermally precipitated catalytic iron sulphide membrane as a first step toward life," *Journal of Molecular Evolution*, vol. 39, no. 3, pp. 231–243, 1994.
- [2] J. T. Trevors and G. H. Pollack, "Hypothesis: the origin of life in a hydrogel environment," *Progress in Biophysics and Molecular Biology*, vol. 89, no. 1, pp. 1–8, 2005.
- [3] G. H. Pollack, X. Figueroa, and Q. Zhao, "Molecules, water, and radiant energy: new clues for the origin of life," *International Journal of Molecular Sciences*, vol. 10, no. 4, pp. 1419–1429, 2009.
- [4] J. T. Trevors, "The composition and organization of cytoplasm in prebiotic cells," *International Journal of Molecular Sciences*, vol. 12, no. 3, pp. 1650–1659, 2011.
- [5] H. J. Morowitz, "A theory of biochemical organization, metabolic pathways, and evolution," *Complexity*, vol. 4, no. 6, pp. 39–53, 1999.
- [6] M. J. Russell and N. T. Arndt, "Geodynamic and metabolic cycles in the Hadean," *Biogeosciences*, vol. 2, no. 1, pp. 97–111, 2005.
- [7] M. J. Russell and W. Martin, "The rocky roots of the acetyl-CoA pathway," *Trends in Biochemical Sciences*, vol. 29, no. 7, pp. 358–363, 2004.
- [8] H. Morowitz and E. Smith, "Energy flow and the organization of life," *Complexity*, vol. 13, no. 1, pp. 51–59, 2007.
- [9] N. Lane, J. F. Allen, and W. Martin, "How did LUCA make a living? Chemiosmosis in the origin of life," *BioEssays*, vol. 32, no. 4, pp. 271–280, 2010.
- [10] E. J. Milner-White and M. J. Russell, "Polyphosphate-peptide synergy and the organic takeover at the emergence of life," *Journal of Cosmology*, vol. 10, pp. 3217–3229, 2010.
- [11] S. D. Copley, E. Smith, and H. J. Morowitz, "A mechanism for the association of amino acids with their codons and the origin of the genetic code," *Proceedings of the National Academy of Sciences of the United States of America*, vol. 102, no. 12, pp. 4442–4447, 2005.
- [12] J. Trefil, H. J. Morowitz, and E. Smith, "The Origin of life," *American Scientist*, vol. 97, no. 3, pp. 206–213, 2009.
- [13] A. G. Cairns-Smith, *Seven Clues to the Origin of Life*, Cambridge University Press, 1985.
- [14] C. J. Davia, "Life, catalysis and excitable media: a dynamic systems approach to metabolism and cognition," in *The Emerging Physics of Consciousness*, J. Tuszynski, Ed., Springer, Heidelberg, Germany, 2006.
- [15] A. G. Cairns-Smith, "Chemistry and the missing era of evolution," *Chemistry*, vol. 14, no. 13, pp. 3830–3839, 2008.
- [16] L. M. Ricciardi and H. Umezawa, "Brain and physics of many-body problems," *Biological Cybernetics*, vol. 4, no. 2, pp. 44–48, 1967.
- [17] C. I. J. M. Stuart, Y. Takahashi, and H. Umezawa, "On the stability and non-local properties of memory," *Journal of Theoretical Biology*, vol. 71, no. 4, pp. 605–618, 1978.
- [18] W. J. Freeman and G. Vitiello, "Dissipation and spontaneous symmetry breaking in brain dynamics," *Journal of Physics A*, vol. 41, no. 30, Article ID 304042, 2008.
- [19] H. Fröhlich, "Longrange coherence and energy storage in biological systems," *International Journal of Quantum Chemistry*, vol. 2, pp. 641–649, 1968.
- [20] E. del Giudice, R. M. Pulselli, and E. Tiezzi, "Thermodynamics of irreversible processes and quantum field theory: an interplay for the understanding of ecosystem dynamics," *Ecological Modelling*, vol. 220, no. 16, pp. 1874–1879, 2009.
- [21] A. N. Mitra, "QFT in physical systems: condensed matter to life sciences," <http://arxiv.org/abs/arXiv:1108.0303>.
- [22] S. D. Filippo and G. Vitiello, "Vacuum structure for unstable particles," *Lettere Al Nuovo Cimento Series 2*, vol. 19, no. 3, pp. 92–96, 1977.
- [23] E. Celeghini, M. Rasetti, and G. Vitiello, "Quantum dissipation," *Annals of Physics*, vol. 215, no. 1, pp. 156–170, 1992.

- [24] M. Blasone, P. Jizba, and G. Vitiello, *Quantum Field Theory and Its Macroscopic Manifestations*, Imperial College Press, London, UK, 2011.
- [25] E. del Giudice, G. Preparata, and G. Vitiello, "Water as a free electric dipole laser," *Physical Review Letters*, vol. 61, no. 9, pp. 1085–1088, 1988.
- [26] E. del Giudice and A. Tedeschi, "Water and autocatalysis in living matter," *Electromagnetic Biology and Medicine*, vol. 28, no. 1, pp. 46–52, 2009.
- [27] E. del Giudice, S. Doglia, M. Milani, and G. Vitiello, "A quantum field theoretical approach to the collective behaviour of biological systems," *Nuclear Physics, Section B*, vol. 251, no. C, pp. 375–400, 1985.
- [28] E. del Giudice, S. Doglia, M. Milani, and G. Vitiello, "Electromagnetic field and spontaneous symmetry breaking in biological matter," *Nuclear Physics, Section B*, vol. 275, no. 2, pp. 185–199, 1986.
- [29] E. del Giudice, P. R. Spinetti, and A. Tedeschi, "Water dynamics at the root of metamorphosis in living organisms," *Water*, vol. 2, pp. 566–586, 2010.
- [30] P.-G. de Gennes, "Soft matter: more than words," *Soft Matter*, vol. 1, no. 1, p. 16, 2005.
- [31] G. Mitra-Delmotte and A. N. Mitra, "Magnetism, entropy, and the first nano-machines," *Central European Journal of Physics*, vol. 8, no. 3, pp. 259–272, 2010.
- [32] G. Mitra-Delmotte and A. N. Mitra, "Magnetism, FeS colloids, and the origins of life," in *The Legacy of Alladi Ramakrishnan in the Mathematical Sciences*, K. Alladi, J. R. Klauder, and C. R. Rao, Eds., Springer, New York, NY, USA, 2010.
- [33] N. V. Katre, "The conjugation of proteins with polyethylene glycol and other polymers. Altering properties of proteins to enhance their therapeutic potential," *Advanced Drug Delivery Reviews*, vol. 10, no. 1, pp. 91–114, 1993.
- [34] R. Arani, I. Bono et al., "QED Coherence and the thermodynamics of the Water," *International Journal of Modern Physics B*, vol. 9, pp. 1813–1841, 1995.
- [35] E. del Giudice and G. Vitiello, "Role of the electromagnetic field in the formation of domains in the process of symmetry-breaking phase transitions," *Physical Review A*, vol. 74, no. 2, Article ID 022105, 2006.
- [36] L. Leplae and H. Umezawa, "Dynamical rearrangement of symmetries - III - Superconductivity," *Il Nuovo Cimento A*, vol. 44, no. 2, pp. 410–426, 1966.
- [37] M. W. Ho, "Towards a theory of the organism," *Integrative Physiological and Behavioral Science*, vol. 32, no. 4, pp. 343–363, 1997.
- [38] L. Brizhik, E. del Giudice, S. E. Jørgensen, N. Marchettini, and E. Tiezzi, "The role of electromagnetic potentials in the evolutionary dynamics of ecosystems," *Ecological Modelling*, vol. 220, no. 16, pp. 1865–1869, 2009.
- [39] H. Umezawa, *Advanced Field Theory: Micro, Macro, and Thermal Physics*, AIP, New York, NY, USA, 1993.
- [40] N. Lahav, S. Nir, and A. C. Elitzur, "The emergence of life on Earth," *Progress in Biophysics and Molecular Biology*, vol. 75, no. 1-2, pp. 75–120, 2001.
- [41] H. Beinert, "Iron-sulfur proteins: ancient structures, still full of surprises," *Journal of Biological Inorganic Chemistry*, vol. 5, no. 1, pp. 2–15, 2000.
- [42] F. W. Cope, "A review of the applications of solid state physics concepts to biological systems," *Journal of Biological Physics*, vol. 3, no. 1, pp. 1–41, 1975.
- [43] J. Hemberger, P. Lunkenheimer, R. Fichtl, S. Weber, V. Tsurkan, and A. Loidl, "Multiferroicity and colossal magneto-capacitance in Cr-thiospinels," *Phase Transitions*, vol. 79, no. 12, pp. 1065–1082, 2006.
- [44] J.-C. P. Gabriel and P. Davidson, "Mineral liquid crystals from self-assembly of anisotropic nanosystems," *Topics in Current Chemistry*, vol. 226, pp. 119–172, 2003.
- [45] J. Breivik, "Self-organization of template-replicating polymers and the spontaneous rise of genetic information," *Entropy*, vol. 3, no. 4, pp. 273–279, 2001.
- [46] C. E. Shannon, "A mathematical theory of communication," *Bell System Technical Journal*, vol. 27, pp. 379–423, and 623–656, 1948.
- [47] E. Schrödinger, *What is Life?* Cambridge University Press, Cambridge, UK, 1944.
- [48] R. W. Chantrell, A. Bradbury, J. Popplewell, and S. W. Charles, "Agglomerate formation in a magnetic fluid," *Journal of Applied Physics*, vol. 53, no. 3, pp. 2742–2744, 1982.
- [49] A. Y. Zubarev, J. Fleischer, and S. Odenbach, "Towards a theory of dynamical properties of polydisperse magnetic fluids effect of chain-like aggregates," *Physica A*, vol. 358, no. 2-4, pp. 475–491, 2005.
- [50] J. Li, Y. Huang, X. Liu, Y. Lin, L. Bai, and Q. Li, "Effect of aggregates on the magnetization property of ferrofluids: a model of gaslike compression," *Science and Technology of Advanced Materials*, vol. 8, no. 6, pp. 448–454, 2007.
- [51] F. J. Dyson, "Is life analog or digital?" *Edge*, vol. 82, 2001.
- [52] J. M. Goodwin, B. E. Rosen, and J. J. Vidal, "Image recognition and reconstruction using associative magnetic processing," *International Journal of Pattern Recognition and Artificial Intelligence*, vol. 6, no. 1, pp. 157–177, 1992.
- [53] R. Palm and V. Korenivski, "A ferrofluid-based neural network: design of an analogue associative memory," *New Journal of Physics*, vol. 11, Article ID 023003, p. 30, 2009.
- [54] M. J. Russell, A. J. Hall, A. J. Boyce, and A. E. Fallick, "On hydrothermal convection systems and the emergence of life," *Economic Geology*, vol. 100, no. 3, pp. 419–438, 2005.
- [55] W. Nitschke and M. J. Russell, "Hydrothermal focusing of chemical and chemiosmotic energy, supported by delivery of catalytic Fe, Ni, Mo/W, Co, S and Se, forced life to emerge," *Journal of Molecular Evolution*, vol. 69, no. 5, pp. 481–496, 2009.
- [56] R. T. Wilkin and H. L. Barnes, "Formation processes of framboidal pyrite," *Geochimica et Cosmochimica Acta*, vol. 61, no. 2, pp. 323–339, 1997.
- [57] D. Rickard, I. B. Butler, and A. Oldroyd, "A novel iron sulphide mineral switch and its implications for earth and planetary science," *Earth and Planetary Science Letters*, vol. 189, no. 1-2, pp. 85–91, 2001.
- [58] J. F. Allen, "Redox control of transcription: sensors, response regulators, activators and repressors," *FEBS Letters*, vol. 332, no. 3, pp. 203–207, 1993.
- [59] M. K. Johnson, "Iron-sulfur proteins," in *Encyclopedia of Inorganic Chemistry*, B. B. King, Ed., vol. 4, pp. 1896–1915, Wiley, Chichester, UK, 1996.
- [60] H. Beinert, R. H. Holm, and E. Münck, "Iron-sulfur clusters: nature's modular, multipurpose structures," *Science*, vol. 277, no. 5326, pp. 653–659, 1997.
- [61] F. Baymann, E. Lebrun, M. Brugna, B. Schoepp-Cothenet, M. T. Giudici-Orticoni, and W. Nitschke, "The redox protein construction kit: pre-last universal common ancestor evolution of energy-conserving enzymes," *Philosophical Transactions of the Royal Society B*, vol. 358, no. 1429, pp. 267–274, 2003.
- [62] L. Noodleman and D. A. Case, "Density-functional theory of spin polarization and spin coupling in iron-sulfur clusters,"

- Advances in Inorganic Chemistry*, vol. 38, no. C, pp. 423–470, 1992.
- [63] L. Noodleman, T. Lovell, T. Liu, F. Himo, and R. A. Torres, “Insights into properties and energetics of iron-sulfur proteins from simple clusters to nitrogenase,” *Current Opinion in Chemical Biology*, vol. 6, no. 2, pp. 259–273, 2002.
 - [64] L. Noodleman, C. Y. Peng, D. A. Case, and J. M. Mouesca, “Orbital interactions, electron delocalization and spin coupling in iron-sulfur clusters,” *Coordination Chemistry Reviews*, vol. 144, pp. 199–244, 1995.
 - [65] S. E. McGlynn, D. W. Mulder, E. M. Shepard, J. B. Broderick, and J. W. Peters, “Hydrogenase cluster biosynthesis: organometallic chemistry nature’s way,” *Dalton Transactions*, no. 22, pp. 4274–4285, 2009.
 - [66] M. J. Russell and A. J. Hall, “The emergence of life from iron monosulphide bubbles at a submarine hydrothermal redox and pH front,” *Journal of the Geological Society*, vol. 154, no. 3, pp. 377–402, 1997.
 - [67] M. J. Russell and A. J. Hall, “The onset and early evolution of life,” in *Evolution of Early Earth’s Atmosphere, Hydrosphere, and Biosphere—Constraints from Ore Deposits*, S. E. Kesler and H. Ohmoto, Eds., vol. 198, pp. 1–32, Geological Society of America, 2006.
 - [68] M. J. Russell, A. J. Hall, and D. Turner, “In vitro growth of iron sulphide chimneys: possible culture chambers for origin-of-life experiments,” *Terra Nova*, vol. 1, no. 3, pp. 238–241, 1989.
 - [69] B. A. Grzybowski, C. E. Wilmer, J. Kim, K. P. Browne, and K. J. M. Bishop, “Self-assembly: from crystals to cells,” *Soft Matter*, vol. 5, no. 6, pp. 1110–1128, 2009.
 - [70] M. J. Russell, A. J. Hall, and A. P. Gize, “Pyrite and the origin of life,” *Nature*, vol. 344, no. 6265, p. 387, 1990.
 - [71] A. J. Boyce, M. L. Coleman, and M. J. Russell, “Formation of fossil hydrothermal chimneys and mounds from Silvermines, Ireland,” *Nature*, vol. 306, no. 5943, pp. 545–550, 1983.
 - [72] A. J. Boyce, *Exhalation, sedimentation and sulphur isotope geochemistry of the silvermines Zn + Pb + Ba deposits, County Tipperary, Ireland*, Ph.D. thesis, University of Strathclyde, Glasgow, U.K., 1990.
 - [73] R. C. L. Larter, A. J. Boyce, and M. J. Russell, “Hydrothermal pyrite chimneys from the Ballynoe baryte deposit, Silvermines, County Tipperary, Ireland,” *Mineralium Deposita*, vol. 16, no. 2, pp. 309–317, 1981.
 - [74] H. Ohfuji and J. Akai, “Icosahedral domain structure of framboidal pyrite,” *American Mineralogist*, vol. 87, no. 1, pp. 176–180, 2002.
 - [75] A. S. Keys and S. C. Glotzer, “How do quasicrystals grow?” *Physical Review Letters*, vol. 99, no. 23, Article ID 235503, 2007.
 - [76] Z. Sawlowicz, “Framboids: from their origin to application,” *Prace Mineralogiczne*, vol. 88, pp. 1–80, 2000.
 - [77] A. Preisinger and S. Aslanian, “The formation of framboidal greigites in the Black Sea,” *Geophysical Research Abstracts*, vol. 6, Article ID 02702, (SRef-ID: 1607-7962/gra/EGU04-A-02702), 2004.
 - [78] G. Vitiello, “Coherent states, fractals and brain waves,” *New Mathematics and Natural Computation*, vol. 5, pp. 245–264, 2009.
 - [79] G. Vitiello, “Fractals and the fock-bargmann representation of coherent states,” in *Quantum Interaction*, P. Bruza, D. Sofge et al., Eds., pp. 6–16, Springer, Berlin, Germany, 2009.
 - [80] Boyce, *Exhalation, sedimentation and sulphur isotope geochemistry of the Silvermines Zn + Pb + Ba deposits, County Tipperary, Ireland*, Ph.D. thesis, University of Strathclyde, Glasgow, UK, 1990.
 - [81] G. Nicolis and I. Prigogine, “Symmetry breaking and pattern selection in far-from-equilibrium systems,” *Proceedings National Academy of Sciences*, vol. 78, no. 2, pp. 659–663, 1981.
 - [82] G. Wächtershäuser, “Before enzymes and templates: theory of surface metabolism,” *Microbiological Reviews*, vol. 52, no. 4, pp. 452–484, 1988.
 - [83] S. Duhr and D. Braun, “Thermophoretic depletion follows boltzmann distribution,” *Physical Review Letters*, vol. 96, no. 16, Article ID 168301, 2006.
 - [84] E. du T. de Lacheisserie, G. Gignoux, and M. Schlenker, Eds., *Magnetism—Fundamentals*, Springer, Grenoble Sciences, 2005.
 - [85] I. Carmeli, V. Skakalova, R. Naaman, and Z. Vager, “Magnetization of chiral monolayers of polypeptide: a possible source of magnetism in some biological membranes,” *Angewandte Chemie*, vol. 41, no. 5, pp. 761–764, 2002.
 - [86] R. Naaman and Z. Vager, “Spin selective electron transmission through monolayers of chiral molecules,” *Topics in Current Chemistry*, vol. 298, pp. 237–257, 2011.
 - [87] R. A. Rosenberg, “Spin-polarized electron induced asymmetric reactions in chiral molecules,” *Topics in Current Chemistry*, vol. 298, pp. 279–306, 2011.
 - [88] M. J. Russell, A. J. Hall, and W. Martin, “Serpentinization as a source of energy at the origin of life,” *Geobiology*, vol. 8, no. 5, pp. 355–371, 2010.
 - [89] K. D. Kwon, K. Refson, S. Bone et al., “Magnetic ordering in tetragonal FeS: evidence for strong itinerant spin fluctuations,” *Physical Review B*, vol. 83, no. 6, Article ID 064402, 2011.
 - [90] G. Vitiello, “The dissipative brain,” in *Brain and Being. At the Boundary between Science, Philosophy, Language and Arts*, G. Globus, K. H. Pribram, and G. Vitiello, Eds., pp. 108–129, John Benjamins, Amsterdam, The Netherlands, 2004.
 - [91] E. del Giudice and G. Preparata, “A new QED picture of water: understanding a few fascinating phenomena,” in *Macroscopic Quantum Coherence*, Sassaroli et al., Ed., pp. 108–129, World Scientific, Singapore, 1998.
 - [92] J. L. Kirschvink, A. Kobayashi-Kirschvink, J. C. Diaz-Ricci, and S. J. Kirschvink, “Magnetite in human tissues: a mechanism for the biological effects of weak ELF magnetic fields,” *Bioelectromagnetics, Supplement*, vol. 1, pp. 101–113, 1992.
 - [93] M. Pósfai, P. R. Buseck, D. A. Bazylinski, and R. B. Frankel, “Iron sulfides from magnetotactic bacteria: structure, composition, and phase transitions,” *American Mineralogist*, vol. 83, no. 11–12, pp. 1469–1481, 1998.
 - [94] M. Pósfai, K. Cziner, E. Márton et al., “Crystal-size distributions and possible biogenic origin of Fe sulfides,” *European Journal of Mineralogy*, vol. 13, no. 4, pp. 691–703, 2001.
 - [95] M. Pósfai, B. M. Moskowitz, B. Arató et al., “Properties of intracellular magnetite crystals produced by *Desulfovibrio magneticus* strain RS-1,” *Earth and Planetary Science Letters*, vol. 249, no. 3–4, pp. 444–455, 2006.
 - [96] J. Reitner, J. Peckmann, A. Reimer, G. Schumann, and V. Thiel, “Methane-derived carbonate build-ups and associated microbial communities at cold seeps on the lower Crimean shelf (Black Sea),” *Facies*, vol. 51, no. 1–4, pp. 66–79, 2005.
 - [97] S. L. Simmons, D. A. Bazylinski, and K. J. Edwards, “South-seeking magnetotactic bacteria in the Northern Hemisphere,” *Science*, vol. 311, no. 5759, pp. 371–374, 2006.

- [98] J. L. Kirschvink, M. M. Walker, and C. E. Diebel, "Magnetite-based magnetoreception," *Current Opinion in Neurobiology*, vol. 11, no. 4, pp. 462–467, 2001.
- [99] J. L. Kirschvink and J.W. Hagadorn, "10 A grand unified theory of biomineralization," in *Biomineralization*, E. Bäuerlein, Ed., pp. 139–150, Wiley-VCH Verlag GmbH, Weinheim, Germany, 2000.
- [100] M. Winklhofer and J. L. Kirschvink, "A quantitative assessment of torque-transducer models for magnetoreception," *Journal of the Royal Society Interface*, vol. 7, no. 2, pp. S273–S289, 2010.
- [101] R. E. Kopp and J. L. Kirschvink, "The identification and biogeochemical interpretation of fossil magnetotactic bacteria," *Earth-Science Reviews*, vol. 86, no. 1–4, pp. 42–61, 2008.
- [102] Z. Merali, "Was life forged in a quantum crucible?" *New Scientist*, vol. 196, no. 2633, pp. 6–7, 2007.
- [103] A. Patel, "Quantum algorithms and the genetic code," *Pramana*, vol. 56, no. 2-3, pp. 367–381, 2001.
- [104] N. Haydon, S. E. McGlynn, and O. Robus, "Speculation on quantum mechanics and the operation of life giving catalysts," *Origins of Life and Evolution of Biospheres*, vol. 41, no. 1, pp. 35–50, 2011.
- [105] J. T. Trevors and L. Masson, "Quantum microbiology," *Current Issues in Molecular Biology*, vol. 13, pp. 43–50, 2011.

Research Article

Tailoring of Magnetocaloric Effect in $\text{Ni}_{45.5}\text{Mn}_{43.0}\text{In}_{11.5}$ Metamagnetic Shape Memory Alloy

W. O. Rosa,^{1,2} L. González,¹ J. García,¹ T. Sánchez,¹ V. Vega,¹ Ll. Escoda,³ J. J. Suñol,³
J. D. Santos,¹ M. J. P. Alves,² R. L. Sommer,² V. M. Prida,¹ and B. Hernando¹

¹Departamento de Física, Universidad de Oviedo, Calvo Sotelo s/n, 33007 Oviedo, Spain

²Centro Brasileiro de Pesquisas Físicas, Rua Dr. Xavier Sigaud, 150, Urca, 22290-180 Rio de Janeiro RJ, Brazil

³Girona University, Campus Montilivi, ed. PII, Lluís Santaló s/n, 17003 Girona, Spain

Correspondence should be addressed to W. O. Rosa, wagner.o.rosa@gmail.com

Received 2 August 2011; Revised 7 November 2011; Accepted 7 November 2011

Academic Editor: Manh-Huong Phan

Copyright © 2012 W. O. Rosa et al. This is an open access article distributed under the Creative Commons Attribution License, which permits unrestricted use, distribution, and reproduction in any medium, provided the original work is properly cited.

We investigate the direct and inverse magnetocaloric effect in $\text{Ni}_{45.5}\text{Mn}_{43.0}\text{In}_{11.5}$ Heusler alloy ribbons comparing the results obtained for the as-quenched sample with the ones after different annealing procedures. An enhancement and shift of the entropy maximum to near room temperature is observed in all annealed samples. A remarkable magnetocaloric effect is observed in samples with short-time treatment (10 minutes) and at the lowest annealing temperature. We show that the suppressing of uncompensated martensitic transition and thermal hysteresis are both influenced by the heat treatment. Also, an improvement on Curie's temperature is observed and, at low magnetic field, it has been risen up to 310 K. Our results demonstrate that the martensitic transformation is highly sensitive to the applied magnetic field and also to the annealing treatment, which means that the magnetocaloric effect can be tuned showing different behaviors for each sample.

1. Introduction

Many first-order phase transition materials have been found to exhibit giant magnetocaloric effect (MCE) [1–3]. Currently, the search for a cheap magnetic material which exhibit a large MCE that works in the temperature range of 100 up to 300 K for a magnetic field variation of $\Delta H = 10$ kOe is carried out. The most extensively studied Heusler alloys have those of the Ni-Mn-Ga system, nevertheless to overcome some of the problems related with practical applications (such as the high cost of Gallium and the usually low martensitic transformation temperature), the search for Ga-free alloys has been recently attempted. In order to reduce such costs and to improve the martensitic transition temperature, the substitution of Ga is proposed and, in particular, by introducing In or Sn [4–7].

These ferromagnetic shape memory alloys (FSMA) exhibit ferromagnetic and shape memory effect simultaneously. The ferromagnetic shape memory effect can be controlled by temperature, stress, and by magnetic field. Recently, Ni-Mn-In Heusler alloys have drawn much

attention due to their potential as ferromagnetic shape memory alloys, which undergo a thermoelastic martensitic transformation (MT) from parent austenitic phase to a martensitic one on cooling [8]. These alloys exhibit notable sensitivity of MT to the applied magnetic field, they seem to be among the most suitable for the room temperature (RT) applications for example, in micro and nanomechanics devices and in alternative energy technologies, due to the giant magnetocaloric effect (MCE) observed in this alloys [9, 10]. Moreover, some authors have reported that such FSMA also present giant magnetoresistance (GMR) due to the first-order phase transition, which can undergo a GMR variation of around 80% [11].

In this work, we present the influence of different annealing treatments on the martensitic transition and magnetic entropy change in a nonstoichiometric Ni-Mn-In Heusler alloy ribbon in order to tailor the MCE around RT. These alloys are of particular interest due to the existence of both direct and inverse magnetocaloric effect in a rather narrow temperature interval. The value of the entropy

change depends on the difference in the magnetic state of the sample corresponding to the austenite and martensite phases and consequently is determined by the magnetic phase diagram. Along with the scientific interest of the results, these materials could be exploited in refrigeration by using positive and negative magnetic entropy changes.

2. Experimental

Polycrystalline $\text{Ni}_{45.5}\text{Mn}_{43.0}\text{In}_{11.5}$ alloy was produced by arc-melting with the appropriate amounts of high purity (99.99%) Ni, Mn, and In. Then, the master alloy was induction melted in quartz tubes and ejected in argon environment onto the polished surface of a copper wheel rotating at an elevated linear speed of 48 m/s. Rapid quenching by melt spinning offers two potential advantages for the fabrication of these magnetic shape memory alloys: the avoiding or reduction of the annealing to reach a homogeneous single phase alloy and the synthesis of highly textured polycrystalline ribbons. During the solidification process, the ribbon is continuously fragmented due to high crystallization kinetics and brittleness of the alloy. The crystal structure was checked by X-ray pattern diffraction technique and additionally the microstructure and elemental chemical composition analyses were performed by means of scanning electron microscope (SEM, JEOL 6100) equipped with electron dispersive X-Ray spectroscopy detector (EDX, Inca Energy 200). From these analyses, we obtain an average composition of $\text{Ni}_{45.5}\text{Mn}_{43.0}\text{In}_{11.5}$ ($e/a = 7.91$) for the produced ribbon. Taking the EDX error into concern, the Heusler alloy ribbons are very close to the nominal alloy value. The magnetic properties were measured using a quantum design VersaLab VSM in the temperature range of 50–400 K and up to 30 kOe applied magnetic field. Martensitic transition (MT) was characterized from the thermomagnetic measurements, which means zero-field cooling (ZFC), field cooling (FC), and field heating (FH) routines that were performed using different applied magnetic fields. The temperature ramping rate used was 4 K/min.

Ribbon flakes were annealed using different thermal treatments, 873, 973, and 1073 K, which it will lead to distinct magnetic behaviors. The annealing was performed under a vacuum chamber with a base pressure of 5×10^{-6} mbar. In addition, we have used different annealing times; in the cases of 873, and 1073 K we let the sample inside the heat chamber for 10 minutes and in the other treatment (973 K) for 20 minutes.

3. Results and Discussion

Figure 1 shows the martensitic transition for the as-quenched ribbon. As one can note, two different peaks are observed (and marked) in ZFC-FC-FH measurements. These peaks are related to uncompensated martensitic transitions and can also be directly affect by the applied magnetic field. For magnetic fields below 5 kOe, the predominant peak is the one denoted with number 1, and above this value, we can note that the peak 2 rules above the other. For an applied

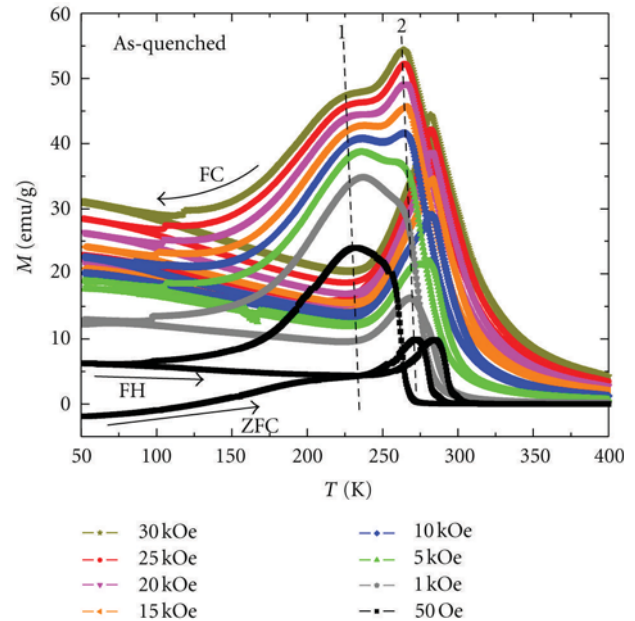


FIGURE 1: ZFC, FC, and FH thermomagnetic curves of as-quenched $\text{Ni}_{45.5}\text{Mn}_{43.0}\text{In}_{11.5}$ ribbon obtained at different magnetic field. Arrows indicate cooling and heating regimes in ZFC, FC, and FH protocols.

small magnetic field (50 Oe), we are also able to observe negative susceptibility during cooling the ribbon below some critical temperature around 125 K. Such a behavior disappears at higher applied field values. This quasidiamagnetism effect has been recently attributed by Prudnikov et al. [12] to a strong nonequilibrium of the system due to the presence of magnetic and structural disorders and exchange anisotropy. The origin of this anisotropy is related to the existence of antiferromagnetic interactions, characteristic in the system under study due to the presence of Mn atoms in In-sites, which means that at low temperature, an exchange bias effect should be appreciable and expected [13]. This could be experimentally demonstrated by the exchange shift of the hysteresis loop of the field-cooled sample at low temperature.

Figure 2(a) shows a comparison among the thermomagnetic measurements at 50 Oe for different ribbons. As we can note, a short time annealing can improve the magnetic response in a temperature interval close to RT, whereas a twice-larger annealing time and higher annealing treatment can dramatically decrease the magnetic moments, as a consequence of the shifting induced by the annealing on the martensitic phase transformation to a higher temperature. Besides, the annealing procedure has an important role on the properties of the martensitic transition. It's remarkable that by annealing the $\text{Ni}_{45.5}\text{Mn}_{43.0}\text{In}_{11.5}$ ribbons, we are able to suppress those uncompensated martensitic transitions (see Figure 1). The annealing has relaxed the residual structural stress originating from the melt spinning fabrication.

The annealing temperatures can be related with the shifting to RT of the first-order transition (see Figure 2(b)), even at high annealing temperature, the magnetic transition

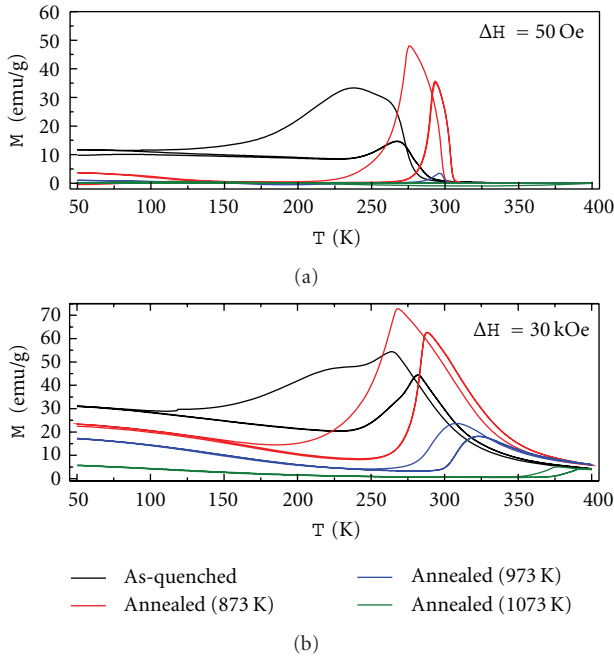


FIGURE 2: Temperature dependence of magnetization of as-quenched and annealed $\text{Ni}_{45.5}\text{Mn}_{43.0}\text{In}_{11.5}$ ribbons at 873 K, 973 K, and 1073 K obtained at a field of 50 Oe (a) and 30 kOe (b).

cannot be observed in the temperature range of 50–400 K for an applied magnetic field of 30 kOe. Other feature related to the different annealing temperatures is the reduction of the thermal hysteresis. In this case, as higher the annealing temperature, smaller is the thermal hysteresis.

This behavior could be explained by the annealing influence due to the increase in the grain size and crystal defects, along with the variation of internal stresses induced during the quenching process. It is also worth mentioning that the excess of Mn atoms, in this non stoichiometric Heusler alloy, are located in different sites leading to exchange interactions very sensitive to the Mn—Mn distance that could be modified by the annealing process.

The evaluation of the magnetocaloric effect has been estimated by the entropy variation, which was calculated using the Maxwell's relation [14]

$$\Delta S_M(T)_H = \int_0^H \left[\frac{\partial M(T)}{\partial T} \right]_H dH, \quad (1)$$

where $\partial M/\partial T$ is obtained directly from thermomagnetic measurements (ZFC-FC-FH). Such route to perform the calculations makes their accuracy improved since there is no need to extrapolate points, like in the case of isothermal curves, therefore the derivatives of thermomagnetic measurements are directly proportional to the entropy variation.

Figure 3 shows the entropy variation for ribbons with different annealing procedures. A very remarkable improvement is seen in the ribbon annealed for 10 minutes at 873 K. The entropy variation in this case had shown an enhancement on the order of 5 times higher than in the as-quenched ribbon, which is a dramatic feat. In addition,

the temperature value at which the inverse magnetocaloric effect achieves its maximum is shifted from 276 K up to 284 K in this case. Thus, this first annealing is proved to be able to enhance the inverse magnetocaloric effect and shift the temperature where its maximum occurs by 8 K. The annealed ribbon at 973 K presents practically the same entropy variation as the as-quenched one, nonetheless, the temperature where the inverse magnetocaloric effect achieves its maximum is, in this case, in the range of RT achieving a value of 307 K. Hence, we obtain using such annealing procedure an impressive temperature shift by 31 K, nevertheless, the inverse magnetocaloric effect is not enhanced like in the previous case. Finally, at 1073 K, it is observed that the entropy variation decreases drastically and the inverse magnetocaloric effect reaches its maximum at 386 K, well above the RT, but the effect is not improved comparing with the other cases. Other feature that is also observed in the sample annealed at 1073 K is the fact that the magnetic phase transition from ferromagnetic to paramagnetic is not displayed since such thermal treatment shifts the Curie temperatures to a higher value, which is found to be above 400 K and, then, we are not able to see this transition due to our equipment limitation.

The refrigerant capacity (q) is defined by [15]

$$q = \int_{T_1}^{T_2} \Delta S(T)_H dT, \quad (2)$$

where T_1 and T_2 are the temperatures of cold and hot reservoir of the refrigeration cycle, respectively. The value of q can be obtained by performing the integration over the full width at half maximum (FWHM) in a ΔS - T curve, according to literature [16]. The different thermally treated ribbons display different refrigerant capacities being 54.8 J/kg (as-quenched), 163.6 J/kg (873 K), 44.6 J/kg (973 K), and 17.6 J/kg (1073 K). Comparing the entropy variation for as-quenched and annealed at 973 K, one should expect that the refrigerant capacities would be similar. However, the presence of uncompleted martensitic transformation in as-quenched ribbon produces a broader entropy peak and thus the increasing in the refrigerant capacity in such sample. In fact, this reduction in the refrigerant capacity for the sample annealed at 973 K is also due to the range of working temperatures T_1 and T_2 that, in such specific case, is narrower than all the previous samples, reducing the working temperature interval. For another annealed ribbon (873 K), the refrigerant capacity was rather increased comparing to the other two. An improvement of around 70% has been observed.

4. Conclusions

In conclusion, we have studied the magnetostructural and magnetocaloric properties of a $\text{Ni}_{45.5}\text{Mn}_{43.0}\text{In}_{11.5}$ ferromagnetic shape memory alloy with ribbon shape and the effect of different annealing treatments. The short annealing at 873 K proved to be the best choice to achieve a high entropy variation, however, the other annealings, at 973 and 1073 K, showed to be very efficient to shift the martensitic transition

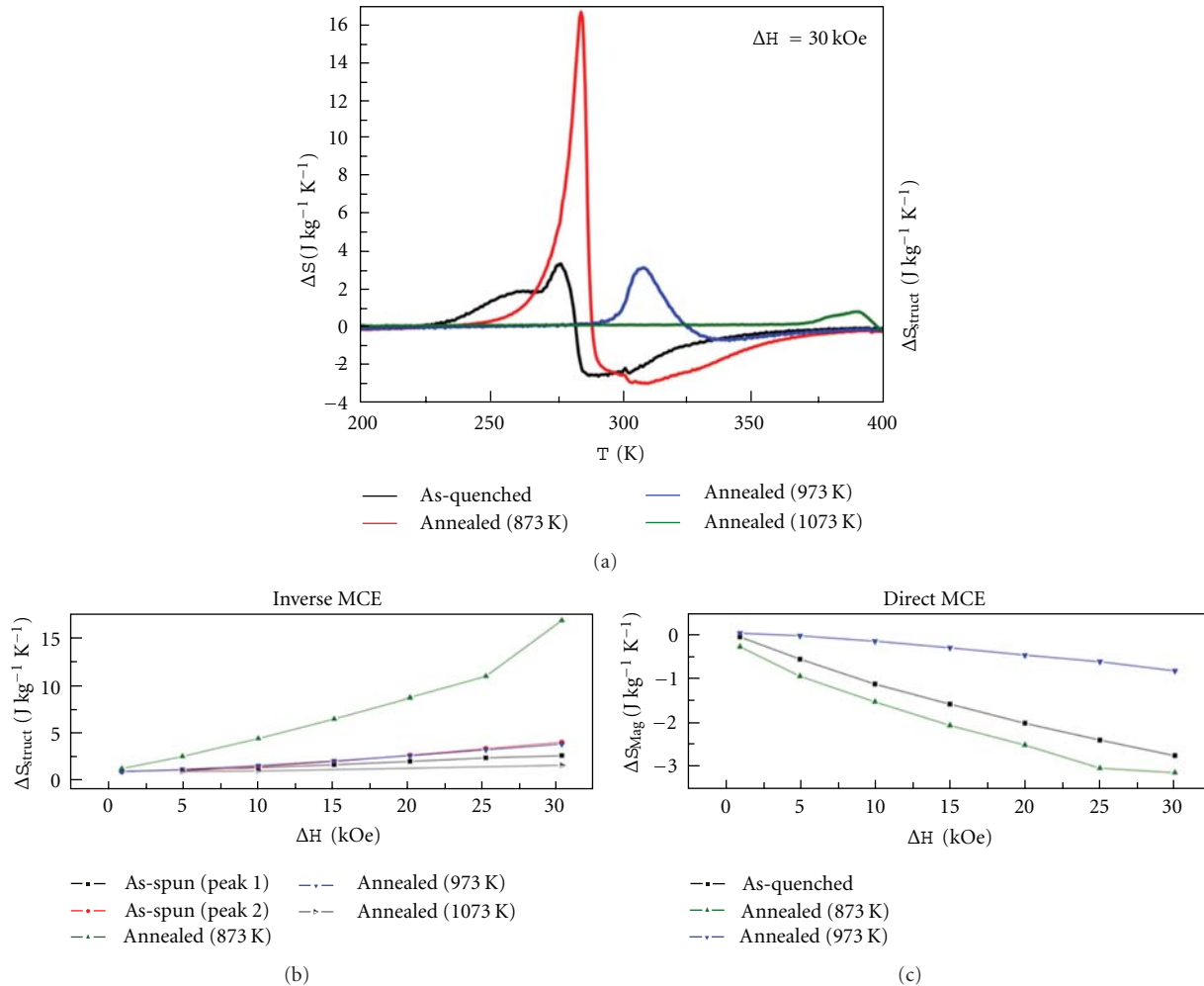


FIGURE 3: Magnetic entropy changes of as-quenched and annealed $\text{Ni}_{45.5}\text{Mn}_{43}\text{In}_{11.5}$ ribbons at 873 K, 973 K and 1073 K obtained at a field of 30 kOe (a). Magnetic entropy change maxima versus field change obtained at the structural transformation (b) and at the magnetic transition (c).

towards a temperature higher than the room temperature (above 300 K), which leads to an entropy variation in the range of potential applications as magnetic coolant. The problem still lies in the working temperature range and the low refrigerant capacity that needs to be enhanced in the future.

Acknowledgments

Authors are thankful to Spanish MICINN for financial support: MAT2009-13108-C02-01-02 and MAT2010-20798-C05-04. L. González also thanks MICINN for a FPI Grant and J. García FICYT for a "Severo Ochoa" Grant.

References

- [1] S. Stadler, M. Khan, J. Mitchell et al., "Magnetocaloric properties of $\text{Ni}_2\text{Mn}_{1-x}\text{Cu}_x\text{Ga}$," *Applied Physics Letters*, vol. 88, no. 19, Article ID 192511, 2006.
- [2] T. Krenke, E. Duman, M. Acet et al., "Inverse magnetocaloric effect in ferromagnetic Ni-Mn-Sn alloys," *Nature Materials*, vol. 4, no. 6, pp. 450–454, 2005.
- [3] Z. D. Han, D. H. Wang, C. L. Zhang, H. C. Xuan, B. X. Gu, and Y. W. Du, "Low-field inverse magnetocaloric effect in $\text{Ni}_{50-x}\text{Mn}_{39+x}\text{Sn}_{11}$ Heusler alloys," *Applied Physics Letters*, vol. 90, no. 4, Article ID 042507, 2007.
- [4] J. L. Sánchez Llamazares, B. Hernando, V. M. Prida et al., "Magnetic field influence on the structural transformation in ferromagnetic shape memory alloy $\text{Mn}_{50}\text{Ni}_{40}\text{In}_{10}$ melt spun ribbons," *Journal of Applied Physics*, vol. 105, no. 7, Article ID 07A945, 2009.
- [5] B. M. Wang, L. Wang, Y. Liu et al., "Strong thermal-history-dependent magnetoresistance behavior in $\text{Ni}_{49.5}\text{Mn}_{34.5}\text{In}_{16}$," *Journal of Applied Physics*, vol. 106, no. 6, Article ID 063909, 2009.
- [6] S. C. Ma, H. C. Xuan, C. L. Zhang et al., "Investigation of the intermediate phase and magnetocaloric properties in high-pressure annealing Ni-Mn-Co-Sn alloy," *Applied Physics Letters*, vol. 97, no. 5, Article ID 052506, 2010.
- [7] R. Y. Umetsu, K. Ito, W. Ito et al., "Kinetic arrest behavior in martensitic transformation of NiCoMnSn metamagnetic shape memory alloy," *Journal of Alloys and Compounds*, vol. 509, no. 5, pp. 1389–1393, 2011.
- [8] Z. D. Han, D. H. Wang, C. L. Zhang et al., "The martensitic transformation and the magnetocaloric effect in

- Ni_{50-x}Mn_{38+x}In₁₂ alloys,” *Solid State Communications*, vol. 146, no. 3-4, pp. 124–127, 2008.
- [9] W. Ito, Y. Imano, R. Kainuma, Y. Sutou, K. Oikawa, and K. Ishida, “Martensitic and magnetic transformation behaviors in Heusler-type NiMnIn and NiCoMnIn metamagnetic shape memory alloys,” *Metallurgical and Materials Transactions A*, vol. 38, no. 4, pp. 759–766, 2007.
- [10] B. Hernando, J. L. Sánchez Llamazares, V. M. Prida et al., “Magnetocaloric effect in preferentially textured Mn₅₀Ni₄₀In₁₀ melt spun ribbons,” *Applied Physics Letters*, vol. 94, no. 22, Article ID 222502, 2009.
- [11] S. Y. Yu, Z. H. Liu, G. D. Liu et al., “Large magnetoresistance in single-crystalline Ni₅₀ Mn_{50-x}In_x alloys (x = 14–16) upon martensitic transformation,” *Applied Physics Letters*, vol. 89, no. 16, Article ID 162503, 2006.
- [12] V. N. Prudnikov, A. P. Kazakov, I. S. Titov et al., “Quasi-diamagnetism and exchange anisotropy in Ni-Mn-In-Co Heusler alloys,” *Physics of the Solid State*, vol. 53, no. 3, pp. 490–493, 2011.
- [13] X. G. Zhao, C. C. Hsieh, J. H. Lai et al., “Effects of annealing on the magnetic entropy change and exchange bias behavior in melt-spun Ni-Mn-In ribbons,” *Scripta Materialia*, vol. 63, no. 2, pp. 250–253, 2010.
- [14] T. Hashimoto, T. Numasawa, M. Shino, and T. Okada, “Magnetic refrigeration in the temperature range from 10 K to room temperature: the ferromagnetic refrigerants,” *Cryogenics*, vol. 21, no. 11, pp. 647–653, 1981.
- [15] K. A. Gschneidner, V. K. Pecharsky, A. O. Pecharsky, and C. B. Zimm, “Recent developments in magnetic refrigeration,” *Materials Science Forum*, vol. 315-317, pp. 69–76, 1999.
- [16] D. L. Schlager, W. M. Yuhasz, K. W. Dennis, R. W. McCallum, and T. A. Lograsso, “Temperature dependence of the field-induced phase transformation in Ni₅₀Mn₃₇Sn₁₃,” *Scripta Materialia*, vol. 59, no. 10, pp. 1083–1086, 2008.

Research Article

Correlation between the Magnetoresistance, IR Magnetorefectance, and Spin-Dependent Characteristics of Multilayer Magnetic Films

V. G. Kravets

Institute for Information Recording, National Academy of Sciences of Ukraine, 2 Shpak Street, Kiev 03113, Ukraine

Correspondence should be addressed to V. G. Kravets, vasyi.kravets@yahoo.com

Received 27 July 2011; Accepted 25 October 2011

Academic Editor: Manh-Huong Phan

Copyright © 2012 V. G. Kravets. This is an open access article distributed under the Creative Commons Attribution License, which permits unrestricted use, distribution, and reproduction in any medium, provided the original work is properly cited.

We present the experimental results on magnetorefractive effect (MRE) in ferromagnetic metal-metal and metal-insulator multilayer films of different composition and different type of magnetoresistive effects. The shape and magnitude of the MRE dependences are found to be very sensitive to the spin-dependent scattering parameters and the effective polarization of the electron density of state around the Fermi level. A study of an MRE in multilayered films is shown to be sufficient for direct extracting of the spin-dependent relaxation times of electron (for GMR-like samples) and energy dependence of the tunnel spin-polarization density of states near the Fermi level for layered TMR films. It is proposed to use the magnetorefractive effect as a noncontact probe of magnetoresistive effects in thin magnetic films through investigations of the field-dependent reflection behaviors of multilayered films in the IR region.

1. Introduction

The discovery [1, 2] of the giant magnetoresistance (GMR) effect has led to many technological applications, especially in data storage devices such as GMR read heads, magnetoresistive random access memory, and in magnetic sensors [3, 4]. The GMR effect reflects changes in resistivity as result of spin-dependent scattering of two spin channels across the interfaces between the magnetic and nonmagnetic metal layers (i.e., GMR effect) or magnetic and insulating layers (i.e., tunneling magnetoresistance) [5]. The key property of these materials is the reduction of their electrical resistivity in magnetic field. Tunneling magnetoresistance effect (TMR) draws much attention for its fascinating transport properties and industrial applications [4, 5].

The most common method of measuring magnetoresistance (MR) involves passing an electrical current through the sample via a four-point probe. On the other hand, Jacquet and Valet [6] proposed and demonstrated an alternative noncontact method for the measurement of magnetotransport effects using electromagnetic radiation of infrared (IR) spectral region. It relies on the fact that at IR wavelengths

the optical properties in metals depend mainly on electron transition within the conduction band (intraband transitions). The method is based on the magnetorefractive effect (MRE). The MRE is the variation of the complex refractive index (dielectric function) of a material due to a change in its conductivity at IR frequencies when a magnetic field is applied. MRE opens a new stage in magneto-optics (MO) because it is not connected with spin-orbit interaction. MRE is an even MO effect, namely, it is linear with magnetization squared, like GMR. Moreover, the MRE is sufficiently larger in the IR region than the corresponding MO values [6–8]. Infrared transmission or reflection spectroscopy can provide a direct tool for probing the spin-dependent conductivity in GMR and TMR samples [6–11].

The MRE of ferromagnetic/nonmagnetic metal multilayer and granular films has been a field of intensive studies over the last decade. This interest in MRE was motivated by three aspects: (i) its importance as an experimental noncontact (*in situ*) magnetoresistance tool, (ii) its being a means of measuring the spin-dependent characteristics of ferromagnetic (FM) materials, and (iii) its application in magneto-optical crystal. The main advantages of the MRE

over other techniques are following: (i) the surface sensitivity with typical information depth of $\sim 10\text{--}30\text{ nm}$; (ii) a time resolution can be down to the subpicosecond regime [6, 8]; (iii) a reasonable spatial resolution tends to $\sim 1\text{--}10\text{ }\mu\text{m}$ [6, 11]; (iv) using robust and inexpensive experimental setups.

The full quantitative MRE information is generally not linked by simple analytic formulas to the material properties, which are the dielectric function of all involved layers and their GMR or TMR values. Moreover, the literature is almost exclusively limited to the MRE in multilayer and granular films with GMR effect. The magnetotransport characterization of metal-dielectric multilayers (TMRs) is more difficult than continuous metallic multilayer (GMR), and hence there is a great tendency to develop a noncontact method for studying their electrical behaviors. The spin-dependent characteristics extracted from modeling of the MRE are also important in fundamental research. From a microscopic point of view the MRE in layered TMR films is due to the interplay of the exchange interaction leading to a splitting of the bands and the spin-dependent density of states around the Fermi level.

In this work we have measured the MRE of CoFe/Cu multilayer films with GMR effect and of CoFe/ Al_2O_3 films with TMR effect. Measurements are made in reflection mode which is the most likely mode for practical remote sensing of magnetoresistance effects. The good agreement at middle IR wavelengths between electrical magnetotransport measurements and noncontact magnetorefractive effect demonstrates the possibilities of using IR reflection spectroscopy for the characterization of giant magnetoresistive systems. We have chosen the multilayer structures with low values of magnetoresistance for checking the sensitivity of magnetorefractive effect. It was shown that the spin-dependent scattering times τ^\uparrow and τ^\downarrow (or mean free path) of majority and minority electrons can be directly extracted from the MRE dependences in the IR region. We also demonstrate how a low-energy spectrum of the tunnel spin-dependent density of states around of the Fermi level for layered TMR films can be reconstructed from its magnetorefractive spectrum. This can be done by modeling the MRE dependences as an effective polarization, $P_{\text{eff}}(E)$, and extracting the optical conductivities of the different layers from the reflection spectra. Our results demonstrate direct schedule for obtaining the energy dependence of the spin-polarization density of states near the Fermi level.

2. Experimental Techniques

The choice of the CoFe/Cu(Al_2O_3)-based film structures was motivated by the fact that spin polarization of the CoFe alloy exceeds those in Co and Fe, while nonmagnetic Cu demonstrates excellent electrical conductivity and insulating Al_2O_3 provides a low tunneling barrier and high values of the TMR. The multilayer films were prepared by dc magnetron sputtering at $\sim 10^{-4}$ Torr Ar gas pressure. The films were deposited on glass and Si substrates using two targets of CoFe and Cu or Al_2O_3 . For the ferromagnetic layers we used $\text{Co}_{75}\text{Fe}_{25}$ target which is a soft magnetic alloy. The room temperature GMR was measured using standard four-point

probe technique in magnetic fields of up to 8 kOe with both current and applied magnetic field H in the films plane. For TMR measurements a 50 nm thick CoFe layer was deposited onto glass (Si) substrates in the form of stripe $10 \times 20\text{ mm}^2$. Then the $[\text{CoFe}(1.6\text{ nm})/\text{Al}_2\text{O}_3(3\text{ nm})]_{10}$ multilayer structures were sputtered onto the center of the CoFe (50 nm) film in form of stripe $10 \times 10\text{ mm}^2$. On top of devices second electrode CoFe (50 nm) was formed in the rectangular shape $10 \times 20\text{ mm}^2$ perpendicular to the long axis of the first thick CoFe layer. In process of TMR measurements the magnetic field was oriented perpendicular to the current direction and parallel to the film plane.

A Bruker IFS 113 Fourier transform spectrometer was employed to study reflectance spectra of multilayer structures at 300 K in the mid-IR range from 2.0 to $25\text{ }\mu\text{m}$. The IR radiation was focused onto the sample placed in the electromagnet gap. The magnetorefectance was determined by analogy with the magnetoresistive effect: $\Delta\rho/\rho = (\rho(H) - \rho(H = 0))/\rho(H = 0)$, and $\Delta R/R = (R(H) - R(H = 0))/R(H = 0)$. These functions describe the changes in the electrical resistivity $\Delta\rho/\rho$ and light reflectivity $\Delta R/R$ of a material in an external magnetic field. The magnetic field was oriented perpendicular to the IR propagation direction and parallel to the film plane. The magnetic field strength was varied from 0 to 4.0 kOe. The angle of incidence of light on the sample was closed to $\sim 45^\circ$. The incoming light was polarized in plane of incidence (p -polarization) using a KRS-5 grid polarizer. The IR reflection spectra were taken for all samples at least 100 scans in the spectral range 2.0– $25\text{ }\mu\text{m}$ and with resolution of 4 cm^{-1} .

3. Experimental Results and Their Discussions

The MRE spectra of the $[\text{CoFe}(2\text{ nm})/\text{Cu}(1.2\text{ nm})]_{10}$ multilayers are presented in Figure 1(a). These spectra have a broad positive peak at short wavelengths ($2\text{--}6\text{ }\mu\text{m}$) followed by a crossover into a reduced reflection region resulting in negative MRE at longer wavelengths. $\Delta R/R$ spectra of CoFe/Cu multilayer films reveal deep minima at $\lambda \sim 20\text{--}21\text{ }\mu\text{m}$ (Figure 1(a)). As the magnetic field increases from 1.2 to 3.75 kOe, $\Delta R/R$ grows in absolute magnitude nonlinearly from ~ 0.3 to $\sim 1.1\%$. The decrease of the reflectivity in an applied magnetic field is consistent with the increase in electrical conductivity resulting from the magnetically induced modification of the scattering of the Drude-like free electrons. The lowest value of the MRE spectrum located at a wavelength $\lambda \sim 20.7\text{ }\mu\text{m}$, which is far away from the short wavelength region where interband transitions are important.

Figure 1(b) shows the dependence of MRE for $[\text{CoFe}(1.6\text{ nm})/\text{Al}_2\text{O}_3(3\text{ nm})]_{10}$ multilayer films. The MRE goes down with increasing wavelength of the incident IR probe light and reaches the maximal negative value at wavelengths $\lambda \sim 13\text{--}14\text{ }\mu\text{m}$. It can be seen that absolute value of the MRE tends to value of $\sim 0.5\%$ in the magnetic field of $H = 3.75\text{ kOe}$. Note that the MRE demonstrates a nonlinear dependence on the magnetic field H and the function $\Delta R/R$ becomes positive (changes its sign) in the low wavelength region $2.0\text{--}5\text{ }\mu\text{m}$ due to contribution of the interband

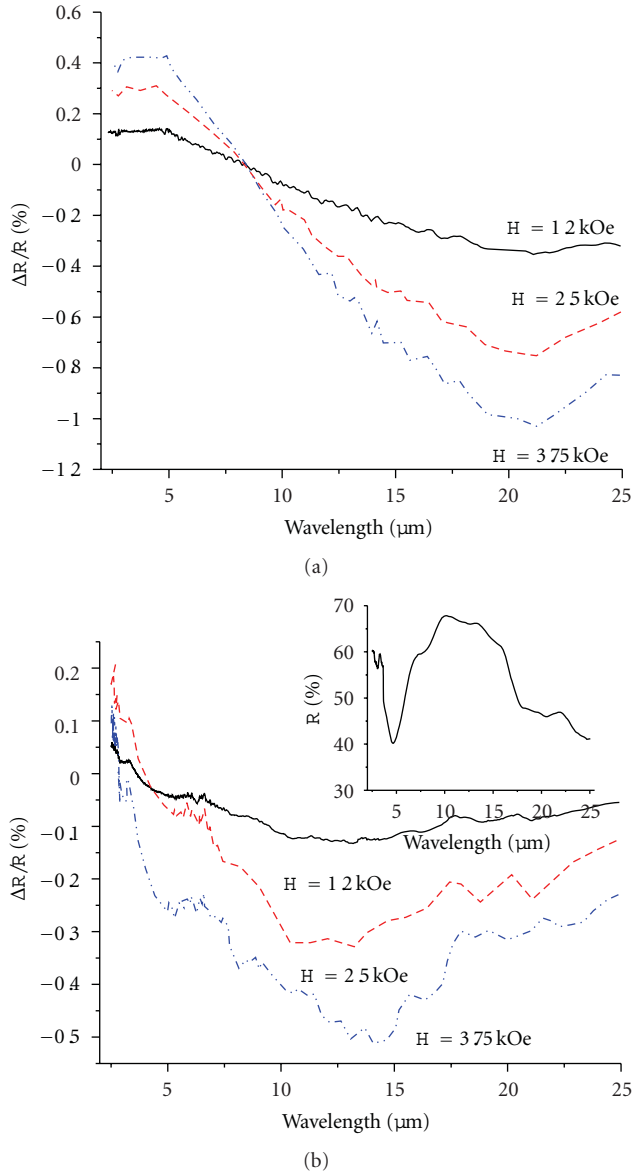


FIGURE 1: The experimental MRE spectra for $[\text{CoFe}(2\text{ nm})/\text{Cu}(1.2\text{ nm})]_{10}$ (a) and $[\text{CoFe}(1.6\text{ nm})/\text{Al}_2\text{O}_3(3\text{ nm})]_{10}$ (b) multilayer films, $H = 1.2, 2.5$, and 3.75 kOe. Inset of (b): the IR reflection spectra of the $\text{CoFe}/\text{Al}_2\text{O}_3$ multilayer films.

electron transitions. Thus, the competition between the intraband and interband contributions leads to a change of sign of MRE as a function of wavelength. This experimental fact contradicts to the predictions of the Drude model [6–10], where the intraband contribution into the conductivity is considered only. Due to such contribution the MRE curve always keeps the same sign. It means that the main mechanism of electron transport in the metal-metal and metal-insulating multilayer structures is the s-d exchange scattering [5]. The shape of the MRE curves as a function of wavelength is therefore sensitive to the s- and d-dependent electron scattering parameters, which determine the GMR and TMR effects.

The IR reflection spectra of the $\text{CoFe}/\text{Al}_2\text{O}_3$ multilayer films (inset of Figure 1(b)) display the complex structure associated with the phonon vibrations in oxide layers. For the spectral region $5\text{--}20\text{ }\mu\text{m}$ the reflectivity $R(\lambda)$ of multilayers becomes similar to the spectrum of the pure Al_2O_3 . Reststrahlen band of high reflectivity between ~ 5 and $20\text{ }\mu\text{m}$ is visible. $R(\lambda)$ spectra show pronounced features at $\lambda \sim 5.0\text{--}7.5$ and $17\text{--}18\text{ }\mu\text{m}$ which can be assigned to the longitudinal optical (LO) and transverse optical (TO) vibration modes of aluminium oxide which is in agreement with previous studies [11]. It should be pointed out that the value of λ_{LO} , where the reflectivity tends to its minimum, is shifted to lower wavelengths with respect to Al_2O_3 , and the reflectivity between LO and TO modes does not reaches the value $R \approx 100\%$.

Figure 2 shows the high correlation between the electrical measured GMR (TMR) and the optically measured MRE for CoFe/Cu and $\text{CoFe}/\text{Al}_2\text{O}_3$ multilayer films. The differences in the nonmagnetic layer Cu or Al_2O_3 lead to different values of the magnetoresistive effect (Figure 2(a)). The maximum value of magnetoresistance of about $\sim 12.5\%$ and $\sim 2.5\%$ in the magnetic field $H = 8.2$ kOe is observed for CoFe/Cu and $\text{CoFe}/\text{Al}_2\text{O}_3$ multilayer films, respectively. The measurements of the MRE profiles were carried out at fixed wavelength when the magnetorefectance reaches a maximum. The experiment was performed by direct recording of the changes in the reflected intensity as a function of applied magnetic field at $\lambda \sim 20.7\text{ }\mu\text{m}$ and $\lambda \sim 13.5\text{ }\mu\text{m}$ for CoFe/Cu and $\text{CoFe}/\text{Al}_2\text{O}_3$ multilayer films, respectively (Figure 2(b)). It has been previously shown [9, 11] that the correlation between the GMR and MRE should be most evident at extreme wavelengths where the MRE reproduces the maximum values. These dependences (Figures 2(a) and 2(b)) clearly show the possibility to perform noncontact magneto-transport measurements on the samples with giant and tunneling magnetoresistance by measuring the variation of their reflected intensity in magnetic field at fixed wavelength, λ . Note that the absolute magnitude of MRE in CoFe/Cu multilayer films is higher than that in $\text{CoFe}/\text{Al}_2\text{O}_3$ films and this trend is consistent with GMR (TMR) dependences.

4. Theoretical Treatments

4.1. MRE Effect in Metallic Magnetoresistive Samples with GMR. To interpret our results we have performed simulations of the MRE for two different systems and their dependence on the scattering and carries characteristics of the different type of magnetoresistance. The calculations of the reflection, transmission, and absorption spectra are performed using a 2×2 characteristic transfer matrix for N number of parallel, homogeneous, isotropic layers [13]. This formalism takes into account the multiple reflections on the interfaces of the multilayer film and could also be used to calculate the MRE in different multilayer structures. The optical response of every layer describes by a complex effective index of refraction. We have simulated the MRE of $[\text{CoFe}(2\text{ nm})/\text{Cu}(1.2\text{ nm})]_{10}$ multilayers using the frequency- and spin-dependent conductivity for FM film. Conductivity $\sigma(\omega)$ of the FM layer is a sum of the Drude

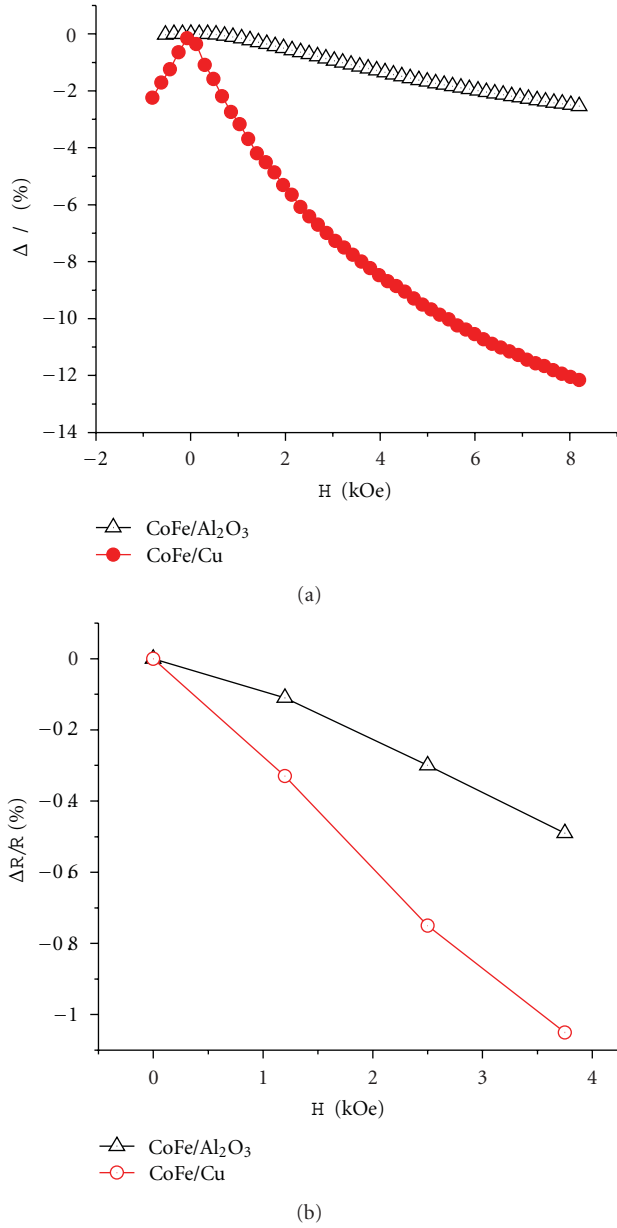


FIGURE 2: (a) The experimental $\Delta\rho/\rho$ data of [CoFe(2 nm)/Cu(1.2 nm)]₁₀ and [CoFe(1.6 nm)/Al₂O₃(3 nm)]₁₀ multilayer films; (b) measured MRE versus magnetic field at fixed wavelength ($\lambda = 20.7 \mu\text{m}$) for [CoFe(2 nm)/Cu(1.2 nm)]₁₀ and ($\lambda = 13.5 \mu\text{m}$) for [CoFe(1.6 nm)/Al₂O₃(3 nm)]₁₀ multilayer films.

contributions from majority- and minority-spin electrons [7, 8, 14]:

$$\sigma(\omega) = \sigma^\uparrow(\omega) + \sigma^\downarrow(\omega) = \frac{\sigma^\uparrow(\omega=0)}{1 + i\omega\tau^\uparrow} + \frac{\sigma^\downarrow(\omega=0)}{1 + i\omega\tau^\downarrow} \quad (1)$$

in which $\sigma^{\uparrow(\downarrow)}(\omega=0)$ and $\tau^{\uparrow(\downarrow)}$ are the spin-dependent dc conductivity and relaxation times, respectively. This conductivity is given by $\sigma^{\uparrow(\downarrow)}(\omega=0) = n^{\uparrow(\downarrow)} e^2 \tau^{\uparrow(\downarrow)} / m$, where $n^{\uparrow(\downarrow)}$ are spin-dependent conduction electron density and m is the mass of an electron. In ferromagnetic alloy CoFe electronic bands are exchange split, which implies different

Fermi wavevectors for the spin-up and spin-down electrons, $k_F^{\uparrow(\downarrow)}$. The values $k_F^\uparrow \sim 7.5 \text{ nm}^{-1}$ and $k_F^\downarrow \sim 4.5 \text{ nm}^{-1}$ were determined assuming a free electron gas [15, 16], and the magnitude of $n^{\uparrow(\downarrow)}$ can be estimated from the relation $n^{\uparrow(\downarrow)} = (k_F^{\uparrow(\downarrow)})^3 / 3\pi^2$. We have introduced the spin-asymmetry parameter α_0 , which is defined as the ratio between the spin-up and spin-down relaxation times for zero magnetic field, $\alpha_0 = \tau_0^\uparrow / \tau_0^\downarrow$. These average spin-dependent scattering times for spin-up and spin-down connect to the spin-independent scattering time, τ_f , in the ferromagnetic CoFe: $\tau_f^{-1} = ((\tau_0^\uparrow)^{-1} + (\tau_0^\downarrow)^{-1})/2$. For fitting experimental results the following parameters were chosen according to literature data [8, 12, 14]: $\tau_f = 1.25 \times 10^{-14} \text{ s}$ closed to the relaxation time of pure Co, $\alpha_0 = 3$ the spin-asymmetry parameter, $\tau_n = \tau_{\text{Cu}} = 2.5 \times 10^{-14} \text{ s}$ the spin-independent scattering time in the nonmagnetic layer, Cu. In the external magnetic field the spin-dependent relaxation time changes as a $\tau^{\uparrow(\downarrow)} = \tau_0^{\uparrow(\downarrow)} (1 \pm \alpha)$. The parameter α is connected to the GMR: $\Delta\rho/\rho = \alpha_0\alpha - \alpha/(\alpha_0 + 1)$. This expression for $\Delta\rho/\rho$ results from (1) at $\omega = 0$, including the spin-asymmetry parameter α_0 . Thus we have all parameters to calculate the spin-dependent conductivity in the middle IR region for ferromagnetic materials. In the next step, the Drude's model was employed to find the complex refractive index for CoFe and Cu layers:

$$n_f - ik_f = \sqrt{\epsilon_{fr} - \frac{i\sigma(\omega)}{\epsilon_0\omega}}, \quad (2a)$$

$$n_n - ik_n = \sqrt{\epsilon_{nr} - \frac{i\omega_p^2 \tau_n}{\omega(1 - i\omega\tau_n)}}. \quad (2b)$$

Here, $\omega_p = 1.0 \times 10^{16} \text{ s}^{-1}$ is the “quasifree” plasma frequency of Cu [12], $\epsilon_0 = 8.85 \times 10^{-12} \text{ A s/V m}$ is the permittivity of free space, ϵ_{fr} , and ϵ_{nr} is the relative dielectric constant of the CoFe and Cu layer, respectively, which is contributed by bound electrons. For the highly conducting films used in our model we can set values ϵ_{fr} , ϵ_{nr} equal to 1; they do not influence on the complex optical constants of ferromagnetic CoFe, $n_f - ik_f$ and nonmagnetic Cu, $n_n - ik_n$ films.

Figure 3(a) shows the theoretical MRE spectra for CoFe/Cu multilayer films. It is shown that the wavelengths dependence of $\Delta R/R$ can be explained quite well, and our fit is satisfactory for spectral region 2–25 μm . In order to exactly reproduce the shape of MRE we modified the effective Drude parameters. According to [17] the spin-dependent relaxation time $\tau_0^{\uparrow(\downarrow)}$ is multiplied by function of $[(\hbar\omega - E_F^{\uparrow(\downarrow)})/E_F^{\uparrow(\downarrow)}]^2$ which includes the contributions from interband electrons transitions into MRE effect. Due to such dependence the MRE changes the sign from positive to negative values at short wavelengths.

The shape of the MRE curves as a function of wavelength is more sensitive to the spin-dependent scattering parameters that determine the GMR. The most important parameters in determining the MRE response are $\omega\tau^{\uparrow(\downarrow)}$, the product of the angular frequency of the IR radiation and relaxation times appropriate to spin-up and spin-down. It is instructive to consider typical values of the critical parameter $\omega\tau^{\uparrow(\downarrow)}$ at

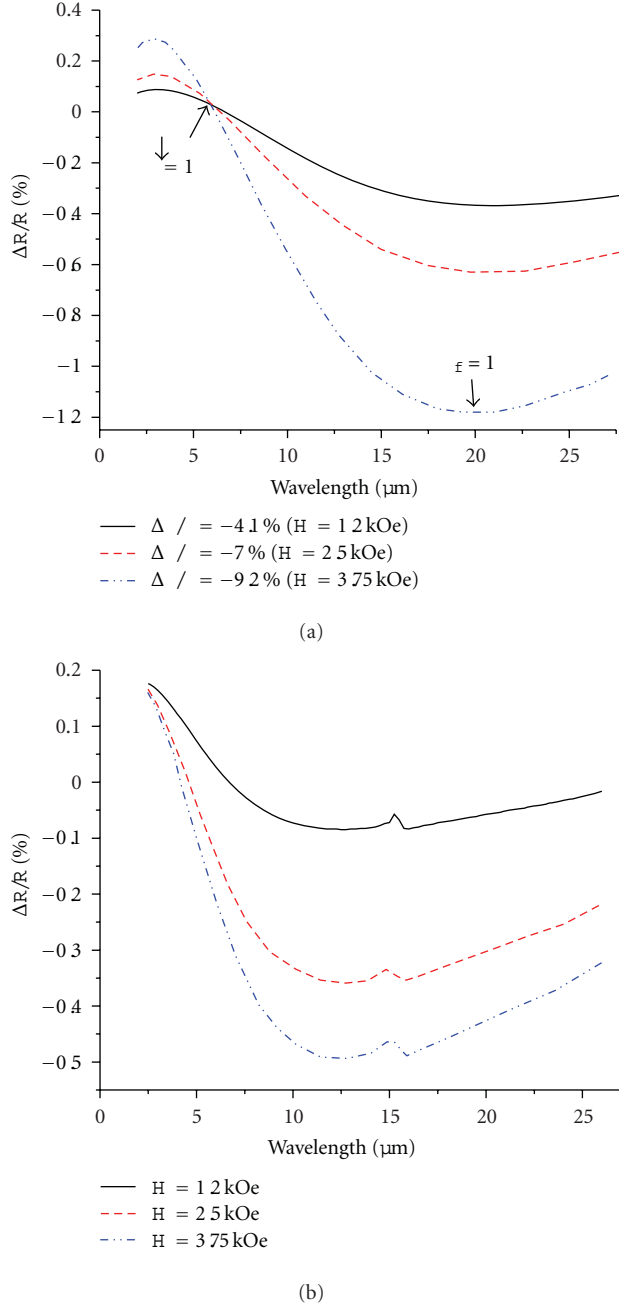


FIGURE 3: The theoretical MRE spectra for $[\text{CoFe}(2 \text{ nm})/\text{Cu}(1.2 \text{ nm})]_{10}$ (a) and $[\text{CoFe}(1.6 \text{ nm})/\text{Al}_2\text{O}_3(3 \text{ nm})]_{10}$ (b) multilayer films, $H = 1.2, 2.5$, and 3.75 kOe .

certain points in the MRE curves. From theoretical point of view [10, 18] the MRE curves are predicted to cross zero values at the frequencies: $\omega_1\tau^\uparrow \approx 1$ and $\omega_2\tau^\downarrow \approx 1$. From dependences represented in Figure 1(a) we can estimate the value of $\tau^\uparrow \approx 4.4 \times 10^{-15} \text{ s}$. As the wavelength is increased the MRE reaches the maximal absolute value where $\omega\tau_f \approx 1$. The extracted value of $\tau_f \approx 1.12 \times 10^{-14} \text{ s}$ is consistent with literature data ($\tau_f \approx 1.25 \times 10^{-14} \text{ s}$ [12]). The measured spectral region is restricted by $25 \mu\text{m}$, and the MRE curves do not cross again the zero value where

TABLE 1: Comparison of the theoretical and extracted from MRE spectra spin-dependent parameters for the CoFe/Cu multilayer films.

Parameters	Theoretical data [8, 12]	Experimental data (MRE)
Average scattering time: τ_f	$1.25 \times 10^{-14} \text{ s}$	$1.12 \times 10^{-14} \text{ s}$
Spin-dependent scattering times:		
spin-up τ^\uparrow	$1.6 \times 10^{-14} \text{ s}$	$1.1 \times 10^{-14} \text{ s}$
spin-down τ^\downarrow	$4.6 \times 10^{-15} \text{ s}$	$4.4 \times 10^{-15} \text{ s}$

$\omega_1\tau^\uparrow \approx 1$. This result shows immediately the effect of the two separate spin directions on the total MRE spectra. The relationship between the relaxation time and GMR depends on the specific scattering mechanism; for example, a high GMR may be the result of a very long τ^\uparrow or a very short τ^\downarrow . The comparison between theoretical and experimental spin-dependent scattering parameters as extracted from the experimental MRE are presented in Table 1. Thus, we have shown that the known dependence of MRE enables a direct extraction of spin-dependent relaxation times $\tau^{(\uparrow\downarrow)}$ (or mean free path) without fitting parameters. Such extraction of $\tau_0^{(\uparrow\downarrow)}$ is possible due to crossing the MRE curves of zero values.

4.2. MRE Effect in Al_2O_3 -Based Magnetic Tunnel Junctions. We now turn to the investigation and discussion of the MRE in $[\text{CoFe}(1.6 \text{ nm})/\text{Al}_2\text{O}_3(3 \text{ nm})]_{10}$ multilayer films with TMR effect. TMR originates from the difference in the density of states (DOS) at the E_F between spin-up $N_\uparrow(E_F)$ and spin-down $N_\downarrow(E_F)$ electrons. In order to fit the TMR data (Figure 2(a)) we have used the known Julliere law for multilayer films [19]. According to this model of spin polarized tunneling [19, 20], TMR is given by

$$\frac{\Delta\rho}{\rho} = \frac{\rho(H) - \rho(0)}{\rho(0)} = \frac{2P_1P_2}{1 + P_1P_2}, \quad (3)$$

where $\rho(0)$ and $\rho(H)$ are the junction resistance for the antiparallel and parallel magnetisation configurations of the two ferromagnetic layers, respectively. P_1 and P_2 are the spin polarization of the two FM materials (for our structures, $P_1 = P_2$): $P = (N_\uparrow - N_\downarrow)/(N_\uparrow + N_\downarrow)$. From modelling the TMR data (3) we obtained the effective tunnel spin-polarization P_{eff} equal to $\sim 11\%$. This value is lower than the spin-polarization of Fe ($P \sim 44\%$) and Co ($P \sim 35\%$), and $\text{Co}_{50}\text{Fe}_{50}$ ($P \sim 55\%$) films, respectively [20]. The lower values of P_{eff} are probably the result of following factors. (1) The tunnelling spin polarization is not only determined by the properties of the FM layers but also depends on the electronic structure of the insulator and ferromagnetic/insulator interfaces. (2) A number of different processes may contribute to the variation of TMR, such as the spin-dependent electronic structure of the FM layers, inelastic scattering by defect/impurity states in the barrier, and electron-phonon, electron-magnon, and electron-electron interactions. The decrease in TMR is also caused by

oxidization of FM layers and roughness of surface at interfaces.

Our investigation of the MRE of CoFe/Al₂O₃ multilayer has shown that magnetorelectance ($\Delta R/R$) is more sensitive to the abovementioned factors than magnetoresistance ($\Delta\rho/\rho$). TMR as a function of $P_{1,2}$ is independent from energy (the values $P_{1,2}$ are taken at fixed energy, E_F). In measured MRE dependences for layered TMR films the functions $P_{1,2}$ stay energy dependent. To model the MRE in CoFe/Al₂O₃ multilayer films, it can be logical to consider the spin-dependent conductivity of two FM layers (1). The tunnel conductivity increases when the magnetizations of the two FM layers are parallel than when they are antiparallel. Analyzing the results in the same way as for TMR the difference in conductivity can be defined as

$$\frac{\Delta\sigma(\omega)}{\sigma(\omega)} = \frac{\sigma(\omega, H) - \sigma(\omega, H=0)}{\sigma(\omega, H)} = -\frac{2P_1(\omega)P_2(\omega)}{1 + P_1(\omega)P_2(\omega)}, \quad (4)$$

where the polarizations $P_1(\omega) = P_2(\omega) = P(\omega)$ are connected to $\Delta\rho/\rho$ at $\omega = 0$ (3). Since spin-flip scattering is neglected, the total conductivity is comprised of two independent electron-tunneling transitions associated with two spin populations.

According to the Hagen-Rubens relation [7, 14], the GMR (TMR) and MRE effects are connected to each other and the reflectivity is a function of the conductivity at low energies, $\sigma(\omega)$, $R = 1 - 2[\varepsilon_0\omega/\sigma(\omega)]^{1/2}$, where ε_0 is the permittivity of free space. The change in reflectivity $\Delta R/R$ can be obtained as a first derivation of $R(\lambda)$:

$$\frac{\Delta R}{R} = \frac{[2\varepsilon_0\omega/\sigma(\omega)]^{1/2}}{1 - [2\varepsilon_0\omega/\sigma(\omega)]^{1/2}} \times \frac{\Delta\sigma(\omega)}{2\sigma(\omega)} = -\frac{1-R}{R} \times \frac{\Delta\sigma(\omega)}{2\sigma(\omega)}. \quad (5)$$

It is evident from (5) that $\Delta R/R$ depends on magneto-conductivity ($\Delta\sigma(\omega)/\sigma(\omega)$). Thus, substituting the wavelength dependence of $R(\lambda)$ and $\Delta\sigma(\omega)/\sigma(\omega)$ in a Hagen-Rubens relation we can accurately describe the MRE in metal-insulating multilayer and find the correlation between the magnetorefractive and magnetoresistive effects ($\omega \rightarrow 0$). Combining (4) and (5), leads to a definition for a fractional change in magnetorelectance as

$$\frac{\Delta R}{R} = \frac{1-R}{R} \times \frac{\Delta\sigma(\omega)}{2\sigma(\omega)} = -\frac{1-R}{R} \frac{P_1(\omega)P_2(\omega)}{1 + P_1(\omega)P_2(\omega)}. \quad (6)$$

This expression shows the proportionality between MRE and polarizations $P(\omega)$ in ferromagnetic/dielectric multilayer films. In the present analysis the reflectivity of the multilayer can be obtained using Fresnel's reflection and transmission coefficients [13]. The complex refractive index of CoFe thin film can be extracted from (2a). In the midinfrared region, where optical phonons can be excited, the dielectric function ε_d of insulating Al₂O₃ can be approximated by a phenomenological Lorentz oscillator model [21, 22]:

$$\varepsilon_d = \varepsilon_\infty \prod_j \frac{\nu_{LOj}^2 - \nu^2 - i\nu\gamma_{LOj}}{\nu_{TOj}^2 - \nu^2 - i\nu\gamma_{TOj}}, \quad (7)$$

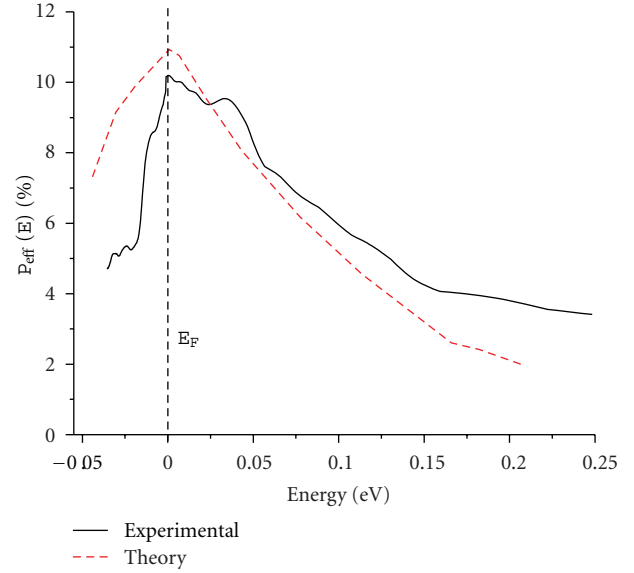


FIGURE 4: Effective tunnel spin polarization versus energy with respect to E_F , extracted from the MRE and reflectivity measurements for [CoFe(1.6 nm)/Al₂O₃(3 nm)]₁₀ multilayer films: experimental and simulated data.

where ε_∞ is the high-frequency dielectric function. The vibrating frequencies and Lorentz widths of the LO and TO modes are ν_{LOj} , ν_{TOj} and γ_{LOj} , γ_{TOj} , respectively. For our calculation only two pairs of phonon modes (LO/TO, $j = 1, 2$) were considered. The abovementioned parameters were taken from [21, 22].

Figure 3(b) displays the theoretical magnetorelectance of the CoFe/Al₂O₃ multilayer films as a function of the wavelength for different values of tunnel magnetoresistance (magnetic field), $\Delta\rho/\rho$ (Figure 2(a)). The shape and spectral position of the dips for the MRE spectra (Figure 1(b)) are well described by our theoretical model (Figure 3(b)). In spectral region of 12–14 μm the absolute value of $\Delta R/R$ becomes maximal.

It was shown above that the TMR dependence (Figure 2(a)) is connected only with the electron states near the Fermi level. For MRE there is a substantial contribution of electrons which tunnel from the occupied states below E_F of one FM layer into the empty states above E_F of the other FM layer. The effective polarization $P_{\text{eff}}(E)$ of the CoFe layer can be obtained by fitting the magnetorelectance $\Delta R/R$ (Figure 3(b)) as a function of $\Delta\sigma(\omega)/\sigma(\omega)$ using (5). The experimental and simulated tunnelling spin-polarization spectra of the CoFe/Al₂O₃ multilayers are shown in Figure 4. The experimental data for $P_{\text{eff}}(E)$ were obtained from optical reflectance, $R(\lambda)$ (inset of Figure 1(b)), and magnetorelectance, $\Delta R/R$, dependences using the expression (6). It is worth noting that we determined the $P_{\text{eff}}(E)$ only in spectral region where the MRE has negative values. In this region we can use the Drude-like model for spin-dependent conductivities (1). Both experiment and theory suggest that the Fermi level falls in a region of maximal density of electron states. The measured and simulated spectra show

a similar profile of $P_{\text{eff}}(E)$ around the Fermi level. However, some differences between simulated and measured data are observed. In particular, the simulated peak in $P_{\text{eff}}(E)$ at E_F is sharper than in the experimental spectra. The measured $P_{\text{eff}}(E)$ seems displaced towards positive energy as compared to the simulated spectra (Figure 4). This discrepancy could be related to the features in $\Delta R/R$ and R spectra which have been attributed to scattering of light at defects in amorphous Al_2O_3 matrix. The maximal values of $P_{\text{eff}}(E)$ extracted from MRE and TMR data (7), (3) at the Fermi level are in good agreement. The $P_{\text{eff}}(E)$ at E_F is the largest ($P_{\text{eff}}(E_F) \approx 11\%$ from fitting TMR data) and is reduced below and above E_F . The value of $P_{\text{eff}}(E_F)$ exhibits small spin polarizations in comparison to pure CoFe alloy due to the particle oxidation of the CoFe surfaces. The $P_{\text{eff}}(E)$ is found to be most strongly reduced below E_F . The $P_{\text{eff}}(E)$ is associated with the filled (unfilled) states near (above) E_F of the CoFe/ Al_2O_3 emitter or receiver interfaces. We determined the $P_{\text{eff}}(E)$ only for energies about 0.2 eV below E_F because of the negligible contribution to the tunnelling from the deepest electron states. Note that the spin-dependent tunnelling DOS of Co/ Al_2O_3 film extracted from the magnetocurrent of transistor-like devices and reported in [23, 24] shows a profile similar to our spectra (Figure 4).

5. Conclusions

We report experimental and theoretical study of the field-dependent IR magnetorefectivity for CoFe/Cu and CoFe/ Al_2O_3 multilayer films. It was found a good correlation between GMR (TMR) and MRE as a function of the applied magnetic field which clearly displays the possibility of performing noncontact magnetotransport measurements by measuring the variation of the IR reflected from samples intensity of light at fixed wavelengths with high surface resolution (in case of focusing light to size of λ). The shape of the MRE curves as a function of wavelength is sensitive to the spin-dependent scattering parameters (in case of the GMR) and spin-dependent density of states at the E_F for layered TMR films. Experimental results show that the MRE is sensitive to this fundamental parameter rather than just the magnitude of the magnetoresistance. The accurate fitting of the shape of the MRE curve as a function of wavelength allows determining the spin-dependent relaxation time, $\tau^{(1)}$, for films possessing GMR effect. The effective tunnel spin polarization $P_{\text{eff}}(E)$ versus energy can be extracted from the experimental dependences of MRE spectrum and reflectivity for CoFe/ Al_2O_3 multilayer films.

This study is of primary importance for applications of such materials in spintronics devices and magnetophotonic crystals.

References

- [1] M. N. Baibich, J. M. Broto, A. Fert et al., "Giant magnetoresistance of (001)Fe/(001)Cr magnetic superlattices," *Physical Review Letters*, vol. 61, no. 21, pp. 2472–2475, 1988.
- [2] G. Binasch, P. Grünberg, F. Saurenbach, and W. Zinn, "Enhanced magnetoresistance in layered magnetic structures with antiferromagnetic interlayer exchange," *Physical Review B*, vol. 39, no. 7, pp. 4828–4830, 1989.
- [3] B. Dieny, B. A. Gurney, S. E. Lambert et al., "Magnetoresistive sensor based on the spin valve effect," US patent 5206590, 1993.
- [4] C. Chappert, A. Fert, and F. N. van Dau, "The emergence of spin electronics in data storage," *Nature Materials*, vol. 6, no. 11, pp. 813–823, 2007.
- [5] A. Fert, A. Barthelemy, and F. Petroff, "Spin transport in magnetic multilayers and tunnel junctions," in *Nanomagnetism: Ultrathin Films, Multilayers and Nanostructures*, D. M. Mills and J. A. C. Bland, Eds., chapter 6, Elsevier, Amsterdam, The Netherlands, 2006.
- [6] J. C. Jacquet and T. Valet, "A new magneto-optical effect discovered on magnetic multilayers: the magnetorefractive effect," in *Magnetic Ultrathin Films, Multilayers and Surfaces*, E. Marinero, Ed., pp. 477–490, Materials Research Society, Pittsburgh, Pa, USA, 1995.
- [7] V. G. Kravets, D. Bozec, J. A. D. Matthew et al., "Correlation between the magnetorefractive effect, giant magnetoresistance, and optical properties of Co-Ag granular magnetic films," *Physical Review B*, vol. 65, no. 5, Article ID 054415, 9 pages, 2002.
- [8] J. van Driel, F. R. De Boer, R. Coehoorn, and G. H. Rietjens, "Magnetic linear dichroism of infrared light in ferromagnetic alloy films," *Physical Review B*, vol. 60, no. 10, pp. R6949–R6952, 1999.
- [9] R. T. Mennicke, D. Bozec, V. G. Kravets, M. Vopsaroiu, J. A. D. Matthew, and S. M. Thompson, "Modelling the magnetorefractive effect in giant magnetoresistive granular and layered materials," *Journal of Magnetism and Magnetic Materials*, vol. 303, no. 1, pp. 92–110, 2006.
- [10] A. B. Granovsky, I. V. Bykov, E. A. Gan'shina et al., "Magnetorefractive effect in magnetic nanocomposites," *Journal of Experimental and Theoretical Physics*, vol. 96, no. 6, pp. 1104–1112, 2003.
- [11] V. G. Kravets, L. V. Poperenko, and A. F. Kravets, "Magnetorefractance of ferromagnetic metal-insulator granular films with tunneling magnetoresistance," *Physical Review B*, vol. 79, no. 14, Article ID 144409, 2009.
- [12] M. Vopsaroiu, D. Bozec, J. A. D. Matthew, S. M. Thompson, C. H. Marrows, and M. Perez, "Contactless magnetoresistance studies of Co/Cu multilayers using the infrared magnetorefractive effect," *Physical Review B*, vol. 70, no. 21, Article ID 214423, 7 pages, 2004.
- [13] M. Born and E. Wolf, *Principles of Optics*, Cambridge University Press, Cambridge, UK, 1999.
- [14] A. V. Sokolov, *Optical Properties of Metals*, Blackie, Glasgow, UK, 1967.
- [15] C. Kittel, *Introduction to Solid State Physics*, Wiley, New York, NY, USA, 1995.
- [16] M. Julliere, "Tunneling between ferromagnetic films," *Physics Letters A*, vol. 54, no. 3, pp. 225–226, 1975.
- [17] K. H. Bennemann, Ed., *Nonlinear Optics in Metals*, Clarendon Press, Oxford, UK, 1998.
- [18] V. G. Kravets, D. Bozec, J. A. D. Matthew, and S. M. Thompson, "Calculation of the magnetorefractive effect in giant magnetoresistive granular films," *Journal of Applied Physics*, vol. 91, no. 10, pp. 8587–8590, 2002.
- [19] J. C. Slonczewski, "Conductance and exchange coupling of two ferromagnets separated by a tunneling barrier," *Physical Review B*, vol. 39, no. 10, pp. 6995–7002, 1989.
- [20] E. Y. Tsybal, O. N. Mryasov, and P. R. LeClain, "Spin-dependent tunneling in magnetic tunnel junctions," *Journal of Physics: Condensed Matter*, vol. 15, pp. R109–R142, 2003.

- [21] M. Schubert, T. E. Tiwald, and C. M. Herzinger, "Infrared dielectric anisotropy and phonon modes of sapphire," *Physical Review B*, vol. 61, no. 12, pp. 8187–8201, 2000.
- [22] V. G. Kravets, "Polaron interpretation of the magnetorelectance effect in insulating α -Al₂O₃," *Physical Review B*, vol. 72, no. 6, Article ID 064303, 2005.
- [23] B. G. Park, T. Banerjee, J. C. Lodder, and R. Jansen, "Tunnel Spin polarization versus energy for clean and doped Al₂O₃ barriers," *Physical Review Letters*, vol. 99, no. 21, Article ID 217206, 2007.
- [24] S. O. Valenzuela, D. J. Monsma, C. M. Marcus, V. Narayana-murti, and M. Tinkham, "Spin polarized tunneling at finite bias," *Physical Review Letters*, vol. 94, no. 19, Article ID 196601, 2005.